

THREE-DIMENSIONAL IRREGULAR-GRID
FINITE DIFFERENCE MODEL OF WIND INDUCED
WATER LEVEL FLUCTUATIONS AND CURRENTS
IN A HOMOGENEOUS LAKE WITH APPLICATIONS
TO THE LAKE OF GENEVA

THÈSE N° 335 (1979)

PRÉSENTÉE AU DÉPARTEMENT DU GÉNIE CIVIL

ÉCOLE POLYTECHNIQUE FÉDÉRALE DE LAUSANNE

POUR L'OBTENTION DU GRADE DE DOCTEUR ÈS SCIENCES TECHNIQUES

PAR

SEBASTIAN WOLFGANG BAUER

Diplom-Ingenieur, Universität für Bodenkultur, Vienne, Autriche
Master of Science, Lehigh University, Bethlehem, États-Unis d'Amérique
originaire d'Autriche

acceptée sur proposition du jury :

Prof. W.H. Graf, rapporteur

Prof. C.H. Mortimer, corapporteur

Prof. J. Sündermann, corapporteur

M. Ch. Emmenegger, Dr ès sc. nat., corapporteur

Lausanne EPFL

1979

to Carol

Ariane

Mutti

Il y a longtemps de cela, c'était en août 1875, j'étais assis sur une pierre de la grève à Romanshorn, et je suivais de l'œil le flotteur de mon plémyramètre qui oscillait sous l'impulsion des seiches du lac de Constance. Un habitant de la ville, un instituteur, je crois, qui m'avait vu stationner, sans motif apparent, pendant quelques heures sur cette plage marécageuse, me questionna sur mes recherches ; je lui expliquai de mon mieux le phénomène des seiches et le but de mes études, mais quand il termina par un : « Zu was nützt das ? » A quoi cela sert-il ? je fus, je l'avoue, un peu interloqué. J'essayai de lui dire que je m'appliquais à la solution d'un problème de la nature ; je ne sus pas lui indiquer d'utilité immédiate ou pratique, et mon interlocuteur se retira évidemment peu satisfait. Il avait l'air de voir en moi « un Monsieur qui ne craint pas de perdre son temps. » — Il est vrai que j'ai consacré à ces recherches bien des heures, bien des journées, bien des années de ma vie. Mais j'avoue que, dans mon for intérieur, je ne me suis jamais senti humilié d'avoir dépensé autant de cette demée précieuse entre toutes, le temps qui s'écoule et ne revient pas, à un thème sans utilité immédiate et pratique. La recherche désintéressée des faits et des lois de la nature n'est pas un travail vain et sans résultat : la grandeur de l'homme ne réside-t-elle pas en partie dans cette curiosité singulière qui l'entraîne à surprendre et à comprendre les secrets de la nature qui l'entoure ? n'est-ce pas une noble tâche que la recherche de la vérité, sous quelque forme qu'elle se présente à nous ?

N'est-ce pas quelque chose d'avoir trouvé une explication plausible des grandes seiches de Genève et une solution satisfaisante du problème de l'Euripe ?

Mais il y a plus, et c'est là une des beautés de nos études scientifiques. Toute recherche, quelque désintéressée qu'elle paraisse au premier abord, peut amener, par des voies souvent bien détournées, à des résultats pratiques et utiles. Notre étude des seiches peut, elle aussi, avoir son utilité pratique. Quand il sera définitivement démontré que les mouvements de balancement de l'eau des lacs répondent aux lois générales de la mécanique pure, que l'oscillation des seiches suit le rythme que Merian a déduit des équations différentielles de la mécanique analytique de Lagrange, ou le rythme que M. du Boys a tiré de considérations d'hydraulique supérieure ; quand nous aurons trouvé une confirmation de quelques données de la théorie pure par l'observation directe d'oscillations qui mettent en mouvement de balancement aussi bien la masse énorme des 89 milliards de mètres du Léman, que les quelques litres d'eau de nos auges d'expérimentation, n'aurons-nous pas là une vérification précieuse ? Sur une échelle vraiment gigantesque, nous aurons la preuve de quelques-unes des lois qui sont à la base de la science humaine ; nous aurons, dans la faible mesure de nos forces, donné une certitude nouvelle au fondement scientifique sur lequel est bâti tout l'édifice du travail de l'humanité agissante, de l'humanité active et industrielle.

Mon cher inconnu de Romanshorn, à ta question : « Wozu nützt es ? » je réponds : « Es nützt doch etwas ».

Table of contents

	Page
List of figures	ii
List of tables	vii
Acknowledgements	viii
Abstract	x
Zusammenfassung	x
Résumé	xi
1. Introduction	1
1.1 Seiches	1
1.2 Mathematical model	4
2. Description of the mathematical model	6
2.1 The hydrodynamic equations	6
2.2 Lake surface (wind)- and lake bottom (bed) shear stress	11
2.3 The finite difference equations	13
2.4 Evaluation of derivatives	16
2.4.1 Vertical derivatives	16
2.4.2 Horizontal derivatives	17
2.5 Lateral boundary condition	19
2.6 Smoothing of calculation results	20
3. Application of mathematical model to hypothetical test lake	22
3.1 Description of computer programs	22
3.1.1 Program FIDI \overline{G} R	22
3.1.2 Program CIRCUL	27
3.2 Model simulation for test lake	29
3.2.1 Discussion of simulation results for three points	30
3.2.2 Discussion of simulation results for entire lake	36
3.3 Conclusions from the test-lake simulation	38
4. Earlier work on seiches and surges in the Léman	41
4.1 Forel	41
4.2 Doodson et al.	51
4.3 Service fédéral des eaux	53
4.4 Mortimer	61
4.5 Concluding remarks on earlier work on Léman seiches	66
5. Mathematical simulations for the Léman	68
5.1 Introductory remarks	68
5.1.1 Geometrical representation of the Léman	69
5.1.2 Choice and discussion of principal constants	72
5.2 Simulation of a Bise including determination of wind shear stress coefficient and discussion of wind set-up in the Léman	73

	Page	
5.3	Determination of period and node of the principal Léman seiche	87
5.3.1	Determination of period	87
5.3.2	Determination of the position of the node	89
5.4	Examination of stability of the coarse-grid model of the Léman	93
5.5	Investigation of the connection between grid configuration, numerical stability and the damping of seiche motion	98
5.6	Application of a "smoothed" Léman grid	113
5.6.1	Construction of a smoothed Léman grid	116
5.6.2	Simulation using the "smoothed-irregular" Léman grid illustrated in Figures 66-68	118
5.6.3	Comparison of spectra from observed and simulated water level fluctuations	124
5.6.3.1	Preparation of data for spectral analysis	130
5.6.3.2	Spectral analysis	131
6.	Summary and conclusions	139
	Appendix - Derivation of equation 28	141
	System of units	151
	List of symbols	152
	Literature	154
	Curriculum vitae	159

List of figures

No	Title of figure	Page
1	Definition sketch for vertical integration in single layered lake	9
2	Definition sketch for vertical integration in multilayered lake	9
3	Definition sketch for angle of wind direction	12
4	Definition of layers for vertical derivatives	16
5	Irregular finite difference grid	17
6	Point within a rectangular grid	19
7	Determination of boundary vectors	19
8	Grid definition for area and volume calculation	21

No.	Title of figure	Page
9	Plan view of irregular finite difference grid of test lake	24
10	Depth and number of layers of one-layer test lake including boundary tangents	24
11	Depth and number of layers of three-layer test lake including boundary tangents	25
12	Three dimensional grid of test lake	25
13	Scales and list of parameters for one-layer formulation	26
14	Scales and list of parameters for three-layer formulation	27
15	Simulation for test lake with the one-layer formulation	28
16	Simulation for test lake with the three-layer formulation	29
17	Simulation of wind-induced, unsteady currents in a homogeneous lake	32-36
18	Site of discovery of Léman-seiches by F.A. Forel	42
19	Historical map of the Léman	44
20	Uninodal transverse seiches at Morges observed by Forel	44
21	Binodal transverse seiches at Morges observed by Forel	44
22	Dicrote transverse seiches at Morges observed by Forel	45
23	Seiches of various types recorded at Geneva, Morges and Rolle, observed by Plantamour, Sarasin and Forel	45
24	Occurrence of longitudinal uninodal seiches and transverse uninodal and transverse dicrote seiches at Morges observed by Forel	46
25	Superposition of various simultaneous seiches observed at Geneva and Morges by Plantamour and Forel	46

No.	Title of figure	Page
26	Longitudinal uninodal seiches at Geneva observed by Plantamour	48
27	Positions of nodes and anti-nodes of longitudinal Léman seiches as determined by Forel	50
28	Vertical displacements of longitudinal Léman seiches according to Doodson et al. (1920)	52
29	Positions of nodes of longitudinal Léman seiches according to Doodson et al. (1920) and Forel (1895)	52
30	Limmigraphs existing in 1950 on the Léman	53
31	Example of extraordinary seiches registered by the Swiss Service fédéral des eaux	54
32	Example of simultaneous records of Léman seiches on 11-12/2/1950	56-57
33	Example of simultaneous records of Léman seiches on 27-28/7/1950	58-59
34	Variation of seiche period with mean water level in the Léman	60
35	Wind set-up in the Léman caused by the "Bise" on 15-16/11/1949	62
36	Wind set-up in the Léman caused by the "Bise" on 17-19/1/1950	62
37	Wind set-up in the Léman caused by the "Vent" on 25-28/9/1952	63
38	Water levels along the Léman shores during various types of wind set-ups	64
39	Mortimer's analysis of a uninodal longitudinal seiche in the Léman	65
40	Plan view of coarse irregular finite difference grid of the Léman	70
41	Depth and number of layers including boundary tangents of coarse finite difference grid of the Léman	70

No.	Title of figure	Page
42	Three-dimensional view of coarse irregular finite difference grid of the Léman consisting of 52 points	71
43	Three-dimensional view of a finite element grid of the Léman consisting of 579 points	71
44	Scales and list of parameters used in coarse Léman grid simulations	72
45	Simulation for the Léman using winds observed at Geneva with wind shear stress coefficients $c_w = 0,0035$, $c_w = 0,003$ and $c_w = 0,0025$	78
46	Simulation for the Léman using composite wind (70 % Geneva, 30 % Lausanne) with wind shear stress coefficients $c_w = 0,0035$, $c_w = 0,003$ and $c_w = 0,0025$	79
47	Simulation for the Léman using composite wind with shear stress coefficient $c_w = 0,003$, showing step numbers at which synoptic view has been produced	82
48	Simulation of wind induced water level fluctuations (storm surges) and currents in the Léman caused by the Bise on 17-19/1/1950	84-85
49	Simulation for the Léman using grid and parameters as shown in Figures 40-42 and Figure 44	88
50	Simulation of wind induced water level fluctuations and currents in the Léman	90-92
51	Range of simulated uninodal seiche nodes in the Léman with nodes N_F determined by Forel and N_D determined by Doodson et al.	93
52	Simulation for coarse Léman grid with $\alpha = 0,95$, showing water levels in three points	94
53	Simulation for coarse Léman grid with $\alpha = 0,90$ and $\alpha = 0,95$, showing water level fluctuations and currents in three points	96
54	Simulation for coarse Léman grid with $\alpha = 0,96$ and $\alpha = 0,99$, showing water level fluctuations and currents in three points	97

No.	Title of figure	Page
55	Rectangular-grid "box" lake	100
56	Seiches simulated for rectangular-grid "box" lake	102
57	Hexagonal-grid "box" lake	101
58	Seiches simulated for hexagonal-grid "box" lake	103
59	Hexagonal-grid "Léman-box" lake	104
60	Seiches simulated for hexagonal-grid "Léman-box" lake	106
61	Hexagonal-grid "Léman-like" lake	105
62	Seiches simulated for hexagonal-grid "Léman-like" lake	107
63	Seiches simulated for hexagonal-grid "Léman-like" lake with further variation of α and c_b	110-111
64	Regular hexagonal grid for the Léman with approximated frontiers	114
65	Regular hexagonal grid for the Léman with exact frontiers	114
66	Plan view of "smoothed-irregular" finite-difference grid of the Léman	115
67	Depth and number of layers including boundary tangents of "smoothed-irregular" finite difference grid of the Léman	115
68	Three-dimensional view of "smoothed-irregular" finite difference grid of the Léman consisting of 151 points	117
69	Seiches simulated for "smoothed-irregular" Léman grid	120-121
70	Seiches simulated for "smoothed-irregular" Léman grid with $\alpha = 0,9999999$	122
71	Demonstration of development of "aliasing" with increasing frequency when using constant sampling interval	125

No.	Title of figure	Page
72	Trace of data digitized from Figure 32 (in its original size) including least square trend lines	126-127
73	Trace of data digitized from Figure 32 with removed trends, ready for spectral analysis	128-129
74	Spectra for the observations and simulations at Geneva for the range of 0-1440 cycles/day	132
75	Spectra of observations and simulations for the stations Geneva, Coppet, St-Prex, Vevey, St-Gingolph and Thonon	134-136
76	Spectrum for observations at Les Grangettes	138
A1	Point P surrounded by points a-f in a regular triangular grid of spacing Δ	148

List of tables

No.	Title of table	Page
1	Principal seiche-periods of the Léman observed by Forel (1895)	43
2	Mean height of seiches reproduced in Figure 26	47
3	Longitudinal seiche periods of the Léman calculated by Doodson et al. (1920)	51
4	Longitudinal seiche periods of the Léman calculated by Mortimer (1979)	63
5	Wind- and water level observations for the Bise on 17-19/1/1950	75

Acknowledgements

The author is deeply indebted to Professor W.H. Graf, "rapporteur et directeur de thèse", for providing him with the opportunity to produce this dissertation within the historical framework of F.A. Forel's classical work on Léman seiches. Thanks are due also to Professor C.H. Mortimer, former (at present acting) director of the Center for Great Lakes Studies at the University of Wisconsin-Milwaukee, USA, who during his stays at the "Ecole Polytechnique Fédérale" (EPFL) greatly encouraged the author in his work. Professor Mortimer also acted as "corapporteur interne", and as such, many of his suggestions have been incorporated into the final version of this dissertation. Further thanks are to be extended to Professor J. Sündermann, director of the Institute of Oceanography at the University of Hamburg, Germany, who was first "corapporteur externe" of the present thesis and to Dr. Ch. Emmenegger, Service fédéral des Eaux, Berne, second "corapporteur externe". The Service fédéral des Eaux, Berne, is to be thanked for the data they have collected on the Léman. Without these data, verification of the model would have been impossible. They also permitted the author access to their coordinatograph. The work of this thesis was also partially sponsored by the Swiss National Science Foundation (FNSRS) under its special program "Fundamental problems of the water cycle in Switzerland".

This dissertation would not have been written had the author not met Dr. W.C. Thacker of the National Oceanic and Atmospheric Administration (NOAA), Miami, Florida, USA, who in an extensive correspondence introduced the author to the secrets of his method. Further help was provided by the discussions the author had with Dr. H.G. Ramming of the Institute of Oceanography at the University of Hamburg. Professor J. Descloux of the Department of Mathematics encouraged the author by showing his interest in assigning the author's model to G. Buchs as "Travail Pratique de Diplôme" for a stability analysis. Further mathematical advice was provided by Klaus D. Schmidt, University of Mannheim, Germany (formerly EPFL), by Dr. Y. Depeursinge and by J. Jaccard, both of the Department of Mathematics, EPFL.

The computational know-how required to perform the present work was acquired by the author initially at Lehigh University, Bethlehem, Pa., USA, while preparing a Master of Science thesis under Professor W.H. Graf and subsequently at the Hydrological Research Unit of the University of the Witwatersrand, Johannesburg, South Africa, under Professor D.C. Midgley. The author's colleagues there, Drs. I.P.G. Hutchison, H.W. Weiss, R.C. Johanson and W.V. Pitman provided the necessary environment to allow this specific experience.

All computer calculations for the present dissertation were performed at the Computer Center of the EPF-Lausanne. The computer-

drawn animated films were produced at the Computer Center of the Swiss Federal Institute of Technology (ETH) in Zurich. The transfer procedures required for the liaison between Lausanne and Zurich were provided by Monsieur S. Jeandrevin.

The author also wishes to thank Mme Barbara Svancar who with great patience and care did the sometimes very difficult typing of this dissertation. All figures not produced by the author on the computer were expertly drawn by Mme Pierrette Rosset. Professor C.H. Mortimer and the author's wife, Carol, were able to provide substantial improvements in style to the original english text. The author's friends and colleagues of the project "Lac Léman" J.-P. Prost and C. Perrinjaquet are to be thanked for providing the warm human relationship so essential for a productive working climate.

Finally the author wishes to thank his dear wife, Carol, to have followed him through three continents the way she did. To really appreciate this effort one must have done it oneself!

Abstract

Combining the neat representation of boundary geometry of finite element models with the advantage of fast numerical solution of finite difference models, an irregular-grid finite difference scheme was developed to solve the hydrodynamic equations of motion in a three-dimensional homogeneous lake. The operation of the model was first demonstrated by applying it in a one- and a three-layer formulation to a lake of arbitrary shape. With an initially coarse irregular grid, the model was then used to simulate water level fluctuations observed in the Lake of Geneva (Le Léman) during a 60-hour episode of strong north-easterly winds. It was found that numerical instabilities arising from the use of a completely irregular finite-difference grid can be largely eliminated if the grid is modified in such a way that each interior grid point is placed centrally with respect to all surrounding points. With a "smoothed-irregular" grid scheme, modified in this way, it was possible to reproduce in considerable detail the water level responses observed by Forel and others in the Léman, i.e., the surges generated by wind stress and the free oscillations (seiches) which follow.

DREIDIMENSIONALES NUMERISCHES MODELL ZUR SIMULATION VON WINDERZEUGTEN WASSERSPIEGELSCHWANKUNGEN UND STRÖMUNGEN IN EINEM HOMOGENEN SEE UNTER VERWENDUNG EINES UNREGELMÄSSIGEN FINITEN DIFFERENZENSCHEMAS MIT ANWENDUNGEN AUF DEN GENFERSEE

Zusammenfassung

Ein mathematisches Modell zur Lösung der hydrodynamischen Bewegungsgleichungen in einem dreidimensionalen homogenen See wurde vorgestellt. Das verwendete finite Differenzen-Schema erlaubt unter Anwendung eines unregelmässigen Gitters die geschmeidige numerische Darstellung der Geometrie von Seen, normalerweise nur bei finiten Element-Modellen möglich, mit der schnellen Rechenweise von finiten Differenzen-Modellen zu verbinden. Die Arbeitsweise des Modells wurde zuerst an einem willkürlich gewählten Test-See in einer ein- und in einer dreischichtigen Formulierung demonstriert. Unter Verwendung eines groben, unregelmässigen Gitters wurden dann Wasserspiegelschwankungen des Genfer-Sees (Le Léman), die während 60 Stunden starker nord-östlicher Winde beobachtet worden waren, simuliert. Weiterhin wurde gezeigt, dass durch Unregelmässigkeiten des Gitters erzeugtes instabiles Modellverhalten weitgehend mittels Platzierung jedes inneren Gitterpunktes in der Mitte seiner umliegenden Punkte eliminiert werden kann. Mit Hilfe eines solchen "gleichmässig-unregelmässigen" Gitters war es dann möglich, die von Forel und anderen beobachteten winderzeugten Wasserspiegelschwankungen und ihre nachfolgenden freien Schwingungen (Seiches) in beachtlichem Detail zu simulieren.

DEVELOPPEMENT D'UN MODELE TRIDIMENSIONNEL AUX DIFFERENCES FINIES
A MAILLES IRREGULIERES PERMETTANT DE SIMULER LES FLUCTUATIONS
DE LA SURFACE D'EAU ET LES COURANTS INDUITS PAR LE VENT DANS
UN LAC HOMOGENE AVEC APPLICATIONS AU LEMAN

Résumé

En associant l'élégance de la représentation géométrique des modèles aux éléments finis avec la rapidité d'exécution des modèles aux différences finies, un modèle aux différences finies à mailles irrégulières a permis de résoudre les équations hydrodynamiques du mouvement tridimensionnel dans un lac homogène. La démonstration du fonctionnement du modèle a été faite sur un lac de forme arbitraire en intégrant les équations sur une ou trois couches. A l'aide d'une maille irrégulière d'abord grossière, ce modèle a ensuite permis de simuler les fluctuations du plan d'eau observées sur le Lac de Genève (Le Léman) pendant une période de fortes bises de 60 heures. Les instabilités numériques provenant de l'utilisation de mailles complètement irrégulières ont pu être largement éliminées, en modifiant la maille de sorte que chaque point intérieur de la grille soit situé au centre de la maille formée par ceux qui l'entourent. Avec une telle grille à mailles "irrégulières-lissées" on a pu reproduire de façon très détaillée les réactions du plan d'eau observées par F.A. Forel et autres sur le Léman, à savoir les oscillations en masse générées par le frottement du vent et les oscillations libres (seiches) qui en résultent.

1. Introduction

F.A. Forel's pioneering work on the Lake of Geneva (Le Léman) has made this lake a classic object for study by limnologists. Apart from the fact that Forel invented the word "limnology", i.e., an oceanography of lakes (Forel, 1895), he is probably best known for his work on the periodic water level fluctuations in the Léman. It was, in fact, this work that made limnologists adopt the word "seiches" (an old Léman-region vernacular) for this phenomenon, and which prompted Chrystal's (1905) reference to Forel as the "Faraday of seiches". A review of other important "firsts" on the Léman is given by Mortimer (1979).

Seiches are free oscillatory movements of water in lakes and bays. Movement of real fluids can be described with the aid of the Navier-Stokes equations. Analytical solutions of the Navier-Stokes equations exist only for simplified situations. If it is desired to solve the Navier-Stokes equations for irregular basins, i.e., for natural lakes, numerical solution procedures must be used. One of the earliest applications of numerical methods for the simulation of wind driven currents and water levels is given by Hansen (1956). Since then, a large number of mathematical models have been developed simulating currents and water levels in oceans, estuaries, lakes and rivers.

1.1 Seiches

The phenomenon of periodic water level fluctuations of lakes has been observed for a long time. The earliest european record of such fluctuations stems from Lake Constance, where on February 23, 1549, Christoph Schulthaiss (Forel, 1893) observed a series of extraordinary seiches with an amplitude of nearly one meter in the narrows of Constance. These seiches were accompanied by dramatic reversals of the normal current direction at this location. Other early observations of seiches were made on November 1, 1755, in northwestern Europe; these being caused

by the great earthquake that devastated Lisbon on the same day (Hutchinson, 1975).

The seiches of the Léman are particularly conspicuous in the vicinity of Geneva due to the narrowing of the lake near that city. Periodic water surface fluctuations of the Léman were first reported by Fatio de Duillier (1730), who mentions three or four seiches attaining a height of about five feet near the harbour of Geneva on September 16, 1600. After this date many more observations of water level fluctuations were recorded on the Léman (Hutchinson, 1975; Forel, 1895). It was however only due to F.A. Forel's painstaking personal observations over many years and his analytic work that the mechanism of these seiches became understood. Forel was also able to show that seiches may exist in seas and oceans by resolving the classic problem of the alternating, violent currents in the straits of Euripe (Forel, 1897) which for over 2300 years had remained unsolved. To study the seiches of the Léman in detail, Forel constructed various portable limnigraphs allowing very precise measurement of changes in water level. In 1876 Forel installed a stationary limnigraph at Morges (Forel, 1876b), which he kept operational until 1884 (Forel, 1895). Analysing his data containing records of seiches of many different periods, he came to the conclusion that seiches are standing waves in the Léman, oscillating between various extremities of the lake. The experimental proof for his hypothesis was obtained by Forel in 1873.

Forel distinguished between "dénivellations continues" (Forel 1895, p. 29), i.e., temporary deviations or "set-ups" of the lake surface from its equilibrium position caused by meteorological forces, notably wind stress on the water surface and "dénivellations rythmiques" (Forel 1895, p. 39) which he describes as follows: "Sous l'influence d'actions mécaniques diverses, l'eau du lac peut subir une dénivellation temporaire très rapide, dont l'impulsion est assez prompte pour qu'elle se transforme en un mouvement rythmique d'oscillation, de ba-

lancement. Sous une impulsion violente et rapide, l'eau subit une dénivellation qui soulève le lac à une des extrémités en le déprimant à l'autre; l'action dénivellatrice ne dure pas et le lac tend à reprendre son niveau; mais au lieu de s'arrêter à l'horizontalité, sous l'entraînement du mouvement acquis, il dépasse ce niveau, et pour revenir à l'état d'équilibre stable, il décrit une série d'oscillations de plus en plus faibles. Ces oscillations rythmiques, ou pendulaires, sont connues sur les bords du lac Léman sous le nom de seiches." Although the term "seiche" has later been loosely applied to lake oscillations in general, a clear distinction should be made between (a) the impulsive oscillations generated during the forcing phase and (b) the free oscillations which follow when the force is removed. In modern terminology the term "surge" or "storm surge" has been reserved for (a) and the term "seiche" for (b). However, in a storm, the distinction between (a) and (b) is not always clear; and the present thesis, concerned with simulation of the generation of seiches by wind impulses therefore treats both (a) and (b) under the general heading of "seiche", i.e., the manner in which (in Forel's sense) "l'impulsion ... se transforme en un mouvement rythmique d'oscillation, de balancement". The model can thus be viewed as a combination of a storm surge model and a seiche model, using the term "seiche" to cover both phases of a lake's oscillatory response to the applied force.

Searching for a mathematical expression for the calculation of the period of seiches, Forel discovered, in 1876, that the formula of Merian (1828) for water surface oscillations in a rectangular vessel was also valid for the seiches of the Léman; thus giving the proof that the two types of oscillations follow essentially the same principle. In cases where the seiche periods of the Léman did not correspond to Merian's formula, Forel was able to show that such seiches were either binodal seiches or superpositions of seiches with different periods. In 1891 Du Bois (1891a) presented an extension of Merian's formula to allow calculation of seiche periods in irregular basins, which Du Bois

(1891b) and Forel applied to the Léman and to the lakes of Zurich and Constance. Further analytical progress on the mathematical determination of seiche periods was made by Chrystal (1904, 1905) for lakes with a basin of a mathematically treatable shape. However, numerical methods proved to be more convenient to use, providing additional information on vertical and horizontal displacements (Defant, 1918, 1961). Using a method developed by Proudman, Doodson et al. (1920) calculated seiche periods for the Léman with very good results. More recent information concerned with the seiches of the Léman is found in a report by the Service fédéral des eaux (1954) and in a paper by Mortimer (1979).

1.2 Mathematical model

To simulate water surface elevations and -currents in a homogeneous, shallow lake, a mathematical model has been developed by Bauer (1979). The present model is a further step in the research program of the Hydraulics Laboratory (LHYDREP) of the Swiss Federal Institute of Technology (EPFL) in Lausanne. In this project on lake currents, mathematical models are being developed, and a measuring program to allow for testing of these models is being undertaken. A steady state finite element model for a homogeneous lake was reported by Bauer et al. (1977); subsequently a calibration with field data of the Léman was presented by Bauer and Graf (1979). The measuring campaign is described by Prost et al. (1977) and by Graf et al. (1979). Data handling and visualization is described by Bauer and Perrinjaquet (1979).

At present there already exists a large number of mathematical models for the simulation of lake currents. A general survey of models for lakes and shallow seas is given by Lindijer (1976). The reason for developing still another model at LHYDREP is that a new method of solution (Thacker, 1977a) has recently be-

come available, offering promising avenues for future research.

The present model is a first attempt at LHYDREP to simulate time dependent lake circulation. Due to the fact that repetitive calculations for the simulation of unsteady flow are necessary, it is highly desirable to develop an algorithm, which requires the least possible amount of numerical operations. Generally two methods for solving the hydrodynamic equations describing flows in shallow bodies of water are available, i.e., the finite difference method and the finite element method. Thacker (1977b) found, comparing the two methods, that the computational requirements for the finite element method are about one order of magnitude larger than those for the finite difference method. One reason for this is that finite element computations, being time implicit, require time consuming matrix inversions and a smaller time step to remain stable (Thacker, 1978a, 1978b).

Comparing however finite element models with conventional, i.e., rectangular, finite difference models, a major disadvantage of finite difference models is found to be their rather inelegant way of representing the boundary lines of a given geometry. This can become a serious problem, if one is required to simulate flow situations in bodies of water such as estuaries, where there is the large, relatively uniform sea, which could well be represented by a rather coarse grid and an often very distorted shore line, which can be represented properly only by a rather fine grid. One way of handling such a situation has been suggested by Ramming (1973), whereby rectangular grids of different mesh size are combined. In a series of applications, Ramming (1976, 1978a, 1978b) demonstrates the workability of such an approach. Some problems however are created at the frontiers between the areas of different mesh size (Ramming, 1976). With finite element models, problems of representing geometry normally do not occur since a completely irregular grid can be selected and thus any complicated geometry can

readily be represented.

Combining the advantages of a smooth geometrical representation of finite element models with the advantages of fast execution of finite difference models, Thacker (1977a) proposed an irregular-grid finite-difference model. Thacker demonstrated successfully the power of his technique by applying it to one- (Thacker 1978a) and two-dimensional (Thacker 1977a, 1978b), linearized shallow water wave equations. In a further article, Thacker (1979) applied his method to the full hydrodynamic, nonlinear, two-dimensional and vertically averaged equations governing a storm surge. He then applied it to the simulation of a storm surge in an ocean bay.

In the present research, the Thacker finite difference method is applied to the equations governing the motions in a shallow, homogeneous lake. The model has been developed such that it can be run either for a lake represented by one layer only, as in Thacker's (1979) model, or for a lake which has been subdivided into several horizontal layers.

2. Description of the mathematical model

2.1 The hydrodynamic equations

The motion in a homogeneous, shallow lake on a large scale can be described by the following equations (Liggett, 1970):

$$\rho \left[\frac{\partial \tilde{u}}{\partial t} + \frac{\partial}{\partial x} (\tilde{u}^2) + \frac{\partial}{\partial y} (\tilde{u}\tilde{v}) + \frac{\partial}{\partial z} (\tilde{u}\tilde{w}) - f\tilde{v} \right] = - \frac{\partial p}{\partial x} + \frac{\partial}{\partial z} \left(\eta \frac{\partial \tilde{u}}{\partial z} \right) + \frac{\partial}{\partial x} \left(\epsilon \frac{\partial \tilde{u}}{\partial x} \right) + \frac{\partial}{\partial y} \left(\epsilon \frac{\partial \tilde{u}}{\partial y} \right) \quad \dots \quad (1)$$

$$\rho \left[\frac{\partial \tilde{v}}{\partial t} + \frac{\partial}{\partial x} (\tilde{u}\tilde{v}) + \frac{\partial}{\partial y} (\tilde{v}^2) + \frac{\partial}{\partial z} (\tilde{v}\tilde{w}) + f\tilde{u} \right] = - \frac{\partial p}{\partial y} + \frac{\partial}{\partial z} \left(\eta \frac{\partial \tilde{v}}{\partial z} \right) + \frac{\partial}{\partial x} \left(\epsilon \frac{\partial \tilde{v}}{\partial x} \right) + \frac{\partial}{\partial y} \left(\epsilon \frac{\partial \tilde{v}}{\partial y} \right) \quad \dots \quad (2)$$

$$\rho g = - \frac{\partial p}{\partial z} \quad (3)$$

$$\frac{\partial \tilde{u}}{\partial x} + \frac{\partial \tilde{v}}{\partial y} + \frac{\partial \tilde{w}}{\partial z} = 0 \quad (4)$$

where

\tilde{u} , \tilde{v} and \tilde{w} are the velocity components in the x, y and z directions respectively

with x being positive towards east,

y being positive towards north and

z being positive upwards,

t is the time,

f is the Coriolis parameter,

ρ is the density of the water,

p is the local pressure,

η and ϵ are the vertical and horizontal components of the eddy viscosity and

g is the acceleration of gravity.

Equation 4 is the equation of continuity for an incompressible fluid. Equations 1 and 2 have been derived under the assumption that, on a large scale, an "eddy" viscosity, several orders in magnitude greater than the molecular viscosity, can parameterize the effects of turbulent fluctuations of the movement in lakes and oceans (Neumann and Pierson, 1966). In the derivation of equation 3, all dynamic effects have been neglected and it expresses thus the hydrostatic equilibrium. For a shallow lake, this is a valid assumption.

Equations 1 and 2 can be further simplified by considering the following:

- (a) the inertia forces are small when compared with the Coriolis forces, i.e., the Rossby number is small. In this case equations 1 and 2 may be linearized:

$$\frac{\partial}{\partial x}(\tilde{u}\tilde{v}) = 0, \quad \frac{\partial}{\partial y}(\tilde{u}\tilde{v}) = 0 \quad \text{etc.}$$

(b) in a shallow lake, the change of vertical shear in the horizontal directions is small compared to the change of horizontal shear in the vertical direction (depth):

$$\frac{\partial}{\partial x} \left(\epsilon \frac{\partial \tilde{u}}{\partial x} \right) = 0, \quad \frac{\partial}{\partial y} \left(\epsilon \frac{\partial \tilde{u}}{\partial y} \right) = 0 \quad \text{etc.}$$

(c) the vertical component of the eddy viscosity is assumed to be constant over the entire lake depth:

$$\frac{\partial}{\partial z} \left(\eta \frac{\partial \tilde{u}}{\partial z} \right) = \eta \frac{\partial^2 \tilde{u}}{\partial z^2} \quad \text{etc.}$$

(d) the influence of external in- and outflows of a lake is negligible. Thus, only in the immediate vicinity of river mouths are equations 1-4 not applicable.

With the above simplifications and assumptions, the system of equations describing wind induced currents in a homogeneous shallow lake becomes:

$$\rho \left(\frac{\partial \tilde{u}}{\partial t} - f \tilde{v} \right) = - \frac{\partial p}{\partial x} + \eta \frac{\partial^2 \tilde{u}}{\partial z^2} \quad (5)$$

$$\rho \left(\frac{\partial \tilde{v}}{\partial t} + f \tilde{u} \right) = - \frac{\partial p}{\partial y} + \eta \frac{\partial^2 \tilde{v}}{\partial z^2} \quad (6)$$

$$\rho g = - \frac{\partial p}{\partial z} \quad (3)$$

$$\frac{\partial \tilde{u}}{\partial x} + \frac{\partial \tilde{v}}{\partial y} + \frac{\partial \tilde{w}}{\partial z} = 0 \quad (4)$$

The above equations may be further manipulated to reduce the number of equations to three by integrating equation 3 between the lake bottom and the water surface as shown in Figure 1. Thus equation 3 becomes

$$\rho g (H - z) = p \quad (7)$$

where H is the water surface elevation.

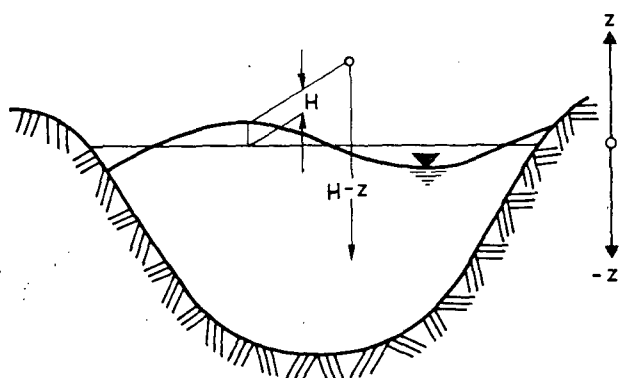


Figure 1:
Definition sketch for
vertical integration
in single layered
lake

Substituting equation 7 in equations 5 and 6 gives

$$\frac{\partial \tilde{u}}{\partial t} - f\tilde{v} = -g \frac{\partial H}{\partial x} + \frac{\eta}{\rho} \frac{\partial^2 \tilde{u}}{\partial z^2} \quad (8)$$

$$\frac{\partial \tilde{v}}{\partial t} + f\tilde{u} = -g \frac{\partial H}{\partial y} + \frac{\eta}{\rho} \frac{\partial^2 \tilde{v}}{\partial z^2} \quad (9)$$

thus eliminating equation 3.

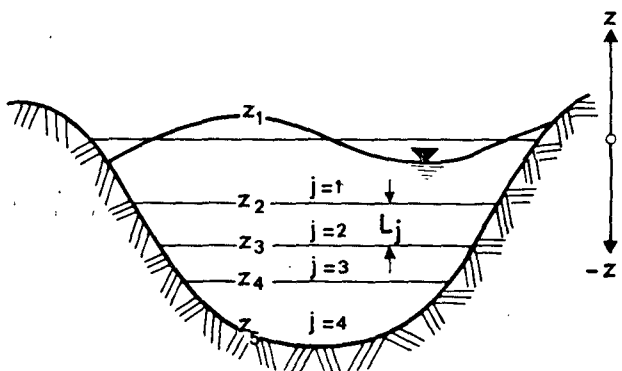


Figure 2:
Definition sketch for
vertical integration
in multilayered lake

Defining the volume transports per unit width in a layer, j , of a multilayered lake as shown in Figure 2, by

$$u_j = \int_{z_{j+1}}^{z_j} \tilde{u} dz = (\bar{u}L)_j \quad (10)$$

$$v_j = \int_{z_{j+1}}^{z_j} \tilde{v} dz = (\bar{v}L)_j \quad (11)$$

equation 4 becomes by integration and summation

$$\sum_{j=1}^M \left(\frac{\partial u}{\partial x} + \frac{\partial v}{\partial y} \right)_j + \frac{\partial H}{\partial t} = 0 \quad (12)$$

where L_j is the thickness of a layer j and
 M is the number of layers.

Similarly, if the viscosity terms in equations 8 and 9 are replaced by unit-mass shear stresses ${}^* \tau_x$ and ${}^* \tau_y$ at the layer interfaces (as shown in Figure 2) in the x and y directions respectively, equations 8 and 9 yield

$$\left[\frac{\partial u}{\partial t} - fv = -gL \frac{\partial H}{\partial x} + ({}^* \tau_{x_{top}} - {}^* \tau_{x_{bottom}}) \right]_{j=1,M} \quad (13)$$

$$\left[\frac{\partial v}{\partial t} + fu = -gL \frac{\partial H}{\partial y} + ({}^* \tau_{y_{top}} - {}^* \tau_{y_{bottom}}) \right]_{j=1,M} \quad (14)$$

where the subscript $*$ indicates shear stress per unit mass and the subscripts "top" and "bottom" indicate the top- and bottom boundaries of a layer j respectively.

Assuming that Newton's law of (laminar) friction is applicable also to the turbulent case, the above shear stresses can be introduced as follows:

$$\tau_x = \eta \frac{\partial \tilde{u}}{\partial z} \quad \text{or} \quad \tau_x / \rho = \frac{\eta}{\rho} \frac{\partial \tilde{u}}{\partial z} = {}^* \tau_x \quad (15)$$

$$\tau_y = \eta \frac{\partial \tilde{v}}{\partial z} \quad \text{or} \quad \tau_y / \rho = \frac{\eta}{\rho} \frac{\partial \tilde{v}}{\partial z} = {}^* \tau_y \quad (16)$$

In terms of transports, equations 15 and 16 may be approximated by

$${}^* \tau_x = \frac{\eta}{\rho} \partial \left(\frac{u}{L} \right) / \partial z \quad (17)$$

$${}^* \tau_y = \frac{\eta}{\rho} \partial \left(\frac{v}{L} \right) / \partial z \quad (18)$$

It should furthermore be noted that in equations 13 and 14, using vectorial notation,

$$[{}^* \vec{\tau}_{\text{top}}]_{j=1} = {}^* \vec{\tau}_{\text{wind}} \quad (19)$$

$$[{}^* \tau_{\text{bottom}}]_{1 \leq j < M} = [{}^* \tau_{\text{top}}]_{1 < j+1 \leq M} \quad (20)$$

$$[{}^* \vec{\tau}_{\text{bottom}}]_{j=M} = {}^* \vec{\tau}_{\text{bed}} \quad (21)$$

where ${}^* \vec{\tau}_{\text{wind}}$ and ${}^* \vec{\tau}_{\text{bed}}$ are shear stress vectors at the water surface due to wind and at the lake bottom (bed) due to bed shear stress respectively.

As can be seen in Figure 2, the number of layers is not constant over the entire lake but depends on the position of the point considered in the lake. Furthermore, equations 12, 13 and 14 are still subject to geometric boundary conditions which will be discussed later.

2.2 Lake surface (wind)- and lake bottom (bed) shear stress

The surface shear stress due to wind action on a lake is generally given by

$$\vec{\tau} = c_w \rho_a \vec{V} |\vec{V}| \quad (22)$$

where $\vec{\tau}$ is a wind shear vector,
 c_w is a dimensionless wind shear coefficient,
 ρ_a is the density of air and
 \vec{V} is a wind velocity vector

Following the conventions for wind directions as shown in Figure 3, the wind shear stress per unit mass, ${}^* \tau$, is given by

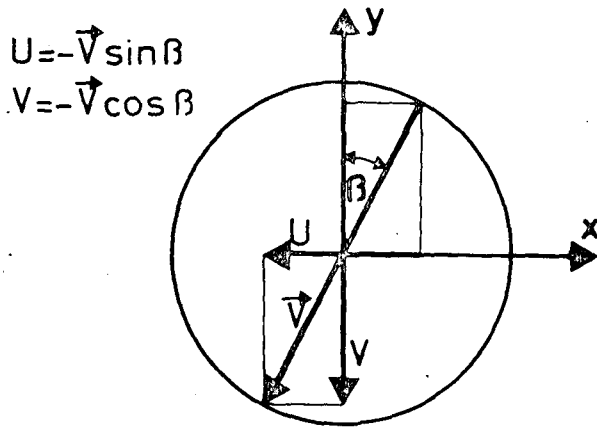


Figure 3:

Definition sketch for angle of wind direction

$$*\tau_{x_{wind}} = c_w \frac{\rho_a}{\rho} U \sqrt{U^2 + V^2} \quad (23)$$

$$*\tau_{y_{wind}} = c_w \frac{\rho_a}{\rho} V \sqrt{U^2 + V^2} \quad (24)$$

where U and V are the x and y components of the wind velocity respectively.

Similarly, the lake bed stress is given by

$$\vec{\tau} = c_b \rho \frac{\vec{v}}{L} \left| \frac{\vec{v}}{L} \right| \quad (25)$$

and

$$*\tau_{x_{bed}} = c_b u \sqrt{u^2 + v^2} / L^2 \quad (26)$$

$$*\tau_{y_{bed}} = c_b v \sqrt{u^2 + v^2} / L^2 \quad (27)$$

where $\vec{\tau}$ is a bottom shear vector,

c_b is a dimensionless lake bed shear stress coefficient and \vec{v} is a water transport vector (in equations 25-27 the division by L is necessary to obtain mean velocities rather than transports).

2.3 The finite difference equations

Equations 12, 13 and 14 can readily be expressed in finite differences. It should be noted however, that if the numerical approximation is to be stable, the spatial grid must be such that the fastest moving disturbance occurring will not pass beyond one grid point within one time step, Δt . In the model described herein the fastest moving disturbance is associated with a surface gravity wave (see for example Elliott, 1976). If one assumes that the grid is uniform with a mesh size of Δx , that there is no depth variation and that there are no boundaries, stability of a finite difference scheme is supposedly guaranteed (Thacker, 1978b), if

$$\Delta t \leq \frac{1,7\Delta x}{\sqrt{gD}} \quad (28)$$

where D is the depth of water.

A derivation of equation 28 and some concluding remarks on the problem of numerical stability of the present model are given in an appendix.

It can be seen from equation 28 that if it is desired to use an optimum, i.e., near maximum allowable constant time step for the entire region, the distance between grid points in an irregular grid should be approximately proportional to the square root of the depth at a point. Also, in order to avoid time consuming matrix inversion techniques, it is highly desirable that the variables H , u and v of equations 12, 13 and 14 be expressed explicitly. Finally, in order to obtain best results, it has been suggested (Simons, 1973; Sündermann, 1966; Thacker, 1977a, 1978a, 1978b, 1979) that a "leap-frog" time scheme be used, in which velocities and water levels are evaluated at times which are $0,5 \Delta t$ time steps apart.

As has been remarked, equation 28 is valid only for regular grids. Thacker (1977a) found that instabilities might still

occur if a very irregular grid is used, and this in spite of the fact that equation 28 has been satisfied. Also, Sündermann (1966) states that equations of the type of equation 28 (also known as Courant's condition) are no longer strictly applicable in the case of non-linear equations such as used in the present model.

With n indicating positions in time, the finite difference forms of equations 13, 14 and 12 become, respectively:

$$[u^{n+\frac{1}{2}} = u^{n-\frac{1}{2}} + \Delta t (fv^{n+\frac{1}{2}} - gL \frac{\Delta H^n}{\Delta x} + * \tau_{x_{top}}^{n-\frac{1}{2}} - * \tau_{x_{bottom}}^{n-\frac{1}{2}})]_{j=1,M} \quad (29)$$

$$[v^{n+\frac{1}{2}} = v^{n-\frac{1}{2}} + \Delta t (-fu^{n+\frac{1}{2}} - gL \frac{\Delta H^n}{\Delta y} + * \tau_{y_{top}}^{n-\frac{1}{2}} - * \tau_{y_{bottom}}^{n-\frac{1}{2}})]_{j=1,M} \quad (30)$$

$$H^{n+1} = H^n - \Delta t \sum_{j=1}^M \left(\frac{\Delta[\frac{1}{2}(u^{n+\frac{1}{2}} + u^{n-\frac{1}{2}})]}{\Delta x} + \frac{\Delta[\frac{1}{2}(v^{n+\frac{1}{2}} + v^{n-\frac{1}{2}})]}{\Delta y} \right) \quad (31)$$

In equations 29-30, the shear stress at the upper layer interface is given for $j = 1$ by

$$* \tau_{x_{top}}^{n-\frac{1}{2}} \approx * \tau_{x_{wind}}^n = c_w \frac{\rho_a}{\rho} U^{n+\frac{1}{2}} |V^{n-\frac{1}{2}}| \quad (32)$$

$$* \tau_{y_{top}}^{n-\frac{1}{2}} \approx * \tau_{y_{wind}}^n = c_w \frac{\rho_a}{\rho} V^{n+\frac{1}{2}} |V^{n-\frac{1}{2}}| \quad (33)$$

Similarly, the shear stress at the lower layer interface for $j = M$ is given by

$$* \tau_{x_{bottom}}^{n-\frac{1}{2}} \approx * \tau_{x_{bed}}^n = [c_b u^{n+\frac{1}{2}} \sqrt{(u^{n-\frac{1}{2}})^2 + (v^{n-\frac{1}{2}})^2} / L^2]_{j=M} \quad (34)$$

$$* \tau_{y_{bottom}}^{n-\frac{1}{2}} \approx * \tau_{y_{bed}}^n = [c_b v^{n+\frac{1}{2}} \sqrt{(u^{n-\frac{1}{2}})^2 + (v^{n-\frac{1}{2}})^2} / L^2]_{j=M} \quad (35)$$

The solution of the system of equations 29-31 proceeds in such a way that first all variables at times $n-\frac{1}{2}$ and n are initialized, i.e., they are either assumed to be zero or they are assigned reasonable initial values. Then, starting with equations 29 and 30, all velocities at time $n+\frac{1}{2}$ can be evaluated. The velocity gradients at time $n+\frac{1}{2}$ can now be calculated, permitting solution of equation 31 for the water surface at time $n+1$, and performing this operation for each point of the model.

At first sight it might be thought that equations 29 and 30 require an implicit solution, since the unknowns $u^{n+\frac{1}{2}}$ and $v^{n+\frac{1}{2}}$ appear on both sides of both equations. This however is not the case, as equations 29 and 30 can be rewritten such that the unknowns are given in explicit form.

Denoting, with $*\tau_{\text{bottom}} = 0$

$$[u_T = u^{n-\frac{1}{2}} + \Delta t (-gL \frac{\Delta H^n}{\Delta x} + *\tau_{x_{\text{top}}}^{n-\frac{1}{2}} - *\tau_{x_{\text{bottom}}}^{n-\frac{1}{2}})]_{j=1,M} \quad (36)$$

$$[v_T = v^{n-\frac{1}{2}} + \Delta t (-gL \frac{\Delta H^n}{\Delta y} + *\tau_{y_{\text{top}}}^{n-\frac{1}{2}} - *\tau_{y_{\text{bottom}}}^{n-\frac{1}{2}})]_{j=1,M} \quad (37)$$

and with $c_b = 0$

$$[d = 1 + \Delta t c_b \sqrt{(u^{n-\frac{1}{2}})^2 + (v^{n-\frac{1}{2}})^2 / L^2}]_{j=1,M} \quad (38)$$

whereby all terms on the right hand sides of equations 36-38 are known, equations 29 and 30 can be written

$$[u^{n+\frac{1}{2}} = (\Delta t f v^{n+\frac{1}{2}} + u_T) / d]_{j=1,M} \quad (39)$$

$$[v^{n+\frac{1}{2}} = (-\Delta t f u^{n+\frac{1}{2}} + v_T) / d]_{j=1,M} \quad (40)$$

Substituting equation 40 into equation 39

$$[u^{n+1/2} = (\Delta t f v_T/d + u_T)/(d + \Delta t^2 f^2/d)]_{j=1,M} \quad (41)$$

After solving equation 41, equation 40 can be solved. To calculate the next step, all variables existing at the end of a time step become the initial variables for the new calculations. This process can thus be repeated any number of times.

Since, so far, no geometric boundary conditions have been imposed, equations 29-31 are only valid at points not situated on the lake boundaries.

In conclusion, it should be noted that equations 29-41 are valid for any finite difference grid. Only for the evaluation of the derivatives the form of the finite difference grid is important.

2.4 Evaluation of derivatives

2.4.1 Vertical derivatives

As follows from equations 17-27, vertical derivatives appear only in a layered lake as shown in Figure 2. Following a scheme as outlined in Figure 4, the vertical derivatives of equations

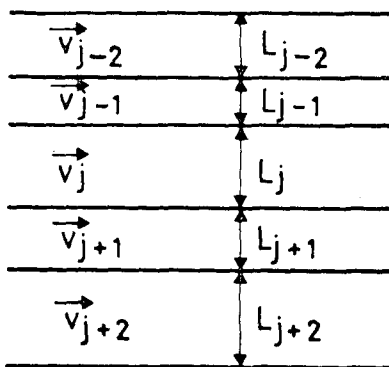


Figure 4:
Definition of layers for
vertical derivatives

17 and 18 are approximated for the top of a layer, j , by

$$\left\{ \left[\frac{\partial \left(\frac{\vec{v}}{L} \right)}{\partial z} \right]_{\text{top}} = \frac{(\vec{v}/L)_{j-1} - (\vec{v}/L)_j}{\frac{1}{2}(L_{j-1} + L_j)} \right\}_{1 < j \leq M} \quad (42)$$

and for the bottom of a layer, j , by

$$\left\{ \left[\frac{\partial \left(\frac{\vec{v}}{L} \right)}{\partial z} \right]_{\text{bottom}} = \frac{(\vec{v}/L)_j - (\vec{v}/L)_{j+1}}{\frac{1}{2}(L_j + L_{j+1})} \right\}_{1 \leq j < M} \quad (43)$$

For $j = 1$, equation 42 is replaced by equations 32 and 33.

For $j = M$, equation 43 is replaced by equations 34 and 35.

2.4.2 Horizontal derivatives

Although there have been attempts to use irregular grids with finite-difference procedures (Crowley, 1971; Boris et al., 1975), it appears that Thacker (1977a) was the first to propose the use of an irregular finite-difference scheme for the solution of the shallow water wave equations.

While in a conventional rectangular finite-difference scheme the approximation of horizontal gradients is straightforward, some thought must be given to the horizontal gradient approximation in an irregular difference scheme as shown in Figure 5.

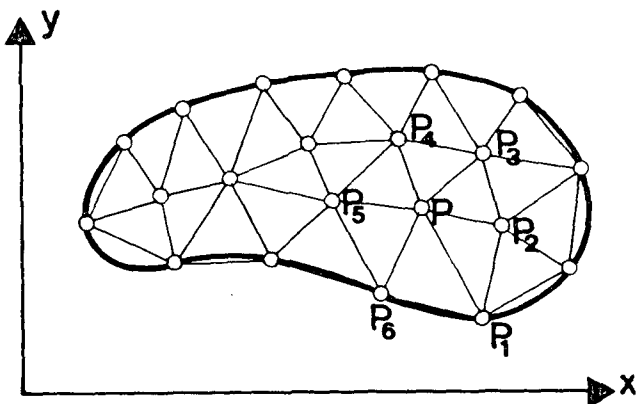


Figure 5:

Irregular finite difference grid (from Bauer, 1979)

As can be seen in Figure 5, an irregular grid can be thought of as being a patchwork of triangles. In the vicinity of each such triangle, the derivatives of a function in the x and y directions can be approximated by the slopes, in the x and y directions respectively, of the plane determined by the values of the function at the three vertices of the triangle.

If it is now required to evaluate derivatives at a grid point, P, as shown in Figure 5, one finds that each grid point, P, is simultaneously a vertex of several triangles. Thacker (1977a) suggested thus a scheme in which the x and y gradients of a function, f, at a point P(x,y) are approximated by the weighted means of the slopes of the planes in the x and y directions, defined by the functions at the vertices of the triangles adjacent to the point P. The weight of each slope is given by the area of the corresponding triangle. If a point P(x,y) is surrounded by N points $P_i(x_i, y_i)$, where the surrounding points, P_i , are indexed counterclockwise about P, the mean gradients in the x and y directions are respectively given by

$$\frac{\partial f}{\partial x} \approx \frac{\sum_{i=1}^N f_i (y_{i+1} - y_{i-1})}{\sum_{i=1}^N x_i (y_{i+1} - y_{i-1})} \quad (44)$$

$$\frac{\partial f}{\partial y} \approx - \frac{\sum_{i=1}^N f_i (x_{i+1} - x_{i-1})}{\sum_{i=1}^N x_i (y_{i+1} - y_{i-1})} \quad (45)$$

where the summation is cyclic, modulo N. When the point P is situated on a lake boundary, it is simply included as one of the surrounding points of equations 44 and 45. It is worth noting that if equations 44 and 45 are applied to a point in a rectangular grid as shown in Figure 6, equations 44 to 45 reduce to the conventional finite difference approximation

$$\frac{\partial f}{\partial x} \approx \frac{f_a - f_c}{x_a - x_c} \quad (46)$$

$$\frac{\partial f}{\partial y} \approx \frac{f_b - f_d}{y_b - y_d} \quad (47)$$

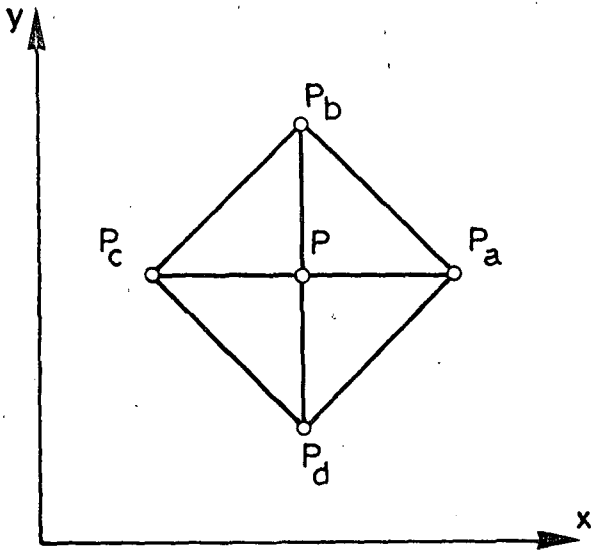
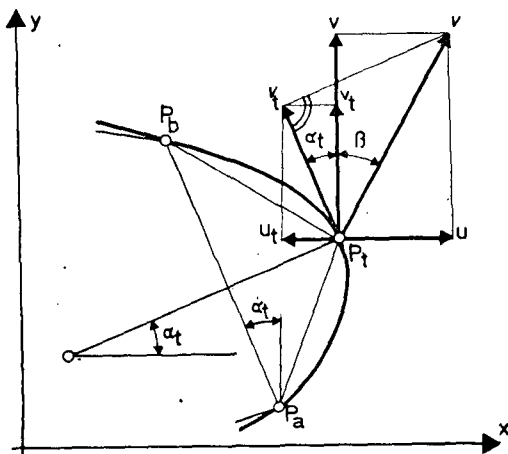


Figure 6:
Point within a rectangular grid

A further question remains: does one not, by introducing an irregular grid, violate the continuity equation? Thacker (1977a) has shown that equations 44 and 45 satisfy Green's lemma (see, for example, Wylie, 1960) and thus the total volume of water remains constant as long as there is no flow across the boundaries.

2.5 Lateral boundary condition

The lateral boundary condition states that, at the lake boundary, there shall be no flow across that boundary. As can be seen in Figure 7, the direction of the tangent to the boundary at a boundary point P is parallel to the straight line defined by



$$\begin{aligned}
 u &= v \sin \beta \\
 v &= v \cos \beta \\
 v_t &= v \cos (\beta + \alpha_t) \\
 v_t &= v \cos \beta \cos \alpha_t \\
 &\quad - v \sin \beta \sin \alpha_t \\
 u_t &= -v_t \sin \alpha_t \\
 v_t &= v_t \cos \alpha_t
 \end{aligned}$$

Figure 7: Determination of boundary vectors

the two neighboring boundary points P_a and P_b . The condition of no flow across the boundary at point P_t requires the flow to be parallel to the tangent at point P_t . From Figure 7 it follows that the x and y components, u_t and v_t of any vector \vec{v}_t , which were obtained by projecting a vector \vec{v} with the components u and v onto the tangent in point P_t , are given by:

$$u_t = (u \sin \alpha_t - v \cos \alpha_t) \sin \alpha_t \quad (48)$$

$$v_t = (v \cos \alpha_t - u \sin \alpha_t) \cos \alpha_t \quad (49)$$

where

$$\sin \alpha_t = \frac{x_a - x_b}{\sqrt{(x_a - x_b)^2 + (y_a - y_b)^2}} \quad (50)$$

$$\cos \alpha_t = \frac{-(y_a - y_b)}{\sqrt{(x_a - x_b)^2 + (y_a - y_b)^2}} \quad (51)$$

Thus, for boundary points, the terms in equations 29 and 30 containing the pressure gradient and the top- and bottom shear stresses must be replaced by their equivalent terms but corrected according to equations 48-51 for the boundary directions. The Coriolis term at boundary points being balanced by an opposing boundary force is zero. The subsequent solution procedure remains unchanged.

2.6 Smoothing of calculation results

As mentioned earlier the system of equations 29-31 may be unstable even if the Courant criterion, equation 28, has been met. To render such a system nevertheless stable, Sündermann (1966) introduced an additional horizontal numerical "viscosity" by replacing the variables u , v and H resulting from equations 29-31 by a weighted mean,

$$\bar{f} = \alpha f + \frac{1 - \alpha}{N} \sum_{i=1}^N f_i \quad (52)$$

where f is a function standing for u , v or H ,
 α is a weighting factor and
 N is the number of surrounding points.

The factor α may vary according to $0 \leq \alpha \leq 1$ (Sündermann, 1966). Since the smoothing of the boundary vectors changes not only their size but also their directions, they have to be corrected once more according to equations 48 and 49. Furthermore, smoothing creates a volume error which is positive for a mean surface that is concave and negative for a mean surface that is convex. This error however can be corrected by moving the entire smoothed surface back over a distance which is equal to the total volume error divided by the lake surface area. Using the same indexing system as shown in Figure 5 and employed in equations 44 and 45, the shaded surface area, A_p , shown in Figure 8 and associated with a point $P(x,y)$ which is surrounded by N points $P_i(x_i, y_i)$, is given by:

$$A_p = \frac{1}{2} \sum_{i=1}^N \{ [(x_{i-1} + x_i + x)/3 - (x_i + x_{i+1} + x)/3] \\ [(y_{i-1} + y_i + y)/3 + (y_i + y_{i+1} + y)/3] \} \quad (53)$$

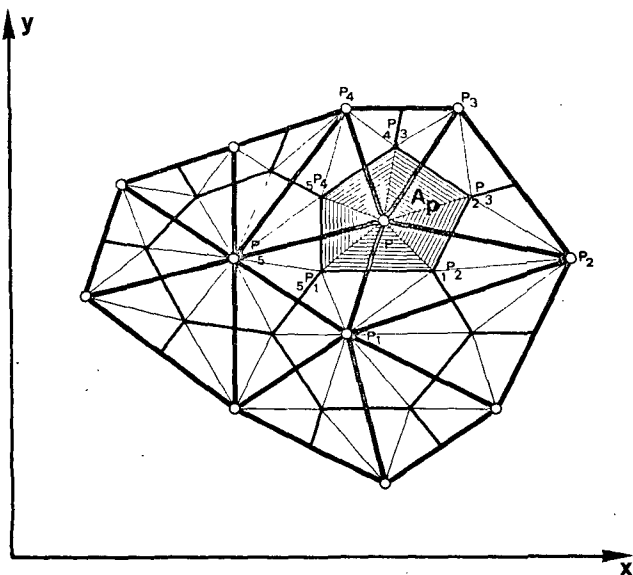


Figure 8:

Grid definition for area and volume calculation

The volume, V_p , associated with a point P is given by

$$\begin{aligned}
 V_p = \frac{1}{2} \sum_{i=1}^N \{ & [(D_{i-1} + D_i + D)/3 + (D_i + D_{i+1} + D)/3 + D]/3 \} \\
 & \{ [(x_{i-1} + x_i + x)/3 - (x_i + x_{i+1} + x)/3] [(y_{i-1} + y_i + y)/3 \\
 & + (y_i + y_{i+1} + y)/3] + [(x_i + x_{i+1} + x)/3 - x] [(y_i + y_{i+1} + y)/3 + y] \\
 & + [x - (x_{i-1} + x_i + x)/3] [y + (y_{i-1} + y_i + y)/3] \} \quad (54)
 \end{aligned}$$

In equations 53 and 54 the summation is again cyclic, modulo N. For points situated on the lake boundaries, equations 53 and 54 must be slightly modified.

3. Application of mathematical model to hypothetical test lake

3.1 Description of computer programs

To perform mathematical simulations as outlined in section 2, program CIRCUL was developed. To allow for control of the lake geometry and the scales and other input parameters to be used by program CIRCUL, program FIDIGR was written.

3.1.1 Program FIDIGR

This program permits control of a Finite Difference GRid as shown in Figures 9-12. The geometry described by Figures 9-12 is for a hypothetical test lake to be used later when demonstrating the operation of the mathematical model. The water surface of the test lake is $4,54 \cdot 10^8 \text{ m}^2$, its volume is $1,5 \cdot 10^{10} \text{ m}^3$ and its mean depth is therefore 33 m.

As can be seen in Figure 9, the irregular finite difference grid strongly resembles a conventional finite element grid. Furthermore, in Figure 9, the number of each point, P, is shown. The small marks on the lines connecting the points

allow control of the counterclockwise sense of rotation necessary for the evaluation of equations 44, 45, 53 and 54. The geometrical data input is in order if there are two marks on all lines having at least one end point not situated on the lake boundary and if there is one mark only on all lines having both end points situated on the lake boundary. The direction of the rotation can be detected with the aid of the position of the marks on the lake boundary.

On Figure 10, the depth and the number of layers are indicated for each point. The lake boundary points in Figure 10 are marked by a small square. Furthermore, the boundary "tangents" as shown in Figure 7 are drawn whereby their associated point- and layer numbers have been indicated.

While Figure 10 shows the number of layers and the boundary tangents for the lake represented by one layer, Figure 11 shows them for the lake represented by three layers. To distinguish the inner from the outer boundary points, the former are surrounded by a square standing on one of its corners.

In Figure 12 the irregular finite difference grid is displayed in three dimensions. It should be noted that in Figure 12 the vertical dimensions are greatly exaggerated. Furthermore, it can be seen that the geometry of the lake is rather irregular. The positions of points 4, 21 and 41 marked in Figure 12 are for later reference.

In Figures 13 and 14, to which reference will be made later on, the parameters used in a model execution are listed. Comparing Figures 13 and 14 with Figure 12, one finds that the "box" of Figures 13 and 14 corresponds exactly to the box of Figure 12 containing the three-dimensional irregular finite difference grid. Thus the boxes of Figures 13 and 14 may be used to visualize the position in space of the lake, the ellipses indicating the mean positions of the layers. The scales shown

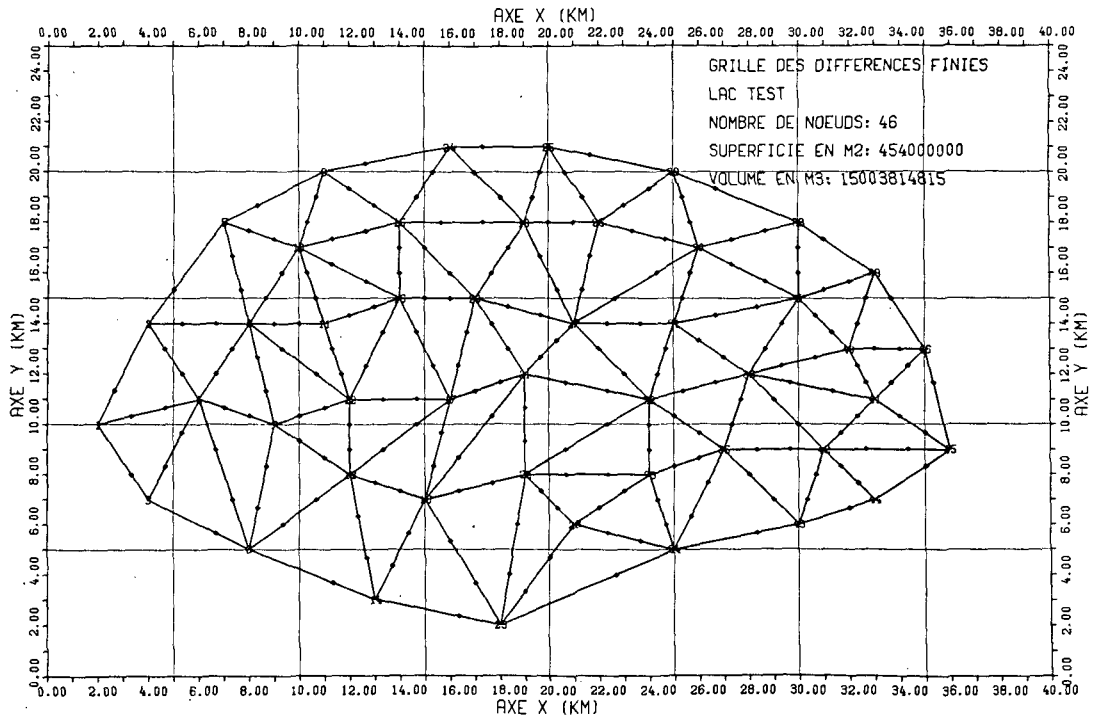


Figure 9: Plan view of irregular finite difference grid of test lake (from Bauer, 1979)

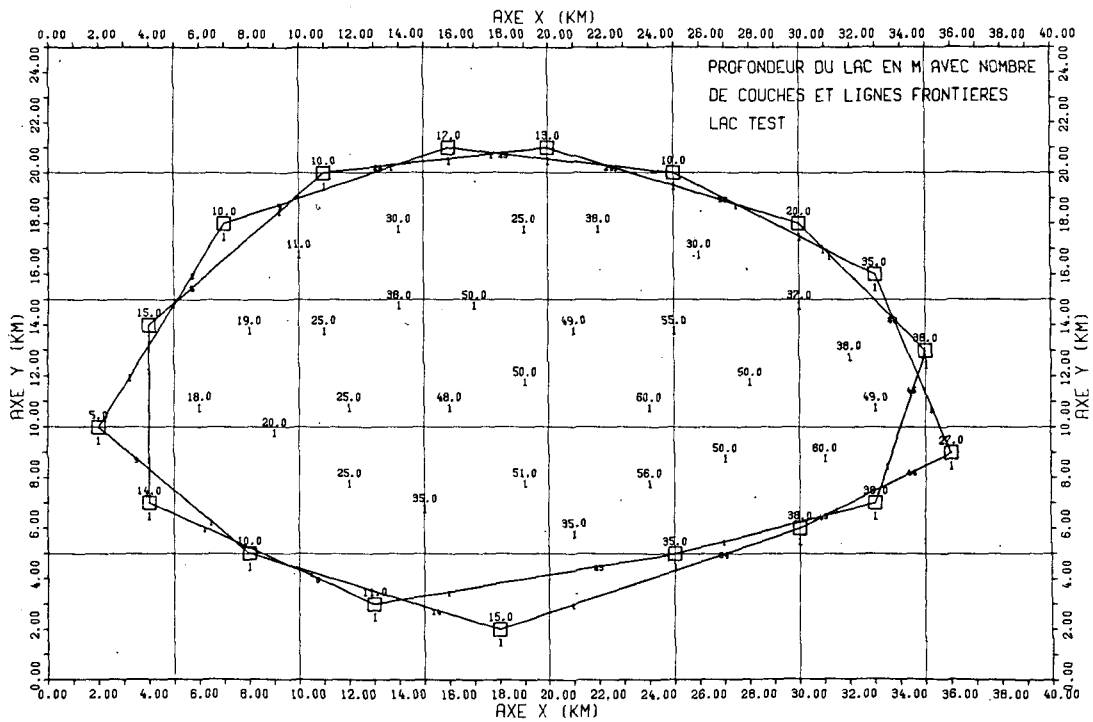


Figure 10: Depth and number of layers of one-layer test lake including boundary tangents (from Bauer, 1979)

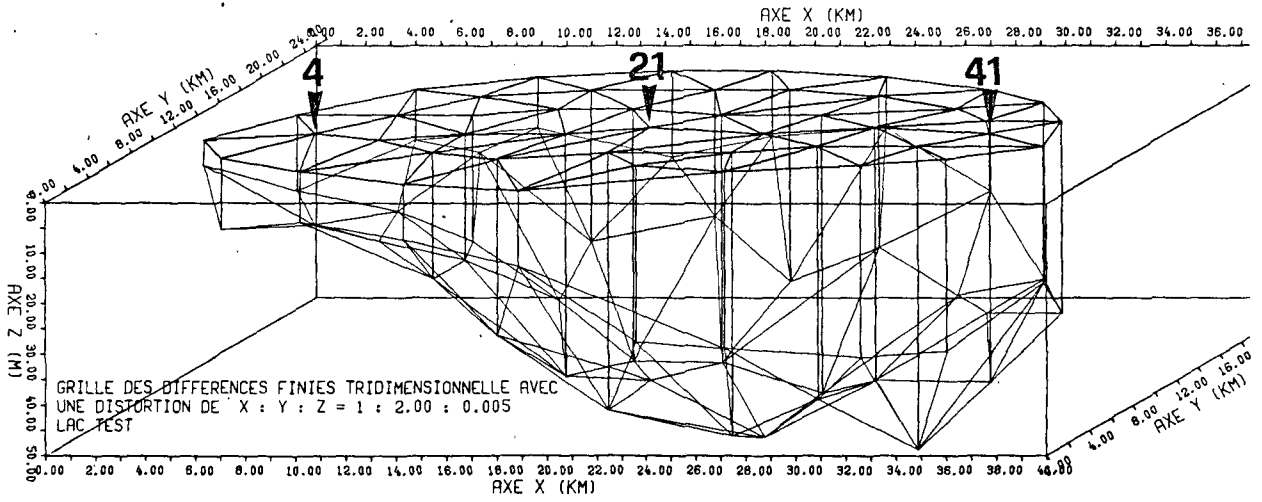


Figure 12: Three dimensional grid of test lake (from Bauer, 1979)

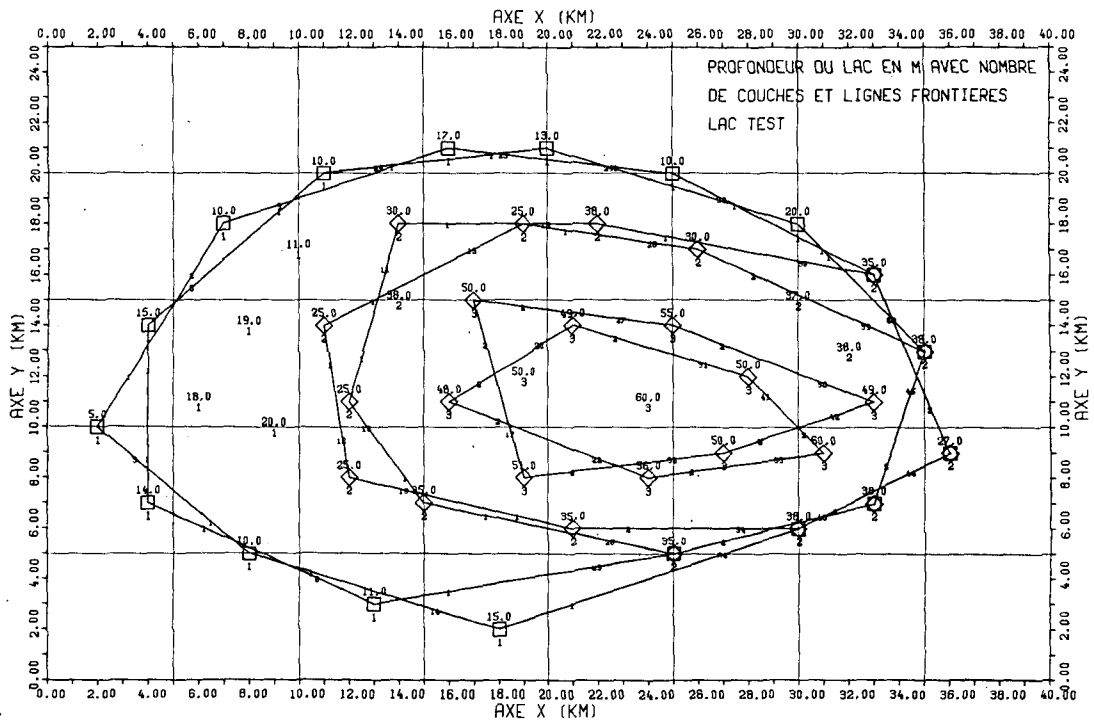


Figure 11: Depth and number of layers of three-layer test lake including boundary tangents (from Bauer, 1979)

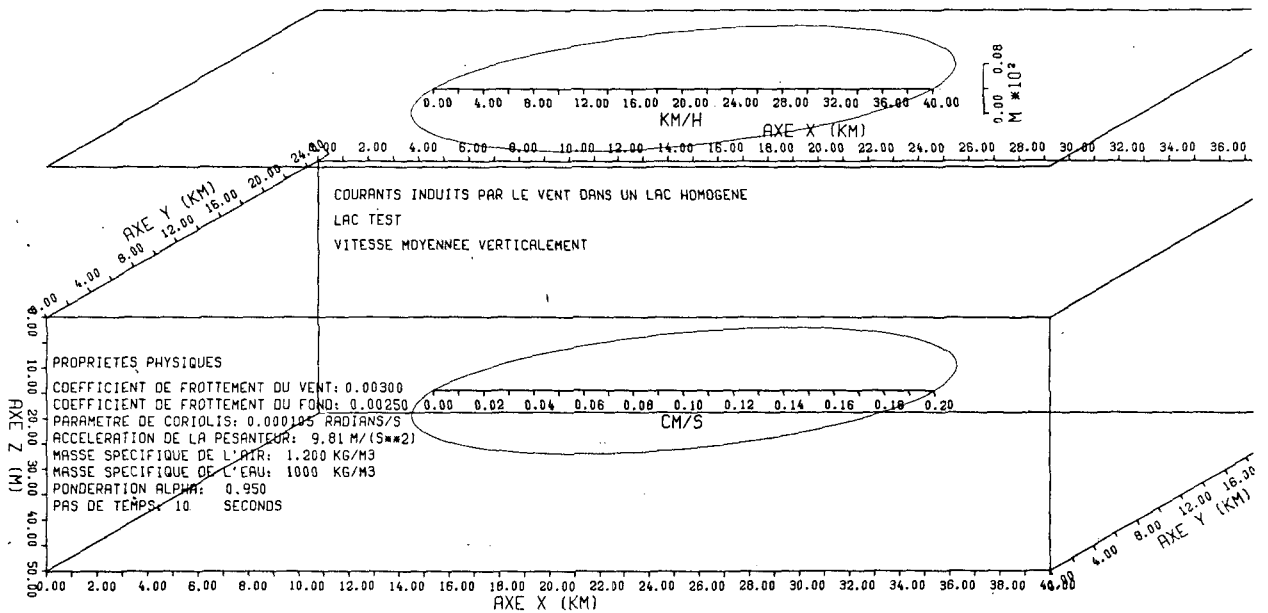


Figure 13: Scales and list of parameters for one-layer formulation (from Bauer, 1979)

within those ellipses refer to the water velocity vectors which will be computed in model runs. The ellipses have been drawn to permit evaluation of velocities in directions which are not parallel to the velocity scales shown. Due to the axonometric presentation, there exists a strong lateral distortion of the horizontal scales. According to the ellipses of Figures 13 and 14, a vector parallel to the short axes of these ellipses appears about one fifth as large as a vector of the same size being parallel to the long axis of an ellipse.

In the model simulation to be presented, the displacement of the water surface will also be shown. To avoid visual confusion with the vectors presented within the box, the lid of the box containing the water surface of the lake has been moved upwards as can be seen in Figures 13 and 14. The velocity scale, also shown in the lid of Figures 13 and 14, is for the wind velocity vector. The distortion for the wind velocity vector is again the same as that of the water velocity vectors. The vertical

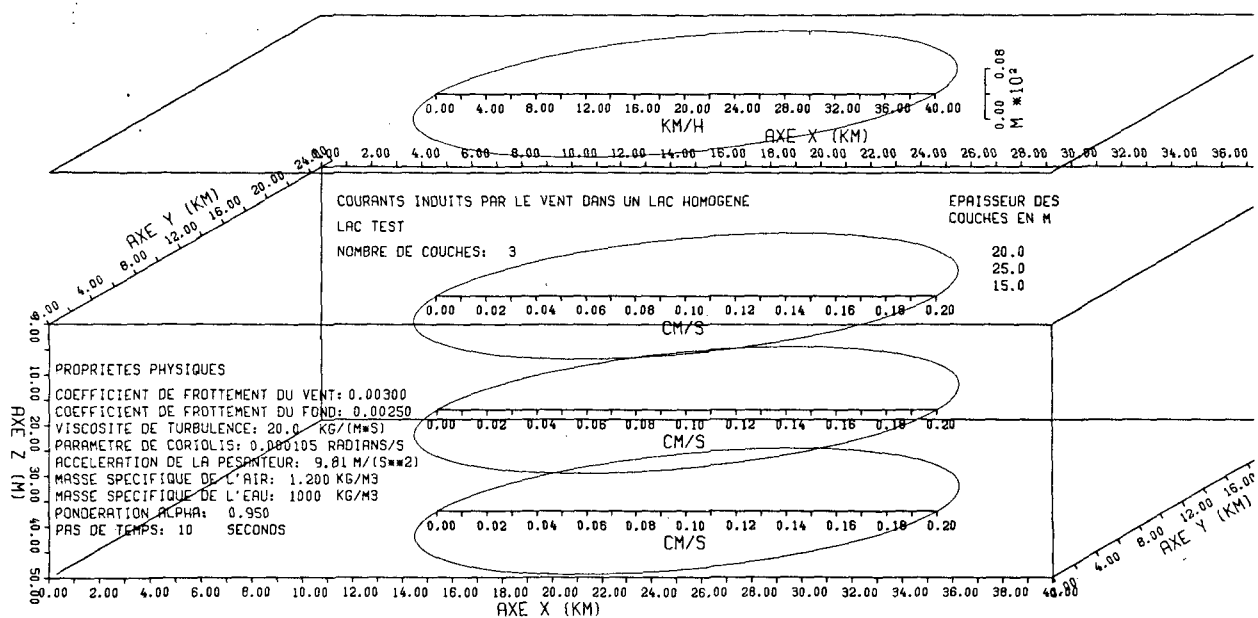


Figure 14: Scales and list of parameters for three-layer formulation (from Bauer, 1979)

scales shown in the "lids" of Figures 13 and 14 are for the displacement of the water levels. It should be noted that in Figures 13 and 14, all parameters and all scales are the same. The only difference with respect to parameters arises because, in the one-layer formulation, no eddy viscosity is required for the model simulation. The value of the eddy viscosity has therefore been omitted in Figure 13.

3.1.2 Program CIRCUL

Program CIRCUL contains the FORTRAN IV code to solve equations 29-31 for the CIRCULATION in a homogeneous lake using the Thacker (1977a) irregular-grid finite difference scheme. Program CIRCUL has been written such that it can simulate currents either in the one-layer or in the multi-layer formulation. The data file describing a lake geometry read by program CIRCUL is the same as the one read by program FIDIGR. In this way the graphical output from program FIDIGR can be used to control

the geometrical input data for program CIRCUL and to correct them where necessary. Parameters and wind input are read from a different file which again is read by program FIDIGR when producing drawings as shown in Figures 13 and 14. Thus, human error is eliminated to a large extent, and agreement between the outputs of programs FIDIGR and CIRCUL is assured. Since, for continuous simulation, the output of program CIRCUL may be rather voluminous, special thought has been given on how best to present simulation results. Two output options are available: output may be either numerical and/or graphical. The numerical output is in a form which can be used by program TRACE (Bauer and Perrinjaquet, 1979) to draw the results as shown in Figures 15 and 16. Graphical output of program CIRCUL is in the form shown in Figure 17.

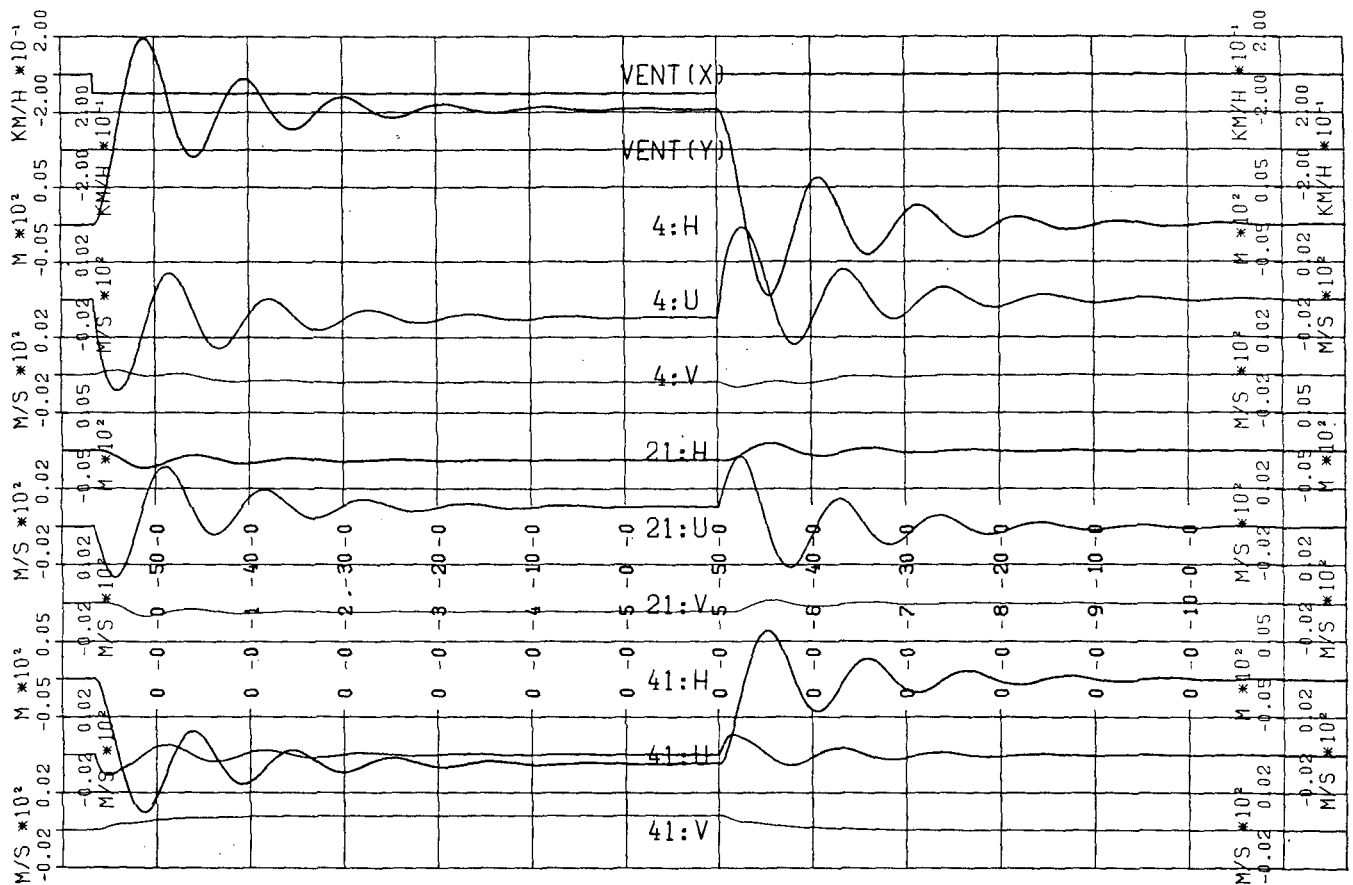


Figure 15: Simulation for test lake with the one-layer formulation (The capital letters U and V in § 3.2.1 correspond to small letters u and v in the remainder of the dissertation; from Bauer, 1979)

3.2 Model simulation for test lake

Program CIRCUL was executed with the geometry of the test lake described by Figures 9-12 and with the parameters listed in Figures 13-14. Although for the test lake shown in Figures 9-12 the model should be stable for times steps of up to about 10 minutes (see equation 28), first simulation attempts showed that the model becomes unstable in the one- and in the three-layer formulation when using time steps even as small as 10 seconds. However, very slight smoothing according to equation 52 with $\alpha = 0,95$ was already sufficient to stabilize the model. Using a time step of 10 seconds, 100 time steps with no wind input were applied to the horizontal lake (to show that the model

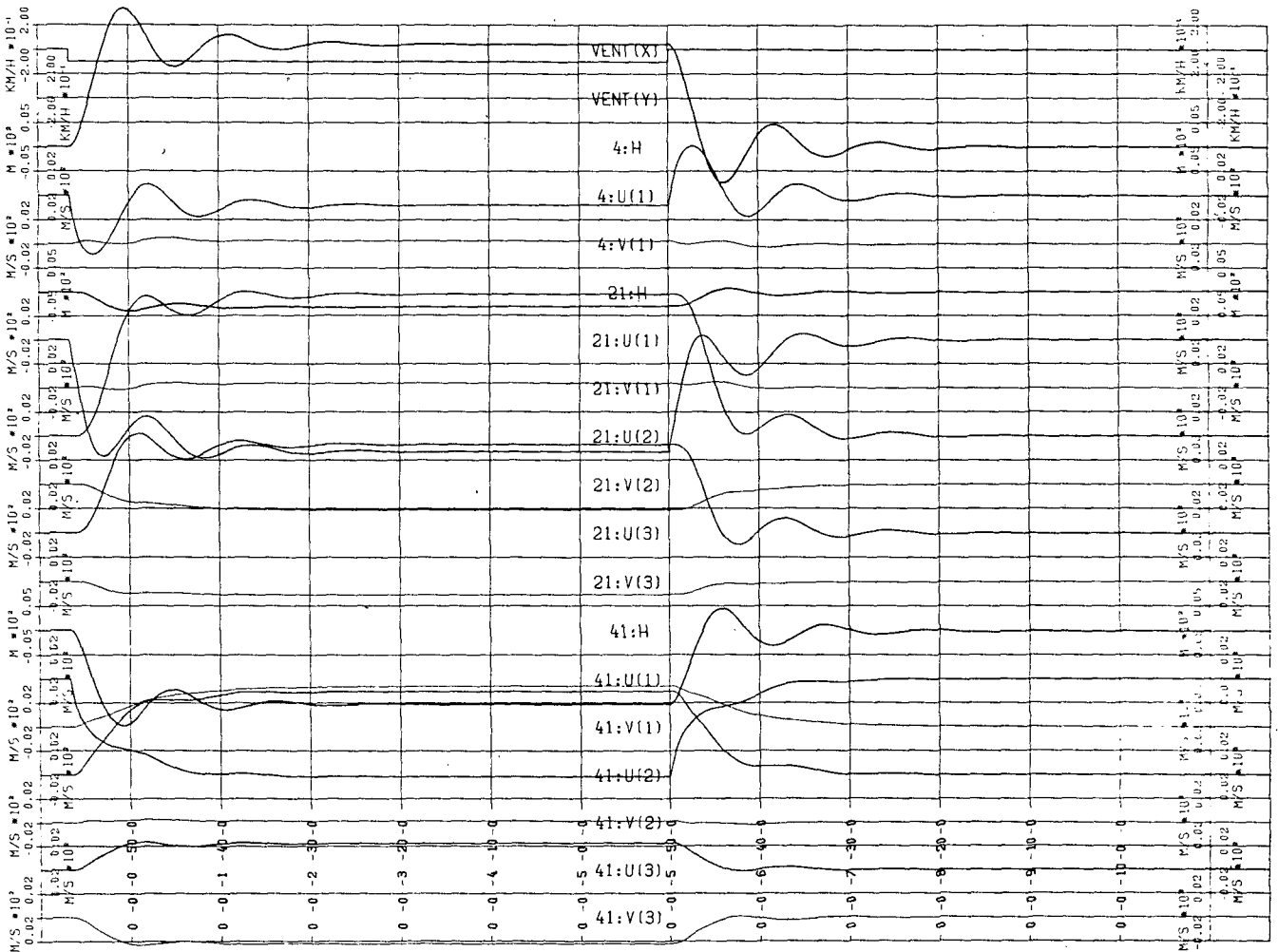


Figure 16: Simulation for test lake with the three-layer formulation (The capital letters U and V in § 3.2.1 correspond to small letters u and v in the remainder of the dissertation; from Bauer, 1979)

itself generates numerically no movement), followed by 2000 time-steps, i.e., 5 hours, 33 minutes and 20 seconds, of constant easterly wind. Subsequently, another 2000 steps without any input were calculated to show the return of the wind induced circulation to zero. These calculations were carried out for the lake in a one-layer and a three-layer formulation, with a wind shear stress coefficient of $3,0 \cdot 10^{-3}$, a bottom shear stress coefficient of $2,5 \cdot 10^{-3}$, the Coriolis parameter of $1,05 \cdot 10^{-4} \text{ s}^{-1}$ and an eddy viscosity in the three-layer formulation of $20 \text{ kg m}^{-1} \text{ s}^{-1}$.

3.2.1 Discussion of simulation results for three points

The results of the simulation using the one-layer formulation for the points 4, 21 and 41 as indicated on Figure 12, are shown in Figure 15. The time axis is horizontal with the date indicated each 300 time steps, starting at step 300. Proceeding from top to bottom the first two bands on which the data are plotted contain the x and y components of the wind. Then the water levels and the x and y velocity components of the points 4, 21 and 41 follow respectively. The vertical scales are indicated at the beginning and near the end of the trace. When the data exceed the band width of one band, their trace is continued over the next band whereby the original scale is maintained.

In Figure 12, it can be seen that the points 4 and 41 are situated near the western and the eastern boundaries of the lake respectively, point 21 is located near the center of the lake. Investigating first the output from the one-layer formulation in Figure 15, one finds that the geographical situations of points 4, 21 and 41 are clearly reflected in their behaviour. The easterly wind produces a rise of water level at the western end of the lake (band 4:H) and a fall of the water level at the eastern end of the lake (band 41:H). The water level near the center of the lake (band 21:H) appears to be little affected.

Considering the velocities, one finds that the x components of the velocities (bands 4:U*, 21:U and 41:U) react much more strongly than the y components (bands 4:V, 21:V and 41:V). This is to be expected, since firstly the wind blows in the x direction and, secondly, the dimensions of the lake in the x direction are larger than those in the y direction. Most notable however, are the forced oscillations (seiches) created by the sudden wind which starts blowing with a force of 10 km/h without any slow build-up. Similarly, when the wind suddenly stops, the equilibrium between all forces that has been established is suddenly disturbed and the lake approaches its starting position, again displaying the phenomenon of seiches. One finds, from Figure 15, that the period of the seiches is about 3200 seconds. Calculating the period, T, of a longitudinal seiche with the simplified formula of Merian (Forel, 1895),

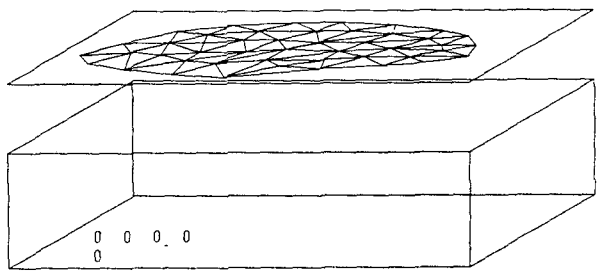
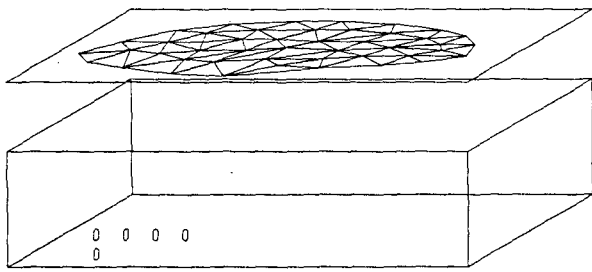
$$T = \frac{2B}{\sqrt{g\bar{D}}} \quad (55)$$

where B is a mean length of the lake and \bar{D} is the mean depth of the lake,

one obtains with $B = 2,9 \cdot 10^4$ m and with $\bar{D} = 33$ m a period of $T = 3224$ seconds which agrees well with the simulated value of 3200 seconds. It should be noted that the period of the water surface and the velocity fluctuations is the same, even though the optical impression might be different. Only in the beginning of the y velocity components at the two extremities of the lake (bands 4:V and 41:V) does it appear that there is a secondary period of about $T = 2200$ s which is probably due to a transverse seiche in the corners of the lake.

In Figure 16, the simulation for the test lake with a three-

* Note that capital letters for velocities U and V in § 3.2.1 correspond to small letters u and v in the remainder of the dissertation.



forced oscillations

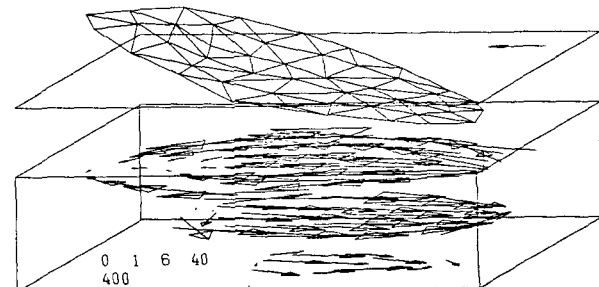
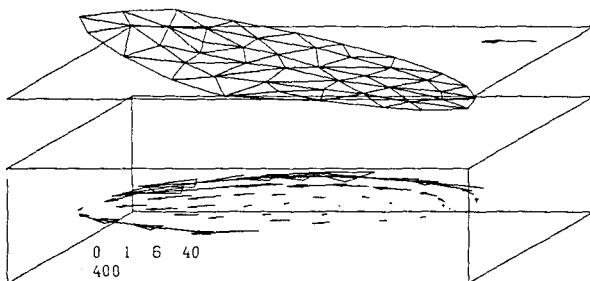
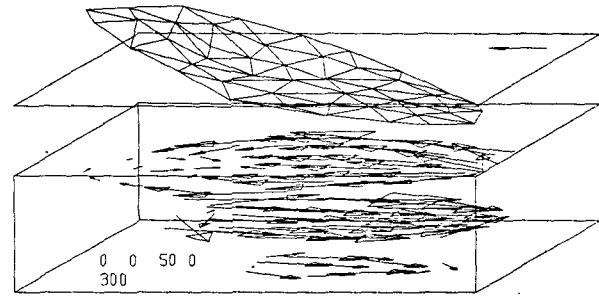
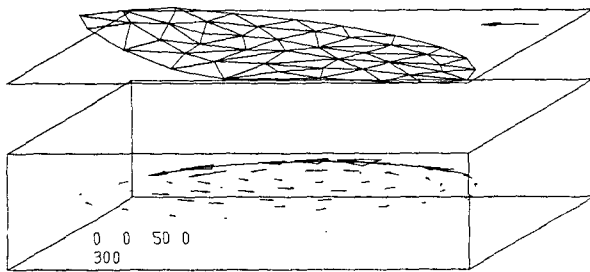
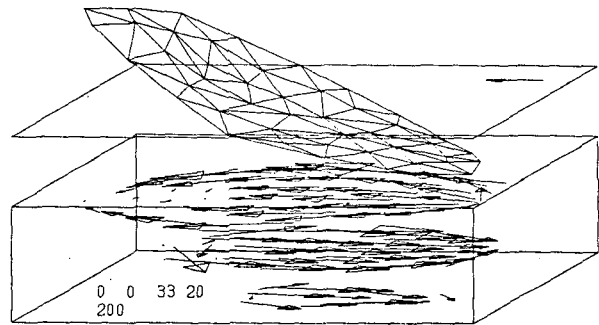
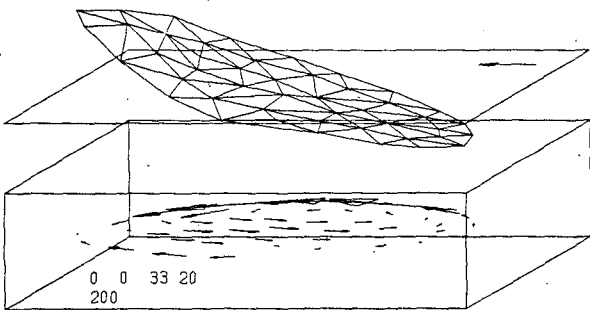
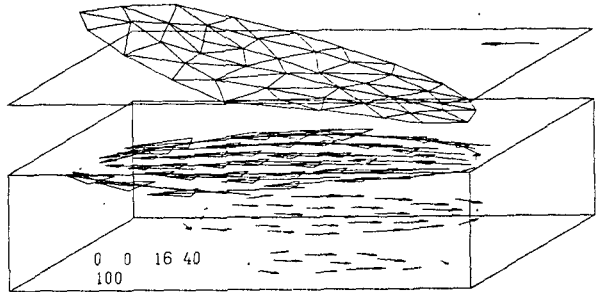
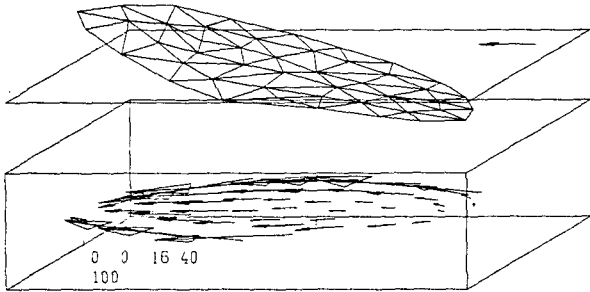


Figure 17: title; see end of images

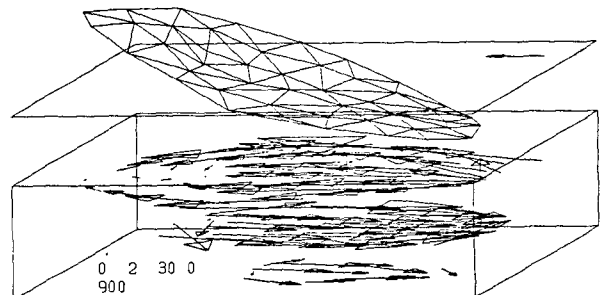
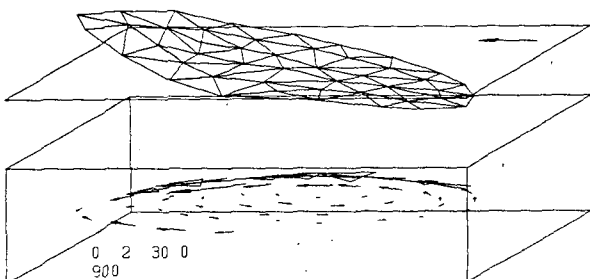
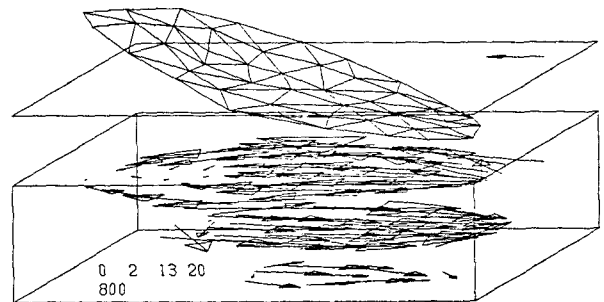
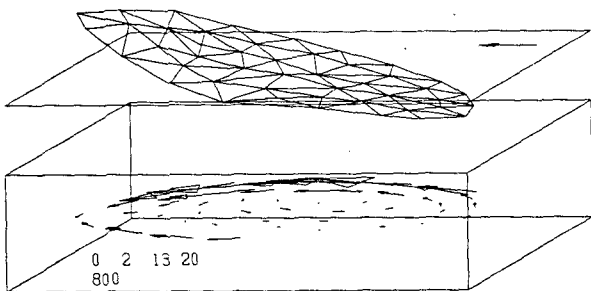
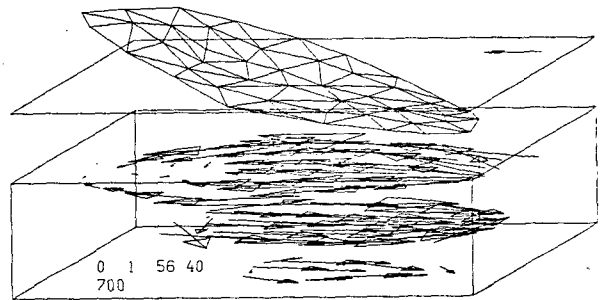
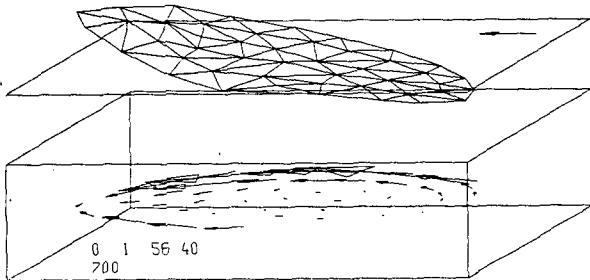
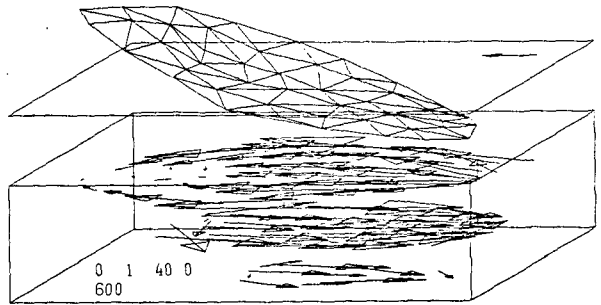
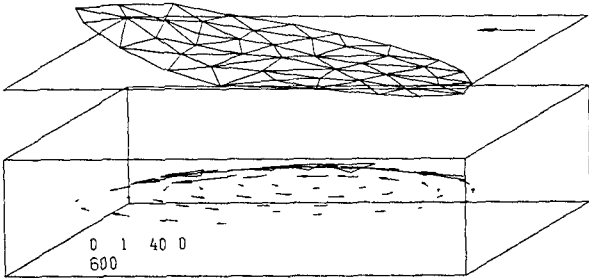
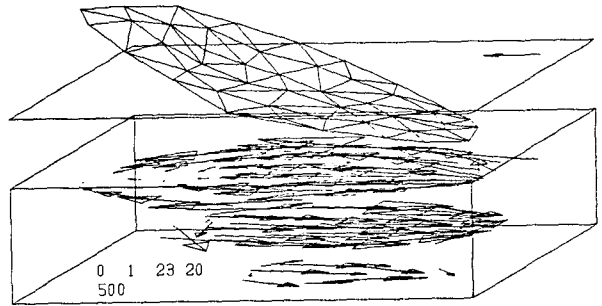
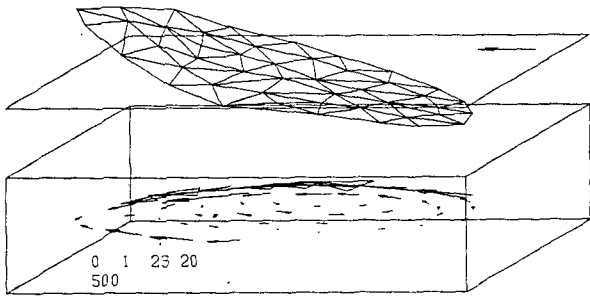
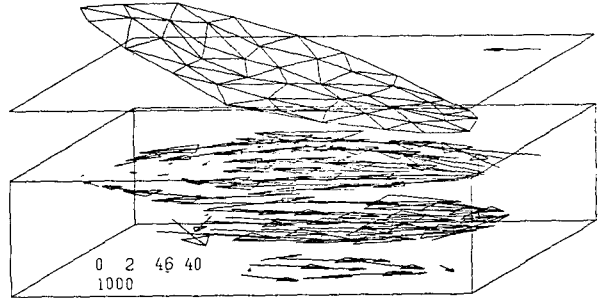
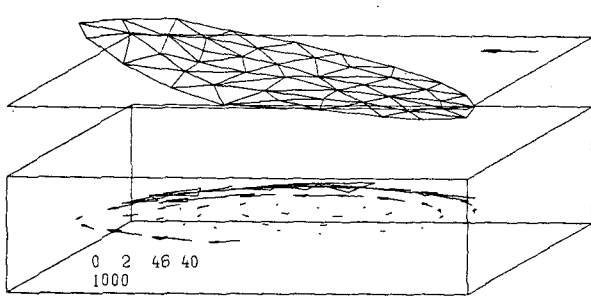


Figure 17: continued



free oscillations

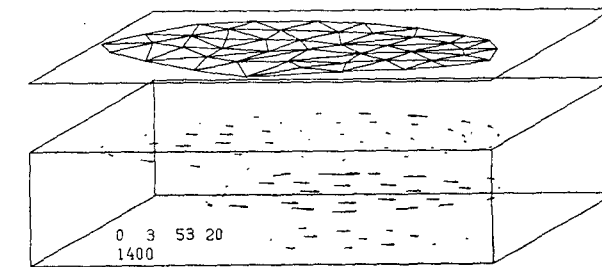
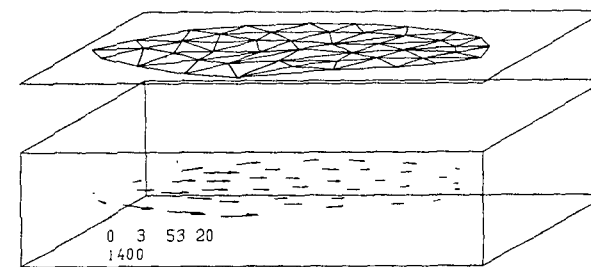
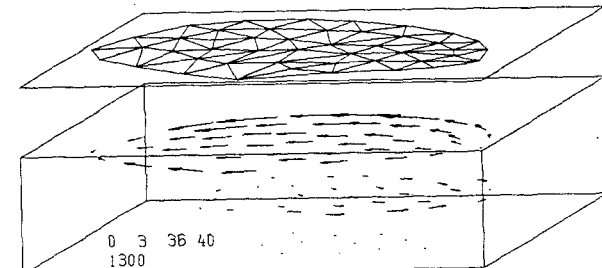
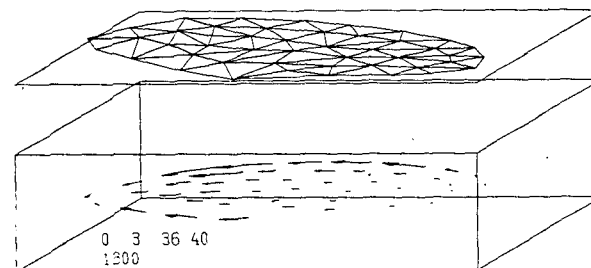
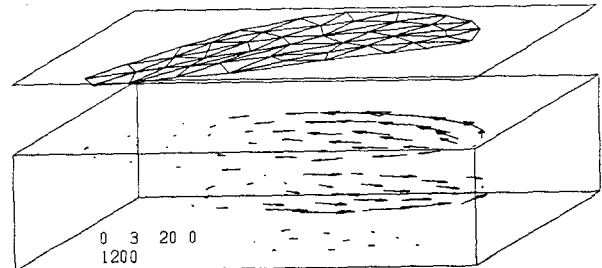
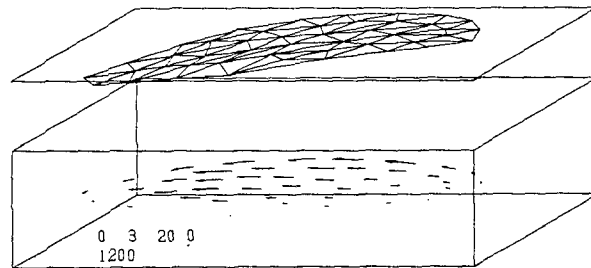
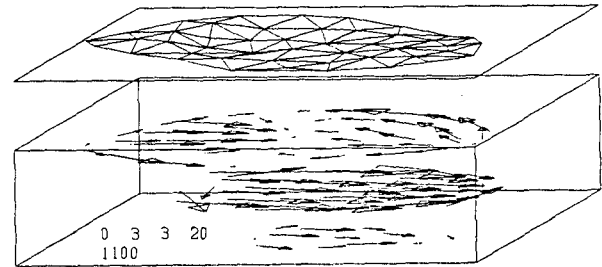
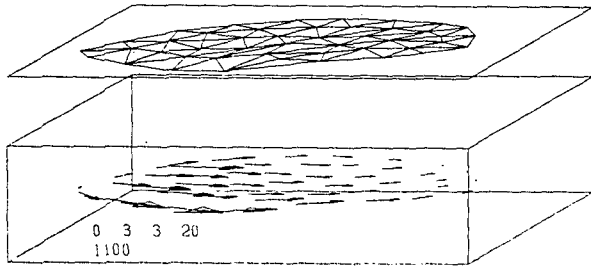


Figure 17: continued

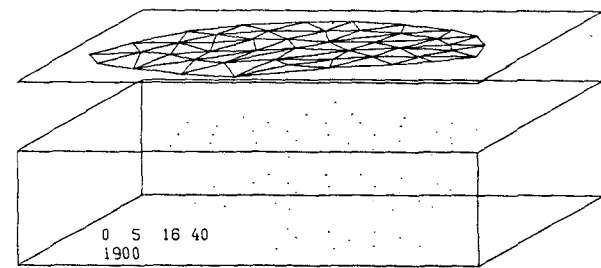
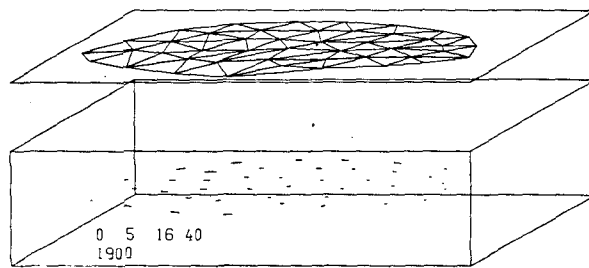
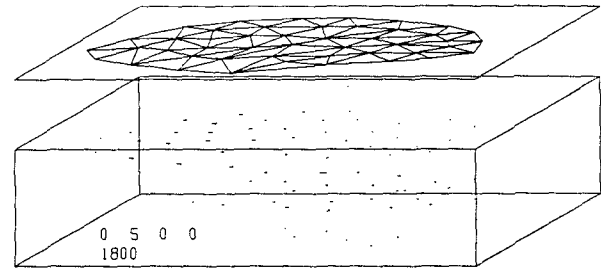
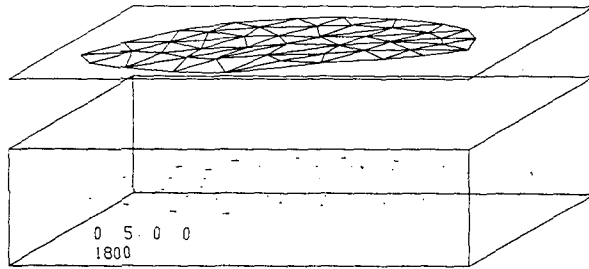
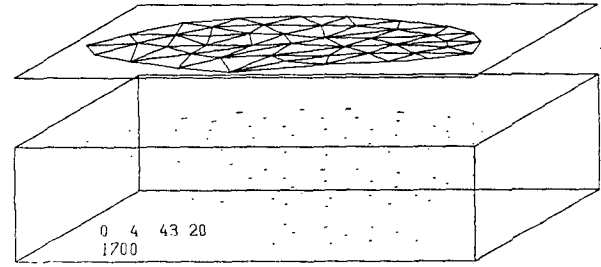
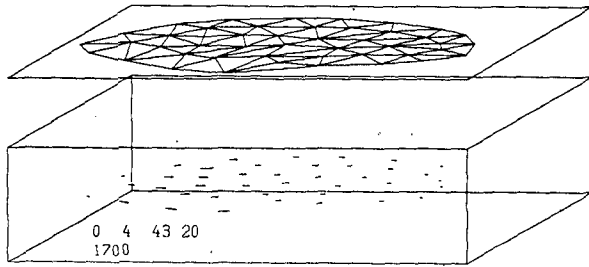
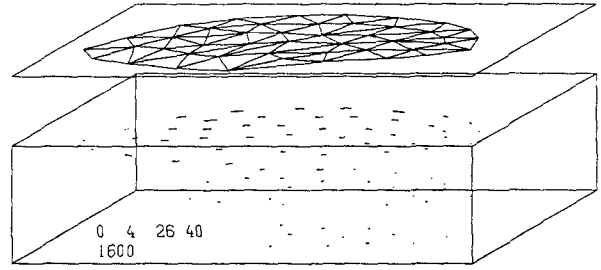
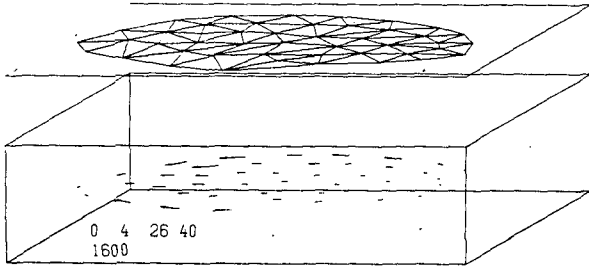
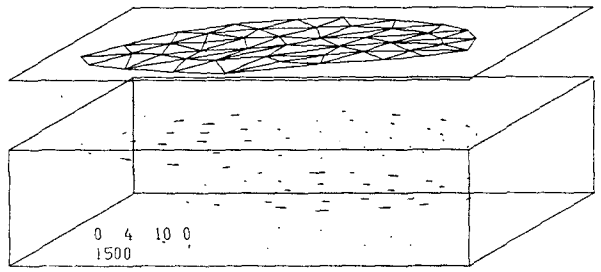
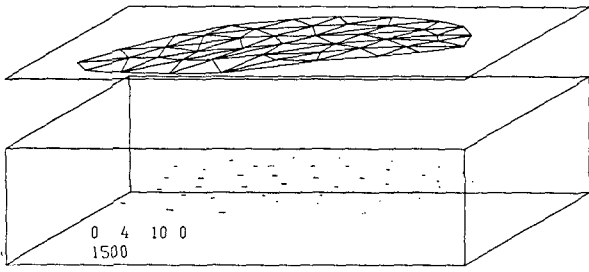
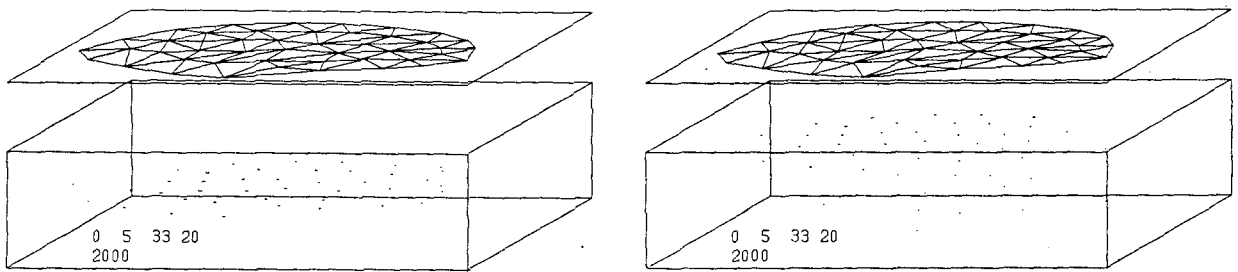


Figure 17: continued



(a) one-layer formulation

(b) three-layer formulation

Figure 17: Simulation of wind-induced, unsteady currents in a homogeneous lake (after Bauer, 1979).

layer formulation is shown. Thus, while point 4 has again only one layer, points 21 and 41 (see Figures 11 and 12) have three layers. This is also reflected by Figure 16, where the point 4 has only one U and V band, and where the points 21 and 41 have three U and V bands respectively. The scales relative to the band width in Figure 16 are the same as those of Figure 15. Comparing now the simulation results of the one-layer formulation, Figure 15, with those of the three-layer formulation, Figure 16, one finds that the principal tendencies have remained the same. However, the amplitudes of the fluctuations have been increased by about one tenth and also, damping is more rapid in the three-layer formulation than in the one-layer formulation. The increase in damping is attributed to the additional internal friction between the layers, as it is introduced in the present model.

3.2.2 Discussion of simulation results for entire lake

In Figure 17 entire vector fields together with the water surfaces are shown every 100 time steps using the principles outlined in § 3.1.1. To save space the simulation sequence has been shortened by omitting the first 100 "idle" steps and by cutting the following two 2000 step sequences to 1000 steps each*.

* A computer drawn film showing every time step for the "unshortened" sequence of Figures 15 and 16 has been produced as well.

In Figure 17, the left side shows the simulation of the one-layer formulation, the right side, the simulation of the three-layer formulation. The time is indicated in days, hours, minutes and seconds in the lower, left corner of each image. Underneath, the number of time steps is shown. The wind velocity vectors are shown in the upper right corner of the "lid". Water velocity vectors are shown within the box.

As can be seen on the first two images of the one- and the three-layer formulation, the lake surface is, at the onset of simulation, horizontal and there are no currents. Considering first the simulation of the one-layer formulation of the lake, one finds that at image 100, all vectors point westwards, resulting in a water level rising at the western extremity of the lake and falling at its eastern extremity. At image 200, the vectors appear to be turning; however, the vectors at the northern and southwestern boundaries remain pointing westward. At image 300, a return current covering the central part and the southeastern boundaries is well established, resulting in a tendency for the water level elevations to reverse. The vectors at the southwestern boundary have been strongly reduced. At image 400, the water level in the west has nearly reached its lowest position. The vectors have again turned indicating a new reversal of trends of the water surface. This oscillatory phenomenon repeats itself until, at image 1000, the equilibrium situation has become almost established. The special behaviour of the boundary points corroborates, to some extent, earlier applications of a stationary model to the Lake of Geneva (Bauer et al., 1977; Bauer and Graf, 1979). A similar oscillatory pattern can be observed after cessation of the easterly wind (images 1100 - 2000). Now however, the boundary points no longer display a behaviour distinctly different from that of the center points.

Turning now to the simulation of the three-layer formulation, it can be seen that the behaviour of the water surface of the three-layer simulation is very similar to that of the one-

layer formulation. Considering the velocities in the two lower layers, one finds that a return current has established itself. This current, although fluctuating in magnitude, changes very little in direction. The vector field of the first layer behaves similarly to the one-layer mean vectors: at image 100, all vectors pointing westwards result in a rise of the water level. In the following images, one finds that the first-layer vectors change their directions in the western extremity of the lake only. Also, velocities in the three-layer formulation are generally higher than those of the one-layer formulation. In image 1000, equilibrium between all forces is almost obtained. At the cessation of the wind, the vector fields of all three layers change their directions periodically, whereby the velocities return gradually to zero.

Comparing the results of the one- and the three-layer formulation, one finds that their behaviour is in principle similar. As might be expected, the three-layer formulation allows visualization of the velocity fields in greater detail. The fact that damping is more pronounced in the three-layer simulation is probably due to internal friction between the layers, which in the one-layer formulation cannot be taken into consideration. Finally however it should be kept in mind that all simulation results have been obtained from hydrodynamic equations which have been simplified as outlined in § 2.1. Further investigations comparing simulation results with observations in real lakes will show to what degree these simplifications are justified.

3.3 Conclusions from the test-lake simulation

Using Thacker's irregular-grid finite-difference method, a three-dimensional mathematical model for the simulation of water level variations and currents in a homogeneous, shallow lake has been developed and applied to a hypothetical test lake in a one- and a three-layer formulation. Application of a steady easterly wind for a limited period to the model resulted in

the development of currents and, most notably, of surges and seiches. The simulation results of the one-layer and the three-layer formulation were very similar. Since the numerical effort of the three-layer formulation is substantially greater than that of the one-layer formulation, a multi-layer simulation is only necessary if detailed knowledge of the lake currents is required for that particular set of simplifying assumptions. This might be the case if it is desired to study current patterns both while the wind is blowing as well as after cessation of the wind. As can be seen in the three-layer simulation of Figure 17, a strong return current exists in the two lower layers while the wind blows. Once the wind has stopped blowing, the currents in all three layers have the same general direction and a return current no longer exists. For the simulation of wind induced seiches in a lake, the one-layer formulation should therefore suffice.

In Figures 15 and 16 it can be seen that the lake response is quasi-immediate, reaching its maximum within half of the natural seiche period of a lake. This is an important finding since a frequently asked question is, how long does it take until a lake gets into motion after a strong wind has started blowing over its water surface. Moreover, measurements in the Léman undertaken by LHYDREP have confirmed this rapid response to wind (see Graf et al., 1979; Figures 10-15).

The parameters for the simulations described in § 3.2 were selected such that they corresponded to findings of earlier research. The wind shear stress coefficient was taken to be 0,003. This value is reasonable and falls well within the wide spread of values quoted in the literature for wind shear stress coefficients. Applying boundary layer theory to wind profile measurements on the water surface of the Léman, Graf and Prost (1979) determined a mean shear stress coefficient, c_w , of about 0,0013. On the other hand, Bauer and Graf (1979), in a model calibration for the Léman had to use a value of $c_w = 0,004$ to

obtain reasonable agreement between simulation results and current observations in the lake. The bottom shear stress coefficient, c_b , was taken to be 0,0025, a value that has been suggested by Simons (1973). The eddy viscosity, η , in the three-layer formulation was chosen to be 20 kg/ms. According to various relationships given by Neumann and Pierson (1966), this is probably a somewhat high value for a wind velocity as low as 10 km/h. For a hypothetical situation however, this value is quite acceptable since it allows the modeler to visualize the effect of the internal shear stress on the simulation results. The Coriolis parameter, f , was taken as $0,000105 \text{ s}^{-1}$, which corresponds to the mean latitude of the Léman.

From a numerical point of view, it was found that the model becomes unstable even if the Courant condition, equation 28, is met. However, the introduction of a smoothing procedure suggested by Sündermann (1966) rendered the system stable. It should be noted that this smoothing of the numerical results of the mathematical simulation corresponds to a filtering by a low-pass filter, i.e., all higher frequencies are eliminated to a degree which depends on the amount of smoothing. This can be observed very well in the computer-drawn films produced in conjunction with this dissertation. In the films corresponding to Figure 17, i.e., calculated with an $\alpha = 0,95$, it can be seen that the lake surface remains rather smooth at all times, moving only up and down and bending itself in a somewhat global fashion. In other films produced with $\alpha = 1,00$, i.e., no smoothing at all the water surface consists of a great number of waves superimposed on the smooth surface. The instability however becomes obvious only after cessation of the wind, when the wind induced motions of the lake no longer return to a state of complete calm.

In § 2.6, it has been stated that the α -mean acts as a numerical viscosity. An increase in smoothing therefore corresponds also to an increase in damping. Thus, when increasing the time step, instability of the simulation will be postponed, and will occur

the later, the higher the degree of smoothing. Investigating the influence of a change of time step on simulation results, it has been found that slight changes in seiche amplitudes, -periods and damping may take place. However, as long as one stays away from a state of instability, these changes are not very important.

4. Earlier work on seiches and surges in the Léman

An excellent general summary on the theory of seiches is given by Hutchinson (1975). Work and observations of seiches in the Léman had already been started well before Forel. In a short chapter on "Histoire ancienne des seiches du Léman", Forel (1895) quotes a dozen names of persons who were concerned with seiches and who put forward theories, some of them quite fantastic, to explain this phenomenon. The first sound work on seiches of the Léman however was that of Forel himself.

4.1 Forel

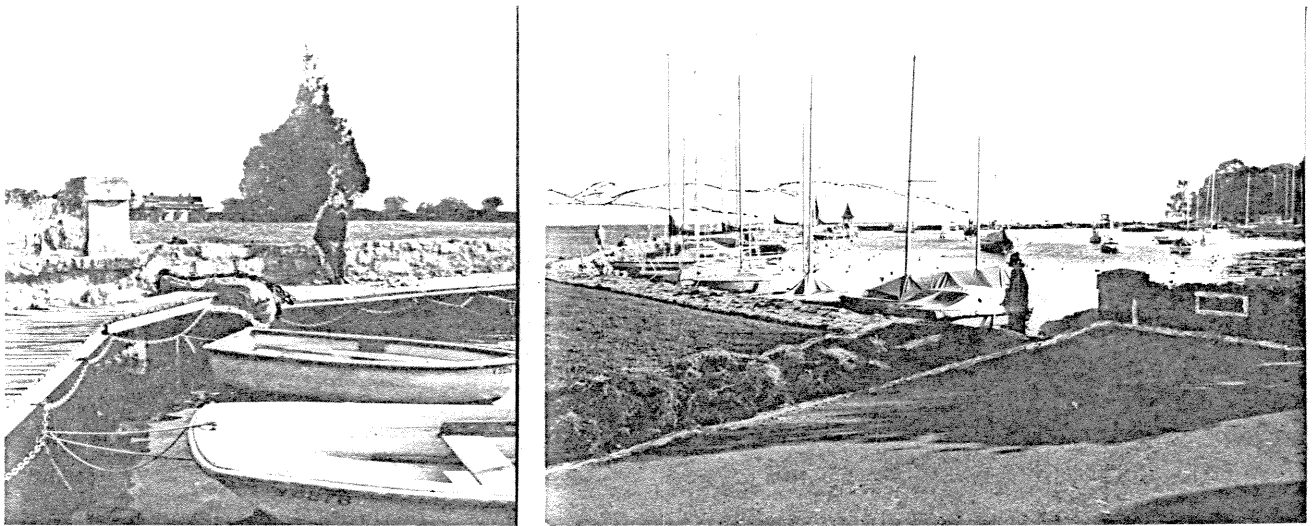
Forel's (1873) first work on seiches of the Léman took place in the harbour of Morges, where, in a small opening of 2 m width in the northern pier of the Morges harbour basin, shown in Figure 18a, the currents changed their direction depending on the rising or falling of the water level. By carefully observing the times at which the current changed, Forel (1873) determined a mean seiche period at Morges of $4\frac{1}{2}$ minutes calculated from 93 current reversals. In order to study seiches in more detail, Forel (1876b) constructed a limnigraph at Morges which, as previously mentioned, he kept operational from 1876 to 1884. It appears that quite a few contemporaries of Forel also worked on Léman seiches and had constructed limnigraphs (Forel, 1895):

Plantamour: in Genève, Sécheron, 1877;

Forel: portable limnigraph, 1878;

Sarasin: portable limnigraph, 1879;

Ingénieurs des Ponts et Chaussées français: in Thonon, 1880.



(a) Opening in the Morges harbour wall (today closed) with sceptical scientist (Prof. Mortimer)

(b) General view of the site with Mont Blanc in the background on the left

Figure 18: Site of discovery of Léman-seiches by F.A. Forel

Forel (1895) states that he has published a large number of papers on seiches alone. Without going too much into detail, it should be noted that Forel understood the mechanism of seiches perfectly, as well as the fact that there are longitudinal-, transverse-, uninodal-, binodal-, multinodal-, etc., seiches, each having a different period depending on their position in the lake and on the number of nodes. Forel was also aware that the period of a seiche increases with a decrease of water level and that the seiche-period is independent of the density of water. Forel's most important findings with respect to seiche-periods of the Léman are summarized in Table 1. (It should be noted that there exist still many more seiches with other periods than those shown in Table 1.) Forel (1895) states that the periods summarized in Table 1 were determined from abundant measurements taken from the limnigraphs of Plantamour, Sarasin and Forel ("une vingtaine de kilomètres de longueur de ces dessins automatiquement figurés par le lac lui-même"). Figure 19 shows a map of the Léman, as it is reproduced in Forel

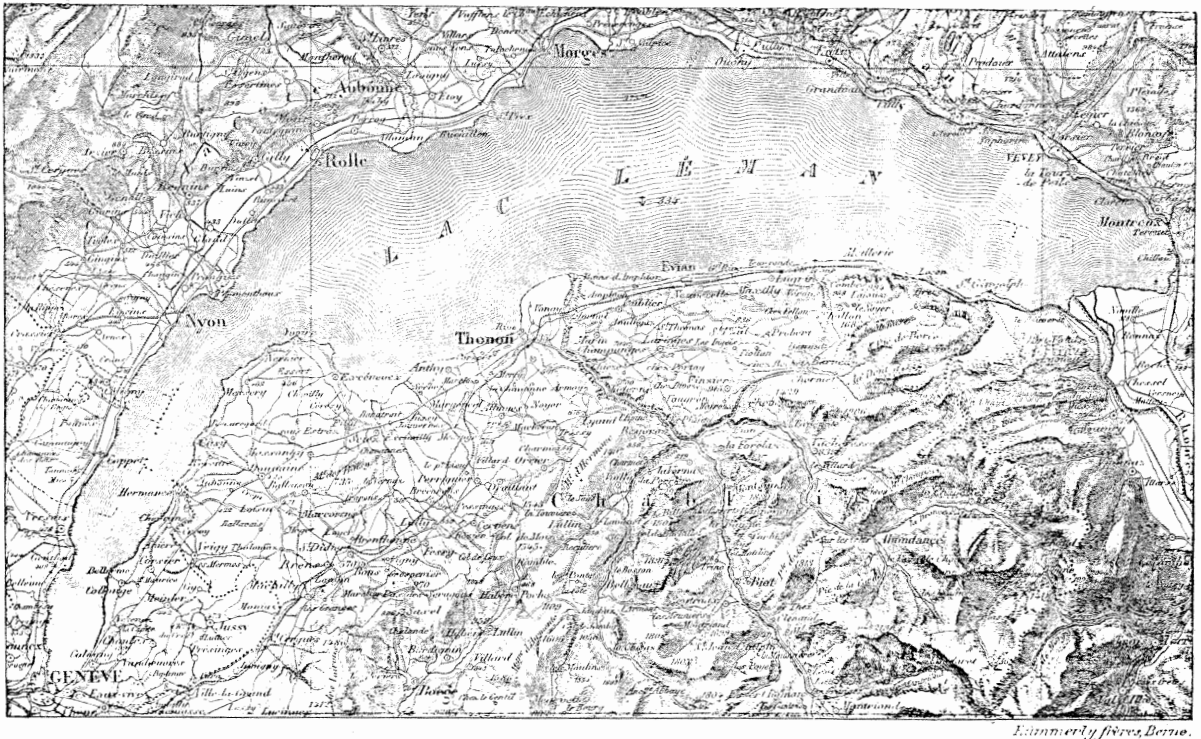
(1895), to allow placement of the stations mentioned in Table 1 (see also Figure 27).

Some of the seiche observations shown by Forel (1895) are reproduced in Figures 20-25. In Figures 20 and 21 the normal transverse uninodal- and binodal seiches at Morges are shown. Figure 22 shows a superposition of the two, termed dicrote seiches by Forel. In Figure 23 various seiches are shown, notably, the longitudinal uninodal seiches at Geneva and Morges and the dicrote seiches and binodal seiches at Geneva. In Figure 24, the occurrence at Morges of longitudinal uninodal seiches, transverse uninodal, and transverse dicrote seiches is shown. A superposition of traces of longitudinal seiches observed at Geneva and Morges with traces of transverse seiches at Morges is shown in Figure 25.

Table 1: Principal seiche-periods of the Léman observed by Forel (1895)

Station	Type of seiche	Period (min.)	Remarks
Genève	longitudinal uninodal	73,5	probable mean values
	longitudinal binodal	35,5	
	longitudinal dicrote*	73 - 35	
Rivage and Bellevue	same as Geneva, but less high		
Rolle and Thonon	longitudinal binodal	35,5	less high than at Geneva
	transverse uninodal	7	
Morges and Evian	longitudinal uninodal	73,5	very weak
	transverse uninodal	10	very distinct
	transverse binodal	5	very distinct
Chillon	same as Geneva, but less high		

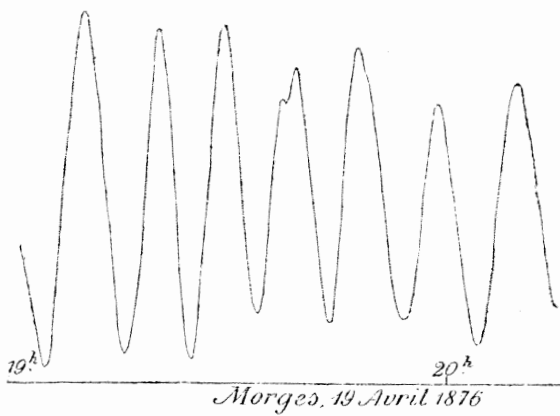
* dicrote seiches are created by superposition of uninodal and binodal seiches as shown in Figure 22.



Reduction de la carte suisse, autorisée par le Bureau topographique fédéral.

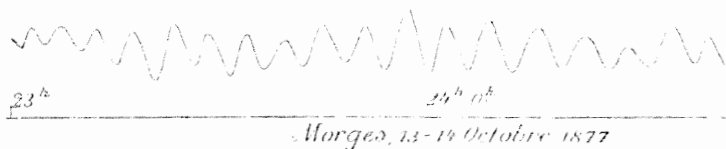
Kunmerly frères, Berne.

Figure 19: Historical map of the Léman (from Forel, 1895)



Seiches de 10 minutes de Morges. Grandeur naturelle: 6 cm. par heure.

Figure 20:
Uninodal transverse seiches at Morges observed by Forel (from Forel, 1895)



Seiches de 5 minutes de Morges. Grandeur naturelle: 6 cm. par heure.

Figure 21: Binodal transverse seiches at Morges observed by Forel (from Forel, 1895)



Figure 22:
Dicrote transverse seiches at Morges observed by Forel (from Forel, 1895)

Seiches dicrotes de 10 minutes de Morges. Grandeur naturelle; 6 cm. par heure.

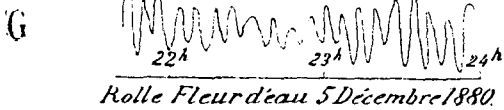
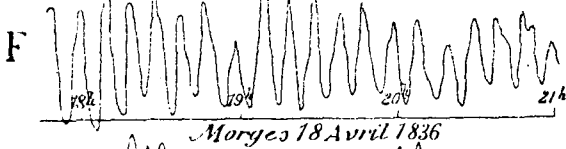
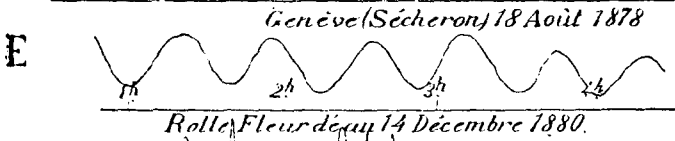
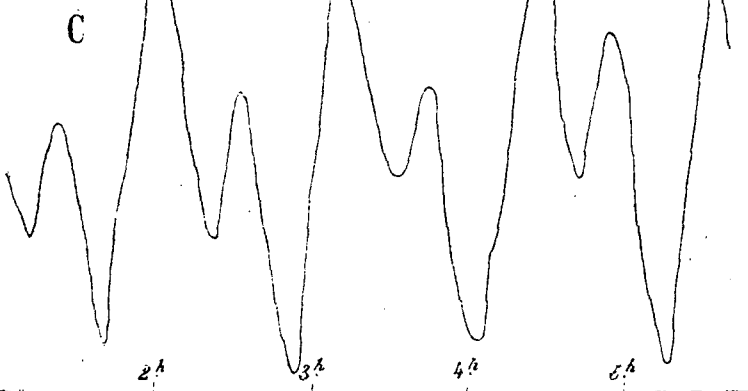
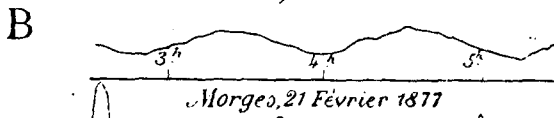
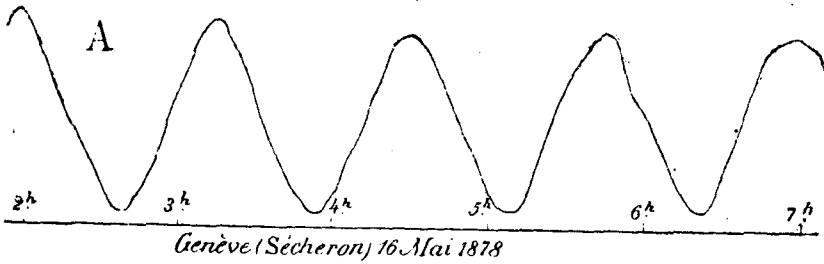


Figure 23:
Seiches of various types recorded at Geneva, Morges and Rolle, observed by Plantamour, Sarasin and Forel (from Forel, 1895)

Types normaux des seiches dans diverses stations. 1/3 grandeur naturelle. 3 cm. par heure, (Linnographes Plantamour, Sarasin et Forel.)

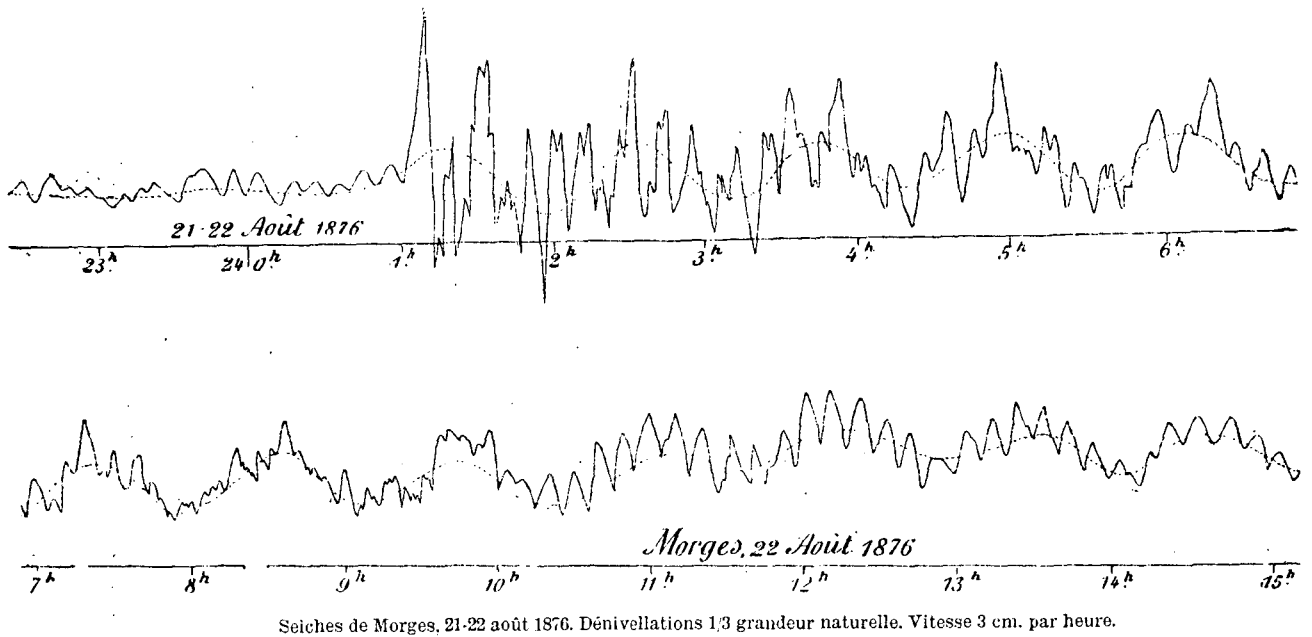


Figure 24: Occurrence of longitudinal uninodal seiches and transverse uninodal and transverse dicrote seiches at Morges observed by Forel (from Forel, 1895)

Forel states that seiches never occur alone, i.e., it is impossible to observe only one singular seiche. Seiches occur in series which may last for a long time, generally until one series of seiches is destroyed by another series of seiches. In Figure 24, it can be seen that there is a first series of small, regular seiches with a period of 10 minutes (i.e., transverse), which is being replaced at 1 hour by a series of higher,

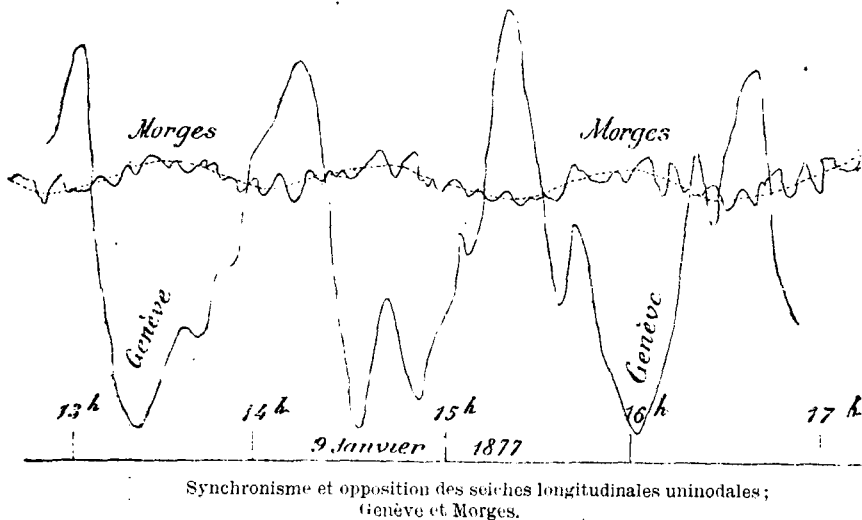


Figure 25: Superposition of various simultaneous seiches observed at Geneva and Morges by Plantamour and Forel (from Forel, 1895)

irregular seiches. Around 5 hours, some dicrote transverse seiches may be observed. At 10 hours, a new series of 10 minute seiches starts, which lasts all the way to the end of the trace. Furthermore, one finds that the event creating the larger irregular seiches at 1 hours also gave rise to a series of longitudinal uninodal seiches, which were not influenced by the subsequent events modifying the transverse seiches. In Figures 20-25 attenuation of seiche motion is not really visible. Seiches however will not last indefinitely long. Even if it is sometimes difficult to show a decrease in amplitude of the seiches in the Léman, their size does diminish, and, if no other event interferes in the meantime, the seiche motion will return to zero. In a most beautiful series of 147 longitudinal uninodal seiches, Forel (1895) observed a decrease of mean amplitude as listed in Table 2, from which it can be seen that the amplitude

Table 2: Mean height of seiches reproduced in Figure 26

Number of seiche	mean height (mm)
1 - 20	167
21 - 40	198
41 - 60	163
61 - 80	169
81 - 100	153
101 - 120	109
121 - 140	81
141 - 145	70

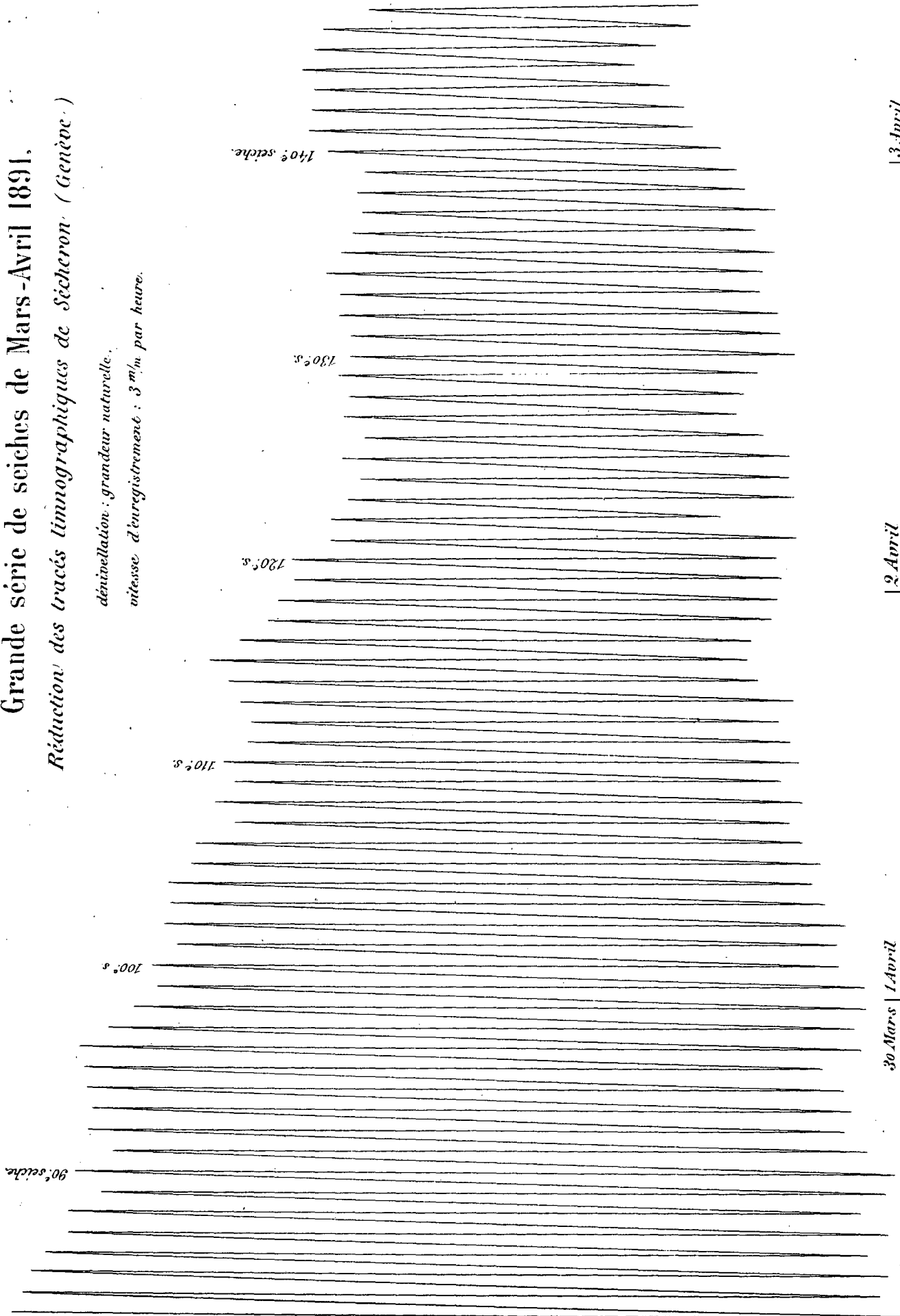
starts to decrease only at the 60th cycle and that the decrease becomes more regular only after the 80th cycle (Forel, 1895). Figure 26 shows the last 64 cycles of this series, i.e., from cycle 83 to cycle 147. At the 148th cycle a new series of dicrote seiches interrupted the regular ones. Between seiches 79 and 139 Forel estimated a mean amplitude decrease rate of 1,65 mm/cycle. Using this rate, Forel (1895) calculated that the series of seiches shown in Figure 26 would have lasted 182 cycles with a to-

Grande série de seiches de Mars-Avril 1891.

Réduction des tracés limnographiques de Sécheron (Genève.)

déviellation : grandeur naturelle.

vitesse d'enregistrement : 3^m/m par heure.



3 Avril

2 Avril

30 Mars 1 Avril

F. A. Forel, Lé Léman.

Reproduced on opposite page:

Figure 26: Longitudinal uninodal seiches at Geneva observed by Plantamour (from Forel, 1895)

tal duration of 224 hours or over 9 days. He noted, furthermore, that Figure 26 corresponded to a period of 74 minutes as compared to the more generally observed mean of 73,5 minutes. Forel attributed this increase in period to the fact that the seiches in Figure 26 were observed at a time when the water level of the Léman was about 30 cm lower than normal.

In the search for a mathematical expression from which the seiche period could be calculated, Forel discovered, in 1876, that Merian's (1828) formula, equation 55 for the water surface oscillation in a rectangular vessel, was also valid for a "vessel" as large as the Léman. The problem with equation 55 was only that of determining a mean equivalent depth, \bar{D} , to enable the seiche period to be calculated. However, it was only in 1890 that Forel was able to determine a mean depth, \bar{D} , since it was then that the first map showing the depth configuration of the Léman became available. Using a mean depth of 112,4 m, Forel (1895) found that the agreement with observations was nevertheless poor. Forel then approached du Boys in order to develop a formula for irregular basins. Du Boys proposed a numerical extension of Merian's formula (Du Boys, 1891a):

$$T = \frac{2}{\sqrt{g}} \sum \frac{2S_i}{\sqrt{D_i} + \sqrt{D_{i+1}}} \quad (56)$$

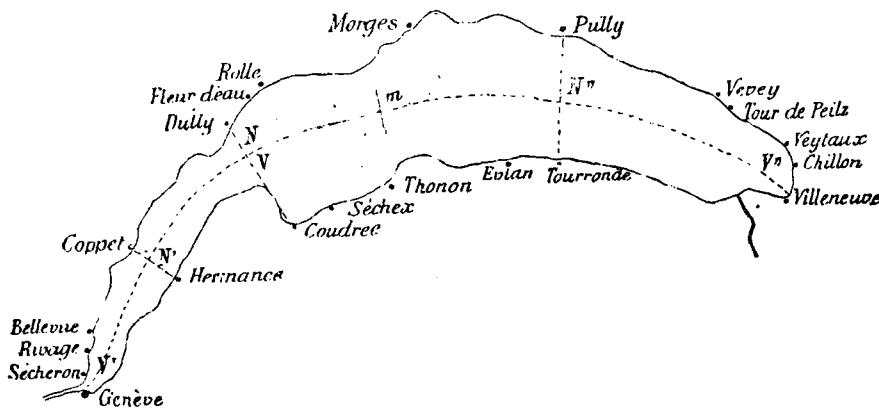
where S_i is the length between two successive lake cross-sections.

Application of equation 56 is difficult insofar as personal judgment is required when tracing a "median track" along the thalweg of the lake. Furthermore, no account is taken of the variations in the width of the lake or of its longitudinal curvature.

Due to the determination of a median track and its associated profiles, equation 56 is even more difficult to apply for the calculation of transverse seiches.

Using equation 56, Forel (1895) obtained 77,4 minutes for the period of a uninodal longitudinal seiche. Du Boys using different subdivisions obtained 74,6 minutes thus already approximating well Forel's observations. From the fact that the longitudinal uninodal seiches are practically absent on the traces of the limnigraphs of Rolle and Thonon, Forel concluded that the node of the longitudinal seiches must be situated near these locations. This he was able to prove also with his calculations using equation 56.

Considering the binodal longitudinal seiches, Forel was not able to explain why they have a period of 35 minutes, i.e., $1 \frac{3}{4}$ minutes less than half the period of a longitudinal uninodal seiche. From the absence of traces of binodal seiches at certain stations, Forel was also able to indicate the positions of the nodes of the longitudinal binodal seiches in the lake. Forel's (1895) positions of the nodes of the longitudinal uninodal and the longitudinal binodal seiches in the Léman are shown in Figure 27.



Ventres et nœuds des seiches longitudinales du Léman.

Figure 27:

Positions of nodes and anti-nodes of longitudinal Léman seiches as determined by Forel (from Forel, 1895)

Studying the causes of seiches, Forel found that, in general, seiches are larger when the barometric pressure is low (i.e., when the weather is bad), and that seiches are largest when the

wind is the strongest. Also, local variations in atmospheric pressure may contribute to the occurrence of seiches. The fact that sometimes uninodal and sometimes binodal seiches are created, Forel (1895) contributed to differences of the time history of the atmospheric perturbations creating the seiches.

4.2 Doodson et al.

Using thirty-one cross-sections for the mathematical representation of the Léman, Doodson et al. (1920) calculated, with Proudman's method, longitudinal seiche periods as summarized in Table 3. According to Doodson et al. (1920), all figures

Table 3: Longitudinal seiche periods of the Léman calculated by Doodson et al. (1920)

Number of nodes	Period (min.)
1	74,45
2	35,1
3	28

shown in Table 3 may be regarded as significant. Comparing the seiche periods of the uni- and binodal longitudinal seiches as observed by Forel (see Table 1) it can be seen that agreement between theory and observations is indeed very good.

Doodson et al. (1920) also determined the elevations of uni- and binodal longitudinal seiches. These elevations have been plotted by the author in Figure 28. In Figure 28 it can be seen that the uninodal longitudinal seiches at Morges are already opposite in phase to the Geneva seiches, and furthermore, that the amplitude of the Morges seiches is about 1/10 that of the Geneva seiches. Comparing these findings with Forel's observations shown in Figure 25, it can again be seen that agreement between theory and observations is excellent. The amplitude of uninodal longitudinal seiches at Montreux is, according to

Figure 28, about 1/6 that of Geneva. Since Forel does not give any traces of seiches near Montreux, no comparison with observations can be made at this stage.

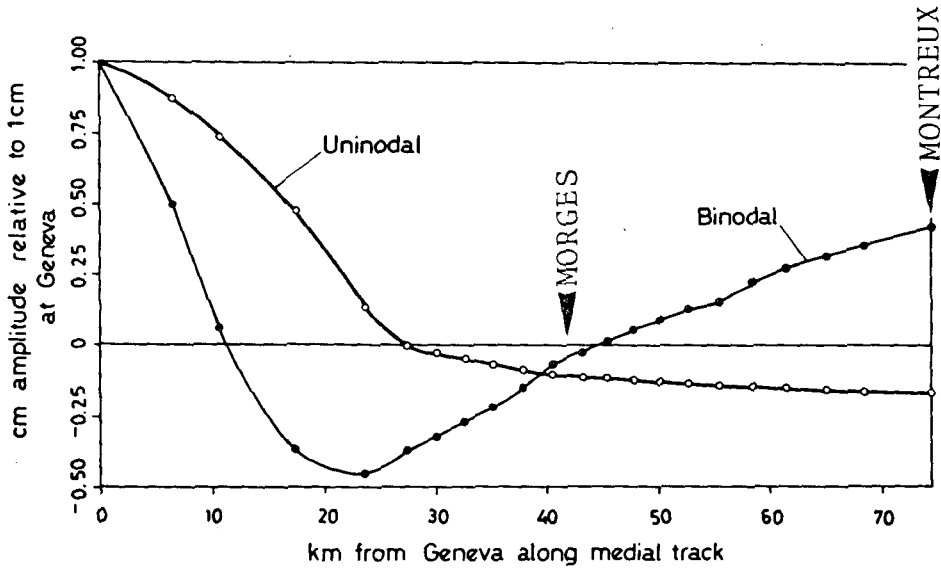


Figure 28: Vertical displacements of longitudinal Léman seiches according to Doodson et al. (1920)

The positions of the nodes of the first two longitudinal Léman seiches have also been determined by Doodson et al. (1920). The author has drawn them on Figure 29 together with the nodes as observed by Forel (1895). As can be seen in Figure 29, there is

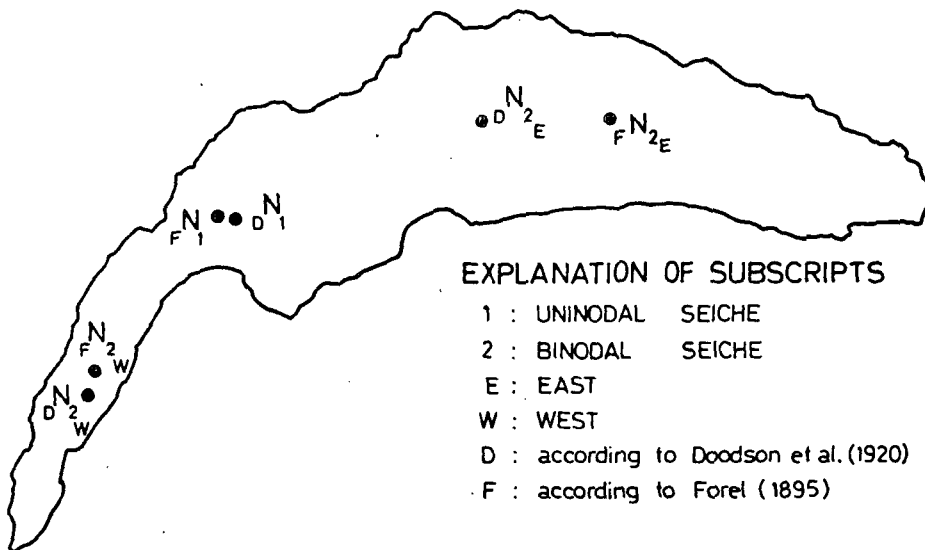


Figure 29: Positions of nodes of longitudinal Léman seiches according to Doodson et al. (1920) and Forel (1895)

again excellent agreement between the theoretical position of the node of the first order longitudinal seiche and its position observed by Forel. As for the positions of the nodes of the binodal seiches, one finds that agreement between Doodson's et al. (1920) positions and those indicated by Forel (1895) is less good. In Figure 29, it can be seen that the second order nodes are both situated a little closer to the Geneva end of the Léman when compared with those indicated by Forel (1895).

4.3 Service fédéral des eaux

In order to study non-periodic water surface fluctuations of the Léman, the service fédéral des eaux (SFdE) set up 14 temporary limnigraphs, which are shown together with the permanent SFdE-stations in Figure 30. An example of a long series of

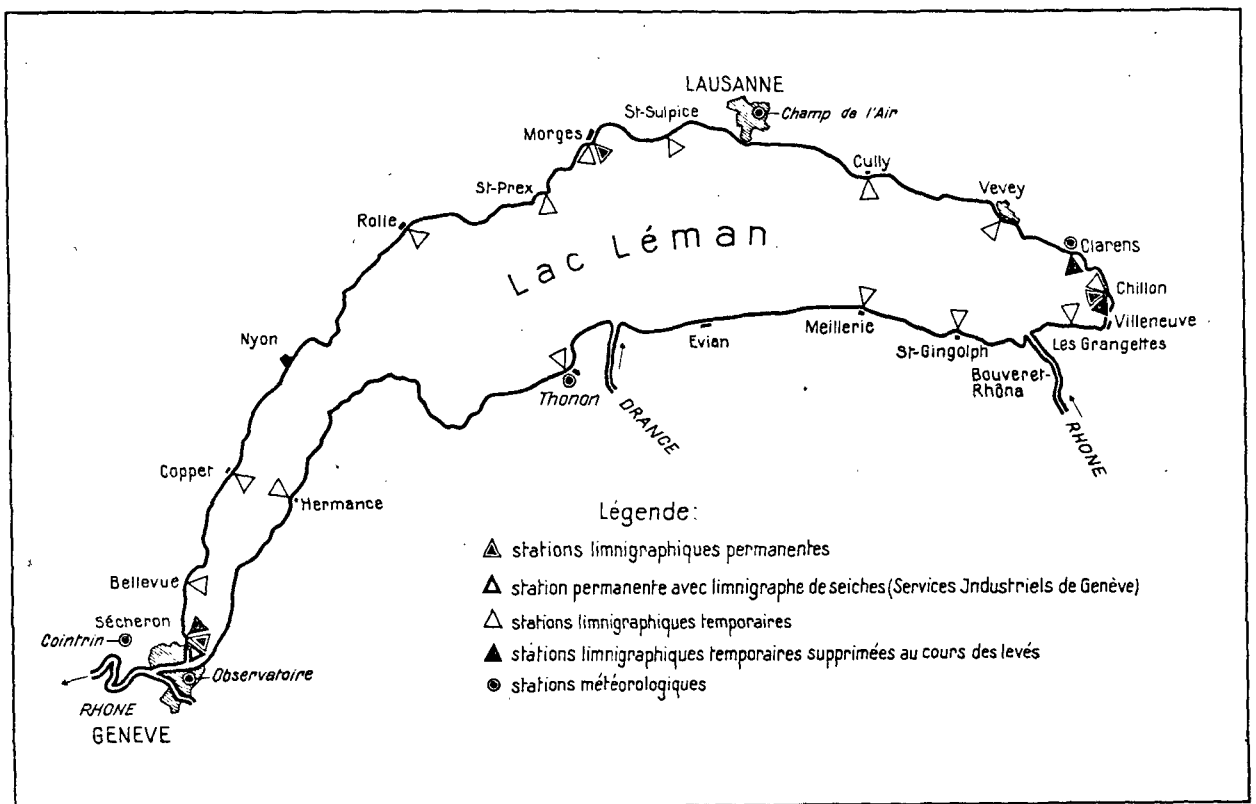
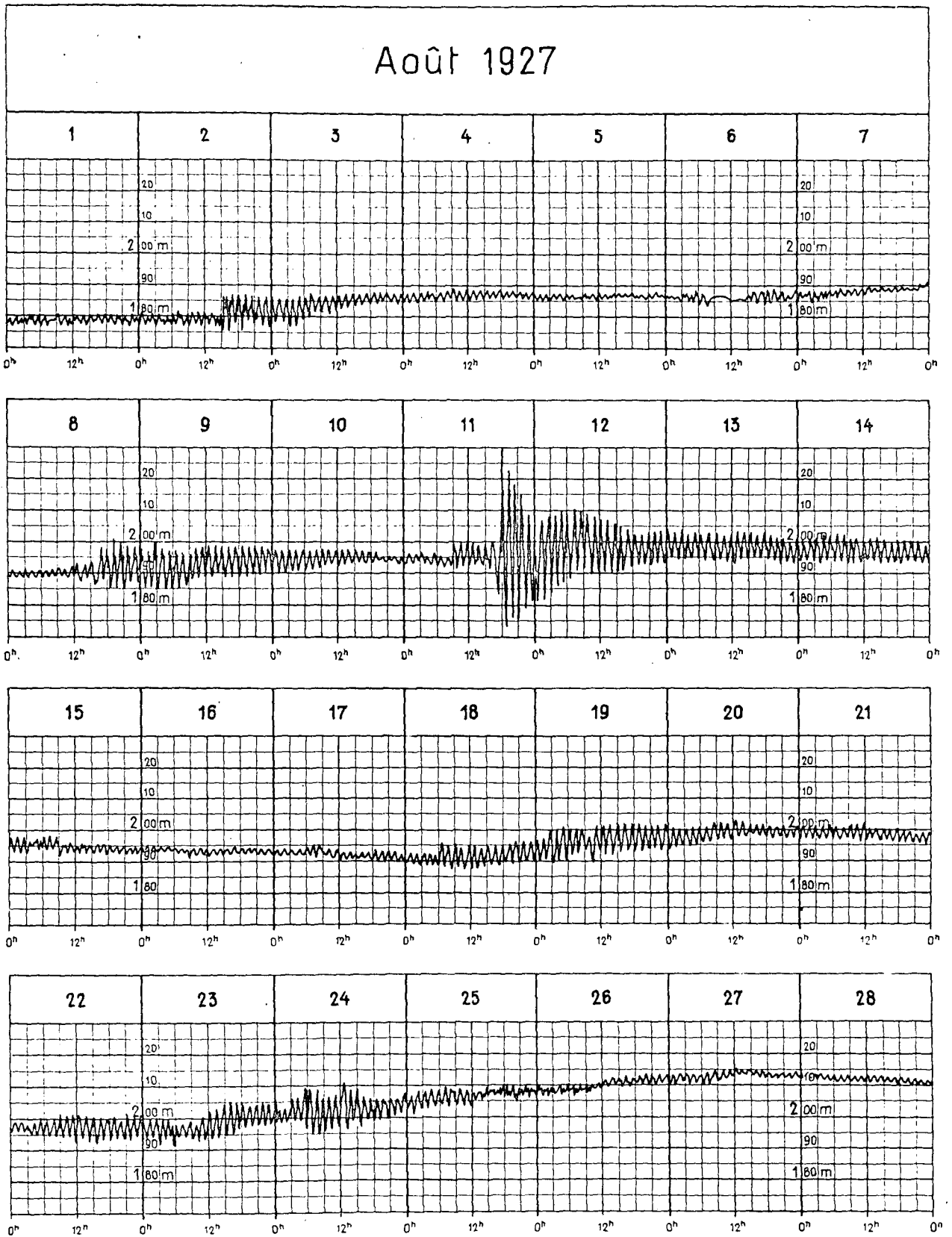


Figure 30: Limnigraphs existing in 1950 on the Léman (from Service fédéral des eaux, 1954)



Station limnographique permanente de Genève-Sécheron.
Exemple d'enregistrement de fortes seiches avec l'appareil du Service fédéral des eaux.

Figure 31: Example of extraordinary seiches registered by the Swiss Service fédéral des eaux (from Service fédéral des eaux, 1954)

seiches, observed by the SFdE in August 1927, is shown in Figure 31. There it can be seen that the decrease in amplitude of a seiche is very slow, and as was already observed by Forel (see Figure 26) at times not readily predictable.

Examples of typical registrations by the SFdE of Léman seiches are shown in great detail on Figures 32 and 33. The positions of the recording stations used for the tracing of Figures 32 and 33 are shown in Figure 30. Without going into too much detail it may be noted in Figures 32 and 33 that the longitudinal uninodal seiches are very conspicuous (see in particular Figure 32; Genève - Sécheron, Coppet). At St. Prex and Thonon, the amplitude of the uninodal longitudinal seiches is again about 1/10 of those at Geneva. The longitudinal uninodal seiches at Vevey are larger than those at St. Prex, i.e., about 1/6 of the Geneva seiches, thus confirming the theoretical deductions by Doodson et al. (1920). A series of binodal longitudinal seiches occurring at St. Gingolph can be observed in Figure 33. Occurring simultaneously with the principal longitudinal seiches are transverse seiches, notably at St. Prex, Thonon, St. Gingolph, St. Sulpice, Rolle, etc. The particular appearance of the seiches at Les Grangettes is, according to the Service fédéral des eaux (1954), due to some interaction with the mouth of the Rhône. In Figure 33, the change from one regime of seiches to another can be observed on July 28, 1950 at 17 hours.

Investigating the change of period of a seiche with changes of water level, the SFdE was also able to show that the principal seiche period increases with a decrease of water level. This can be seen in Figure 34.

The SFdE also investigated the influence of wind on the water surface of the lake. For this purpose, the Service fédéral des eaux (1954) determined 6-hourly mean water levels, every 3 hours, for all stations situated on the shores of the Léman. Using these

ECHELLE DES HAUTEURS
0 4 8 12 16 20 24 28 32 36 40
cm

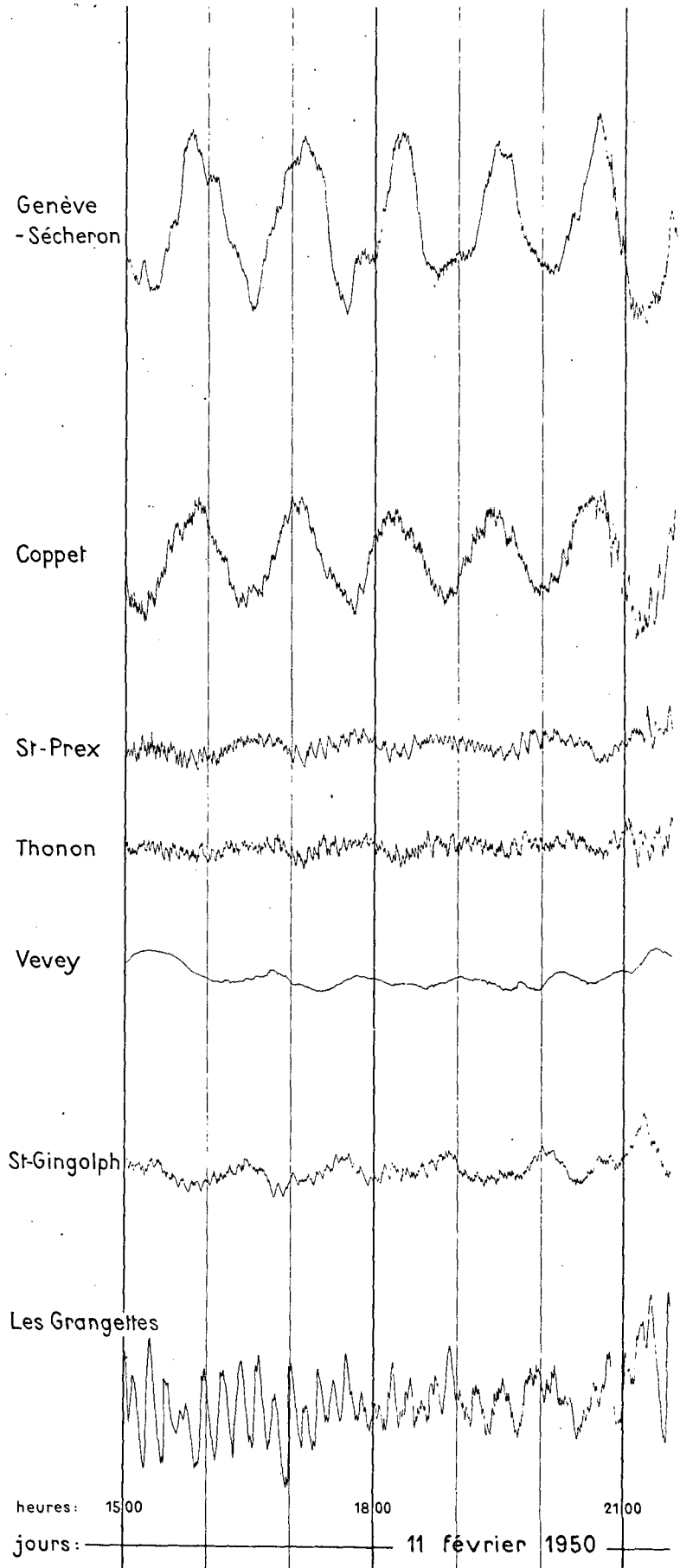
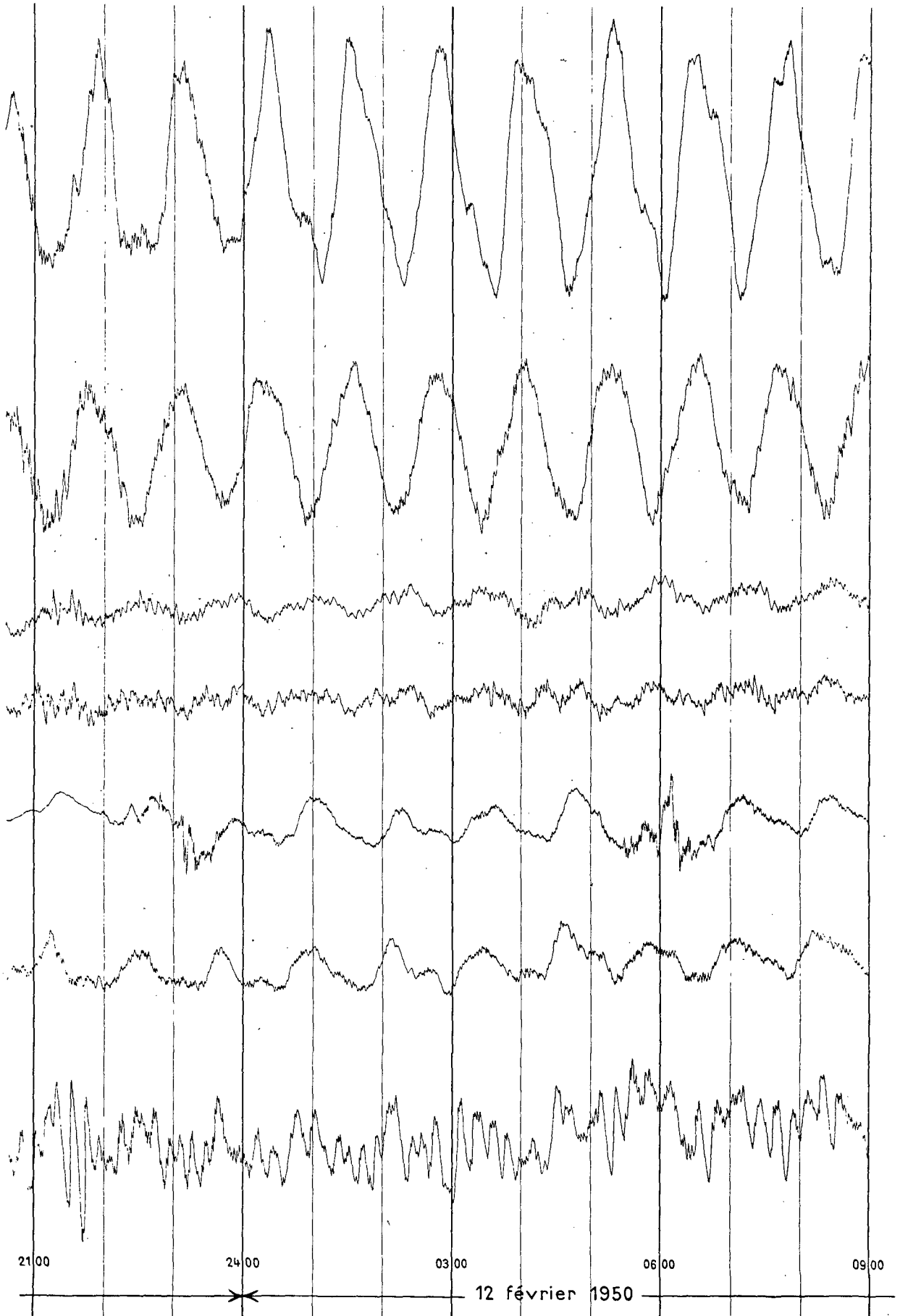


Figure 32:
Example of simultaneous records of Léman seiches on 11-12/2/1950 (from Service fédéral des eaux, 1954)



ECHELLE DES HAUTEURS
 0 4 8 12 16 20 24 28 32 36 40
 cm

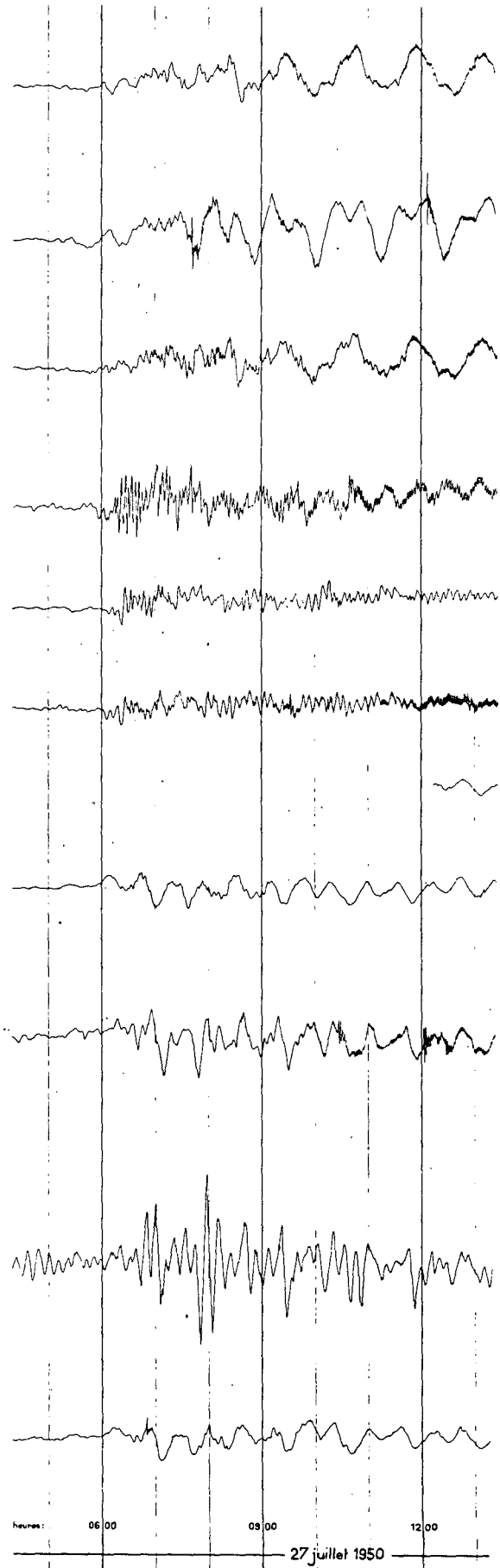
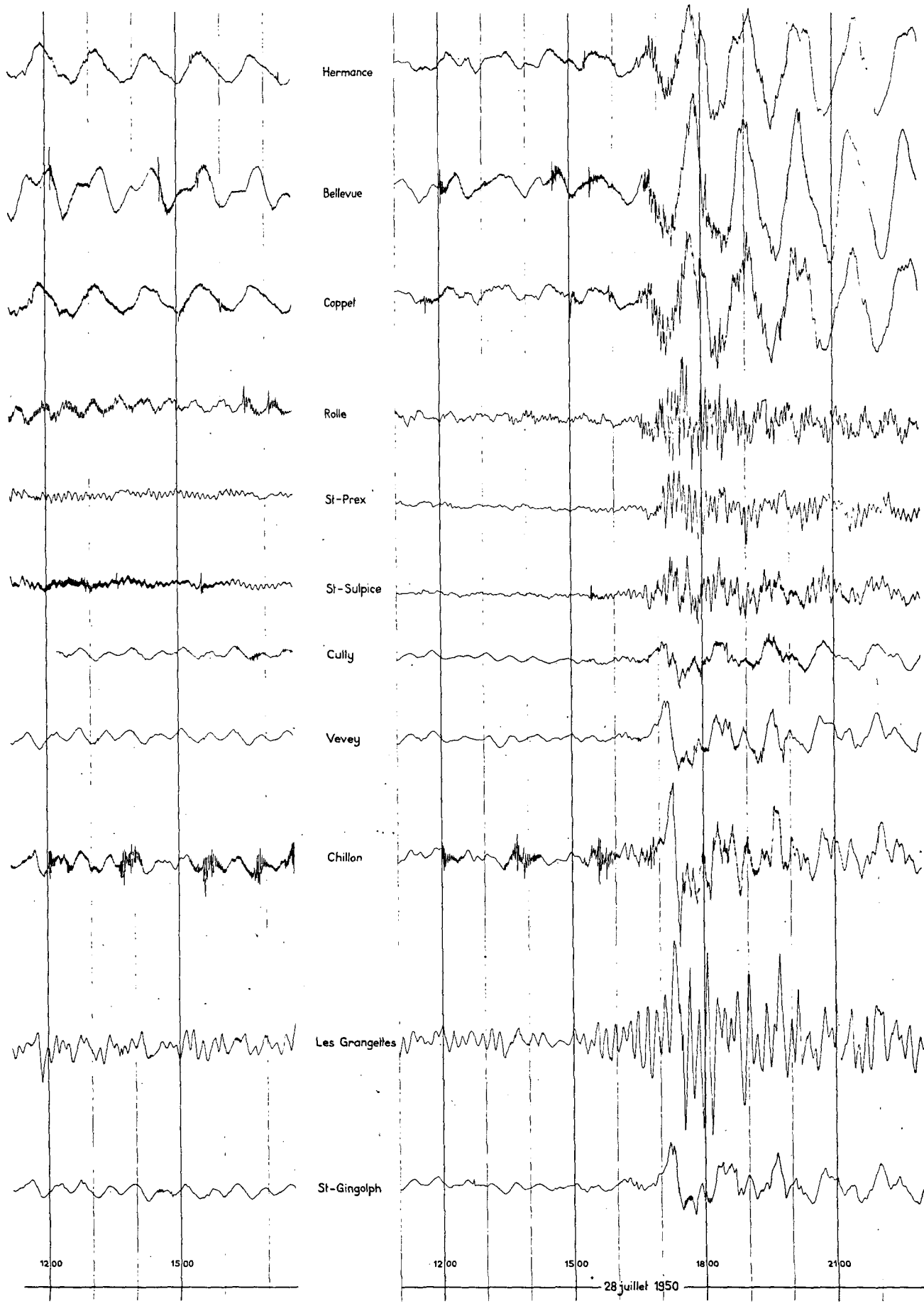


Figure 33:
 Example of simultaneous records of Léman seiches on 27 - 28/7/1950 (from Service fédéral des eaux, 1954)



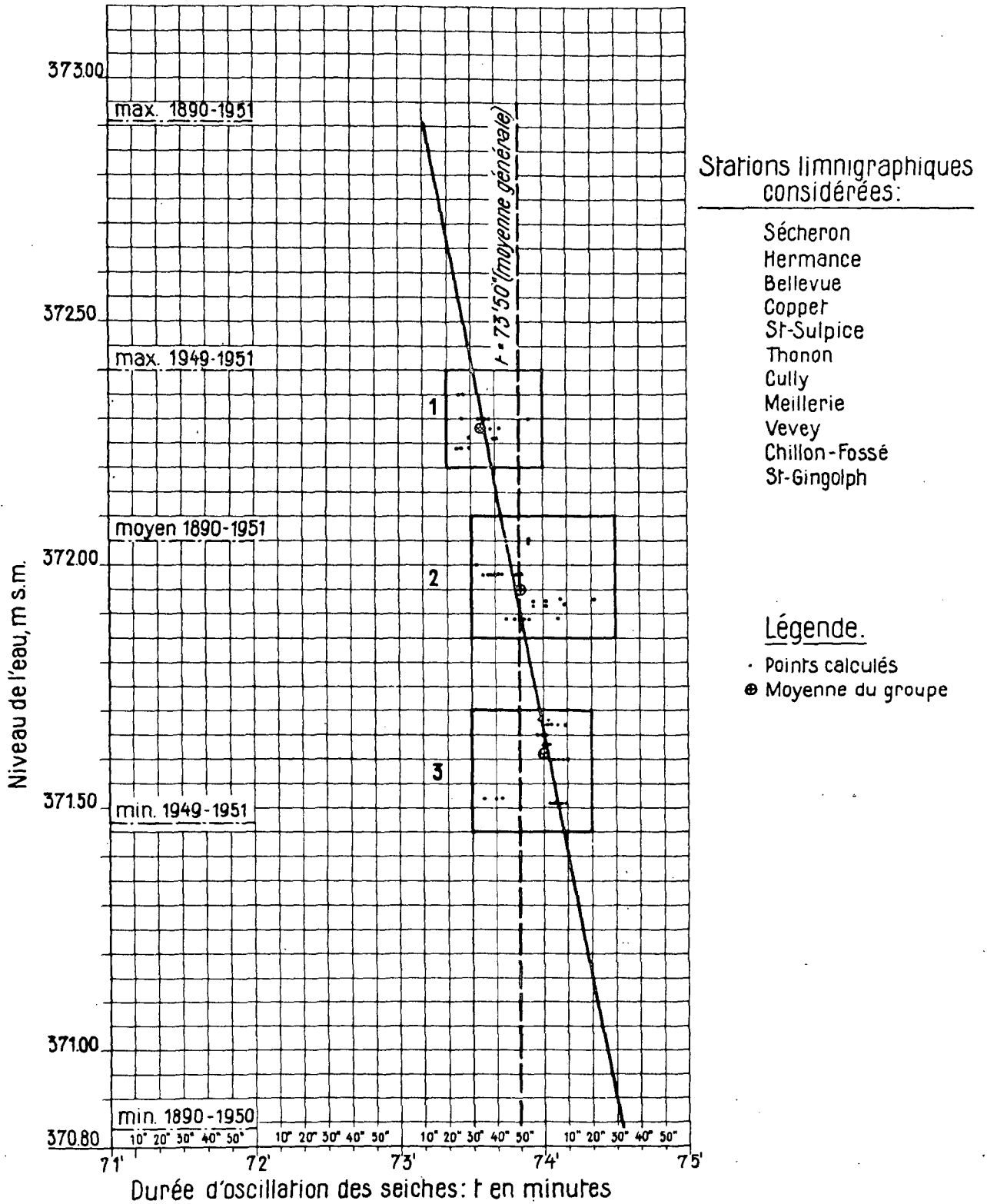


Figure 34: Variation of seiche period with mean water level in the Léman (from Service fédéral des eaux, 1954)

values, the SFdE calculated a mean level each time by means of a weighted mean procedure, the weights being proportional to the water surface surrounding each station. In this way, the SFdE obtained changes of water levels relative to the mean lake level as shown in Figures 35-37. The wind set-up for a "Bise", a northeasterly, rather regular strong wind is shown in Figures 35 and 36. In Figure 37, the wind set-up for a typical "Vent" situation is shown. Comparing the two types of winds, it appears that the two Bises were both of a more regular nature than the Vent. In Figures 35 and 36, i.e., for Bises, it should be noted that the wind set-up near Geneva is substantially larger than that at Chillon. In Figure 38, the water level elevations along the northern and the southern lake shores for some Bise- and Vent (Sudois) situations are shown. For the Bise it can again be seen that, at Geneva, the wind set-ups are substantially more important than at Chillon. Furthermore, it should be noted that the intersection of the water levels with the mean lake level, in the case of Bises, does not coincide with the node of the longitudinal uninodal seiche (situated near Rolle), but is located near the line St. Prex - Thonon, i.e., at about the midpoint of the thalweg Genève - Villeneuve (see also Figure 30).

4.4 Mortimer

Although Mortimer's work on the Léman was mainly concerned with internal seiches, i.e., fluctuations of the thermocline (Mortimer; 1953, 1963, 1974, 1979), he also performed calculations on the surface seiches of this lake. Applying a Defant (1918) method for the determination of seiche periods and using the same cross-sections of the Léman as Doodson et al. (1920), Mortimer (1979) calculated the periods of longitudinal seiches as summarized in Table 4. Considering first the uninodal seiche, one finds that Mortimer's period was the shortest one when compared with other calculated periods, i.e., Forel's (1895) calcu-

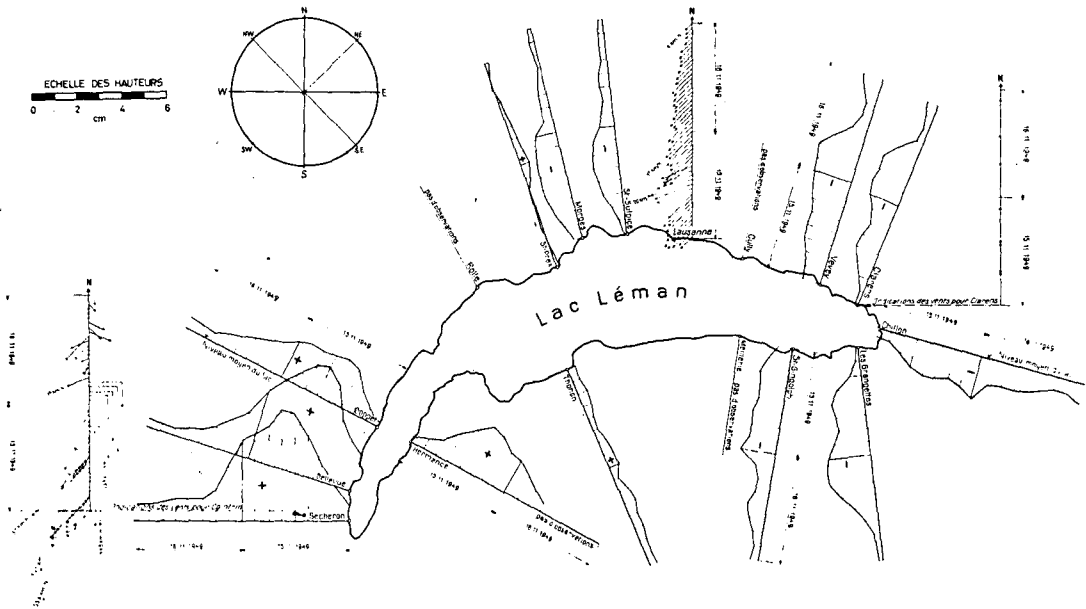


Figure 35: Wind set-up in the Léman caused by the "Bise" on 15-16/11/1949 (from Service fédéral des eaux, 1954)

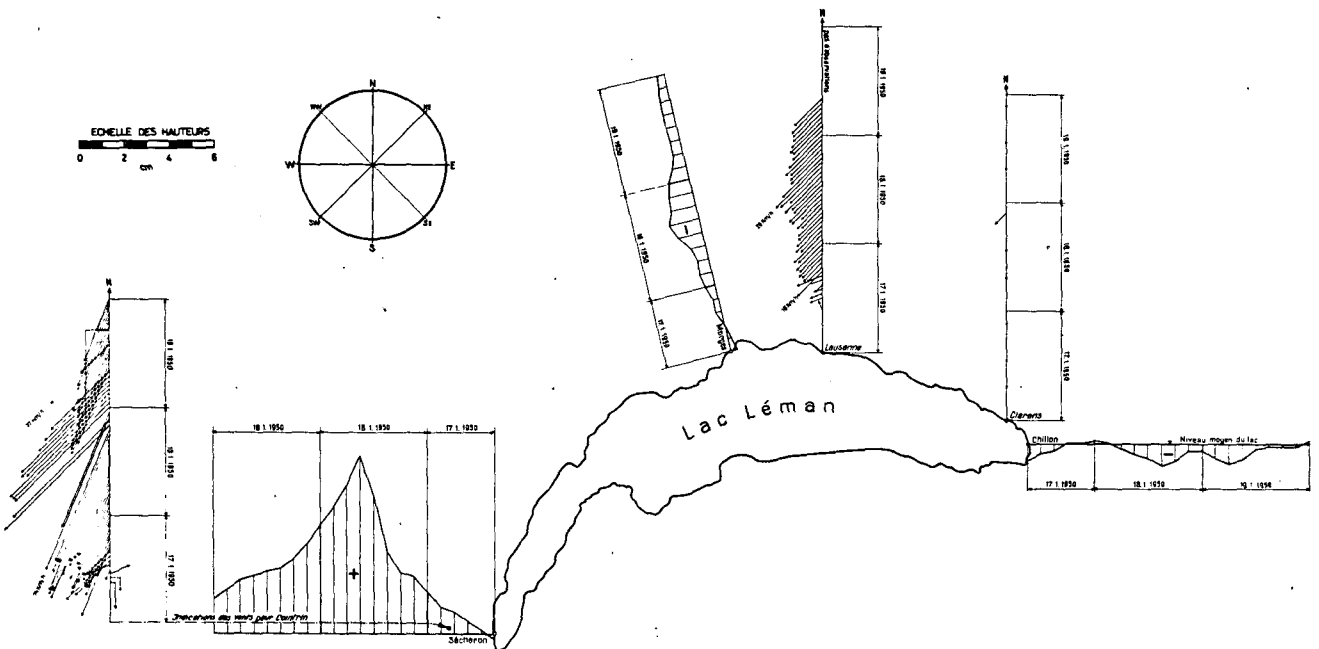


Figure 36: Wind set-up in the Léman caused by the "Bise" on 17-19/1/1950 (from Service fédéral des eaux, 1954)

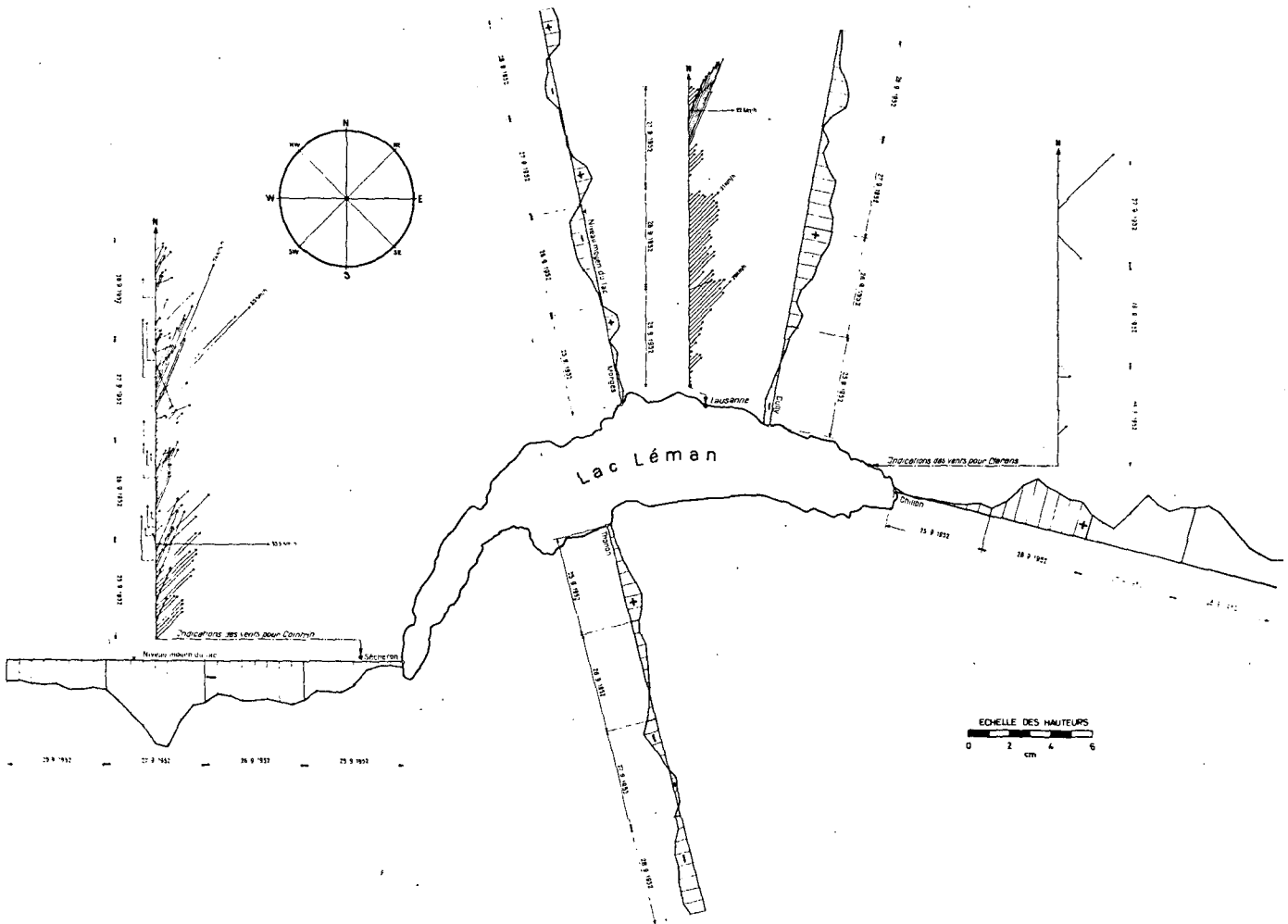


Figure 37: Wind set-up in the Léman caused by the "Vent" on 25-28/9/1952 (from Service fédéral des eaux, 1954)

Table 4: Longitudinal seiche periods of the Léman calculated by Mortimer (1979)

Number of nodes	Period (min.)
1	74,1
2	35,5
3	29,1
4	21
5	18

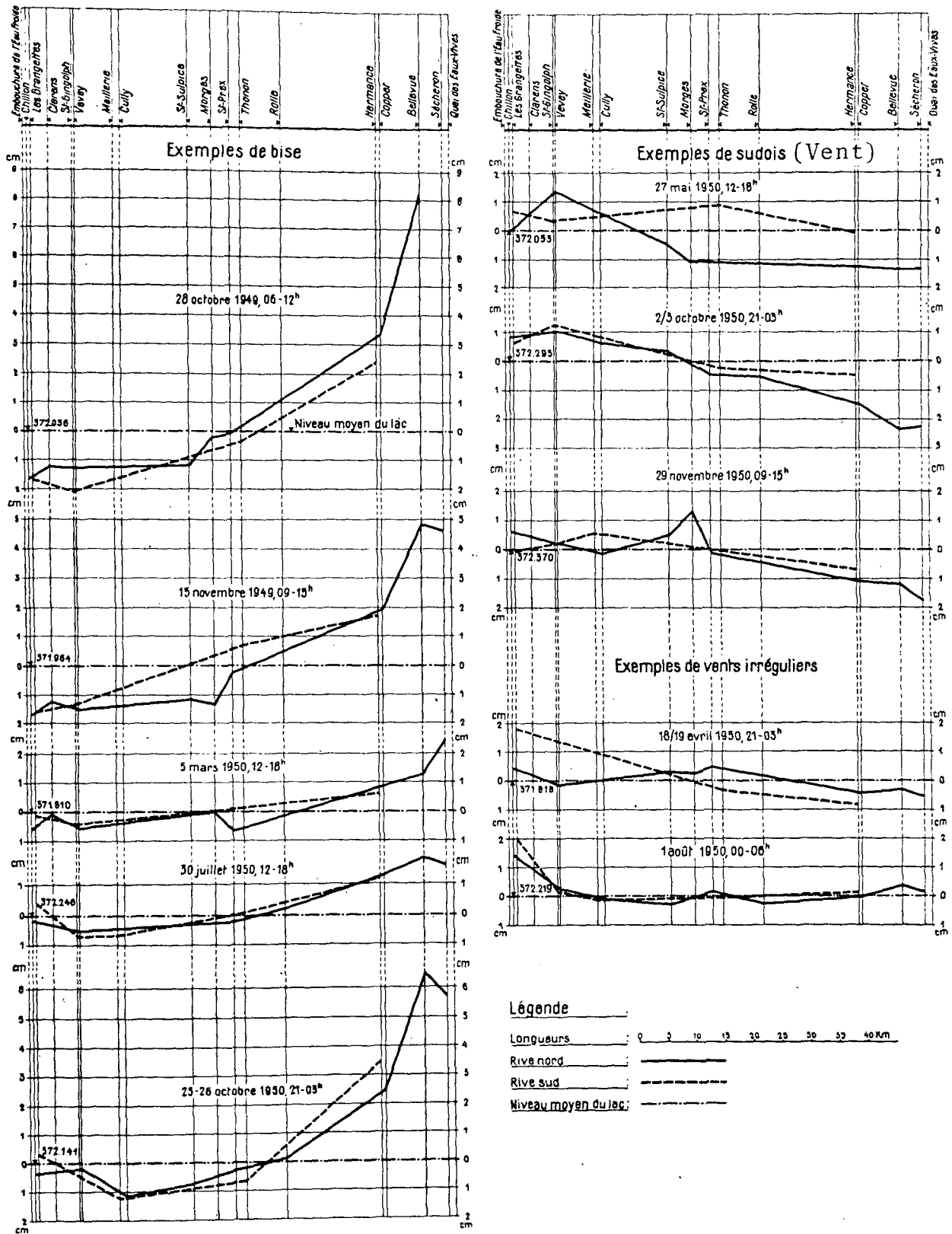


Figure 38: Water levels along the Léman shores during various types of wind set-ups (from Service fédéral des eaux, 1954)

lated period of 77,4 minutes, Du Boys' (Forel, 1895) calculated period of 74,6 minutes and Doodson's et al. (1920) calculated period of 74,45 minutes. As such, Mortimer's calculations for the longitudinal uninodal seiches compare best with Forel's (1895) observed value of a mean period of 73,5 minutes. Mortimer's (1979) period of a binodal seiche being 35,5 minutes is slightly longer than that obtained by Doodson et al. (1920) of

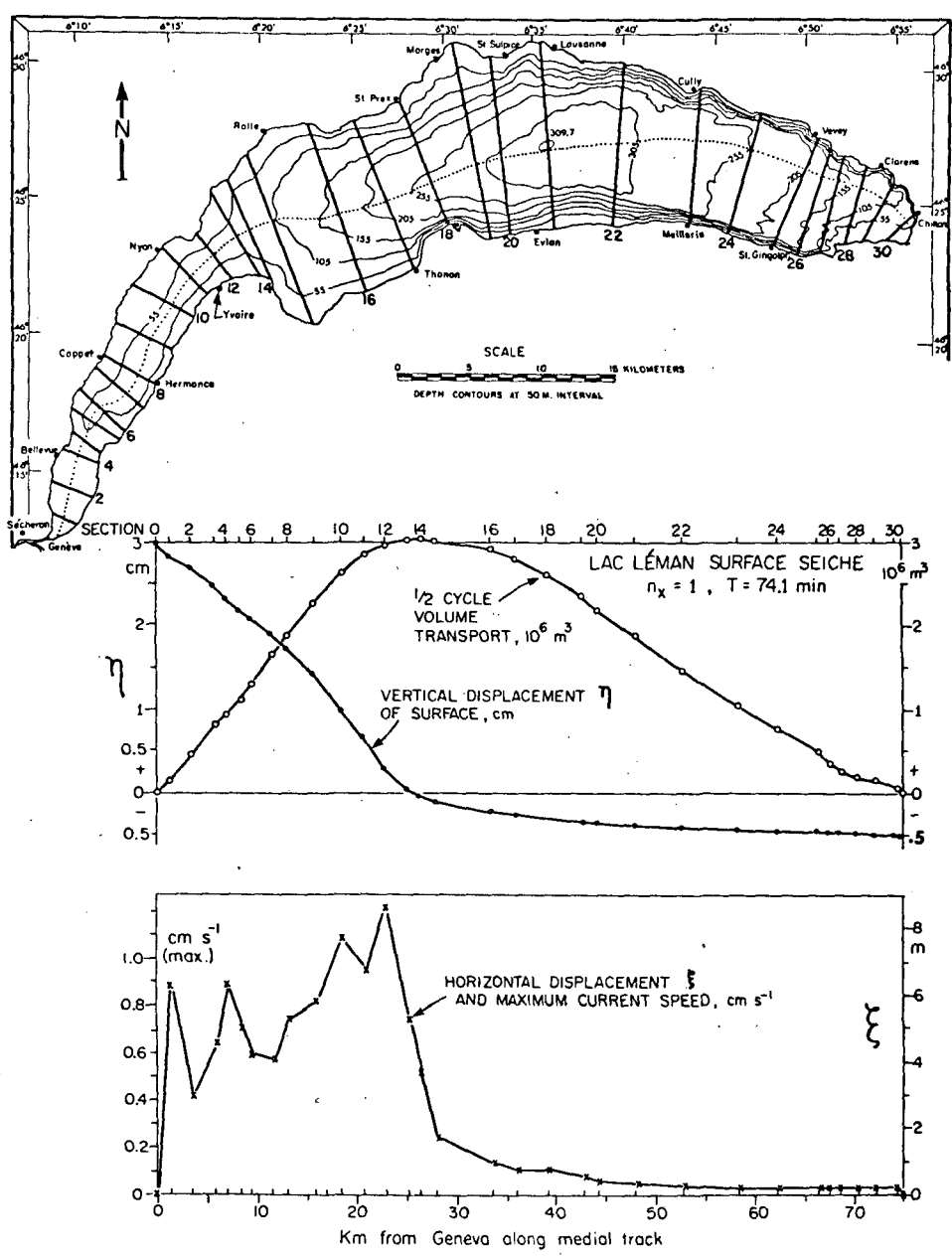


Figure 39: Mortimer's analysis of a uninodal longitudinal seiche in the Léman (from Mortimer, 1979)

35,1 minutes, and coincides exactly with Forel's (1895) observed period of 35,5 minutes.

In contrast to other earlier calculations, Mortimer's (1979) work also gives information on mass transport and horizontal displacement, as can be seen in Figure 39. The maximum horizontal current speed associated with a "typical" surface seiche amplitude of ± 3 cm at Geneva only exceeds 1 cm/s near the uninode. In the main basin the corresponding maximum velocities are 0,1 cm/s or less. Compared with internal seiches therefore, the effect of surface seiches on water transport is small. The vertical displacement calculated by Mortimer is very similar with that of Doodson et al. (1920) and consequently agrees well with the observations by Forel (1895) and with those of the Service fédéral des eaux (1954). The node of the uninodal seiche, according to Mortimer, is again situated at the same place as observed by Forel (1895) and calculated by Doodson et al. (1920).

4.5 Concluding remarks on earlier work on Léman seiches

Comparing Forel's observations of surface seiches of the Léman with later investigations, one finds that Forel's work has, in general, been confirmed. This, in particular, applies to seiche periods and -durations (compare Figures 31 and 26), to the large number and variability of seiches (compare Figures 32 and 33 with Figures 20-25) and to the change in seiche period with changes in water level (compare Figure 34 and the increase in seiche period, noted by Forel, at water levels lower than normal of the seiches shown in Figure 26).

The position of the node of the uninodal longitudinal seiche as deduced by Forel (1895) has been confirmed by later theoretical investigations (compare Figures 39, 29, 28 and 27). Slight discrepancies, however, do exist between the theoretical positions of the nodes of binodal longitudinal seiches as indicated by Doodson et al. (1920) and Forel (1895). This can be seen in Figure 29.

Theoretical determination of seiche periods appear to be improving with time since they agree more closely with Forel's observations, the more recently they have been performed (compare seiche periods shown in Tables 4 and 3 with the periods calculated respectively by Du Boys and Forel of 74,6 and 77,4 minutes with Forel's observations summarized in Table 1). Although progress has been made, it seems, nevertheless, that all theoretical seiche period determinations still consider the problem only in one dimension, i.e., for lakes with an elongated shape, and are neglecting possible influences of the curvature along the thalweg of a lake. If one were to calculate transverse seiche periods using a one-dimensional procedure, it would be necessary to chose a transverse thalweg and lake profiles parallel to the longer axis of a lake. This is, particularly when the lake has a curved longitudinal thalweg such as the Léman, practically impossible. The reason for the apparent absence of calculations of transverse seiche periods is probably due to these difficulties.

The variations of seiche amplitude along the shores of the Léman, already observed by Forel (1895), were also confirmed by later theoretical work. From Figures 39 and 28 it can be seen that the theoretical amplitudes of a longitudinal uninodal seiche at Chillon are about $1/6$ and at Morges about $1/10$ that of a seiche amplitude at Geneva. This can also be confirmed by observations (see Figures 32 and 33 and Figure 25).

Finally, considering wind set-ups as shown in Figure 38, it can be seen that in cases of Bise the wind set-up at Geneva is always much larger than near Chillon and also more pronounced than in the cases of a Vent (Sudois). It can also be seen that the intersection of the inclined lake water surface with its mean elevation does not coincide with the node of a uninodal seiche, but is situated about midway between Geneva and Chillon (see Figure 38, particularly cases of Bise).

5. Mathematical simulations for the Léman

5.1 Introductory remarks

Using observations of Léman water levels as described in chapter 4, it will be shown that the mathematical model presented in chapter 2 and demonstrated with a hypothetical test lake in chapter 3 can also successfully be applied to a real lake, i.e., le Léman. It will be shown furthermore that the wind shear stress coefficient obtained by model calibrations corresponds reasonably with values known from the literature.

In chapter 2 it can be seen that the only external forces admitted in the present model are surface wind shear stress and lake bottom stress. This approximation must be considered as a first step in the model development since barometric pressure effects may not always be safely neglected (Hamblin and Hollan, 1978). The model runs will show that results obtained without barometric pressure influences can nevertheless be acceptable. It should be noted, however, that the present model has been written for a homogeneous lake only. Thus, if model simulations for the Léman are to be meaningful, the period of simulation must coincide with a time in which the Léman is more or less homogeneous. This condition is usually fulfilled in the winter months (Forel, 1895).

The simulation of seiches will be restricted to demonstrate that the major seiches occurring in the Léman can be simulated, and that the principal properties of seiches such as periods, position of nodes and ratios of their heights at the extremities of the lake correspond well to theoretical results and to observations.

The quality of simulation depends obviously on how well the real lake geometry has been represented by the network of discrete points at which the hydrodynamic equations are solved. It will be seen that the only major drawback to a coarse, irregular

grid is the fact that instabilities are created. To stabilize the system, smoothing of the calculations with $\alpha \approx 0,90$ is necessary. This smoothing results in a strong damping of seiche motion making it impossible to simulate seiches of long duration. However, as will be demonstrated, choice of a "smoothed-irregular" grid eliminates this problem.

5.1.1 Geometrical representation of the Léman

If it is required to simulate the behaviour of the Léman for long time periods and with greatest computational economy, it is necessary to choose a very coarse grid, thus allowing larger time steps (see equation 28). At the same time the number of calculations necessary per time step will be a minimum since the amount of calculations per time step is roughly proportional to the number of points. On the other hand, the coarser the grid, the poorer the geometric representation of the lake. A grid should therefore be chosen such that the specified purpose of the simulation run can be achieved.

As a first attempt, the Léman is represented by the irregular grid system shown in Figures 40-42. The grid of the Léman, shown in Figure 40, consists of 52 points; its water surface is $5,42 \cdot 10^8 \text{ m}^2$, and its volume is $7,86 \cdot 10^{10} \text{ m}^3$, resulting in a mean depth of 144,90 m. The point numbers 1, 22 and 52, nearest to Chillon, Morges and Geneva respectively, are for later reference. Figure 41 shows the depth at all points and the number of layers. Since, as has been stated in § 3.3, the behaviour of a single- and a multi-layer model is essentially the same, simulation will be performed using a one-layer formulation only. The boundary tangents shown in Figure 41 correspond to the principles explained in § 2.5. A three-dimensional view of the coarse Léman grid is shown in Figure 42. Comparing Figures 42 and 43, one finds that although the grid of Figure 42 is rather coarse when compared with that of Figure 43, all principal fea-

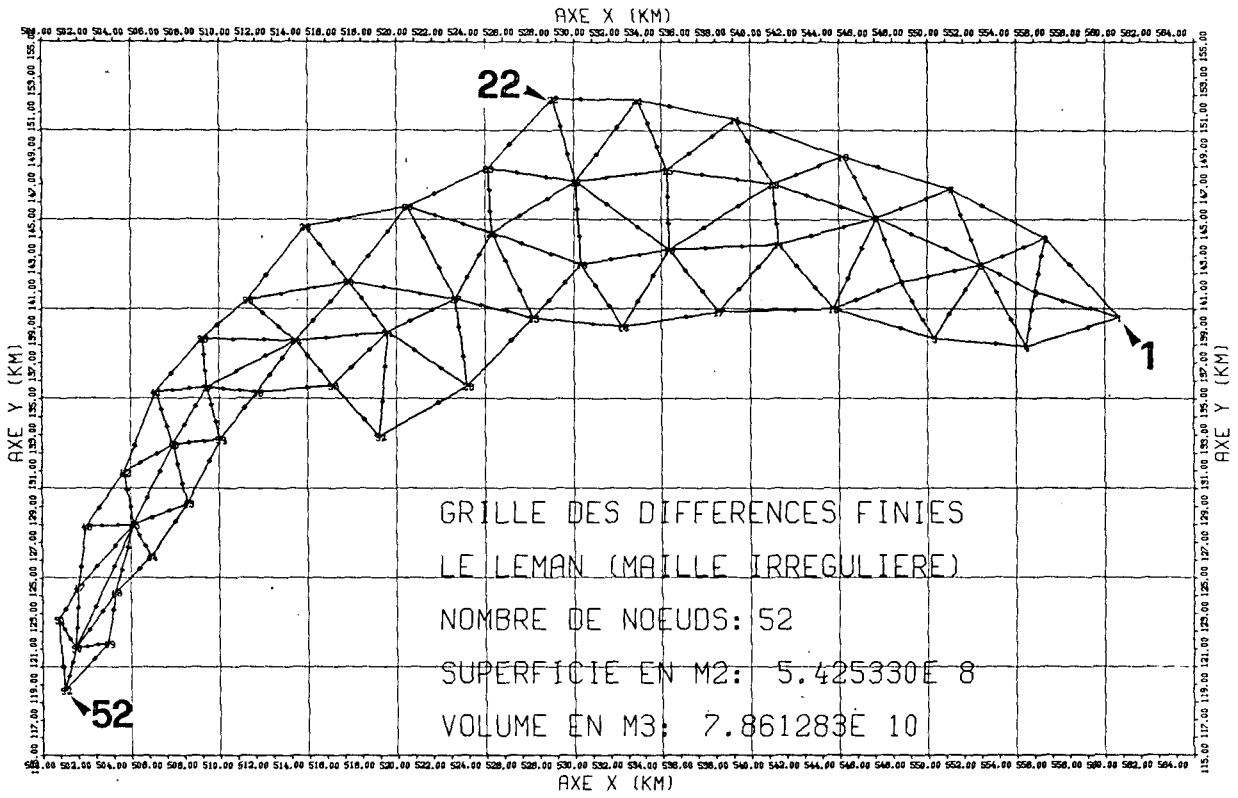


Figure 40: Plan view of coarse irregular finite difference grid of the Léman

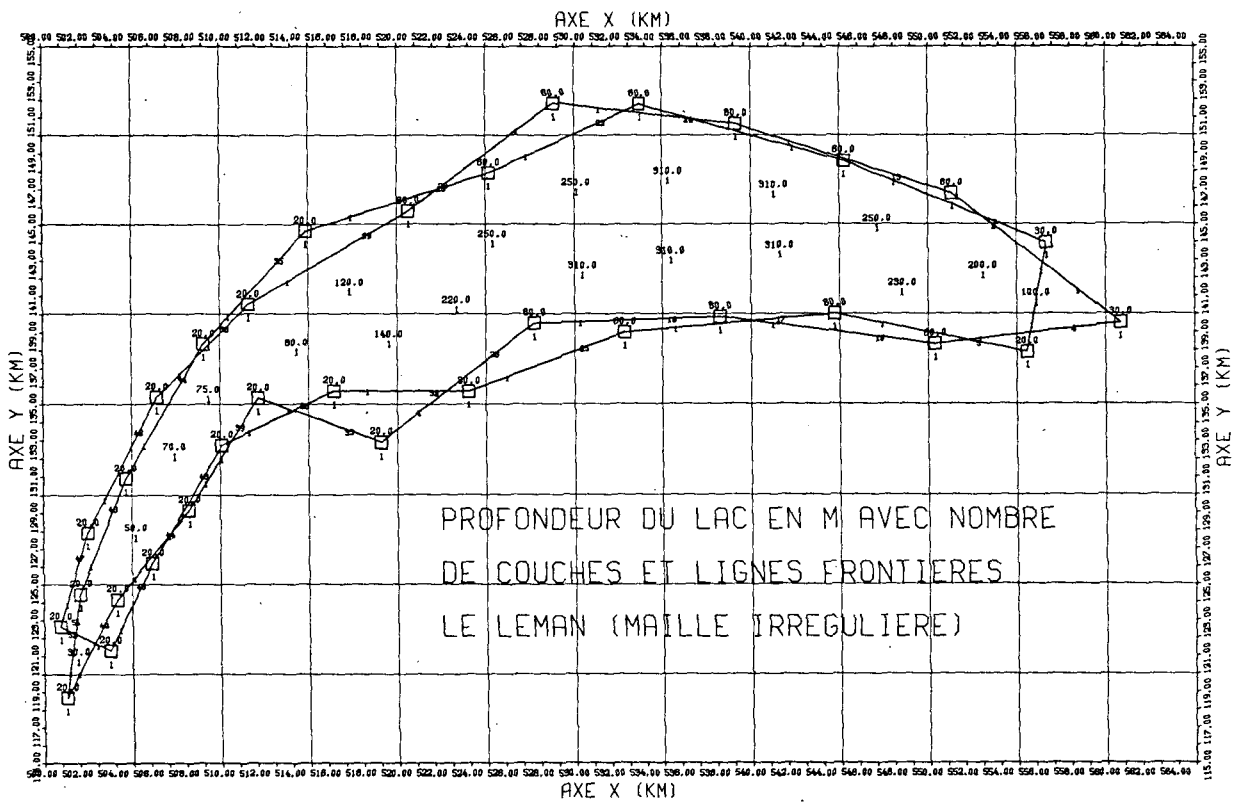


Figure 41: Depth and number of layers including boundary tangents of coarse finite difference grid of the Léman

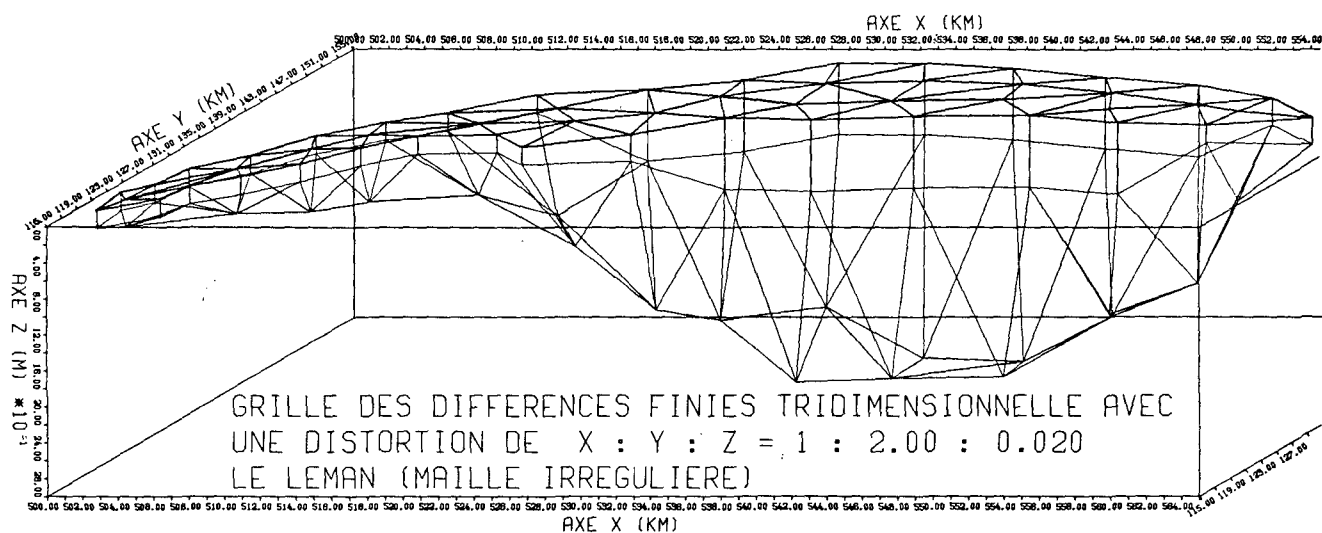


Figure 42: Three-dimensional view of coarse irregular finite difference grid of the Léman consisting of 52 points

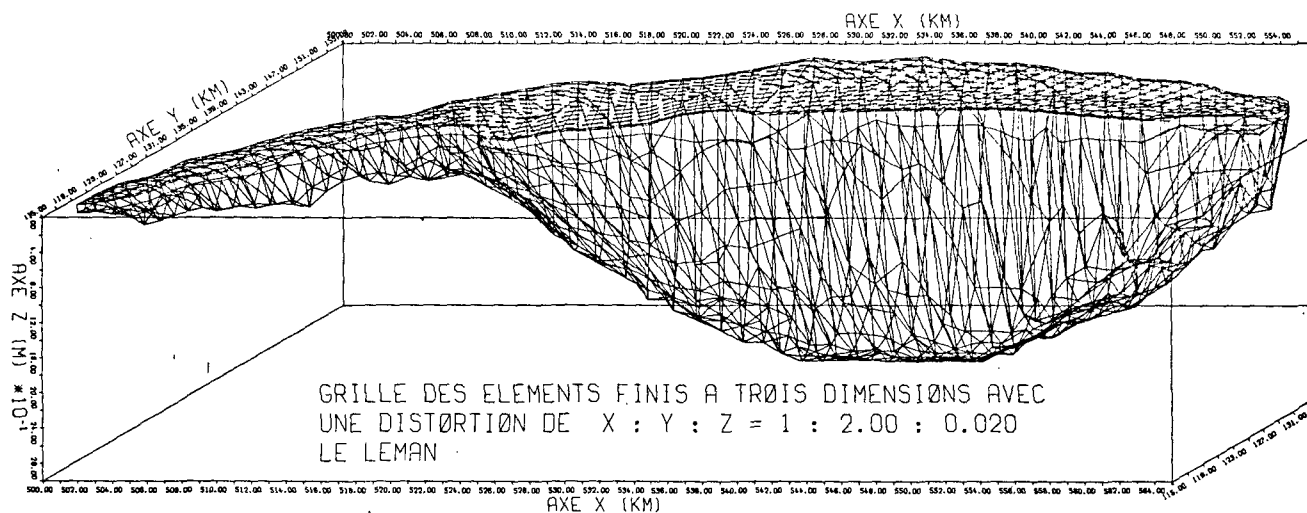


Figure 43: Three-dimensional view of a finite element grid of the Léman consisting of 579 points (from Bauer et al., 1977)

tures of the Léman are already quite well represented by the coarse grid.

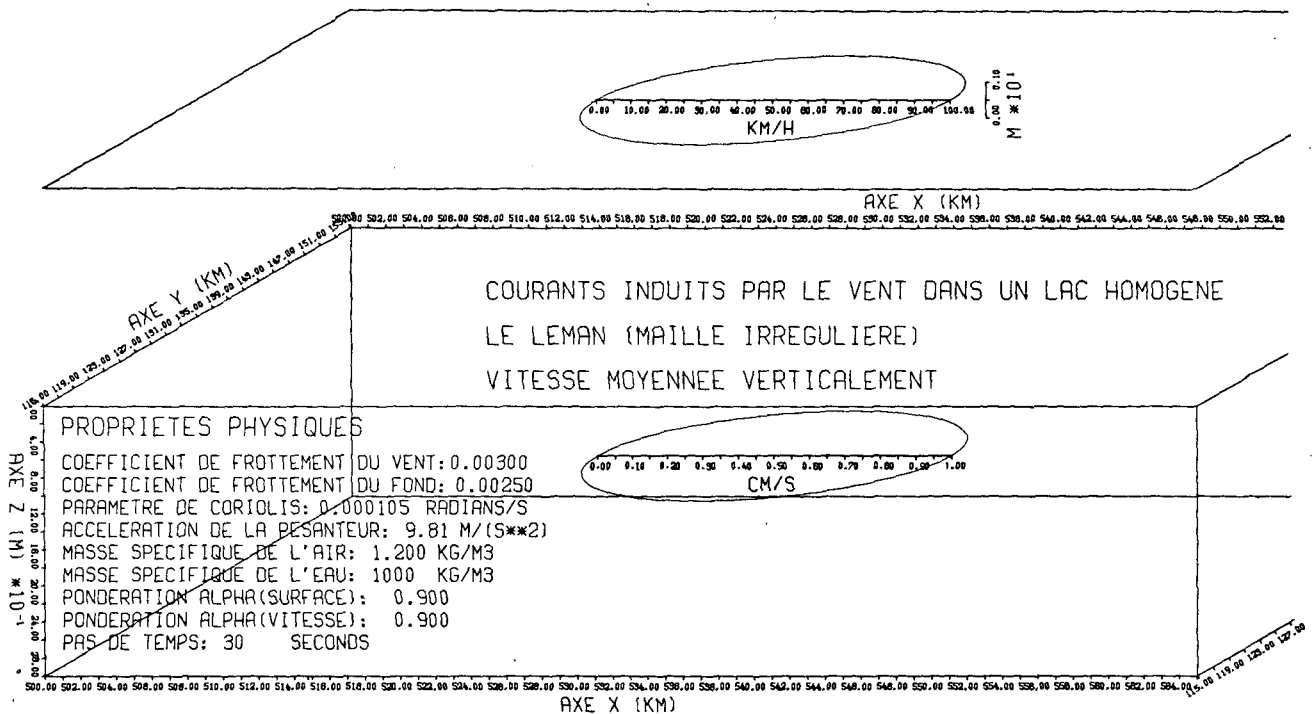


Figure 44: Scales and list of parameters used in coarse Léman grid simulations

5.1.2 Choice and discussion of principal constants

Unless indicated differently, all runs using the Léman grid shown in Figures 40-42 will be executed using the parameters indicated on Figure 44. These parameters correspond to those used for the simulations with the test lake discussed in chapter 3. The criteria used for the choice of these parameters are found in § 3.3. However, since the model is to be applied to the Léman only in its one-layer formulation, no eddy viscosity has to be calibrated. Assuming the basic physical constants such as acceleration of gravity, etc., as invariable, the only parameters subject to calibration are the wind shear stress-coefficient, the bottom shear stress coefficient and the α -mean. (It should be noted that the α -mean for the water surface is not necessarily equal to that of the velocities). Preliminary runs with the coarse Léman grid varying the α -mean showed that the model goes unstable for $\alpha = 1,0$. For $\alpha = 0,95$ the simulation

seemed to be stable with a time step of $\Delta t = 30$ s. For a time step of $\Delta t = 30$ s, the model did remain stable with $\alpha = 0,90$ for both water surfaces and velocities.

Keeping wind shear stress- and bottom shear stress coefficients constant, variation of Δt and α does not significantly influence the simulation of mean water levels. Furthermore, it should be noted that the influence of the bottom shear stress coefficient, c_b , was found to be extremely small. Comparing runs with $c_b = 0,0$ and $c_b = 0,0025$, it was found that there is no visible difference in the graphical display of the two runs. Numerically it was found that the first 4 significant figures were at all times identical in the two executions. Performing a rough analysis of magnitudes assuming a wind velocity of 50 km/h and a (very high) mean water velocity of 1 cm/s, equation 23 yields with the parameters listed in Figure 44 the shear stress $*\tau_{wind} = 6,94 \cdot 10^{-4} \text{ m}^2/\text{s}^2$ and equation 26 (rewritten for velocities rather than transports) yields $*\tau_{bottom} = 2,50 \cdot 10^{-7} \text{ m}^2/\text{s}^2$. The difference of the two stresses is thus at least three orders of magnitude which confirms the numerical observations. The only parameter remaining to be calibrated for a given wind is thus the wind shear stress coefficient.

5.2 Simulation of a Bise including determination of wind shear stress coefficient and discussion of wind set-up in the Léman

In order to simulate wind set-up in a lake, the wind should be known, with good resolution in time and in space for the entire period of simulation. Moreover, for testing the model results, at least water level recordings around the shoreline are necessary. These requirements, however, can be met only by means of an extensive measuring program that is beyond the scope of the present study.

In a literature survey the only data sets having a potential for wind set-up calculations in the Léman were found in Service

fédéral des eaux, 1954, in the form shown in Figures 35-37. As has been stated in § 4.3, six-hourly mean water levels were plotted every three hours for water level recorders situated on the banks of the lake. Also shown are mean wind vectors every hour at Geneva and Lausanne and some sporadic wind measurements at Clarens. With this information the data requirements for simulations with respect to time are reasonably well satisfied. Not much, however, is known on how representative the Geneva and Lausanne wind measurements are for the Léman water surface as a whole. Even in the vicinity of these two cities application of the above winds on the lake surface is problematic. Furthermore, due to the mountains surrounding the eastern one-third of the Léman, winds in this region may be quite different from those observed in Lausanne and Geneva. The spatial requirements of the data are thus very poorly fulfilled.

To allow nevertheless some use of the available data it was assumed that the wind will be the more evenly distributed over the Léman the more the winds observed at Geneva and Lausanne are similar to each other and the smaller the variation of the winds are with respect to time. From Figures 35-37 it can be seen that this condition is best satisfied for the Bise on 17-19 January 1950 shown in Figure 36. For this period one may also assume that the Léman was homogeneous as required by the present model.

From the considerations in chapter 4 it is clear that the maximum wind set-up must be expected at Geneva. From this it follows that changes in wind (or wind shear stress-) intensity will be most notable in simulation results for Geneva. This is very fortunate since, due to the configuration of the mountains surrounding the Léman, it can be expected that the winds over the western two-thirds of the lake will correspond to a large degree to those measured in Geneva and Lausanne. Winds blowing over the eastern third of the lake will have very little influence on Geneva

Table 5: Wind- and water level observations for the Bise on 17-19/1/1950 (abstracted from Figure 36 in its original size)*

Y	M	D	H	WG	DG	WL	DL	W	D	GE	MO	CH
1	1	17	8	0,0	0,0			0,0	0,0			
1	1	17	9	12,0	0,0	5,0	154,0	7,1	5,3	-0,25	0,30	-0,74
1	1	17	10	6,0	0,0	0,0	0,0	4,2	0,0			
1	1	17	11	9,5	24,0	0,0	0,0	6,6	24,0			
1	1	17	12	5,5	22,0	6,0	70,0	5,2	36,8	0,15	0,15	-0,41
1	1	17	13	11,5	22,0	6,0	70,0	9,8	46,8			
1	1	17	14	22,0	22,0	6,0	70,0	6,5	46,8			
1	1	17	15	28,0	22,0	5,0	45,0	21,1	45,0	0,55	0,0	-0,29
1	1	17	16	15,5	22,0	6,0	70,0	22,2	48,6			
1	1	17	17	33,5	22,0	6,0	70,0	26,0	27,9			
1	1	17	18	16,0	22,0	16,0	44,5	15,7	22,8	0,98	-0,28	0,05
1	1	17	19	28,0	22,0	10,0	44,5	22,4	22,5			
1	1	17	20	26,0	22,0	12,0	44,5	21,6	22,5			
1	1	17	21	28,0	22,0	13,0	44,5	23,0	22,5	1,20	-0,25	0,09
1	1	17	22	29,0	22,0	15,0	44,5	24,5	22,6			
1	1	17	23	26,0	22,0	14,0	44,5	22,1	22,6			
1	1	17	24	31,0	22,0	17,0	44,5	26,5	22,6	1,88	-0,45	0,19
1	1	18	1	33,0	22,0	15,0	44,5	25,9	22,5			
1	1	18	2	37,0	22,0	13,0	44,5	30,1	24,9	2,56	-0,58	0,09
1	1	18	3	45,0	22,0	18,0	44,5	35,1	24,9			
1	1	18	4	44,0	22,0	17,0	44,5	35,6	22,5			
1	1	18	5	37,0	22,0	16,0	44,5	30,4	22,5			
1	1	18	6	37,0	22,0	15,0	44,5	30,1	22,5	2,72	-0,49	-0,20
1	1	18	7	46,0	22,0	15,0	44,5	36,4	24,8			
1	1	18	8	37,0	22,0	13,0	44,5	29,5	22,5	3,65	-0,66	-0,45
1	1	18	9	44,0	22,0	16,0	44,5	33,2	22,5			
1	1	18	10	44,0	22,0	13,0	44,5	33,5	22,4			
1	1	18	11	46,0	22,0	19,0	44,5	37,5	22,5			
1	1	18	12	56,0	22,0	21,0	44,5	45,1	22,5	6,10	-1,08	-0,61
1	1	18	13	68,0	22,0	18,0	44,5	52,6	22,4			
1	1	18	14	67,0	22,0	19,0	44,5	52,2	22,4			
1	1	18	15	71,0	22,0	24,0	44,5	56,2	24,4	7,95	-1,37	-0,96
1	1	18	16	71,0	22,0	20,0	44,5	55,3	24,4			
1	1	18	17	60,0	22,0	26,0	44,5	49,3	22,5			
1	1	18	18	66,0	22,0	29,0	44,5	54,3	22,5	6,64	-1,11	-0,78
1	1	18	19	63,0	22,0	25,0	44,5	51,1	22,5			
1	1	18	20	64,0	24,0	20,0	44,5	50,8	45,0			
1	1	18	21	61,0	22,0	20,0	44,5	48,7	45,0	5,68	-1,09	-0,31
1	1	18	22	74,0	22,0	20,0	44,5	57,4	24,3			
1	1	18	23	56,0	22,0	23,0	44,5	45,6	22,4			
1	1	18	24	59,0	22,0	21,0	44,5	47,6	45,0	4,82	-0,92	-0,29
1	1	19	1	61,0	22,0	19,0	44,5	48,4	45,0			
1	1	19	2	63,0	22,0	18,0	44,5	49,5	45,0			
1	1	19	3	52,0	22,0	20,0	44,5	42,4	45,0	4,00	-0,62	-0,65
1	1	19	4	56,0	22,0	18,0	44,5	44,9	45,0			
1	1	19	5	45,0	22,0	18,0	44,5	44,6	45,0			
1	1	19	6	45,0	22,0	18,0	44,5	44,6	45,0	3,35	-0,45	-0,89
1	1	19	7	41,0	22,0	17,0	44,5	36,9	45,0			
1	1	19	8	37,0	22,0	17,0	44,5	31,0	45,0			
1	1	19	9	36,0	22,0	17,0	44,5	36,0	22,0	2,95	-0,45	-0,69
1	1	19	10	44,0	22,0	17,0	44,5	44,0	22,0			
1	1	19	11	44,0	22,0	17,0	44,5	44,0	22,0			
1	1	19	12	44,0	22,0	17,0	44,5	44,0	22,0	2,78	-0,50	-0,20
1	1	19	13	37,0	22,0	17,0	44,5	37,0	22,0			
1	1	19	14	37,0	22,0	17,0	44,5	37,0	22,0			
1	1	19	15	37,0	22,0	17,0	44,5	37,0	22,0	2,60	-0,50	-0,12
1	1	19	16	36,0	22,0	17,0	44,5	36,0	22,0			
1	1	19	17	33,0	22,0	17,0	44,5	33,0	22,0			
1	1	19	18	36,0	22,0	17,0	44,5	36,0	22,0	2,39	-0,48	-0,11
1	1	19	19	42,0	22,0	17,0	44,5	42,0	22,0			
1	1	19	20	27,0	22,0	17,0	44,5	27,0	22,0			
1	1	19	21	36,0	22,0	17,0	44,5	36,0	22,0	1,96	-0,39	-0,11
1	1	19	22	36,0	22,0	17,0	44,5	36,0	22,0			
1	1	19	23	33,0	22,0	17,0	44,5	33,0	22,0			
1	1	19	24	29,0	22,0	17,0	44,5	29,0	22,0	1,55	-0,35	0,15

* for explanations of headings see accompanying text

water levels. Disregarding the one wind measurement at Clarens, simulations can thus be performed assuming that the Geneva- or a combination of the Geneva- and Lausanne winds blow over the entire lake. Under the given circumstances, calibration of the model must be considered to be good if the water levels observed and simulated at Geneva agree well. While the agreement of water levels observed and simulated at Morges and Chillon is only of secondary importance, it will be seen that even there, the simulation results are quite good.

For the purpose of simulation the information contained in Figure 36 was abstracted and tabulated in Table 5, in which the first four columns headed by Y, M, D and H contain the date of observation in years, months, days and hours respectively. The next two pairs of columns headed by WG and DG and by WL and DL contain the wind velocities in km/h and the wind direction in degrees for Geneva and Lausanne respectively. The contents of the columns headed by W and D will be explained later. The last three columns headed by GE, MO and CH present (in cm) the six-hourly mean vertical displacements from the whole-lake mean of the water levels observed at Geneva, Morges and Chillon respectively.

Since the primary interest is centered around the Geneva water levels, simulation was started with the assumption that the winds observed in Geneva have been blowing over the entire lake. Using the same principles as outlined in § 3.2.1 and already used in Figures 15 and 16, the results of this simulation using wind shear coefficients $c_w = 0,0035$, $c_w = 0,003$ and $c_w = 0,0025$ are shown in Figure 45. For each simulation 5 horizontal bands are used for plotting. The vertical scales are indicated at the beginning and towards the end of each band. In case data to be plotted exceed the width of one band, their trace is continued over the neighbouring bands without change of their original scale. The time is indicated every 6 hours in years, months, days, hours and minutes. On the first two bands the components

in the x and y directions of the winds used for simulation are plotted in km/h respectively; see Figure 3 for the conventions used. The simulated water levels for Geneva, Morges and Chillon are plotted in m on the next three bands respectively. As can be seen, points 52, 22 and 1, as indicated in Figure 40, are assumed to represent the above three locations. To allow comparison of simulation results with the observed water levels listed in Table 5, the observed water levels have also been drawn as thicker lines on the three water level bands. For easier distinction between the various traces it is useful to note that, as can be seen in Table 5, wind data are available every hour and water level data only every three hours and that furthermore the three-hourly water levels are not point-measurements but six-hourly means. The observed water level changes are therefore very smooth when compared with the water levels simulated every 30 seconds. The wind input required every 30 seconds was obtained by linear interpolation. Finally, in Figure 45 it can also be seen that the lines of observed water levels are drawn thicker than those of the simulated water levels.

Considering now in detail the simulation results, the following can be observed in Figure 45:

- (a) Simulated water levels are much more variable than observed water levels. Since the observed water levels are six-hourly means only, this is to be expected.
- (b) The simulation with $c_w = 0,0035$ yields water levels that are generally too high at Geneva and too low at Chillon. With the exception of the time period 18/1/1950 12:00 h - 19/1/1950 6:00 h the water levels at Morges are very well simulated.
- (c) Decreasing the wind shear stress coefficient to $c_w = 0,003$ and to $c_w = 0,0025$, the simulation of the water levels at Geneva is improved (see in particular the time periods

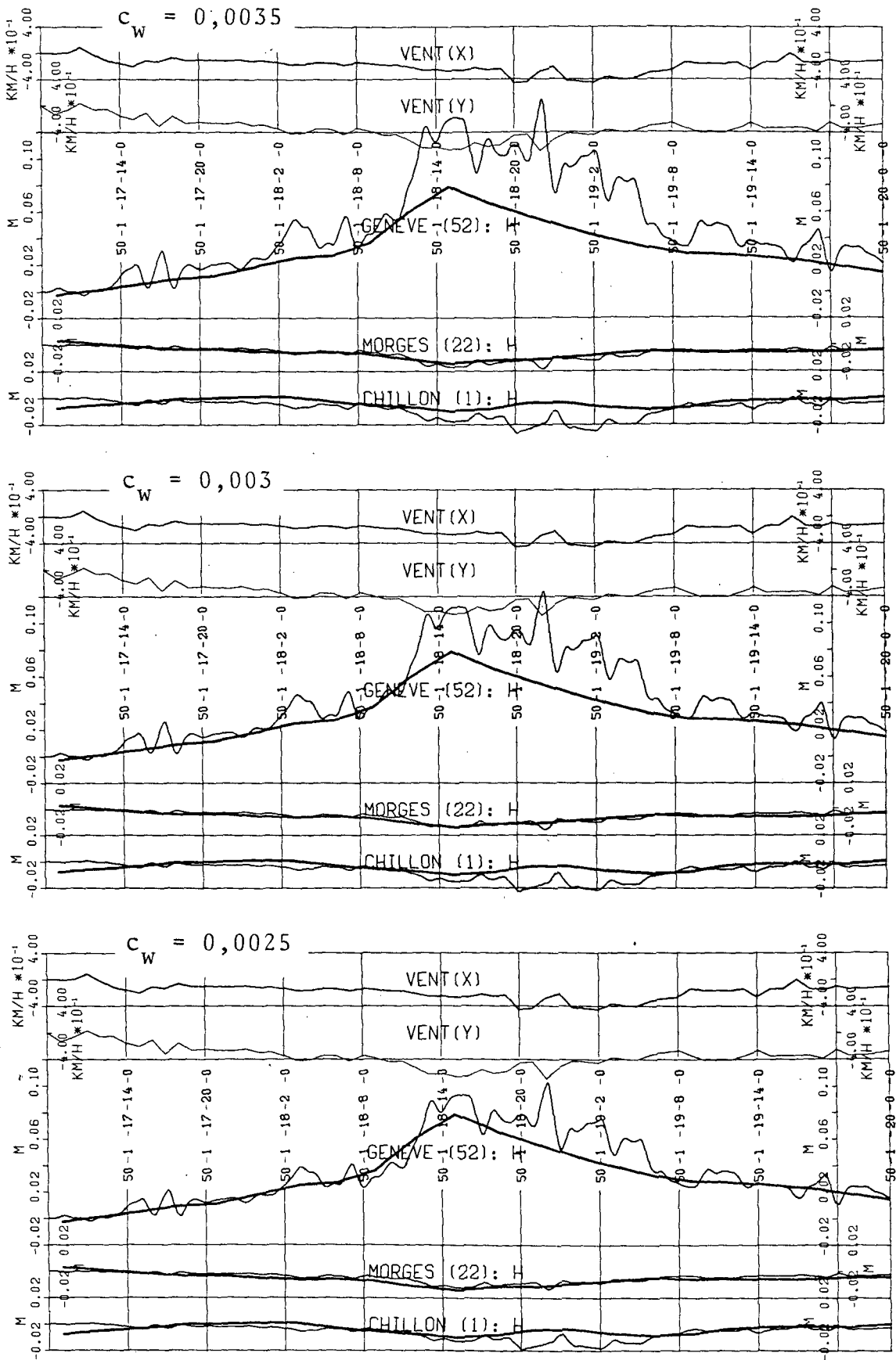


Figure 45: Simulation for the Léman using winds observed at Geneva with wind shear stress coefficients $c_w = 0,0035$, $c_w = 0,003$ and $c_w = 0,0025$

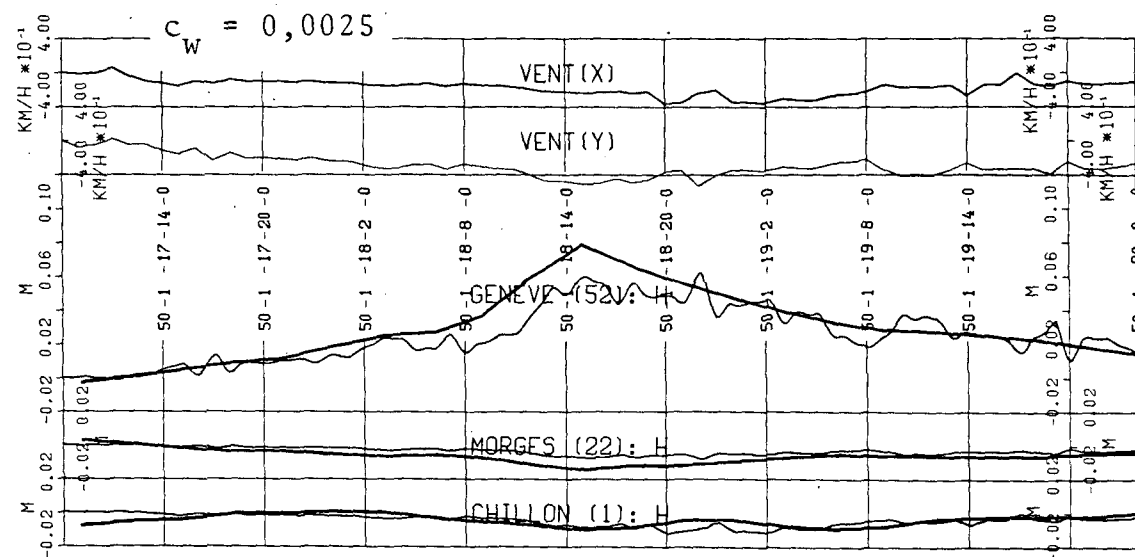
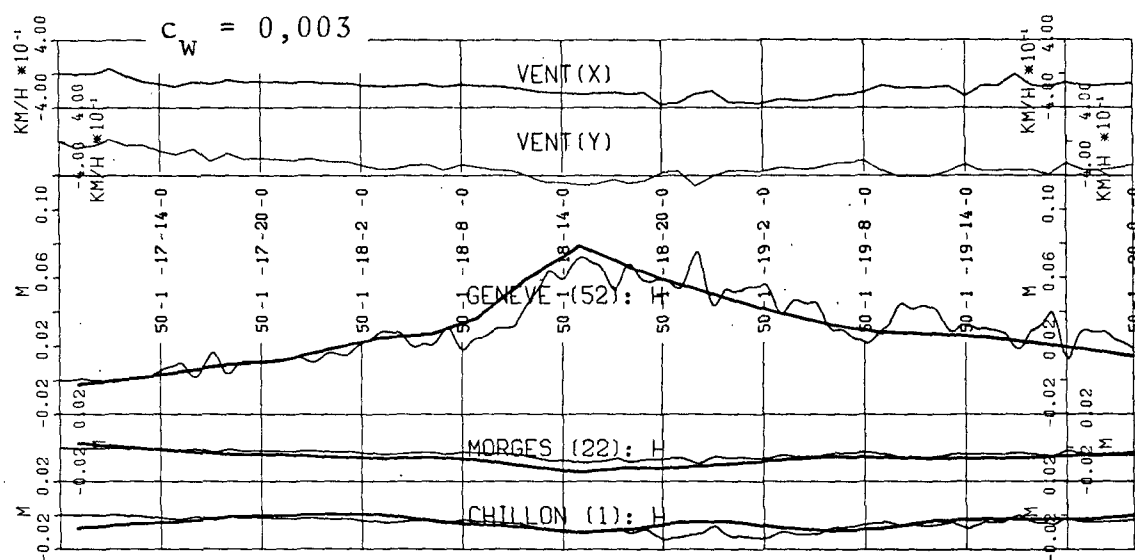
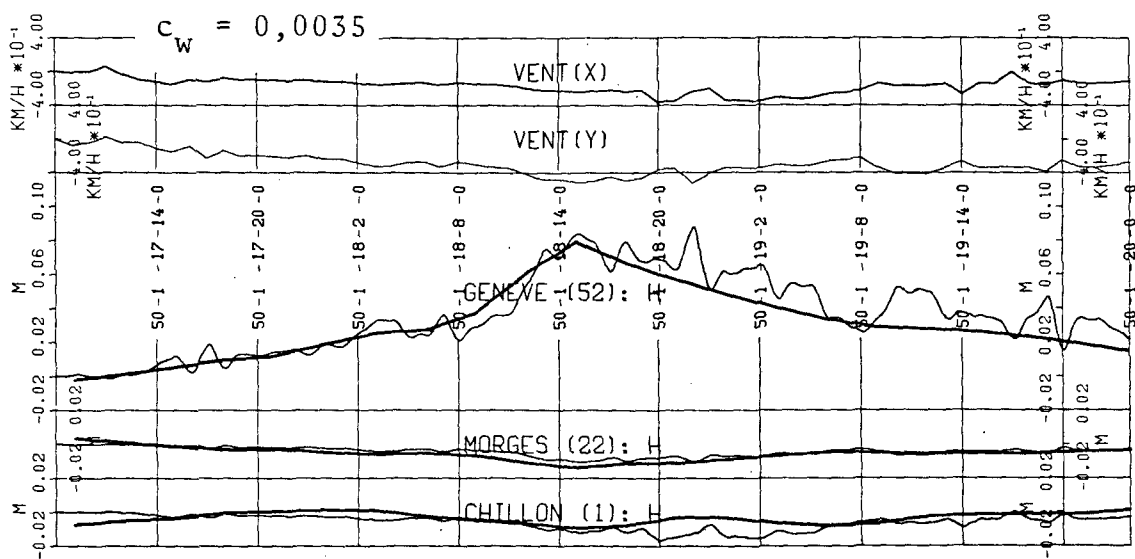


Figure 46: Simulation for the Léman using composite wind (70 % Geneva, 30 % Lausanne) with wind shear stress coefficients $c_w = 0,0035$, $c_w = 0,003$ and $c_w = 0,0025$

17/1/1950 8:00 h - 18/1/1950 12:00 h and 19/1/1950 8:00 h - 20/1/1950 0:00 h with $c_w = 0,0025$). The simulation for Morges is excellent with $c_w = 0,003$. The results for Chillon are best for $c_w = 0,0025$ or possibly even lower.

- (d) The period 18/1/1950 12:00 h - 19/1/1950 8:00 h, containing the strongest winds within the simulation period, seems to be subject to a different regime than the rest of the entire simulation period. With the exception of this period, agreement between simulated and observed water levels is excellent with $c_w = 0,0025$, a value that corresponds well to findings of Wu (1969) for wind velocities higher than 50 km/h. To achieve agreement of the water levels for the period 18/1/1950 12:00 h - 19/1/1950 8:00 h, however, a wind shear stress coefficient still smaller would have to be selected. This in turn would result in disagreement of simulated and observed water levels for the rest of the simulation.

From the above considerations it follows that if one accepts the Geneva wind to be representative for the entire water surface of the Léman, good agreement between simulation and observation can only be obtained if the wind shear stress coefficient decreases with wind velocity. From an analysis of wind measurements on the Léman (Graf and Prost, 1979) it can be seen that the wind shear stress coefficient, in this range of wind velocities, is about 0,0015 and that if there is a tendency for variation of this coefficient, then it is one of increase up to the above value. The reason for the disagreement seems therefore to be due to the fact that the wind observed at Geneva cannot be accepted as being representative for the entire lake. Having only two sets of wind observations, i.e., from Geneva and Lausanne available, it was tried to determine a representative wind vector series using the two data sets from Geneva and Lausanne.

Keeping in mind the preeminence of the Geneva water level fluctuations, a mean overall wind was calculated by a weighted vector mean whereby 70 % of the weight was assigned to the Geneva winds

and 30 % to the Lausanne winds. In case no record was available at Lausanne the winds observed at Geneva were assumed to be representative. The velocities in km/h and the directions in degrees of this "representative" wind are listed in Table 5 in the columns headed by W and D respectively. The results of the simulation with the composite wind as input using again wind shear stress coefficients of $c_w = 0,0035$, $c_w = 0,003$ and $c_w = 0,0025$ are shown in Figure 46. Comparing Figures 45 and 46, one finds that using a composite wind as input results in an elimination of the particularly high response of water levels for the period 18/1/1950 12:00 h - 19/1/1950 8:00 h. Considering the water levels at Geneva and Chillon, it can be seen in Figure 46 that simulation with $c_w = 0,003$ yields the best agreement between simulation and observation. This value is about two times the experimental value determined by Graf and Prost (1979), a fact that corresponds well to statements by Donelan (1977). Even though agreement is not perfect, it is certainly better than anything that can be achieved using Geneva winds only. Thus, longitudinal wind set-up can be well simulated. Surprising however, is the fact that the simulated transverse wind set-up, which manifests itself by the water levels at Morges, is in better agreement with observations if Geneva winds alone are used (see Figure 45), but amplitudes there are small.

To allow a more global description of the movements of the Léman as simulated for the Bise on 17-19/1/1950, a synoptic view of the simulation results has also been produced. In Figure 47, the step numbers at which a synoptic view has been drawn are indicated. Figure 48 shows the synoptic views following the same principles as used in Figure 17. Comparing Figures 42, 44 and 48, one finds that the "boxes" of Figures 42 and 44 correspond to those in Figure 48 and serve as an indication of the position of the lake body in space only. The water surface of the Léman is situated in the lid of the box of Figure 42. To avoid visual confusion between water surface and velocity

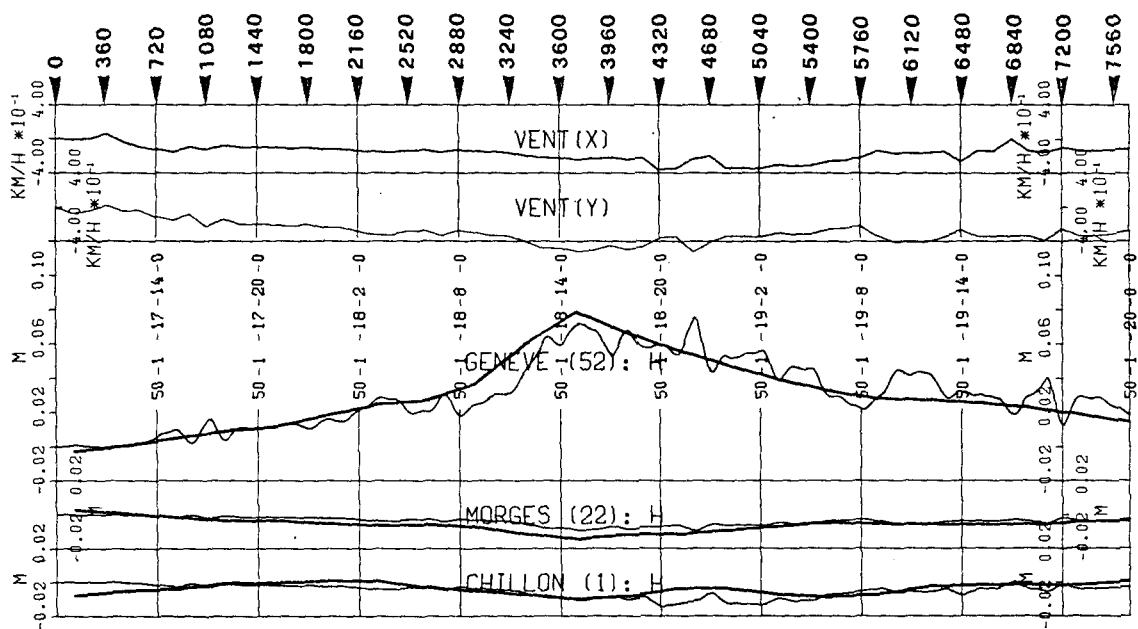


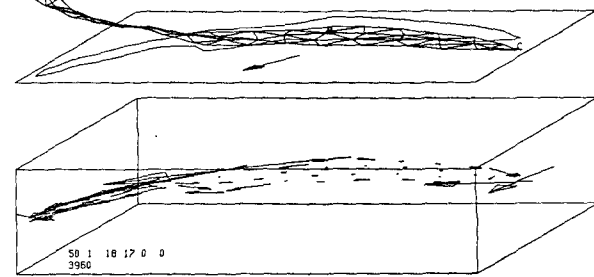
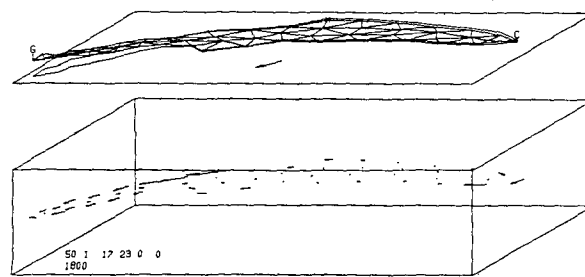
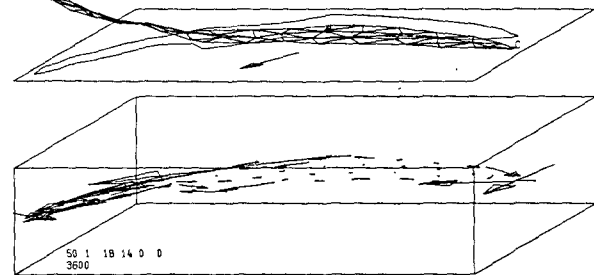
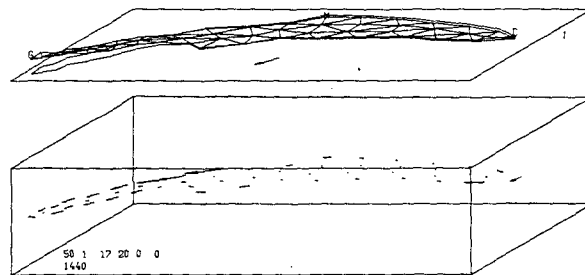
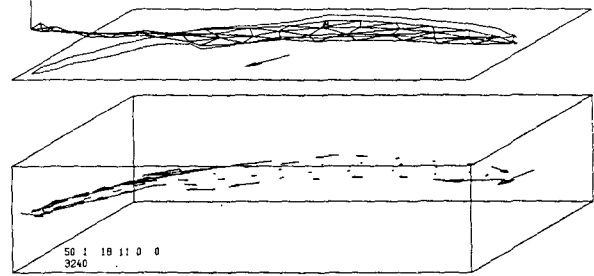
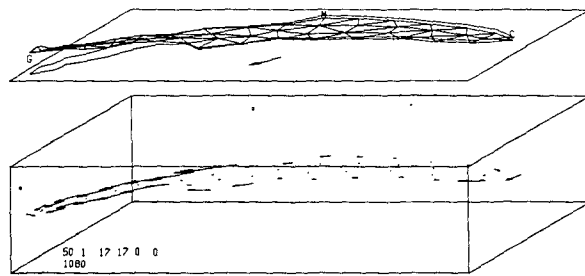
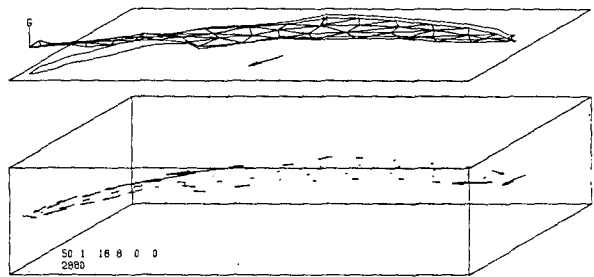
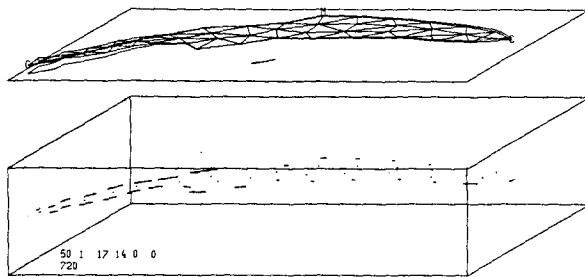
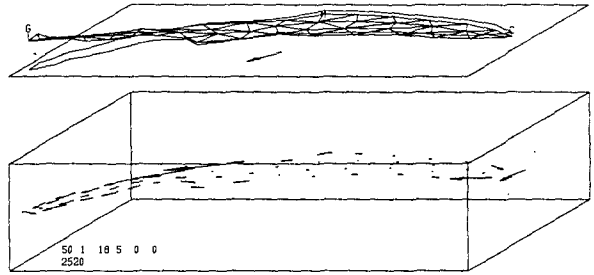
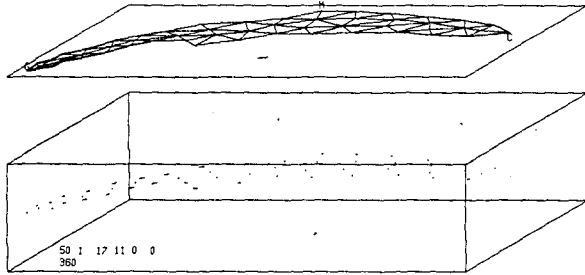
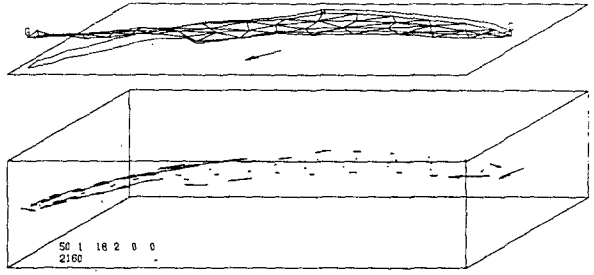
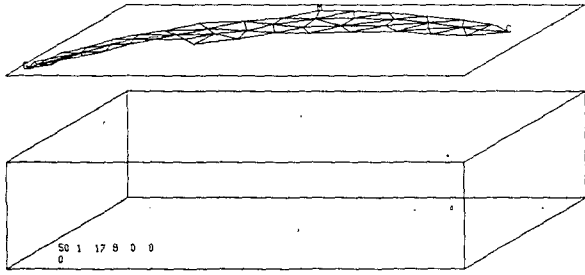
Figure 47: Simulation for the Léman using composite wind with shear stress coefficient $c_w = 0,003$, showing step numbers at which synoptic view has been produced

vectors, the lid of the box containing the Léman has again been moved upwards as can be seen in Figures 44 and 48. The vertical scale shown in the lid of Figure 44 is for the displacement of the water level, the horizontal scales placed within the ellipses are; in the lid for the wind velocity vector, and in the box for the water velocity vectors. The ellipses allow evaluation of velocity vectors not parallel to the velocity scales. It should be noted that the scales of Figure 44 have to be reduced when applied to Figure 48 using the same degree of reduction as that of the boxes.

In Figure 48 the date in years, months, days, hours, minutes and seconds is indicated in the lower left corner of each image together with its step number corresponding to those indicated in Figure 47. Also shown in Figure 48 are the observed water levels, indicated by the lower edges of the letters G, M and C standing for Geneva, Morges and Chillon respectively. In the first image of Figure 48 with the date 50 1 17 8 0 0 and step

number 0, it can be seen that the water surface of the lake has been assumed to be horizontal. No velocity vectors are visible within the box indicating that at the onset of simulation no currents were assumed to exist. In the next image with step number 360 the lake surface is still horizontal, the observed water levels M and C however have moved from their original positions. Point M is higher, point C is lower than the calculated lake level. This can also be confirmed in Figure 47.

Appearing in the lid, outside of the lake surface, is a small vector indicating the wind velocity and direction at this instant. Within the box, small vectors can be seen which are markedly larger in the "Petit Lac" (western shallower region of the Léman). In the next image with step number 720 the water surface of the Léman is no longer horizontal; now also point G has left its original position, the wind vector has grown larger, the current vectors have increased in size indicating a clear movement of water towards Geneva. In the following images the trend so far established continues. In image 1440 one notes that a return current has established itself in the center points of the Petit Lac. It should be noted here that the vectors are indicating mean velocities, i.e., vertically integrated velocities and then divided by the depth of integration. Comparing for example images 2520 and 2880 having about the same water level at Geneva (i.e., the same volume in the Petit Lac), one might be misled to believe that the strong westward lateral current cannot be balanced by the relatively weak return current in the center of the Petit Lac. As however can be seen in Figure 42, this conclusion is wrong since the depth in the center of the Petit Lac, as it is numerically represented, is about four times that of the lake boundaries. Investigating the water level at Geneva in Figure 47 for this time period, it can be seen that the situation is even more complicated by the fact that between steps 2520 and 2880 the water level did not remain constant as one might have assumed when considering the "snapshots" 2520 and 2880 in Figure 48. In images 2520-3960 it can



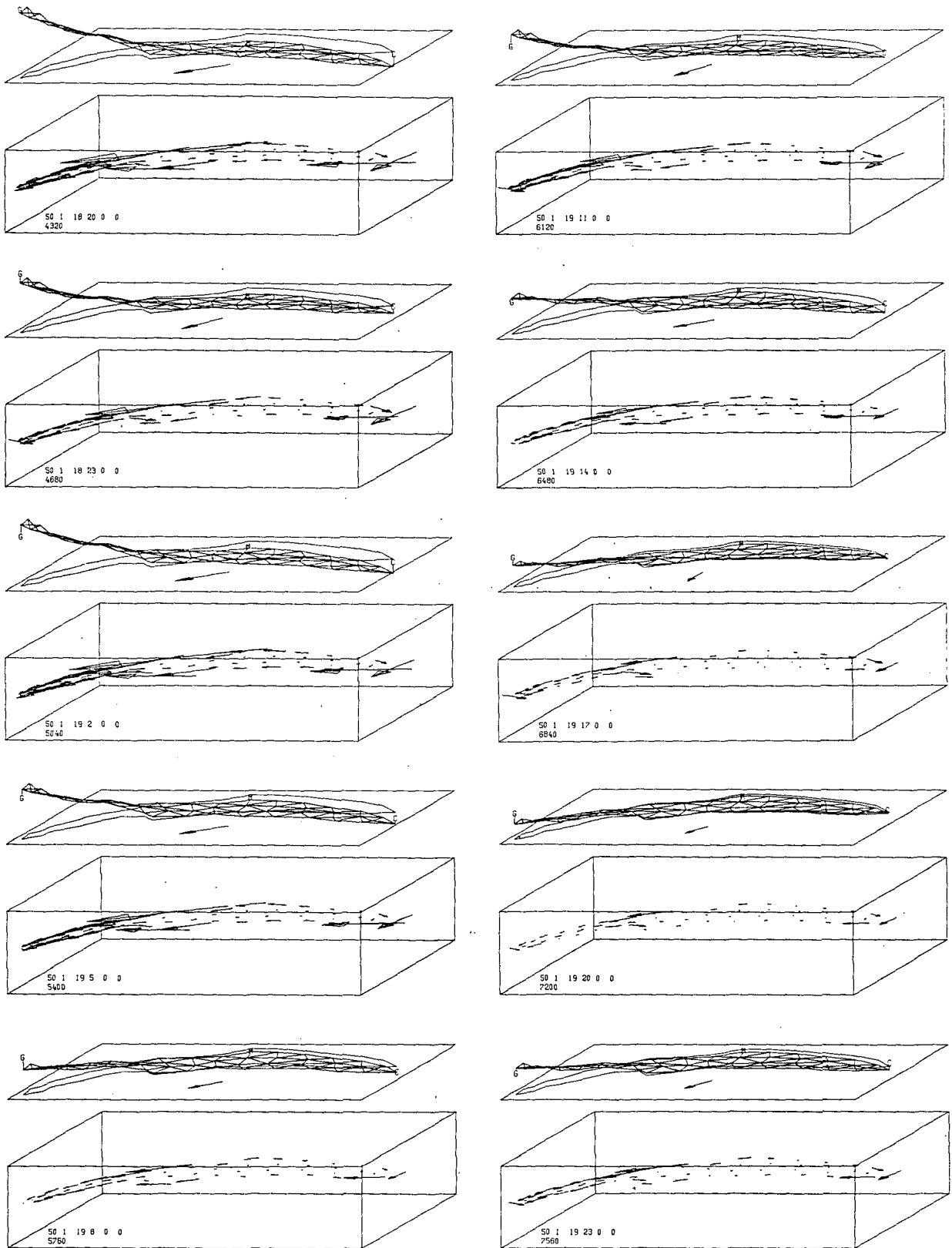


Figure 48: Simulation of wind induced water level fluctuations (storm surges) and currents in the Léman caused by the Bise on 17-19/1/1950. (It should be noted that a computer-drawn film has also been produced for the same period)

also be seen that there is quite some discrepancy between the simulated and the observed water levels at Geneva and, in an accordingly smaller proportion, at Morges. Currents are ever increasing and reach their maximum around images 3600-4320. It can also be seen that the maximum currents coincide with the maximum wind set-up.

As has already been observed in the test lake, the northern lake boundaries show a stronger tendency for the westbound currents than the southern ones. Comparing images 3600-5400 of Figure 48 with the longitudinal profiles of wind set-ups observed by the Service fédéral des eaux (1954) during various cases of Bise and shown in Figure 38, one finds that there is excellent agreement of the general tendencies, qualitatively as well as quantitatively. As in the observed wind set-ups (see in particular the Bises on 28 October 1949 and on 30 July 1950 of Figure 38) the intersection of the simulated water surface with the mean lake water surface is situated near the midline of the Léman between Geneva and Chillon (line St-Prex - Thonon). The shapes of the longitudinal profile of the simulated wind set-ups are the same as those shown in Figure 38. The ratios between the surelevations at Geneva and the depressions at Chillon, as have been observed by the Service fédéral des eaux (1954) and shown in Figure 38, are very close to those obtained by simulation. In image 5760 it can be seen that the wind has decreased in force, resulting in a first decrease of the wind set-up. In spite of this decrease, the velocity vectors at the lake boundaries of the Petit Lac are still pointing westwards. The return current in the center line of the Petit Lac however has become stronger in relation to the current on the boundaries.

Concluding, it can be noted that, considering the lack of detailed information on winds blowing over the Léman, excellent agreement between observed and simulated water levels on the Léman for the Bise 17-19/1/1950 has been obtained. The wind shear stress coefficient used was $c_w = 0,003$, which falls well

within the range of wind shear stress coefficients quoted in the literature. One may postulate that the disagreements between observation and simulation are mainly due to the assumptions made with respect to a "representative wind" and in a secondary degree due to the smoothing of the observed water levels. Finally, it should be noted that agreement between observed and simulated water levels does not necessarily imply that the calculated currents, shown in Figure 48, agree with real currents in the lake (Sündermann, 1979). Since however no current observations for this period are available, no further calibration attempts are possible.

5.3 Determination of period and node of the principal Léman seiche

The principal, i.e., uninodal longitudinal seiche is simulated using the coarse Léman grid shown in Figures 40-42 and the parameters listed in Figure 44. Similar to Figures 15-17, a constant wind of 50 km/h with a direction of 60 degrees lasting for 8 hours 31 minutes is applied to the Léman until equilibrium between all forces has been established and accelerations no longer exist anywhere in the lake. Then the wind is suddenly stopped, allowing the lake to return to its starting position, i.e., horizontal water surface and no currents.

5.3.1 Determination of period

Using the method applied in Figure 15, the simulation results for the Léman are presented in Figure 49. In Figure 49 the first two bands show the components of the wind velocity in the x and y directions respectively. The next three bands contain the water level surface elevations of the points 52, 22 and 1 corresponding to Geneva, Morges and Chillon respectively. As can be seen in Figure 49, the easterly wind results in a rise in the water level at Geneva and in a fall of the water levels at Morges and Chillon, whereby the amounts of water level displacements

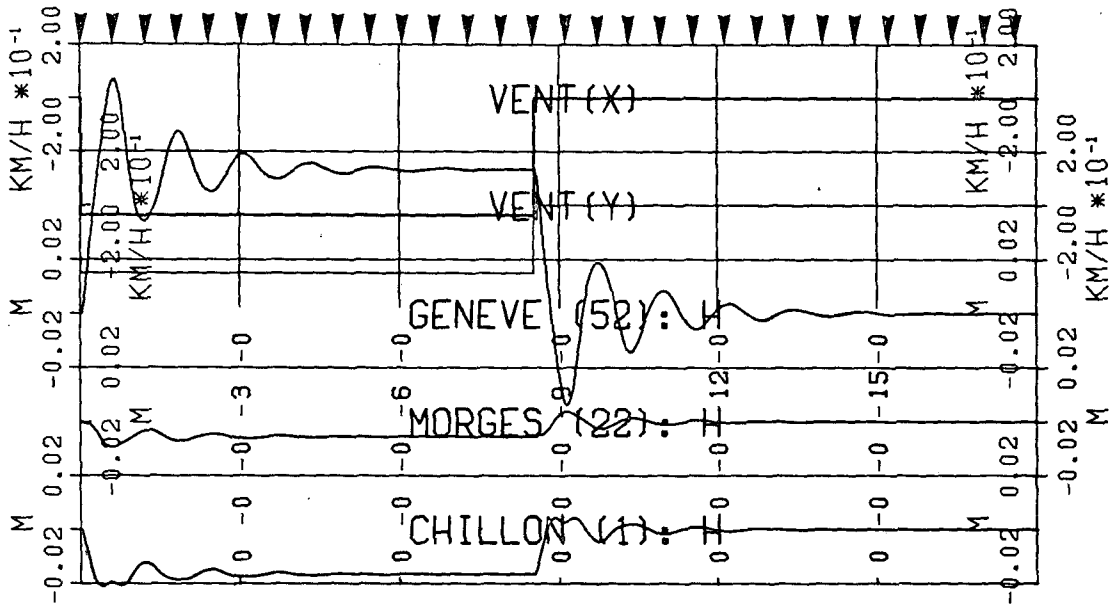


Figure 49: Simulation for the Léman using grid and parameters as shown in Figures 40-42 and Figure 44

reflect well the geometry of the Léman. From Figure 49 the period can be estimated to be 74 minutes. Assuming the exact, i.e., observed seiche period to be between 73,5 minutes (see Table 1) and 74,0 minutes (see Figure 26 and accompanying text), the agreement between simulation and observation must be considered to be excellent, keeping in mind that the Léman was represented by only 52 points. For comparison it might be interesting to note that Hamblin and Hollan (1978), using a finite element model with some 200 points for Lake Constance (a lake with dimensions similar to those of the Léman), obtained a period of 55,5 minutes of the principal longitudinal seiche, resulting in a difference of 2,10 minutes between their simulations and the observations.

Comparing Figure 49 however with, say, Figure 26, one finds that damping of the seiche motion does not at all correspond to reality. As will be shown later, this damping is due to the smoothing procedure introduced by the α -mean, which in turn is associated with the choice of grid.

5.3.2 Determination of the position of the node

Following the scheme identical to that of Figure 48, images of the Léman are shown in Figure 50 for the same interval covered by Figure 49. The arrows on top of Figure 49 indicate the position in time of each image of Figure 50. The scales and parameters are again indicated in Figure 44. In contrast to Figure 48 which showed the simulation for a Bise, i.e., an observed wind, the wind input for Figure 50 is purely hypothetical. During the time when the constant wind blows, it can be seen in Figure 50 that there exist uninodal longitudinal seiches (storm surges). As can be observed however from images 73-1022, i.e., during the wind-forces phase, the hinge-line of these oscillations does not correspond to the nodal point of the free seiches as shown in Figures 27 and 29, but rather to the "region of intersection" between the undisturbed water surface and that during wind set-up as indicated in Figure 38 (see cases of Bise). The last picture showing the wind set-up is image 1022. The wind stops blowing immediately afterwards. In image 1095, i.e., the snap-shot following image 1022, it can be seen that the node of the uninodal longitudinal seiche, now no longer under the influence of wind, has moved westwards and now coincides well with the positions indicated in Figures 27 and 29. The following images show the "dying away" of the seiche motion. The wind- and seiche-induced currents behave similarly to those already shown in Figure 17. In Figure 51 the region defined by the eastern and western extreme positions of the points of intersection of the water surface of images 1095-1533 with the undisturbed surface on the lake boundaries has been indicated. The position of the simulated uninodal node lies well within this region. From Figure 50, exact determination of this position is not readily possible. To allow comparison of the simulation results with earlier work, the node positions according to Forel (1895) and to Doodson et al. (1920) are shown as well. As one can see in Figure 51, agreement between the present results and those of Forel and Doodson et al. is quite good.

forced oscillations

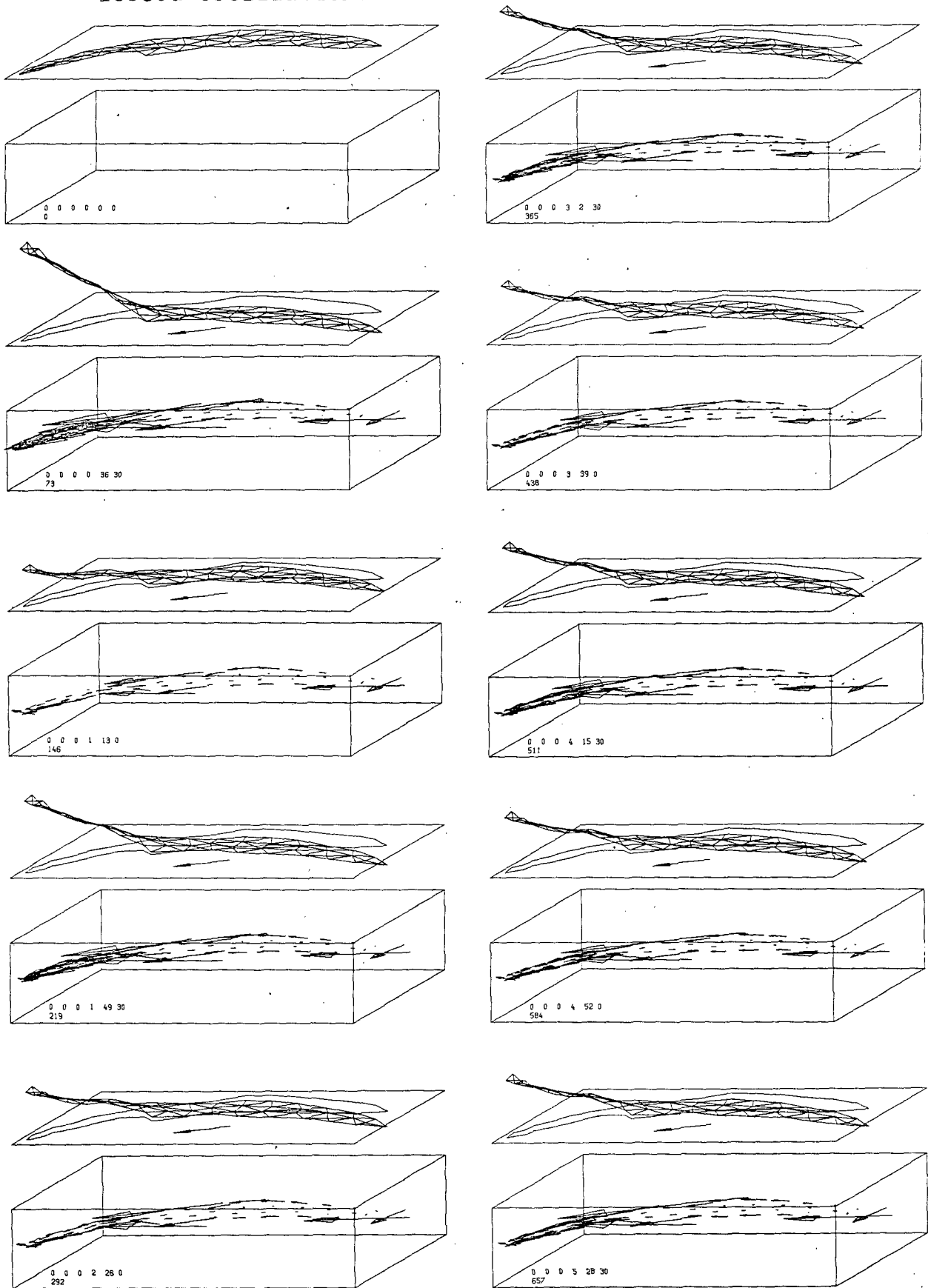


Figure 50: title; see end of images

free oscillations

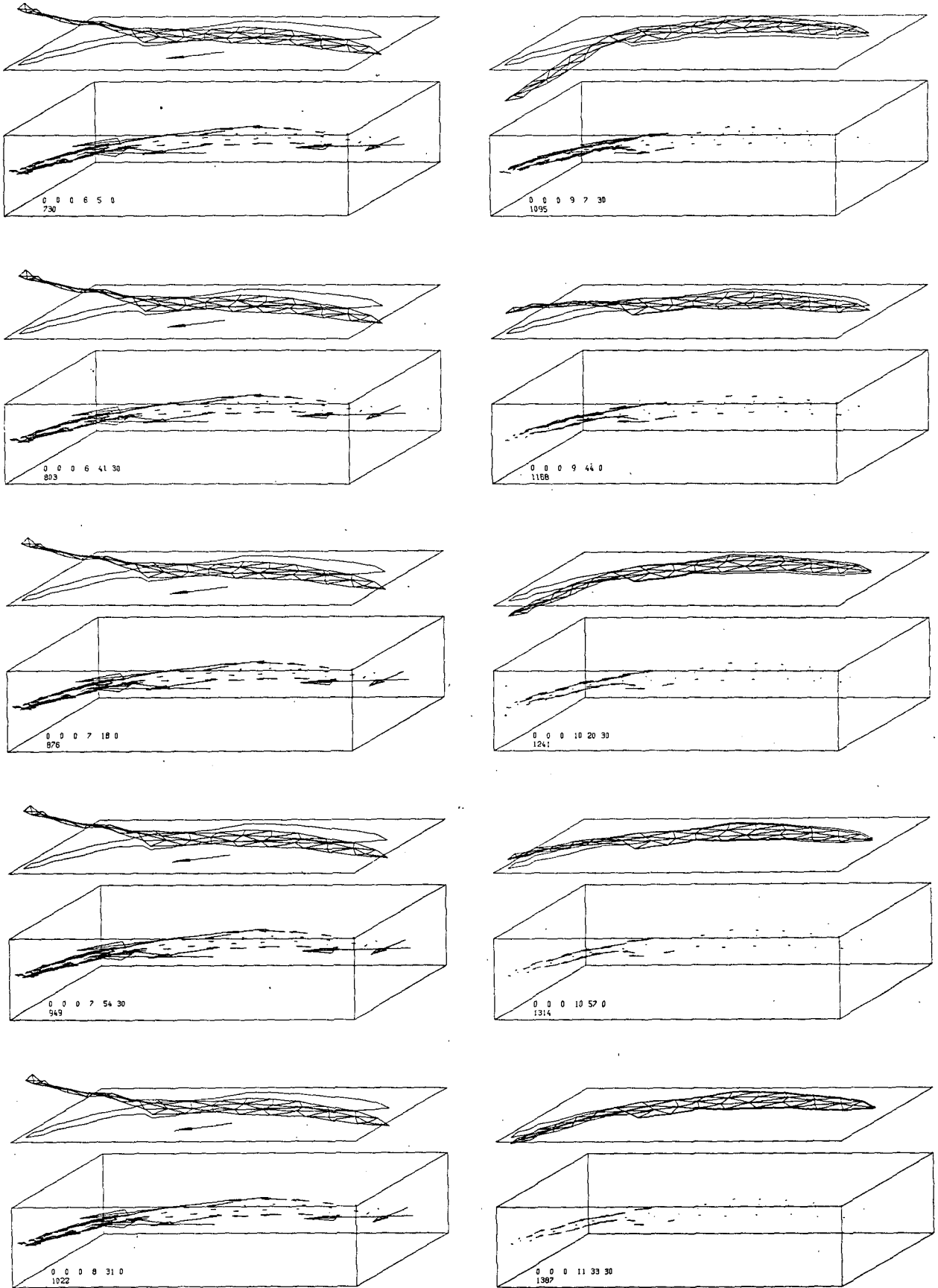


Figure 50: continued

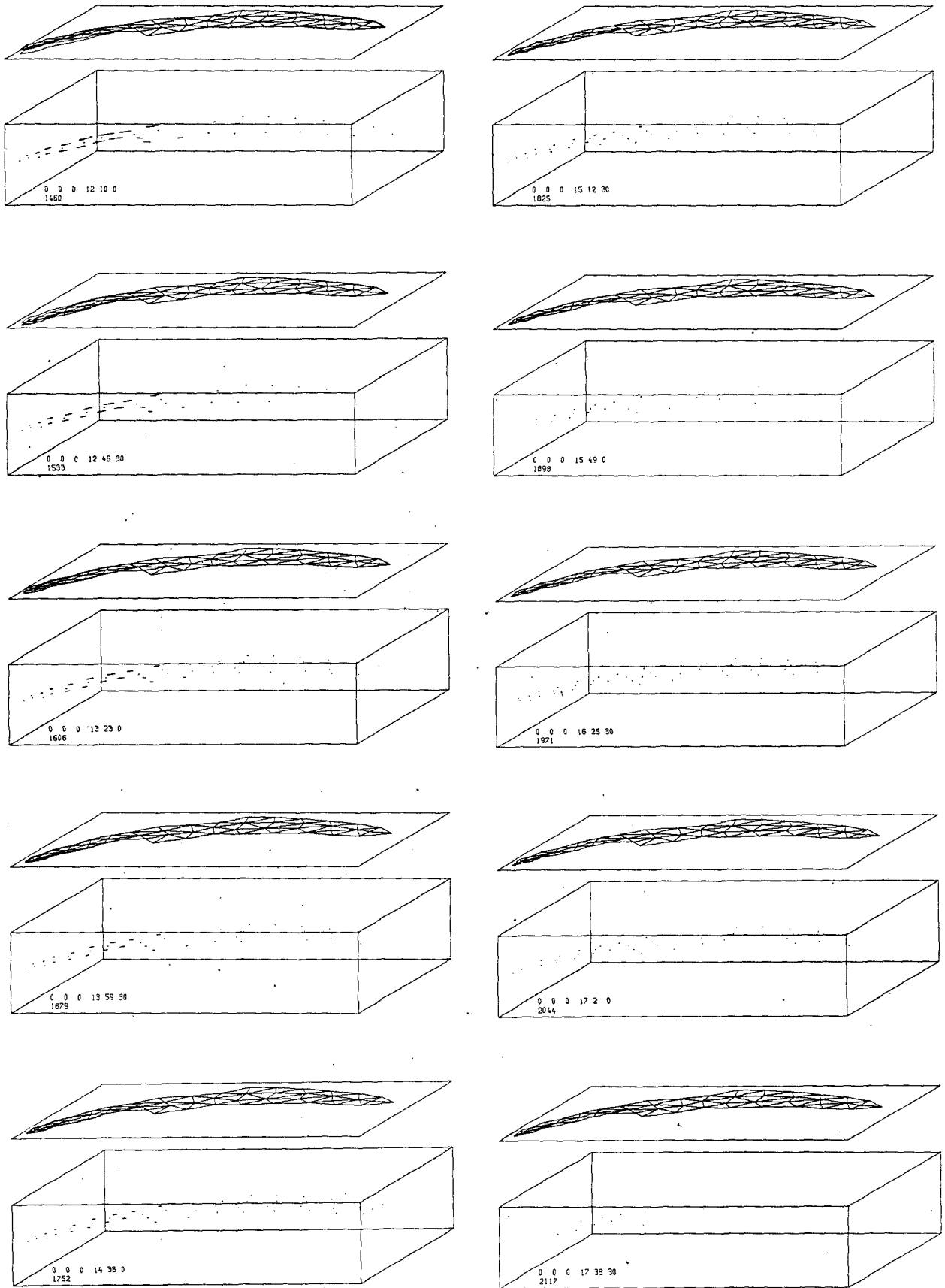


Figure 50: Simulation of wind induced water level fluctuations and currents in the Léman

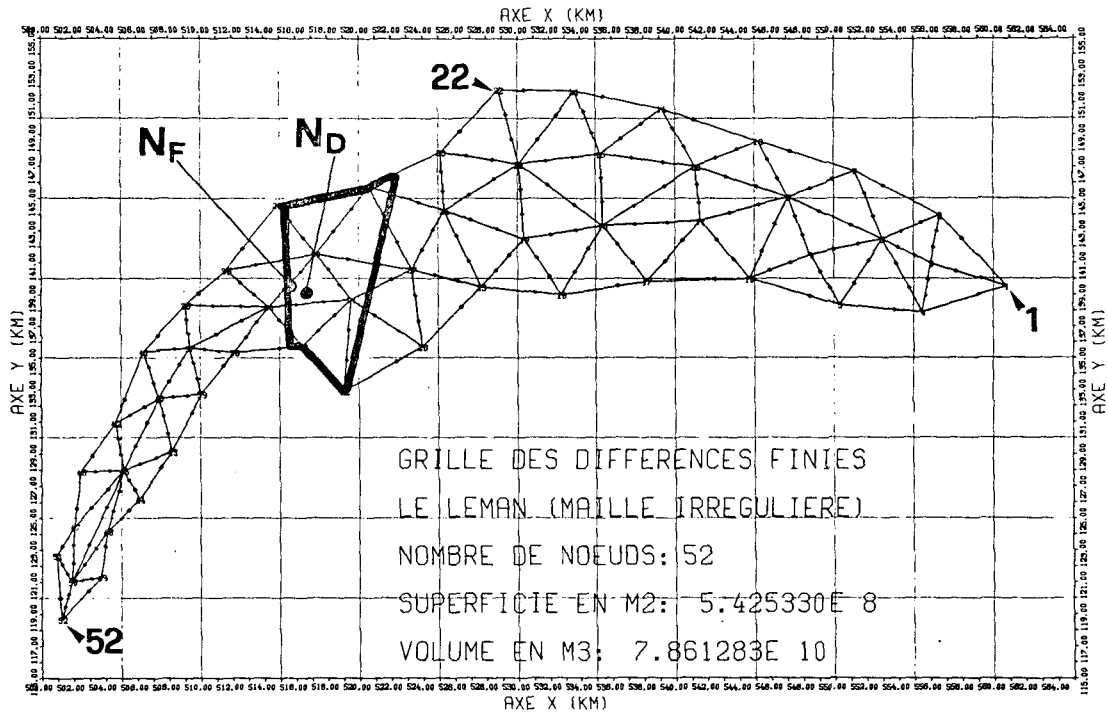


Figure 51: Range of simulated uninodal seiche nodes in the Léman with nodes N_F determined by Forel and N_D determined by Doodson et al.

5.4 Examination of stability of the coarse-grid model of the Léman

In Figures 49 and 50 it can be seen that at the onset of simulation the Léman water level was horizontal and that there were no currents in the lake. Applying wind shear stress, a state of equilibrium between all forces was attained. This equilibrium was disturbed when the wind stopped blowing and, consequently, the lake approached asymptotically a new equilibrium. This equilibrium was (almost) attained at the end of simulation, when the lake had returned to its original state. It should be noted that the time step used in the simulations shown in Figures 49 and 50 was 30 seconds, the smoothing was performed with $\alpha = 0,90$ (see Figure 44) and the grid was that shown in Figures 40-42. Varying only α and keeping all other parameters constant, the consequences of the α -mean on an irregular grid

were investigated by applying a 75 km/h easterly wind for one hour and then simulating the return of the lake to its undisturbed state.

In Figure 52 this simulation is shown for $\alpha = 0,95$. Comparing Figures 52 and 49, one finds that there is no principal dif-

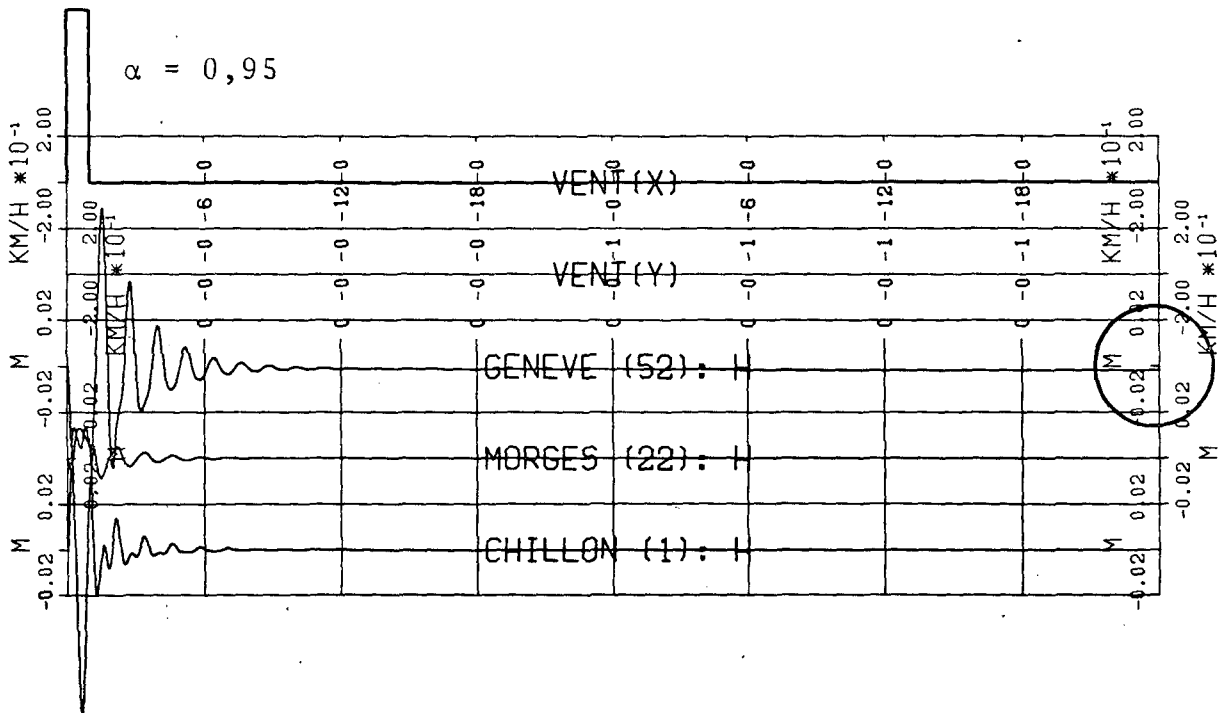


Figure 52: Simulation for coarse Léman grid with $\alpha = 0,95$, showing water levels in three points

ference in appearance and one might therefore conclude that runs with $\alpha = 0,95$ are also stable. Examining however Figure 52 more carefully, one finds that the water level at Geneva, point 52, no longer returns exactly to zero but remains slightly below zero (see encircled region). A first conclusion could be that the lake has lost water. This however is impossible since trial runs of the model with $\alpha = 1$, i.e., without volume correction, showed that continuity is numerically well preserved. From early test runs of the model it was found that instabilities are not

always obvious and that they may be noticed first either at the water levels or at the velocities. For this reason, runs were performed showing also the velocities. Outputs of these runs with $\alpha = 0,90$, $\alpha = 0,95$, $\alpha = 0,96$ and $\alpha = 0,99$ are shown in Figures 53 and 54. In Figure 53 it can be seen that apparently $\alpha = 0,90$ really stabilizes the system since all water levels and velocities return well to zero. In the output for the execution with $\alpha = 0,95$ it should be noted first that the scales of the velocity bands have been changed in order to keep the traces of the velocities within the figure. It can be seen that the water levels are identical to those of Figure 52 and very similar to those obtained with $\alpha = 0,90$. The velocities however behave differently. In particular, considering the velocity components of point 52, one finds that they no longer return to zero but that they stabilize at values around 0,275 m/s and - 0,12 m/s in the x and y directions respectively. All other velocities however seem to return to zero. It is evident that the non-zero water level at point 52 is associated with this phenomenon. In the output for the run with $\alpha = 0,96$ shown in Figure 54 the velocity scales have again been changed. It can be seen that the tendency (first noted with $\alpha = 0,95$) is now roughly ten times greater than with $\alpha = 0,95$. In all three runs so far however, the seiche period remained unchanged. In the output for $\alpha = 0,99$, also shown in Figure 54, the scales have again been changed; this time for both the water levels and the velocities. Apart from the enormous changes in amplitude (not immediately obvious due to the changes of scales), the most important new phenomenon seems to be a change in seiche period. As will be seen in the next paragraph, it seems that this is not a real change of period but rather the phenomenon of "beating" between oscillations of frequencies close to each other. The phenomenon of "beating" will be demonstrated in Figure 71. Comparing the last two runs, one finds that the maximum amplitude of the run with $\alpha = 0,99$ occurs each three standard seiche periods as produced by the run with $\alpha = 0,96$. On the trace of the water level for point 52, calculated

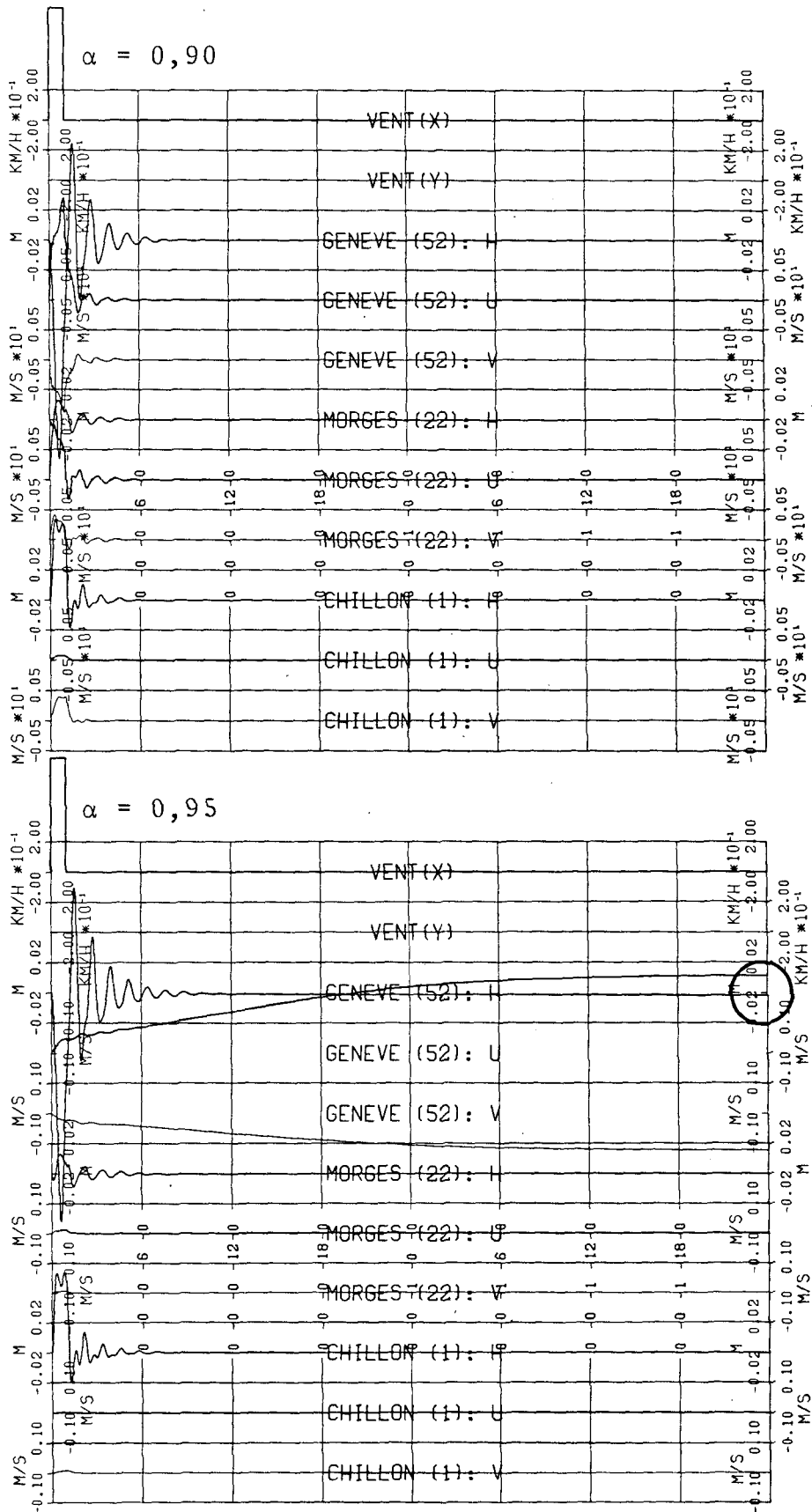


Figure 53: Simulation for coarse Léman grid with $\alpha = 0,90$ and $\alpha = 0,95$, showing water level fluctuations and currents in three points

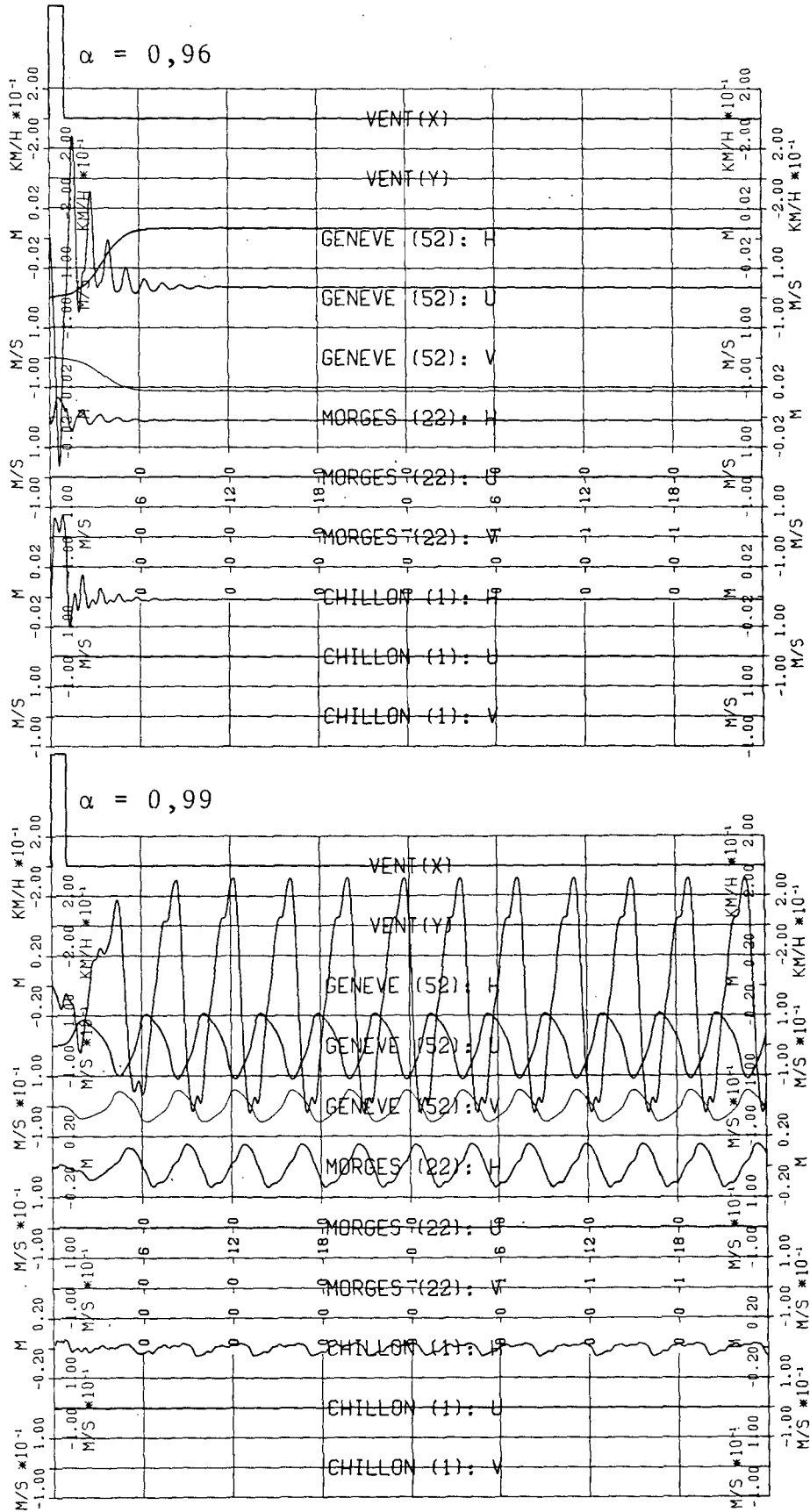


Figure 54: Simulation for coarse Léman grid with $\alpha = 0,96$ and $\alpha = 0,99$, showing water level fluctuations and currents in three points

with $\alpha = 0,99$, the influence of the standard seiche period can even be distinguished.

Concluding, it can be stated that for the Léman grid shown in Figures 40-42 the system is unstable for executions with $\alpha \geq 0,90$. The instability can be identified by the fact that after cessation of the disturbing influence, the system no longer returns to the initial undisturbed state. Nevertheless, with $\alpha = 0,90$, very useful results can already be obtained from this rough grid.

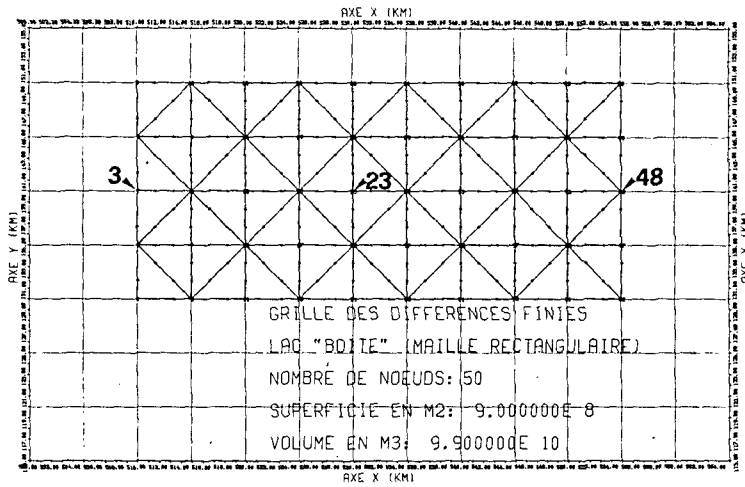
5.5 Investigation of the connection between grid configuration, numerical stability, and the damping of seiche motion

Comparing Figures 15, 16, 49, 52, 53 and 54 (representing simulation results of seiches by the present model) with Figures 20-26, i.e., with Forel's (1895) observations of seiches and with Figures 31-33, i.e., the seiche observations of the Service fédéral des eaux (1954), one finds that the major difference between simulated and observed seiches is to be found in their persistence. Compared with observed seiches, the simulated seiches display an extremely strong rate of damping. The reason for the strong damping of the simulated seiches appears to be the smoothing effect of the α -mean. On the other hand, as stated in §§ 3.2, 5.1 and 5.1.2 and investigated in § 5.4, smoothing is essential when using irregular finite difference grids, as in Figures 9-12 and 40-42, since otherwise the system is unstable. As already mentioned in § 2.3, it appears from statements by Thacker (1977a) that instabilities are associated with the irregularities of the grid being used. In order to simulate seiches without an excessive rate of damping it is therefore necessary to use a grid which does not display instabilities for $\alpha = 1$ or at least α very close to unity. To establish some criteria for a better choice of grid, four types of grid were investigated.

From the literature it can be seen that conventional, i.e.,

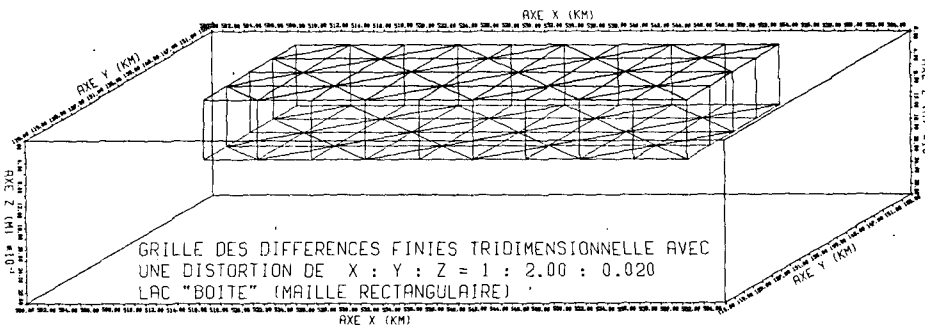
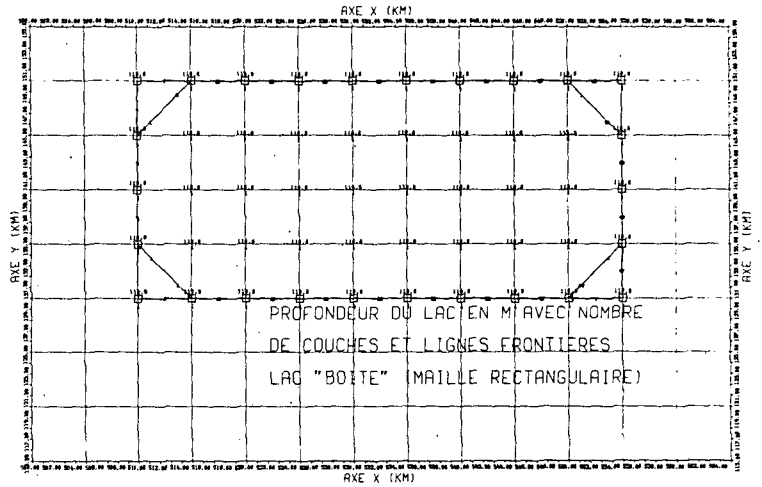
rectangular finite difference schemes do not display damping effects unless physical causes are present (see for example Sündermann, 1966). Furthermore, it has been stated in § 2.4.2 that the present irregular finite difference system becomes equivalent to a conventional finite difference system if a rectangular grid is used (compare equations 44-45 with equations 46-47 and Figures 5 and 6. The first grid investigated is therefore a rectangular, box-like lake with a rectangular grid as shown in Figure 55. As can be seen in Figure 55, the rectangular-grid "box" lake has dimensions in the same order of magnitude as the Léman. Its water surface is $9,0 \cdot 10^8 \text{ m}^2$, its volume is $9,9 \cdot 10^{10} \text{ m}^3$ and its depth is 110 m. To induce seiche motion, an easterly wind of 75 km/h was again applied for one hour. Varying only the α -mean, all other parameters were kept constant at the values listed in Figure 44. The results are shown for points 3, 23 and 48 (as marked in Figure 55a) in Figure 56 following the scheme used earlier. In Figure 56 it can be seen that damping of seiche motion clearly increases with the intensity of smoothing. With $\alpha = 0,999$ a seiche motion similar to that shown in Figures 26 and 31 can be produced. The simulated seiche period, T , is 2760 seconds when determined from 59 seiches calculated with $\alpha = 0,999$ and $\alpha = 0,99$. For $\alpha = 0,95$ the seiche period is the same. From equation 55, the theoretical period is $T = 2739,75$ seconds calculated with a length $B = 4,5 \cdot 10^4 \text{ m}$. There exists thus excellent agreement between the simulated and the theoretical seiche period. It may also be noted that the amplitudes of points 3 and 48 are the same and that the seiches of these two points are opposite in phase. The amplitude of point 23, being situated close to the center of the lake, is substantially smaller.

It has been demonstrated that, with a rectangular grid applied to a box as shown in Figure 55, seiches displaying natural rates of damping can be well reproduced. Since however using a rectangular grid implies loss of one of the principal advantages of the



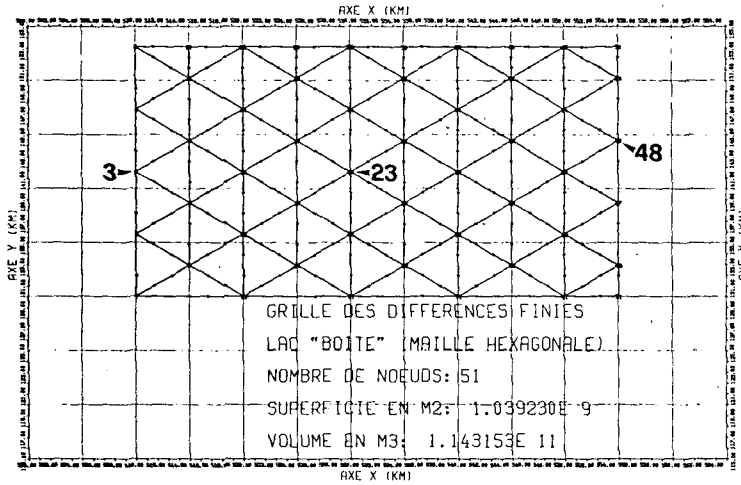
(a) Plan view of rectangular-grid "box" lake

(b) Depth and boundary tangents of rectangular-grid "box" lake



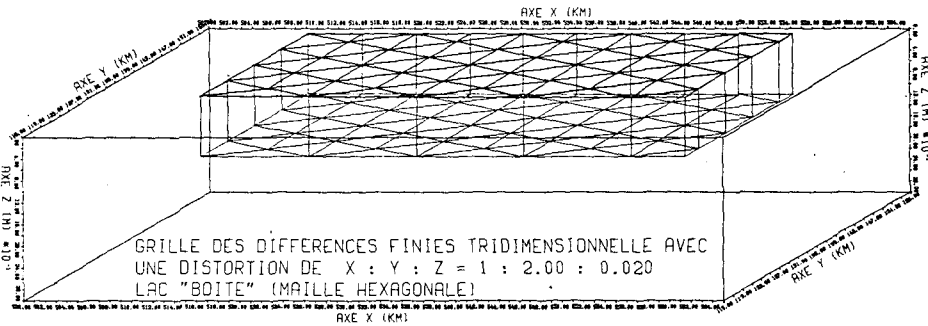
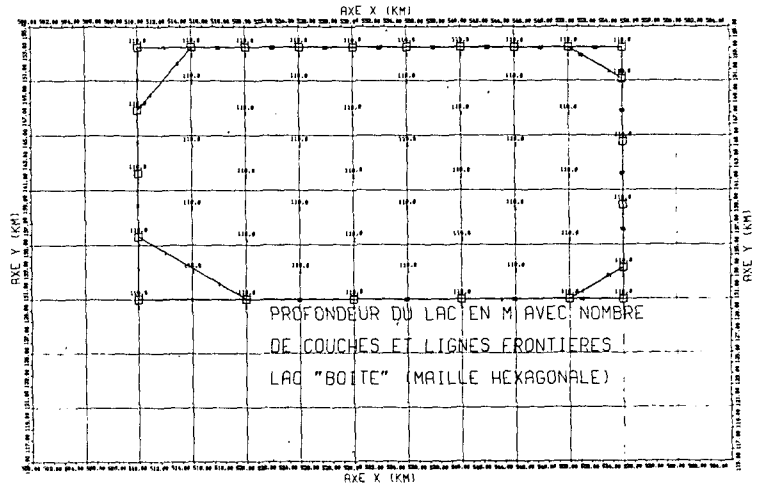
(c) Three-dimensional view of rectangular-grid "box" lake

Figure 55: Rectangular-grid "box" lake



(a) Plan view of hexagonal-grid "box" lake

(b) Depth and boundary tangents of hexagonal-grid "box" lake



(c) Three-dimensional view of hexagonal-grid "box" lake

Figure 57: Hexagonal-grid "box" lake

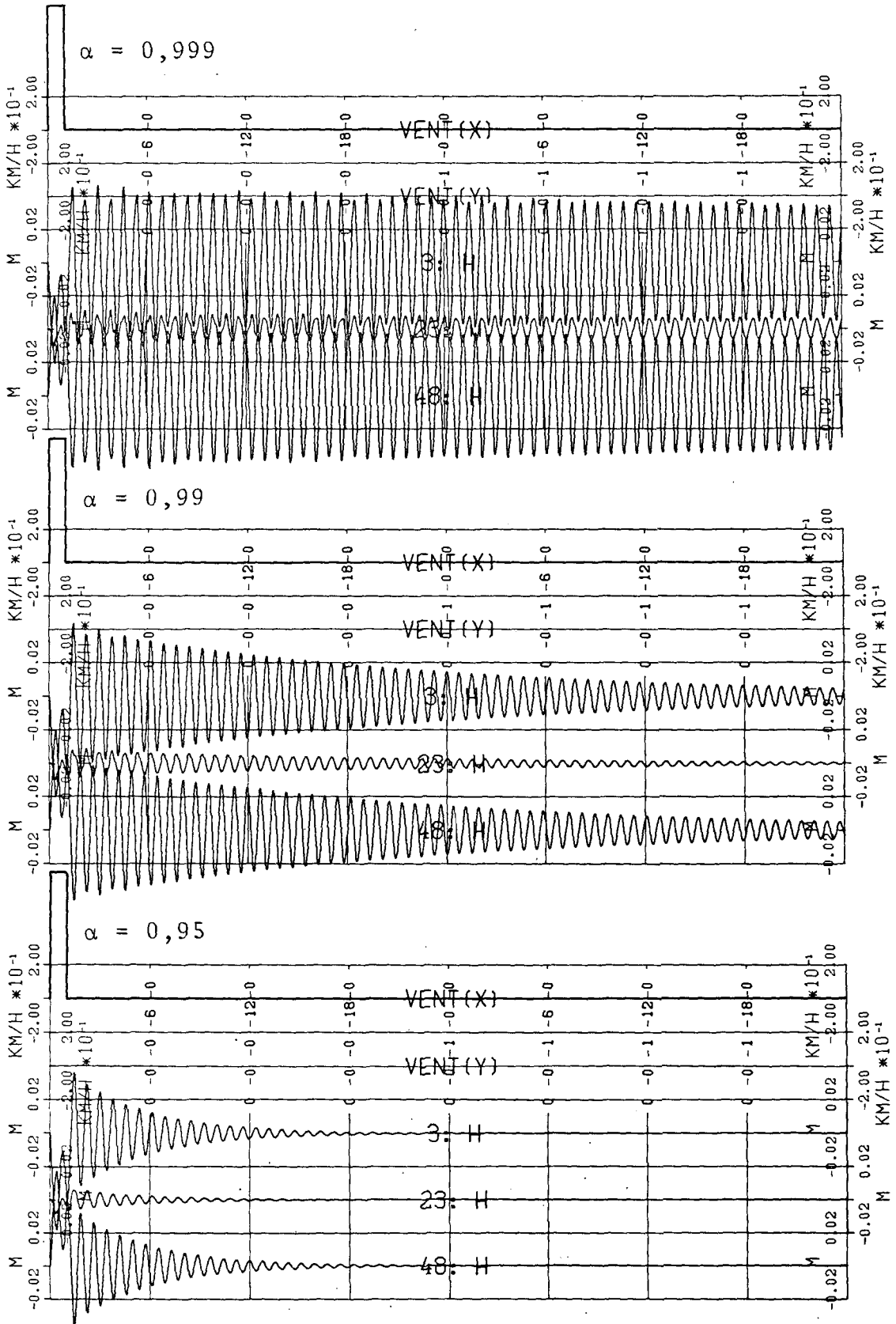


Figure 56: Seiches simulated for rectangular-grid "box" lake

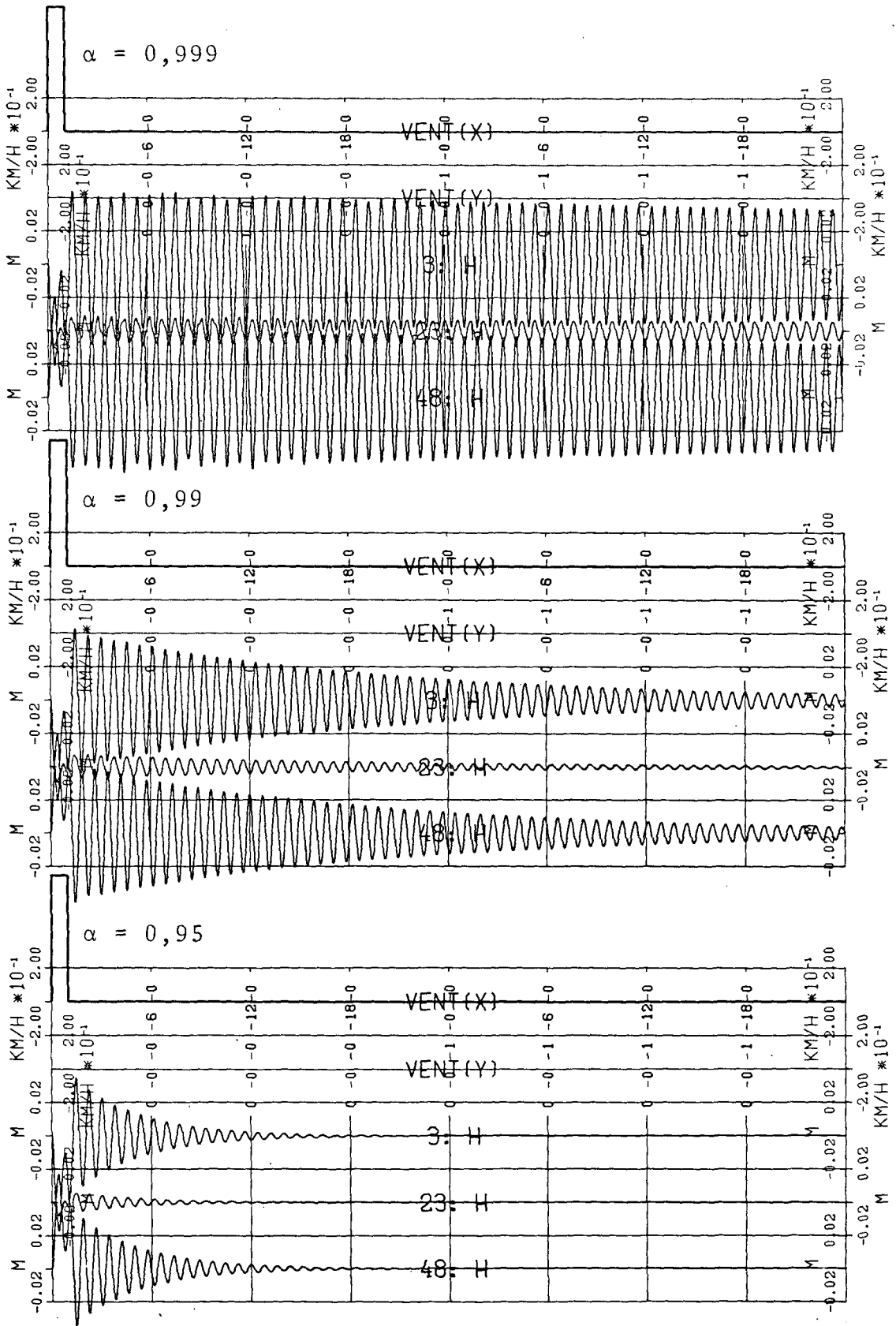
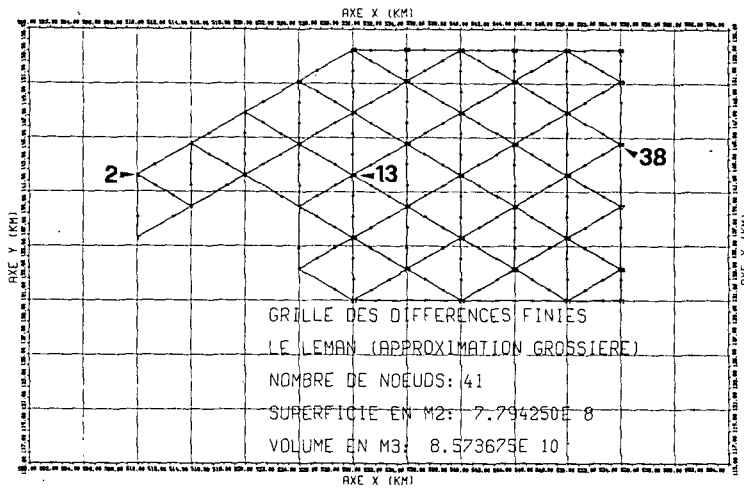
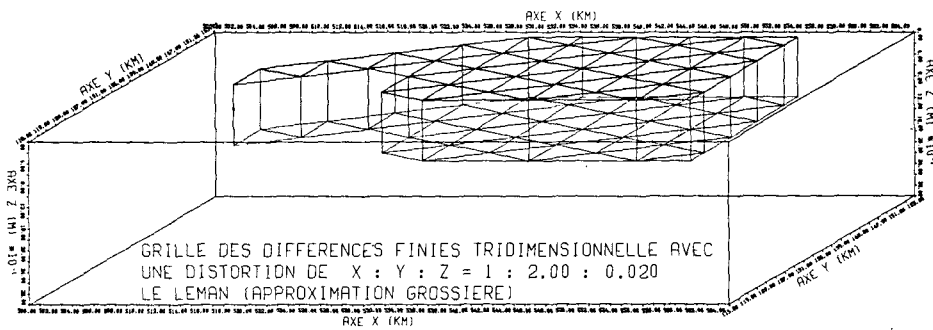
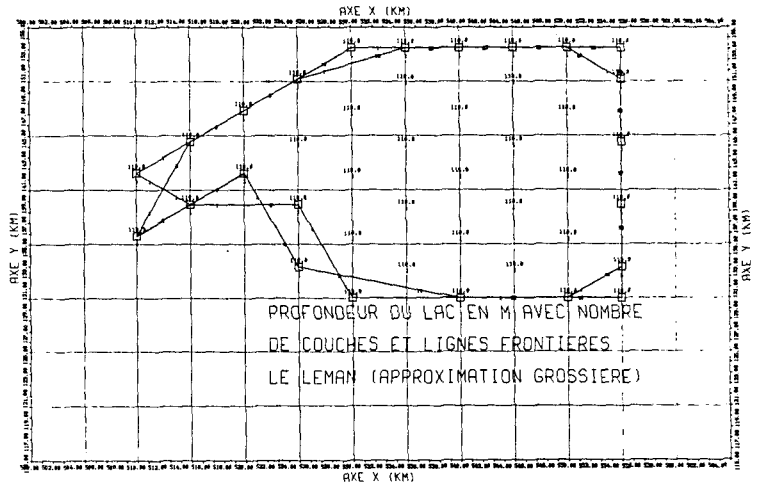


Figure 58: Seiches simulated for hexagonal-grid "box" lake



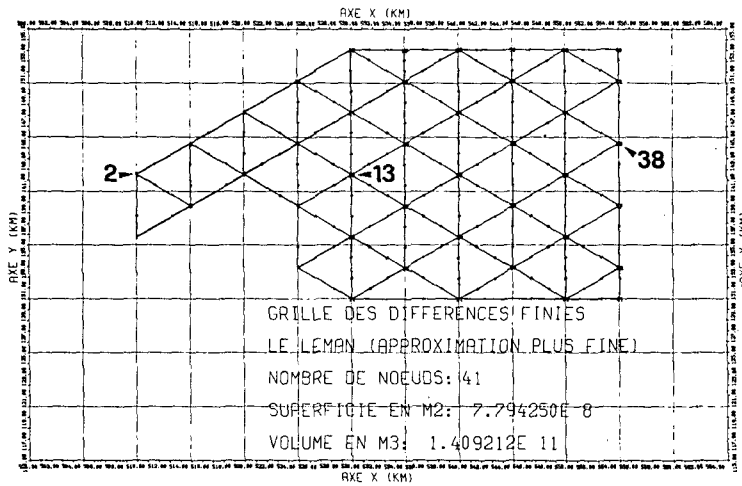
(a) Plan view of hexagonal-grid "Léman-box" lake

(b) Depth and boundary tangents of hexagonal-grid "Léman-box" lake



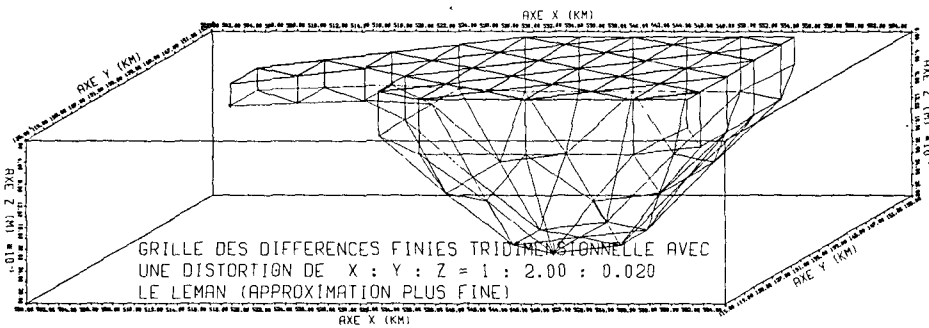
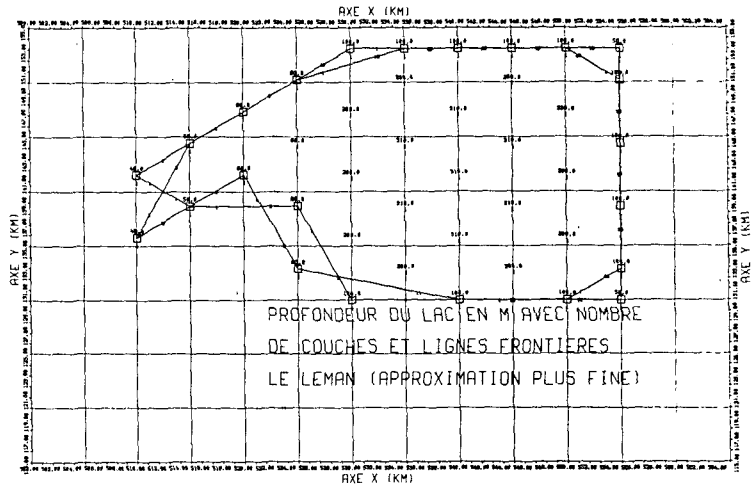
(c) Three dimensional view of hexagonal-grid "Léman-box" lake

Figure 59: Hexagonal-grid "Léman-box" lake



(a) Plan view of hexagonal-grid "Léman-like" lake

(b) Depth and boundary tangents of hexagonal-grid "Léman-like" lake



(c) Three-dimensional view of hexagonal-grid "Léman-like" lake

Figure 61: Hexagonal-grid "Léman-like" lake

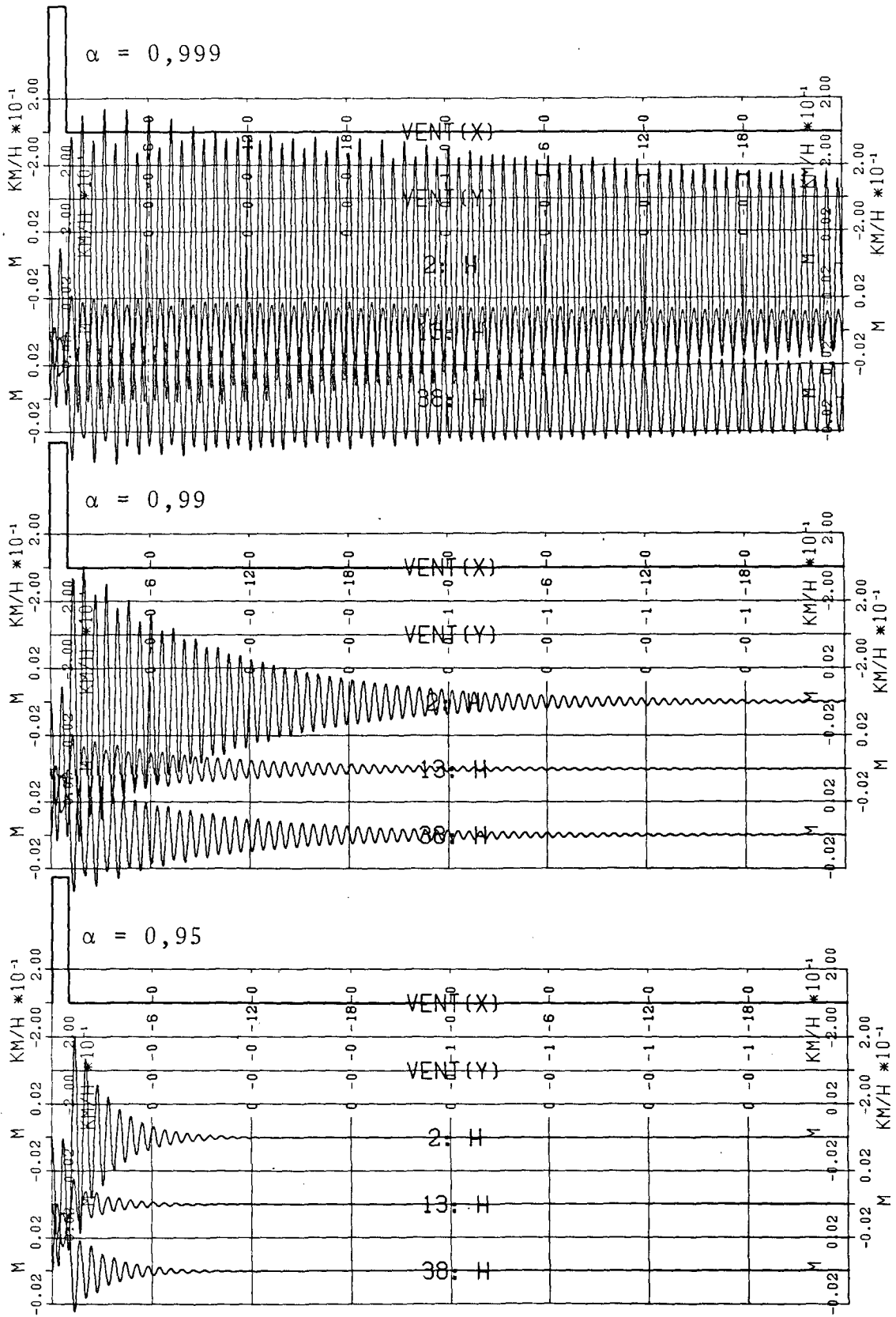


Figure 60: Seiches simulated for hexagonal-grid "Léman-box" lake

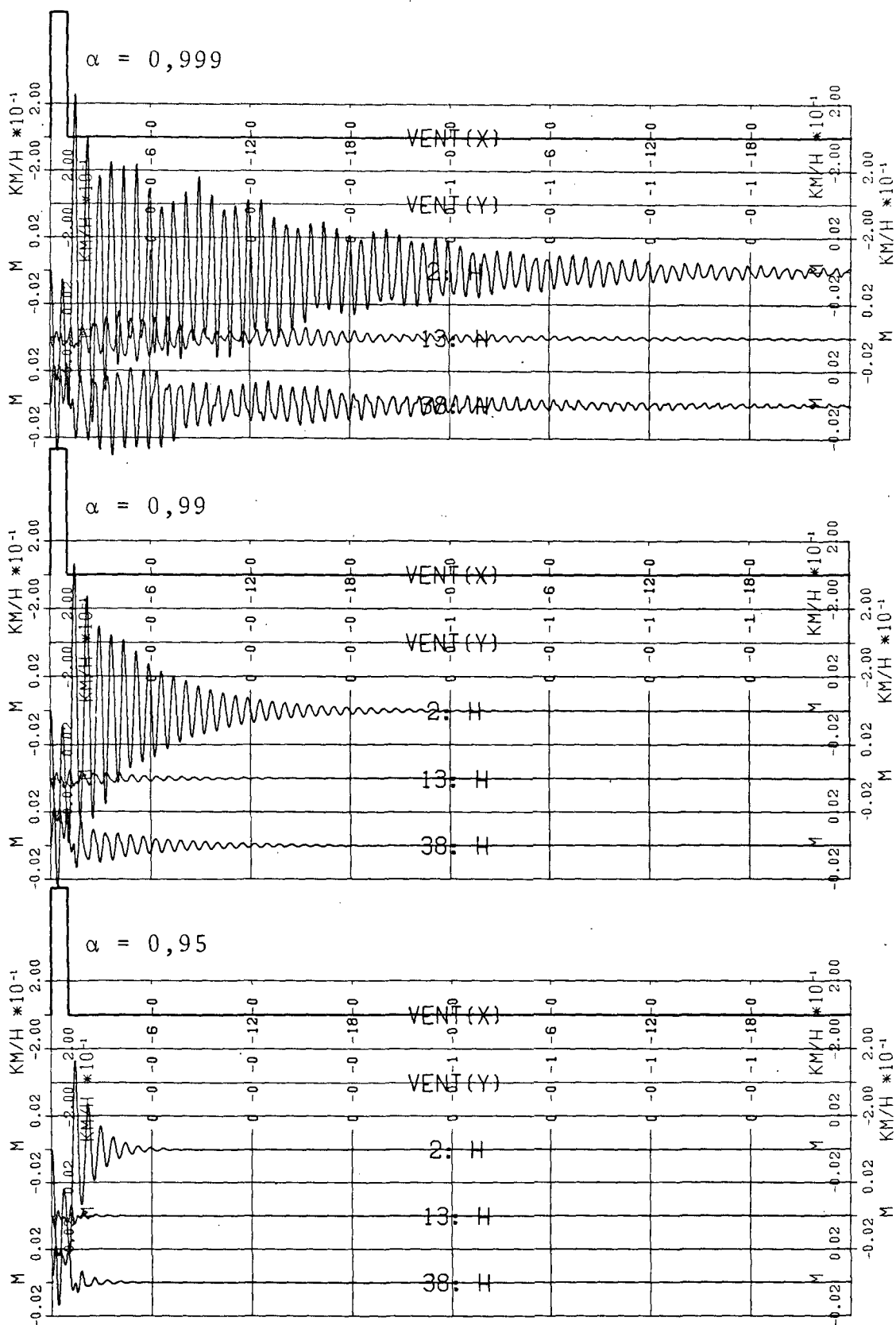


Figure 62: Seiches simulated for hexagonal-grid "Léman-like" lake

present model, i.e., smooth representation of geometry, the next grid tested was that shown in Figure 57. There it can be seen that, again, a box-like lake is represented. This time however the grid is no longer rectangular but hexagonal, i.e., each point is surrounded by a regular hexagon. The hexagonal-grid "box" lake shown in Figure 57 has the same length and the same depth as the rectangular-grid "box" lake of Figure 55. To accommodate regular hexagons however, the width of this lake is somewhat larger. The water surface of the hexagonal-grid "box" lake shown in Figure 57 is $1,04 \cdot 10^9 \text{ m}^2$, its volume is $1,14 \cdot 10^{11} \text{ m}^3$. Simulation results for points 3, 23 and 48 (as marked in Figure 57a) are shown in Figure 58. Comparing Figures 58 and 56, it can be seen that the simulation results for these two lakes are practically identical. There exists thus again excellent agreement between simulated and theoretical seiche period and seiches of long duration can easily be simulated if so desired.

The two grids tested so far were both situated within a rectangular box, a shape that does not readily correspond to that of natural lakes. The next step was therefore to investigate how a lake with a plan resembling somewhat that of the Léman, but having a horizontal bottom, reacts. Such a lake is shown in Figure 59. It should be noted that the grid within the lake shown in Figure 59 is still perfectly regular, i.e., each "inner" point is surrounded by regular hexagons. The water surface of this hexagonal-grid "Léman-box" lake is $7,79 \cdot 10^8 \text{ m}^2$, its volume is $8,57 \cdot 10^{10} \text{ m}^3$ and its depth is again 110 m. Applying the same procedures as for the two earlier model lakes, the simulation results for points 2, 13 and 38 (as marked in Figure 59a) are shown in Figure 60. Comparing Figure 60 with Figures 56 and 58, one finds that the principal features of behaviour have remained unchanged. One feature that differs from the previous simulations is that the seiche amplitudes of points 2 and 38 are no longer the same. From Figure 60 it can be seen that this is due to the difference in width of the lake at its eastern and western ex-

tremities. Furthermore, it seems that a decrease of α in the hexagonal-grid "Léman-box" lake results in stronger damping than in the two previous lakes. Natural durations of seiches however can still readily be simulated with $\alpha = 0,999$. The simulated seiche period, T , is now 2421 seconds. Solving equation 55 for the mean length, B , a value of $B = 3,98 \cdot 10^4$ m is obtained, which fits the given geometry well.

While the lake shown in Figure 59 already somewhat resembles the shape of the Léman, its lake bottom does not yet correspond to natural conditions. As a final step, a hexagonal-grid "Léman-like" lake shown in Figure 61 was tested. In this lake the grid is identical to that of the hexagonal-grid "Léman-box" lake shown in Figure 59 but the depth varies to simulate the real form of the Léman. Its volume is $1,41 \cdot 10^{11} \text{ m}^3$ which, with a water surface of $7,79 \cdot 10^8 \text{ m}^2$ yields a mean depth $\bar{D} = 181$ m. Following the principles enunciated earlier, the simulation results for points 2, 13 and 38 (as marked in Figure 61a) are shown in Figure 62. In Figure 62 it can be seen that the tendencies are again the same. The influence of the α -mean is still stronger and it seems now that even with an $\alpha = 0,999$ natural seiche durations can no longer be simulated. A notable new phenomenon is the occurrence of dicrote seiches, which can be seen particularly well at point 38. Furthermore, a secondary, not very well defined fluctuation of magnitude of seiche amplitude is present. A similar phenomenon has been observed in the real Léman as can be seen in Figure 26 and to a lesser degree in Figure 31. The period of this observed, secondary fluctuation is about half a day. The period of the principal longitudinal seiche is 2697 seconds. With a mean depth of $\bar{D} = 181$ m the equivalent length, \bar{B} , according to equation 55 is thus $5,68 \cdot 10^4$ m. From Figure 61 it can be seen that this is substantially longer than the length of the lake. Consequently, for this lake, equation 55 no longer gives good results, an observation that has already been made by Forel (1895; see also § 4.1). Nevertheless it should be noted that this is also in contradiction with the

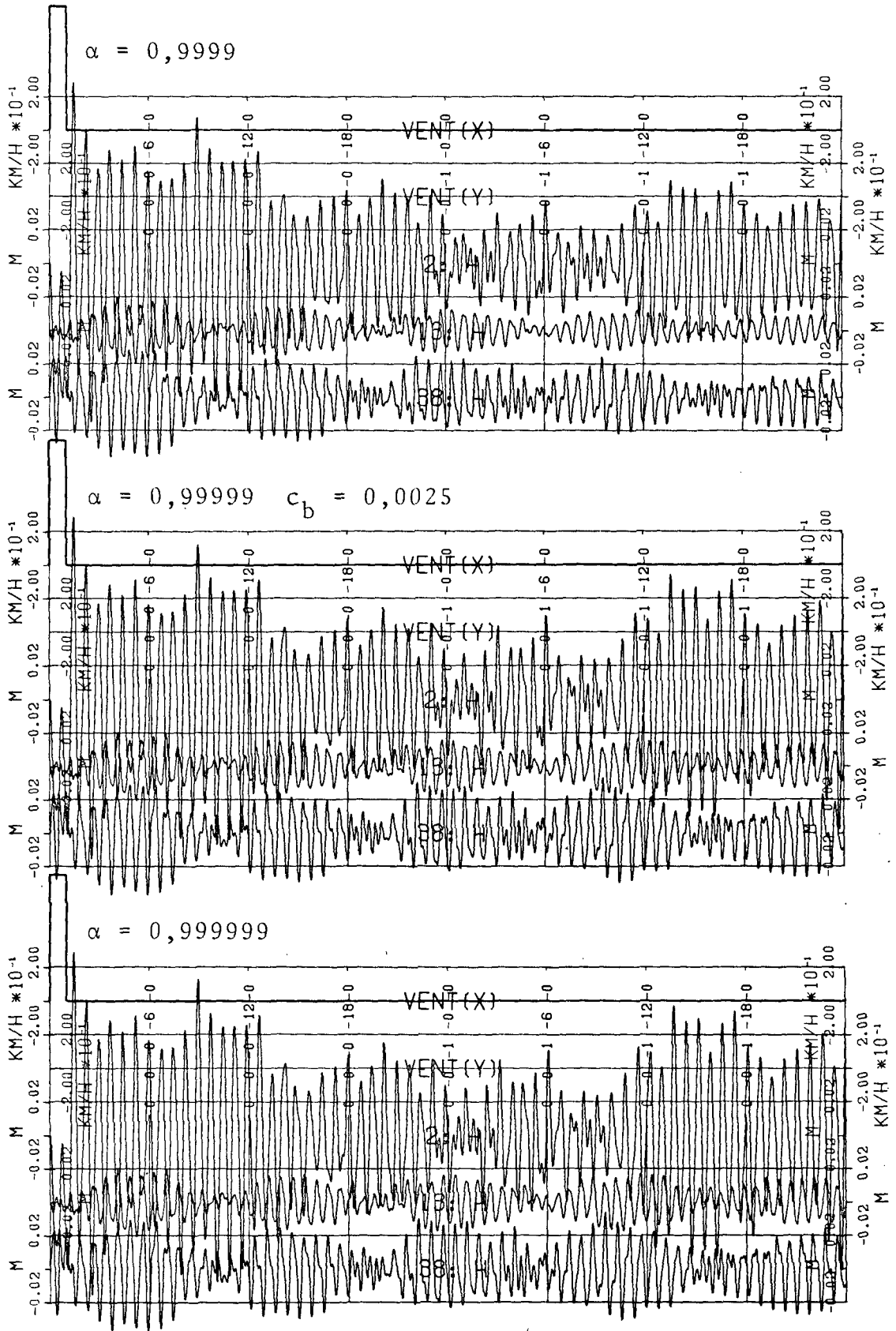


Figure 63: title; see opposite page

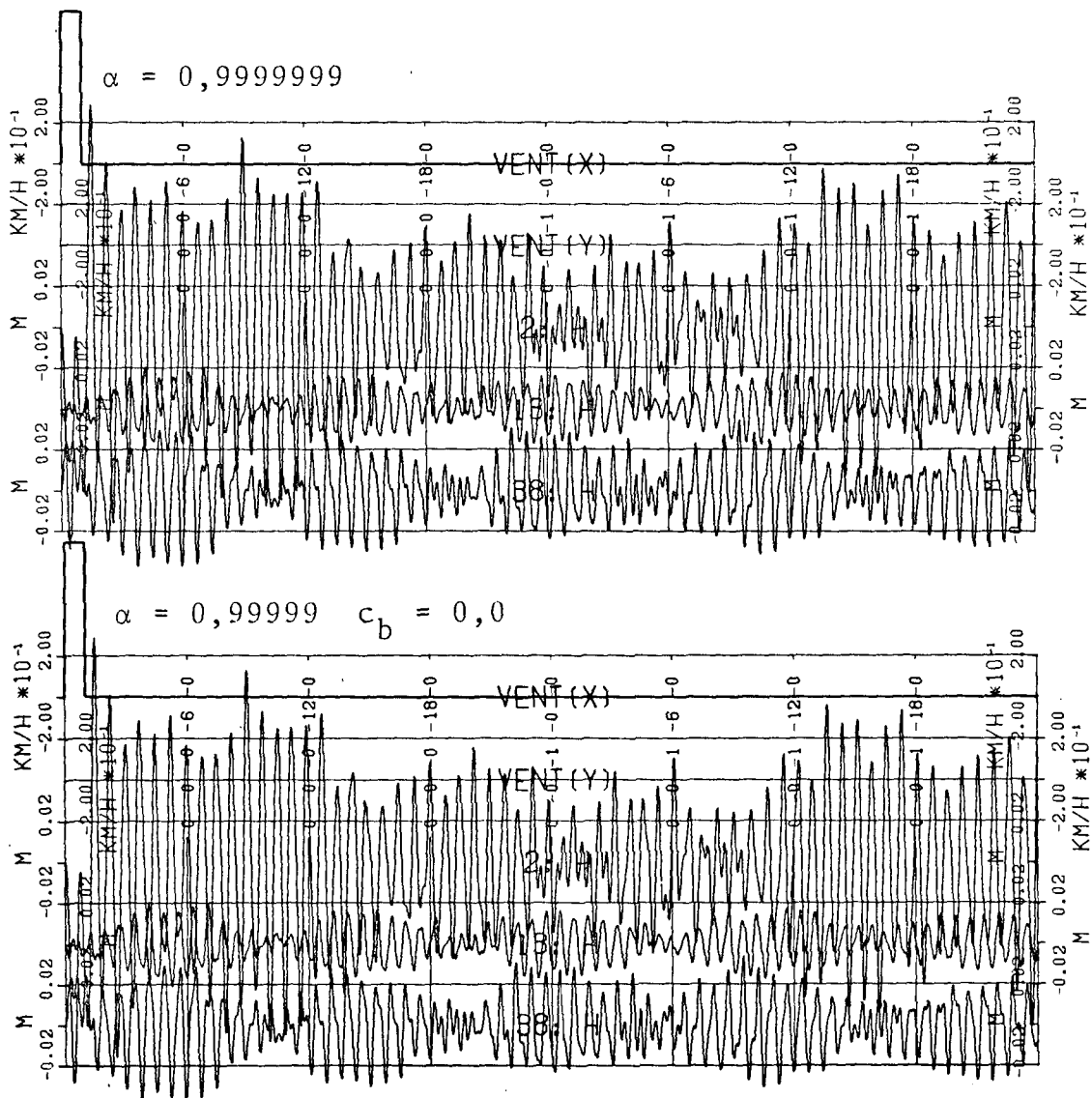


Figure 63: Seiches simulated for hexagonal-grid "Léman-like" lake with further variation of α and c_b

results obtained from the test lake simulations as discussed in § 3.2.1.

To investigate whether further increase of α allows simulation of long duration seiches, the hexagonal-grid "Léman-like" lake of Figure 61 was used for further simulations with $\alpha = 0,9999$, $\alpha = 0,99999$, $\alpha = 0,999999$ and $\alpha = 0,9999999$. The output of those runs is shown in Figure 63. There it can be observed that di-

dicrote seiches occur with a maximum intensity just about every ten hours. This can be observed best at the fluctuations of point 38. Comparing these dicrote seiches with Léman observations, one finds that they strongly resemble seiches shown in Figures 22 and 23 (Genève). It has been mentioned in § 4.1 that Forel (1895) already explained the phenomenon of dicrote seiches by superposition of seiches whose periods (or multiples of periods) are very close to each other but not identical. In Figure 63 it can furthermore be seen that the amplitude is at its maximum when the phenomenon of dicrote seiches is not visible, i.e., at times when the peaks of the two different seiches coincide. In this way the fluctuations in seiche amplitude can now also be explained by resonance of the two different seiche motions. In Figure 63 it can be seen that an increase of α results generally also in an increase of amplitudes (decrease in damping). The maximum value which still gives some noticeable effect is $\alpha = 0,999999$ since there is no longer any visible difference if one increases α from $\alpha = 0,999999$ to $\alpha = 0,9999999$ (noting that all calculations were performed with 14 significant figures). To investigate again any possible influence of a change in the bottom shear stress coefficient, c_b , a run was performed with $\alpha = 0,99999$ and $c_b = 0,0$. Comparing the output from this run with the output of the run with $\alpha = 0,99999$ and $c_b = 0,0025$, one finds that, this time, there are visible differences (compare statement of § 5.1.2, that with $\alpha = 0,90$ no visible difference was observed). These differences are however so small that it is not worth considering the problem of the bottom shear stress coefficient in a one-layer formulation in further detail. Runs with $\alpha = 1,0$ were found to be unstable at all times (using a time step of $\Delta t = 30$ seconds) with or without bottom friction. This instability was observed in spite of the fact that, according to equation 28, a time step of about three minutes should still be stable. In this context it is interesting to note that, as has been remarked already in § 2.3, according to Sündermann (1966) instabilities are also due to the non-linear-

ity of the system of equations being solved. Using a conventional finite difference grid, Sündermann (1966) demonstrated that his conventional finite difference grid produced stable results using a linear bottom friction, i.e., a friction which is a linear function of velocity. It has not been investigated whether the same holds for the present grid.

It should be noted that in the hexagonal-grid "Léman-like" lake the distance between the grid points is not roughly proportional to the square root of the depth at each point as it has been shown to be desirable if an optimum time step is to be applicable for the entire lake (see § 2.3). Since in a lake of the shape of the Léman this criterion can not readily be applied (see § 5.6.1), it has not been investigated further.

In conclusion, it can be stated that seiches with very low rates of damping can apparently be simulated as long as a "smoothed" grid is used for the representation of the lake.

5.6 Application of a "smoothed" Léman grid

In §§ 5.2 and 5.3 it was shown that, with a coarse, irregular Léman grid consisting of only 52 points, very useful results can be obtained. However, because of the instabilities created by the irregularities of such a grid it is necessary to apply a smoothing procedure with $\alpha \approx 0,90$ to stabilize the system. The investigation of regular grids of various shapes in § 5.5 demonstrates that those instabilities are largely eliminated if the grids are made more regular and that calculations with α very close to unity yield water level fluctuations that closely resemble the seiches observed in the Léman. It follows that, if a grid for the Léman can be established which satisfies the "smoothness" criterion, it should be possible to perform calculations of seiches with a rate of damping which corresponds to natural conditions.

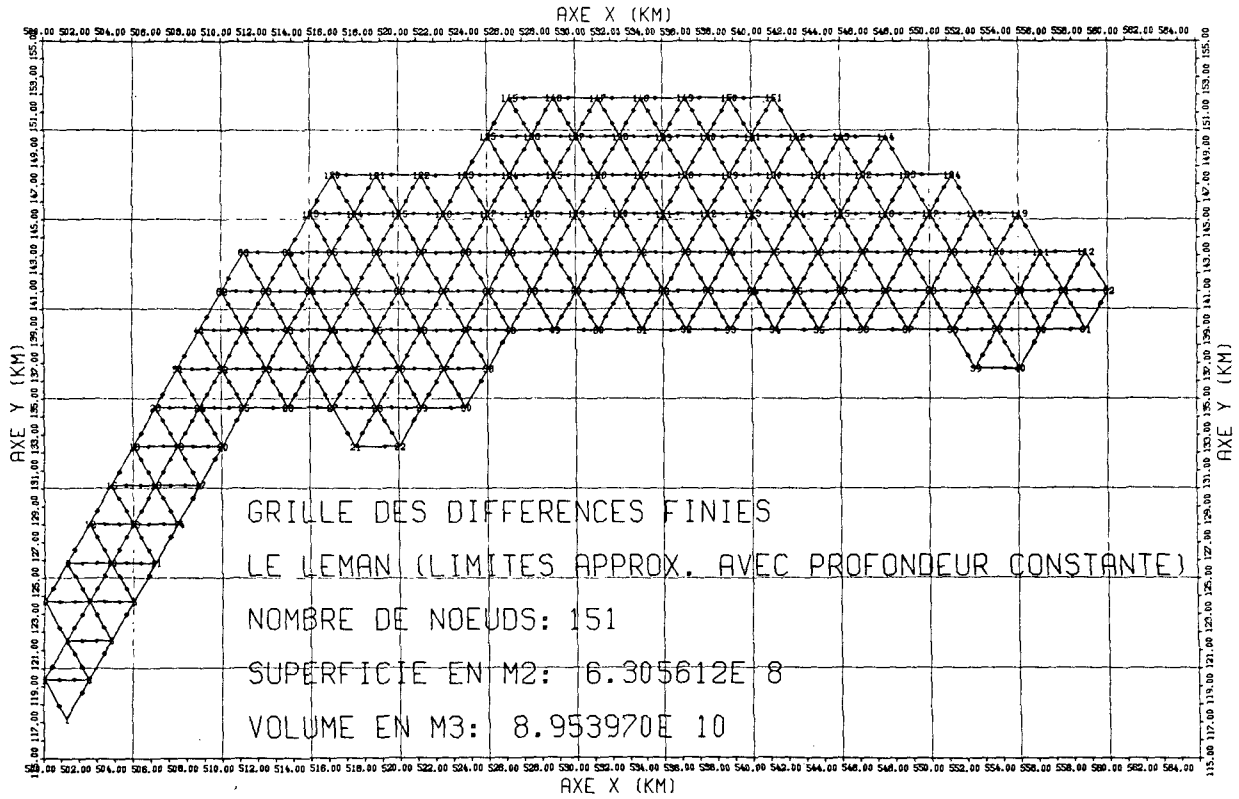


Figure 64: Regular hexagonal grid for the Léman with approximated frontiers

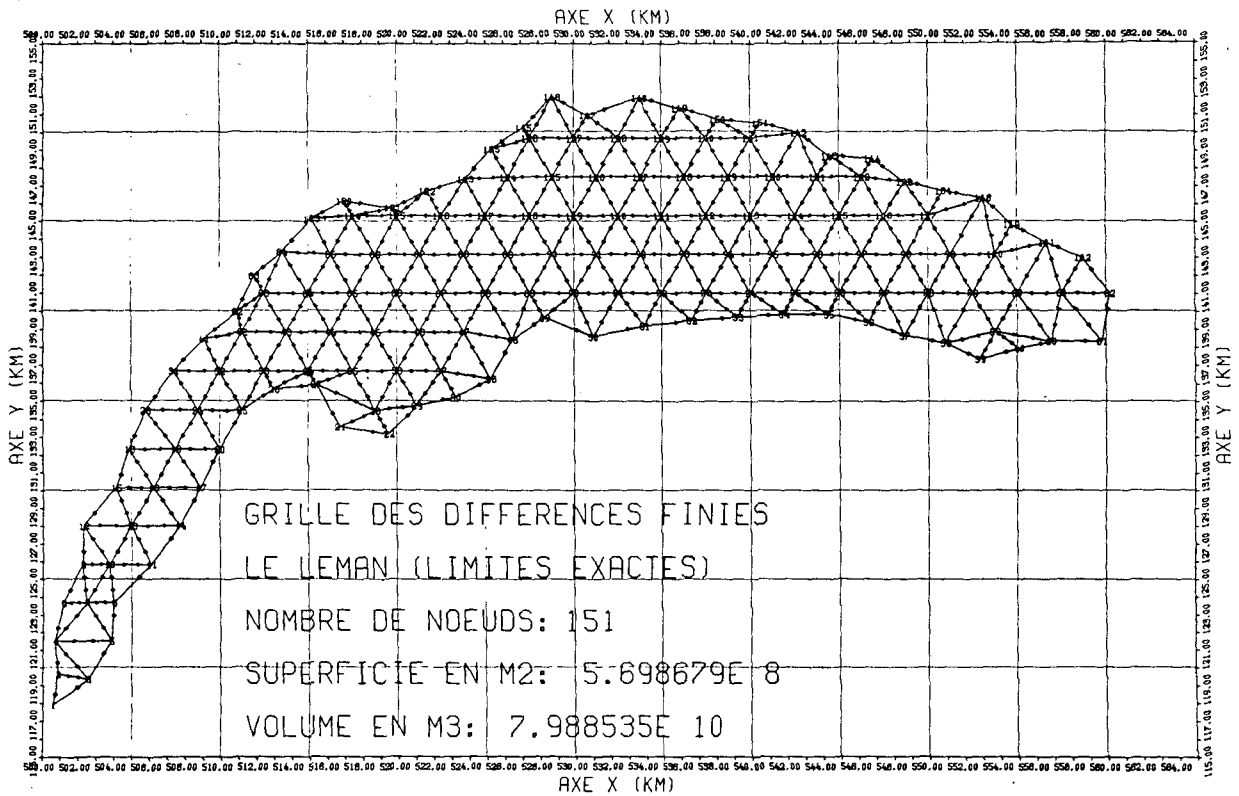


Figure 65: Regular hexagonal grid for the Léman with exact frontiers

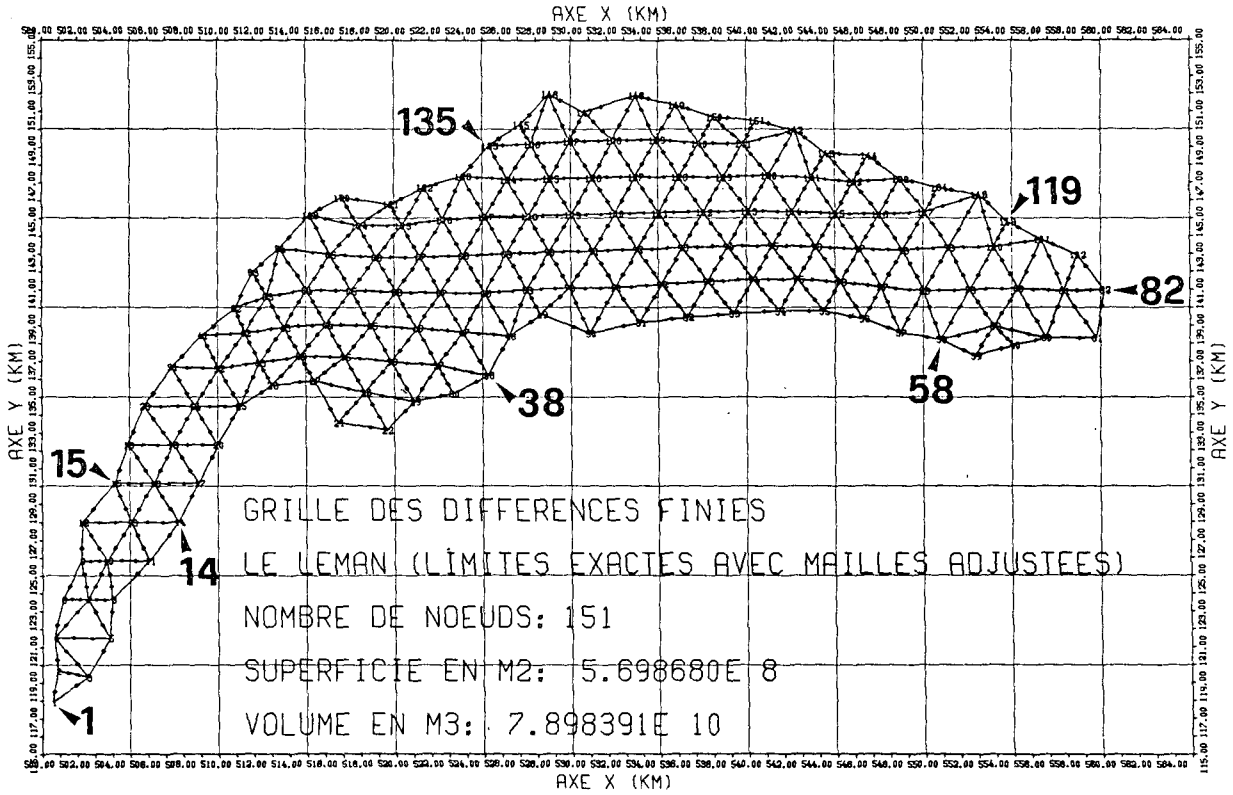


Figure 66: Plan view of "smoothed-irregular" finite-difference grid of the Léman

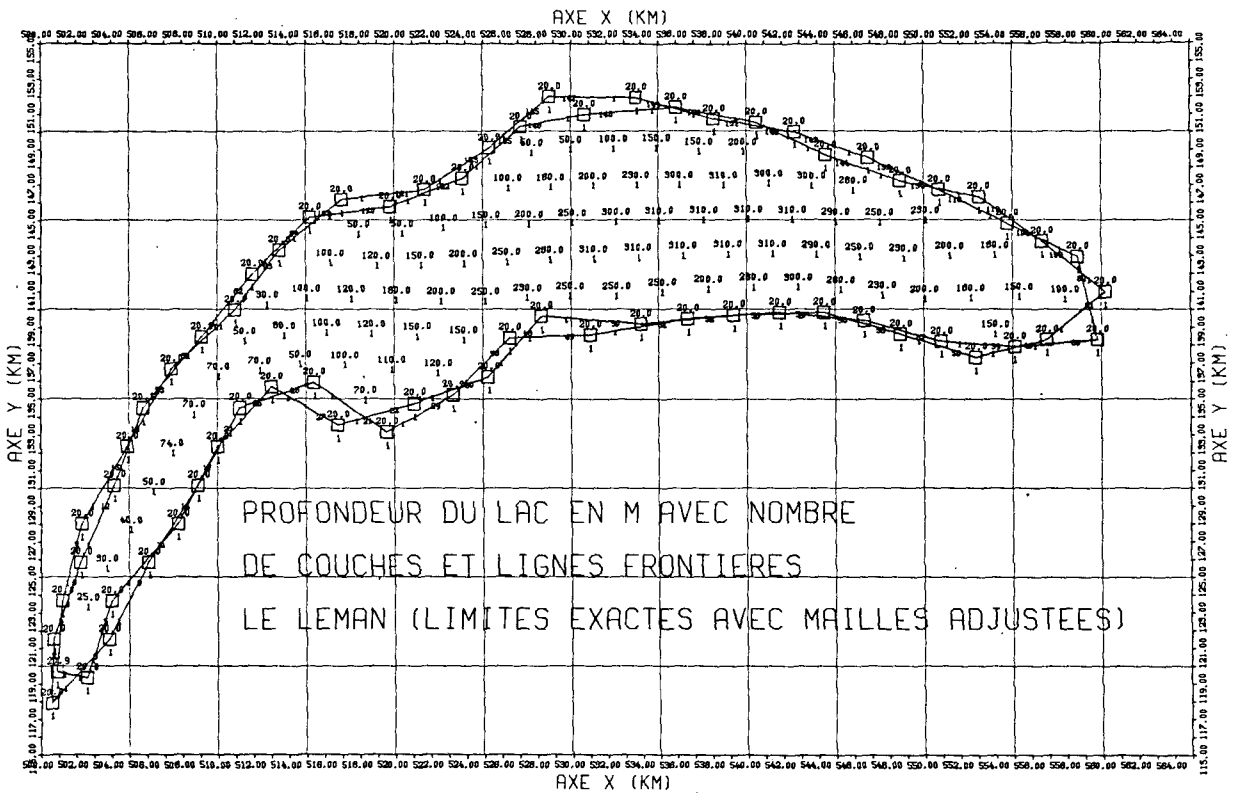


Figure 67: Depth and number of layers including boundary tangents of "smoothed-irregular" finite difference grid of the Léman

5.6.1 Construction of a smoothed Léman grid

In an initial attempt to establish a smoothed grid it was decided that a distance of about 1,5 km between grid points might be small enough to allow construction of a reasonably smooth grid for the Léman and still be large enough to limit the number of grid points needed. The criteria to be considered in such a choice have already been discussed in § 5.1.1. The procedures established for this purpose are semi-automatic, i.e., generation of the grid is carried out by programs combined with manual adjustment.

As a first step, a hexagonal mesh was generated covering a region greater than the water surface of the Léman. Then, as shown in Figure 64, a set of hexagons was selected to roughly resemble the plan of the lake. Then, as demonstrated in Figure 65, the frontiers of this grid were adjusted to coincide with the Léman shoreline. Thus, while in the interior of this grid all hexagons are still absolutely regular, those bordering the lake frontiers have been more or less distorted, depending on their position. To distribute these irregularities, the grid was then "smoothed" by shifting each interior point in such a way that its x and y coordinates are equal to the means of the x and y coordinates of all its surrounding points. The resultant smoothed finite-difference grid is shown in Figure 66. The numerical procedure was one of iteration; and only 28 iterations were necessary to arrive at the final solution with an error tolerance of less than one meter in distance. The points marked on the grid of Figure 66 are for later reference. The smoothed grid shown in Figure 66 (with a three-dimensional view in Figure 68) contains 151 points; the water surface is $5,69 \cdot 10^8 \text{ m}^2$ and the volume is $7,98 \cdot 10^{10} \text{ m}^3$, resulting in a mean depth of 140,19 m. Figure 67 shows the depth at all points and the number of layers as well as the boundary tangents. A three-dimensional view of the smooth Léman grid is shown in Figure 68. Comparing Figures 68 and 42, one finds that the

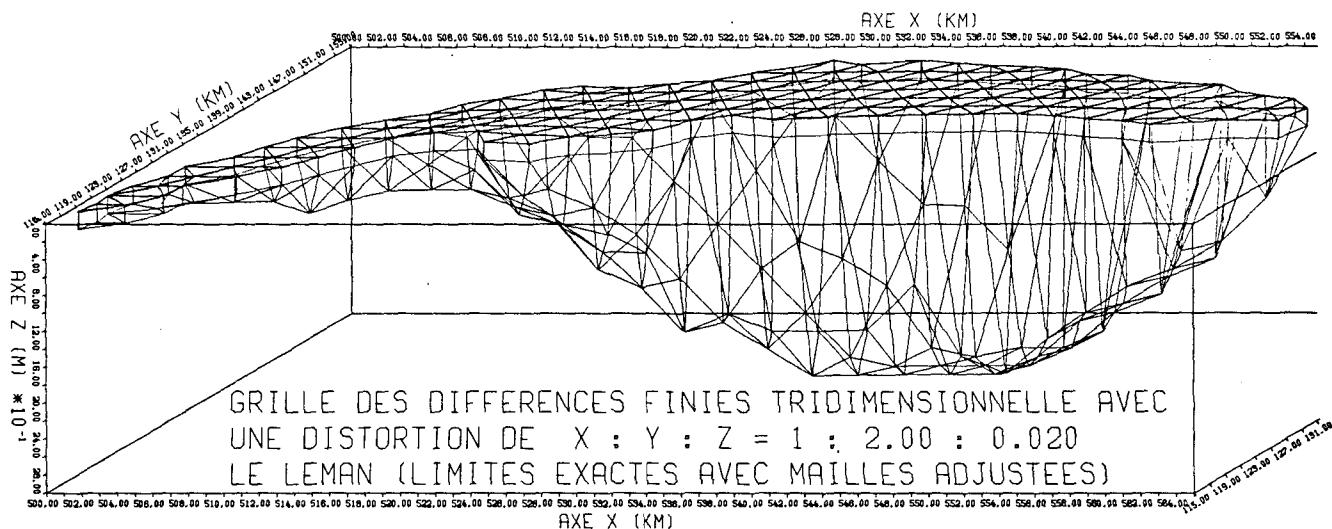


Figure 68: Three-dimensional view of "smoothed-irregular" finite difference grid of the Léman consisting of 151 points

smooth Léman grid clearly shows more detail than the coarse Léman grid. When compared with Figure 43 however, it can be seen that particularly in the "Petit Lac", i.e., the western portion of the Léman, improvements of representation are still possible.

In § 2.3 it was stated that it is desirable to design the grid in such a way that the distance between points is roughly proportional to the square root of the depth at that point since in this way a nearly maximum time step can be applied to the entire lake. A grid based on this principle has been used by Thacker (1979) for the simulation of a storm surge in an ocean bay with a gently sloped bottom configuration. If one wishes to construct a smoothed grid for the Léman in which the mesh size is a function of depth, possibly several thousand points would be required. This is because of the extremely steep bottom topography of the Léman near its north-eastern and south-eastern borders.

5.6.2 Simulation using the "smoothed-irregular" Léman grid illustrated in Figures 66-68

With the grid shown in Figures 66-68 simulations were again performed using the same wind input and for the same duration as in §s 5.4 and 5.5. The water levels are shown for 8 sites well distributed around the basin and coinciding with some stations from which observations are shown in Figures 32 and 33. The sites selected are, with their point numbers indicated in parentheses, Genève (1), Coppet (15), St-Prex (135), Vevey (119), Chillon (82), St-Gingolph (58), Thonon (38) and Hermance (14). The exact positions of these sites are indicated on Figure 66. With the exception of α , all parameters used were again those listed in Figure 44. Following the same principle as in Figure 63, outputs for various values of α and using the "smoothed-irregular" Léman grid are shown in Figure 69. In order to save space, the band showing the y component of the wind (which is zero at all times) has been omitted. The bands which follow below that showing the x-component of wind velocity, show water levels at the locations in the above listed sequence.

Comparing Figure 69 with Figures 62 and 63, one finds that apparently the behaviour of the "smoothed-irregular" Léman grid is identical to that of the hexagonal-grid "Léman-like" lake. Again, with $\alpha = 0,999$ damping is still too strong, when compared with natural seiches; and an increase of α corresponds to a further decrease in damping. There is no longer any visible difference between the calculations with $\alpha = 0,999999$ and $\alpha = 0,9999999$. The less the seiche motion is smoothed, the more seiches of higher order appear on the traces creating a multitude of dicrote seiches. A notable difference between Figures 69 and 63 arises from the fact that the number of secondary seiches is substantially larger in Figure 69 than in Figure 63. The reason for this is most probably due to the boundary geometry of the "smoothed-irregular" Léman grid shown in Figure 66, which when compared with the boundaries of the hexagonal-

grid "Léman-like" lake is indeed very irregular.

Having shown that the use of a "smoothed-irregular" grid permits simulation of seiches with natural rates of damping, it should be recalled that the final objective of these calculations is the demonstration that, in principle, any seiche observed in the Léman (or any other lake) can be simulated by this model. Accepting the run with $\alpha = 0,9999999$ as closest to reality, its output has been reproduced on a larger scale in Figure 70. Comparing Figure 70 with Figures 32 and 33, it can immediately be seen that, on a large scale, there is substantial similarity. Within the scope of the present study it is not possible, however, to perform an exhaustive analysis of the similarities and differences that exist between the simulation results and observations. Nevertheless, the following short discussion will present the most important results.

First, considering Figure 33, one finds that two different "seiche regimes" were generated; the first between July 27, 1950 9:00 h and July 28, 1950 17:00 h and the second for the remainder of the interval studied. This second regime appears to be similar to that of Figure 32 and corresponds probably better to the simulations shown in Figure 70. Comparison of the simulation results of Figure 70 will therefore be restricted to this second "regime". Considering first the amplitude of the simulated seiches, one observes in Figure 70 that the mean seiche range at Geneva is of the order of 16 cm. This seiche was created by an easterly wind of 75 km/h lasting for one hour. The mean seiche amplitude of the observed Geneva seiches in Figure 32 is around 17,5 cm. Considering the fact that the seiche amplitude in Geneva is the one most sensitive to variations in wind regime, one may speculate that, because these two values are reasonably close to each other, the Geneva seiches of Figure 32 were also generated by a wind with a speed of about 75 km/h.

Comparing next the seiche amplitudes, one finds that the ratios

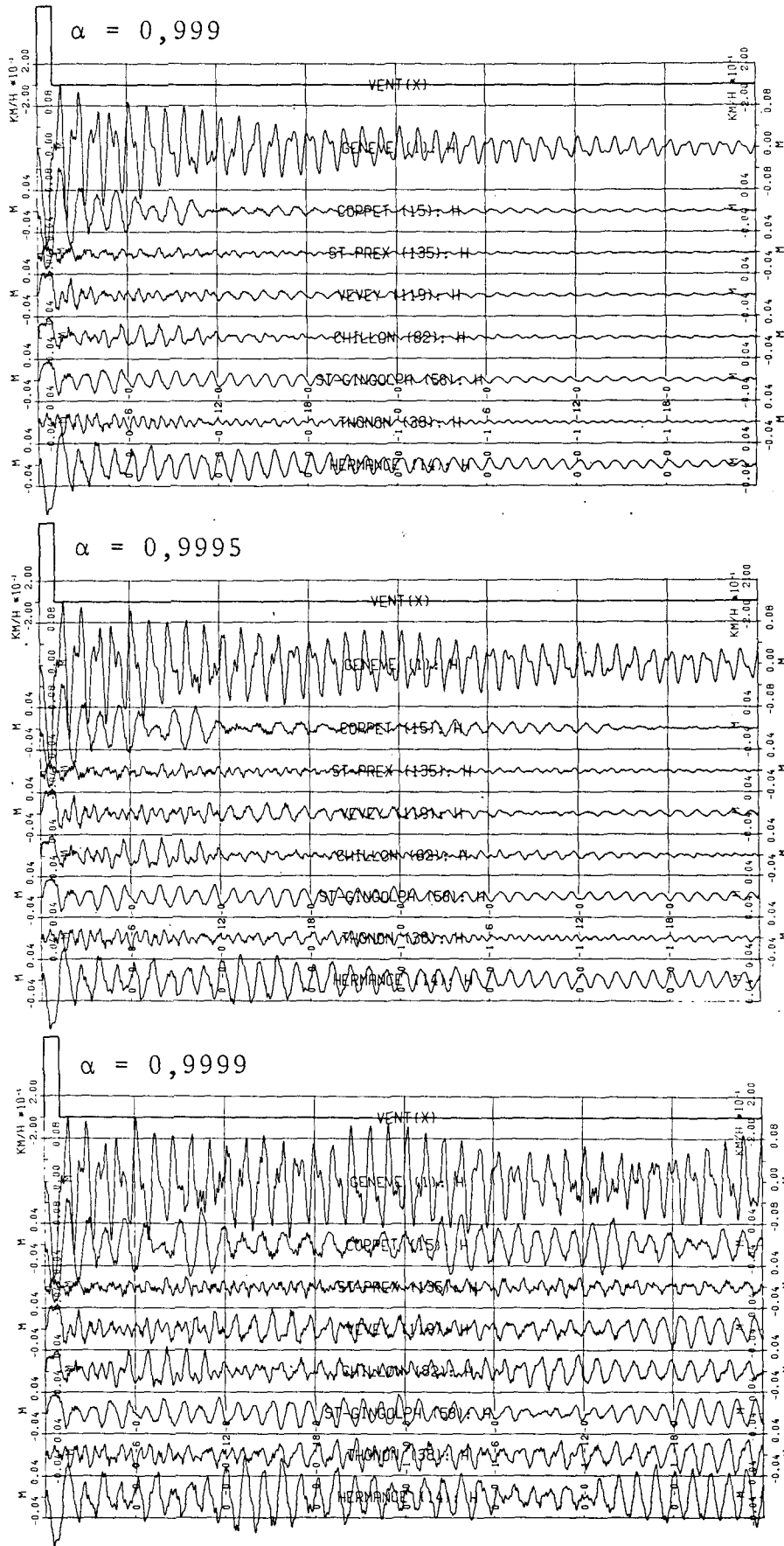


Figure 69: title, see opposite page

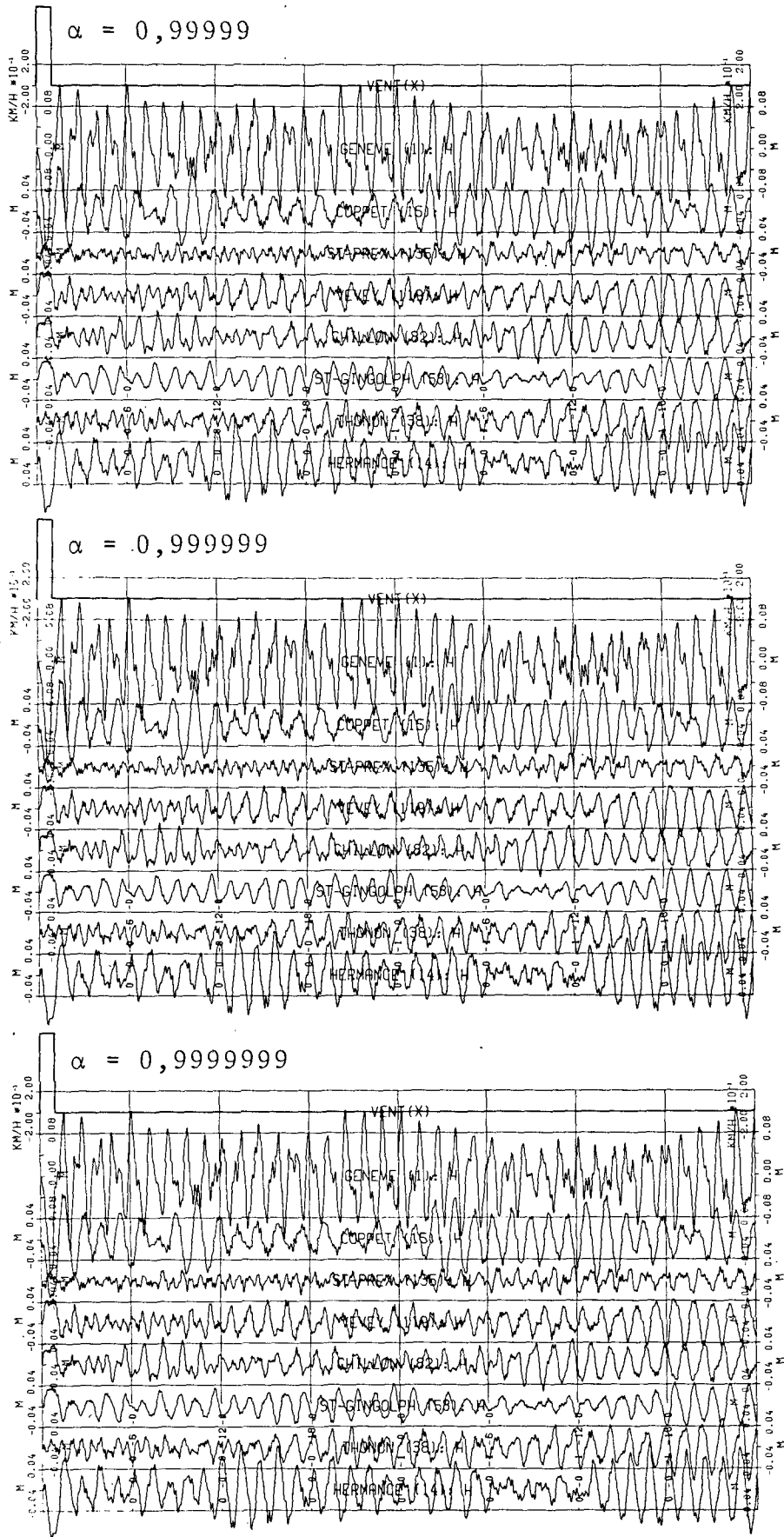


Figure 69: Seiches simulated for "smoothed-irregular" Léman grid

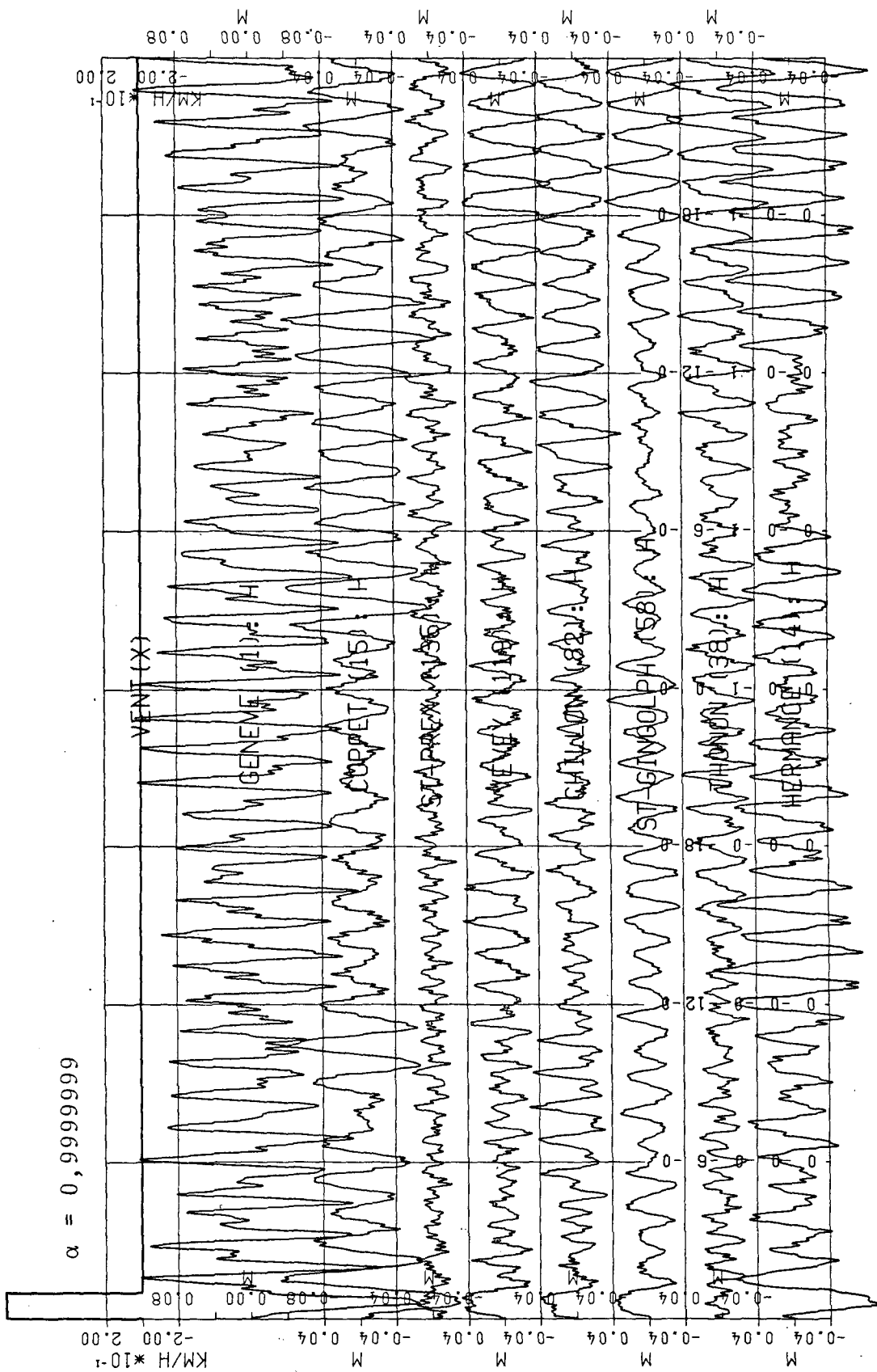


Figure 70: Seiches simulated for "smoothed-irregular" Léman grid with $\alpha = 0,9999999$

of sizes of amplitude of the different stations are about the same in the observations and the simulations. Exact numerical evaluation of these ratios is however difficult, particularly for the simulated seiches since, in these, the phenomenon of resonance creates a variation in seiche amplitude at each site. Also a statement about a possible resonance observed in the Léman is difficult to make since the number of seiches shown for the second "regime" in Figures 32 and 33 is not long enough.

In Figure 32 it can be seen that at St-Prex and Thonon and to a lesser degree also at Coppet, Vevey and St-Gingolph very short seiches are superimposed on the major, longitudinal seiches. In the simulation results shown in Figure 70 a similar phenomenon can be observed. The fact that the secondary fluctuations are of smaller amplitude in Figure 70 than in Figure 32 is probably a consequence of the size of the grid selected for the simulation, since obviously seiches with a wave length smaller than the mesh size of the grid cannot be simulated.

Examination of amplitude changes in Figure 70 suggests that the run with $\alpha = 0,9999999$ may be slightly unstable, since towards the end of the simulation it appears that the amplitudes increase slightly, even allowing for "beating". A conclusive statement, however, cannot be made since the simulation does not last long enough.

In conclusion, the "smoothed-irregular" grid model, retaining the advantages of an irregular grid but smoothed according to the principles outlined in § 5.6.1, is able to simulate seiches as they are observed in nature. Even if discrepancies remain, the basic principles of seiche motions are well preserved by the model, bearing in mind that the model output depends to a large degree on the precision with which the grid represents the natural lake.

5.6.3 Comparison of spectra from observed and simulated water level fluctuations

In this paragraph, results of spectral analysis applied to the water level fluctuations shown in Figure 32 (observed water level elevations) and in Figure 70 (simulated water level elevations) will be discussed. Since the meteorological conditions which generated the oscillations shown in Figure 32 are not known, no absolute comparison of amplitudes of peaks in spectra for Figure 32 and of amplitudes of peaks in spectra for Figure 70 can be made. However, the frequencies of peaks in these spectra are comparable. The degree of agreement is a test of the model simulations.

As described in textbooks concerned with data analysis (see for example Bloomfield, 1976), the input for spectral analysis is a digitized "time series" sampled at equal intervals, Δt , yielding n discrete points. The information content of spectra is strongly influenced by the number of points, n , and by the sampling interval, Δt . In Figure 71, the behaviour of constant interval sampling of various sine-functions is demonstrated. It can be seen in Figure 71a-c, that as long as the period is much greater than $2\Delta t$, the frequency of the sine-function is well determined by the series of discrete points at which the sine-function has been sampled. The highest frequency that can be observed (Figure 71e-f) is the Nyquist frequency, i.e., $1 \text{ cycle}/2\Delta t$ (Bloomfield, 1976). As can be seen in Figure 71h-i, frequencies higher than the Nyquist frequency will appear as very low frequencies when sampled at Δt . This phenomenon is known as "aliasing". If possible, the sampling rate should therefore be chosen such that aliasing cannot occur. If however this is not possible, all frequencies higher than the Nyquist frequency should be removed before the signal is recorded by appropriate instrumental or numerical filtration (Mortimer and Fee, 1976; Bloomfield, 1976). The phenomenon of "beating" as mentioned earlier, which occurs at frequencies close to the Nyquist frequency can be observed in Figure 71d and 71g.

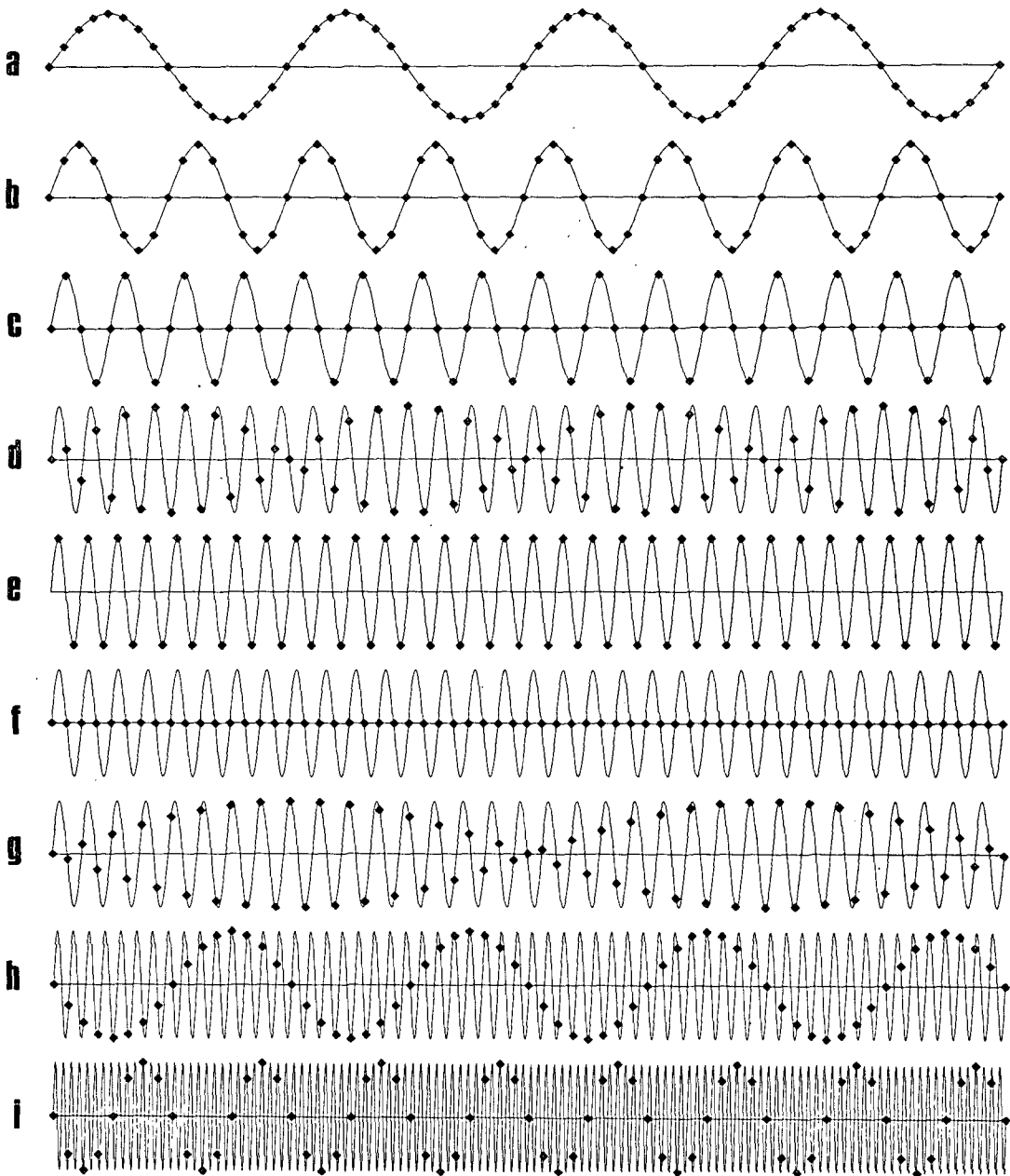


Figure 71: Demonstration of development of "aliasing" with increasing frequency when using constant sampling interval

Investigating the importance of aliasing in the present situation, it should be noted that the time step, Δt , of the simulation results shown in Figure 70 is 30 seconds, resulting in a Nyquist frequency of 1 cycle/min. Due to the fact that in a mathematical simulation with a time step, Δt , the maximum

GENEVE-SECHERON

COPPET

ST-PREX

THONON

VEVEY

ST-GINGOLPH

LES GRANGETTES

ECHELLE DES HAUTEURS
cm
0 4 8 12 16 20 24 28 32 36 40

heures : 15 00 18 00 21 00
jours : 11 février 1950

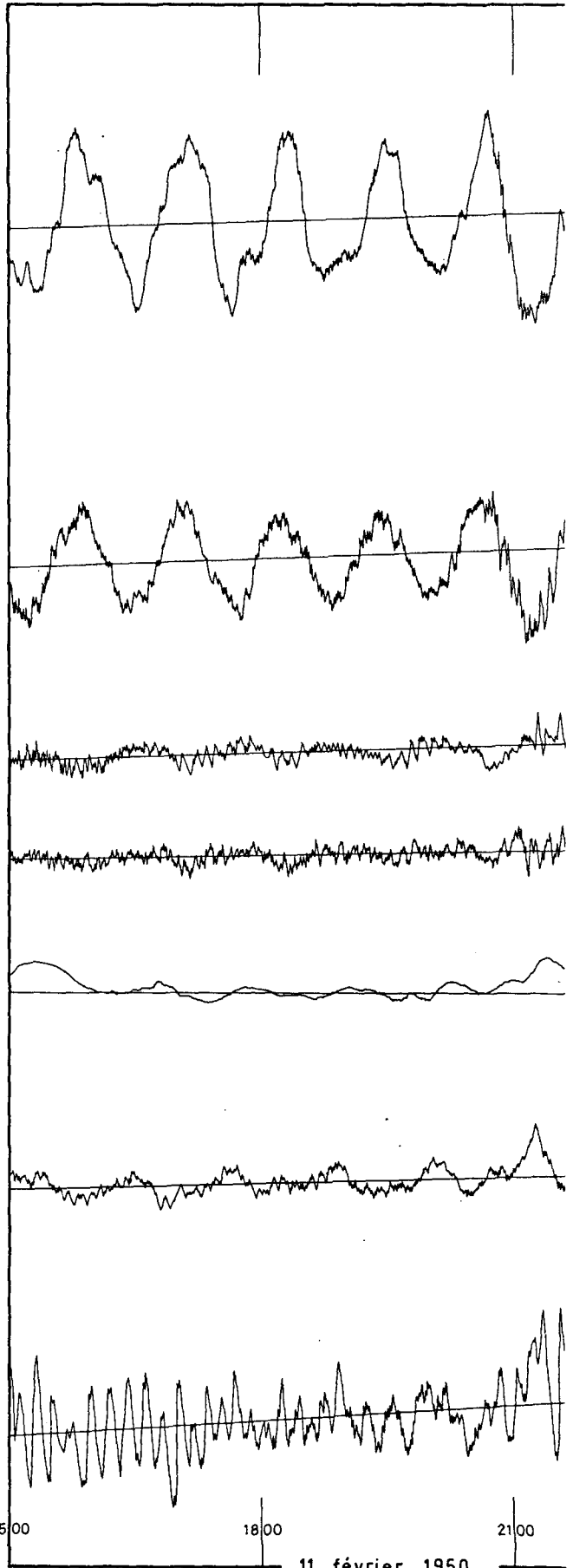


Figure 72:

Trace of data
digitized from
Figure 32 (in
its original
size) including
least square
trend lines

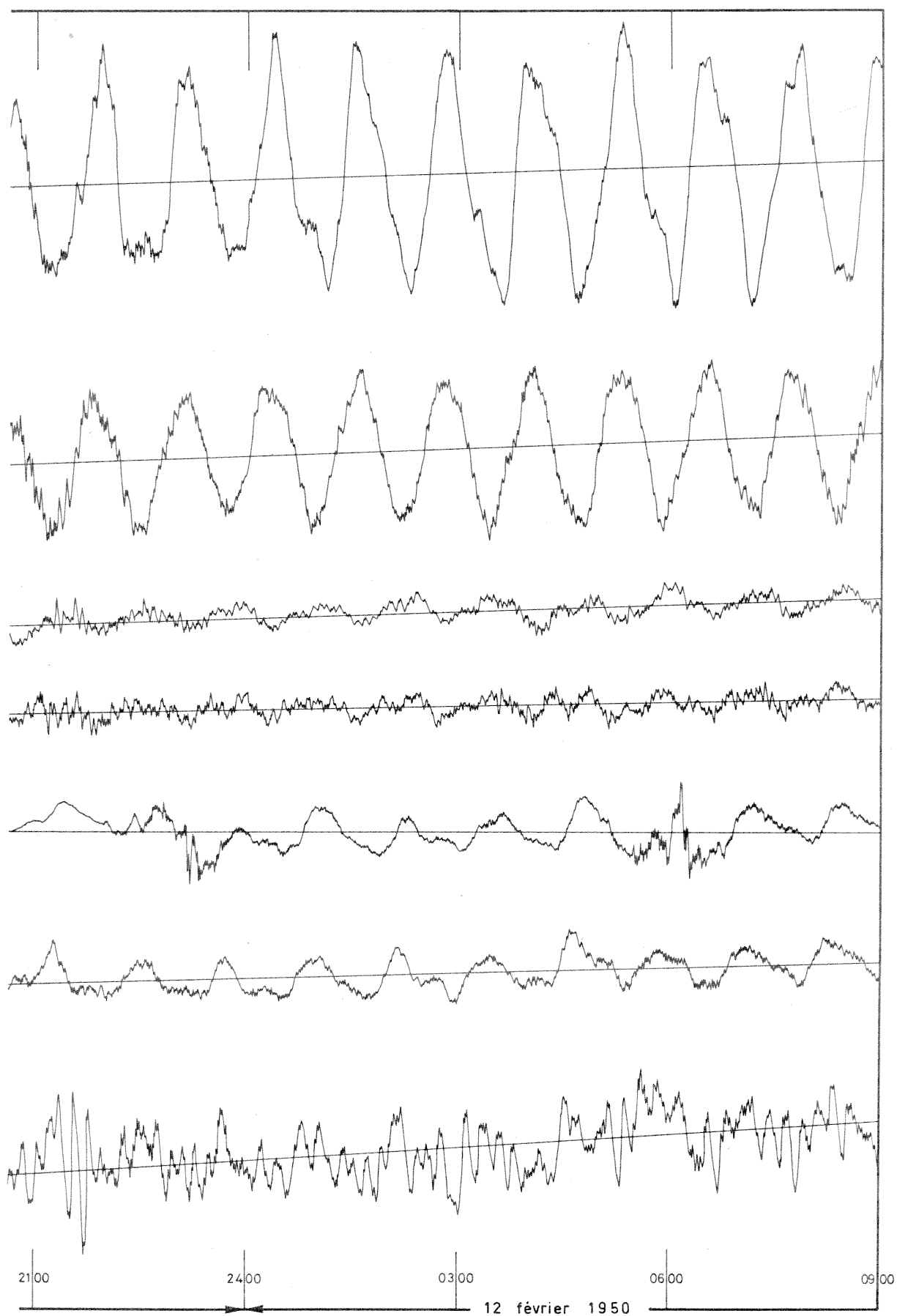
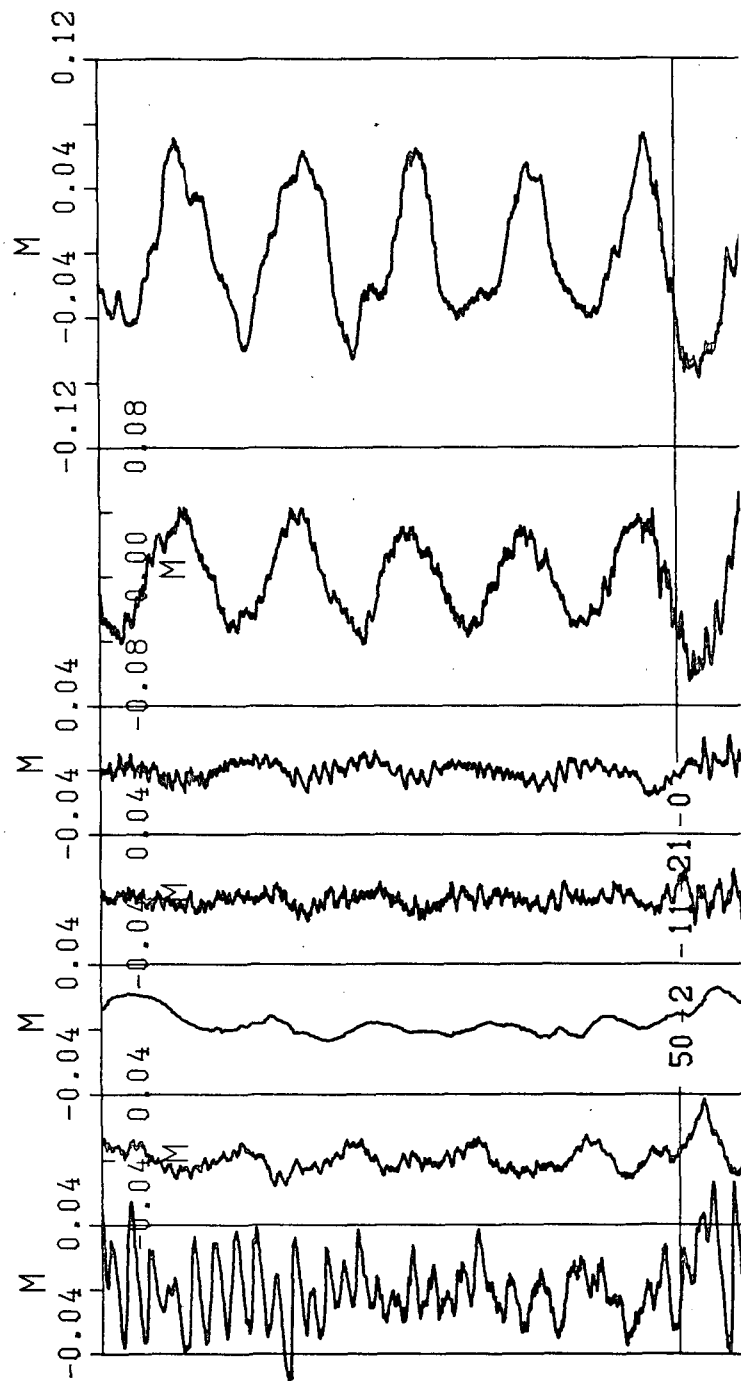
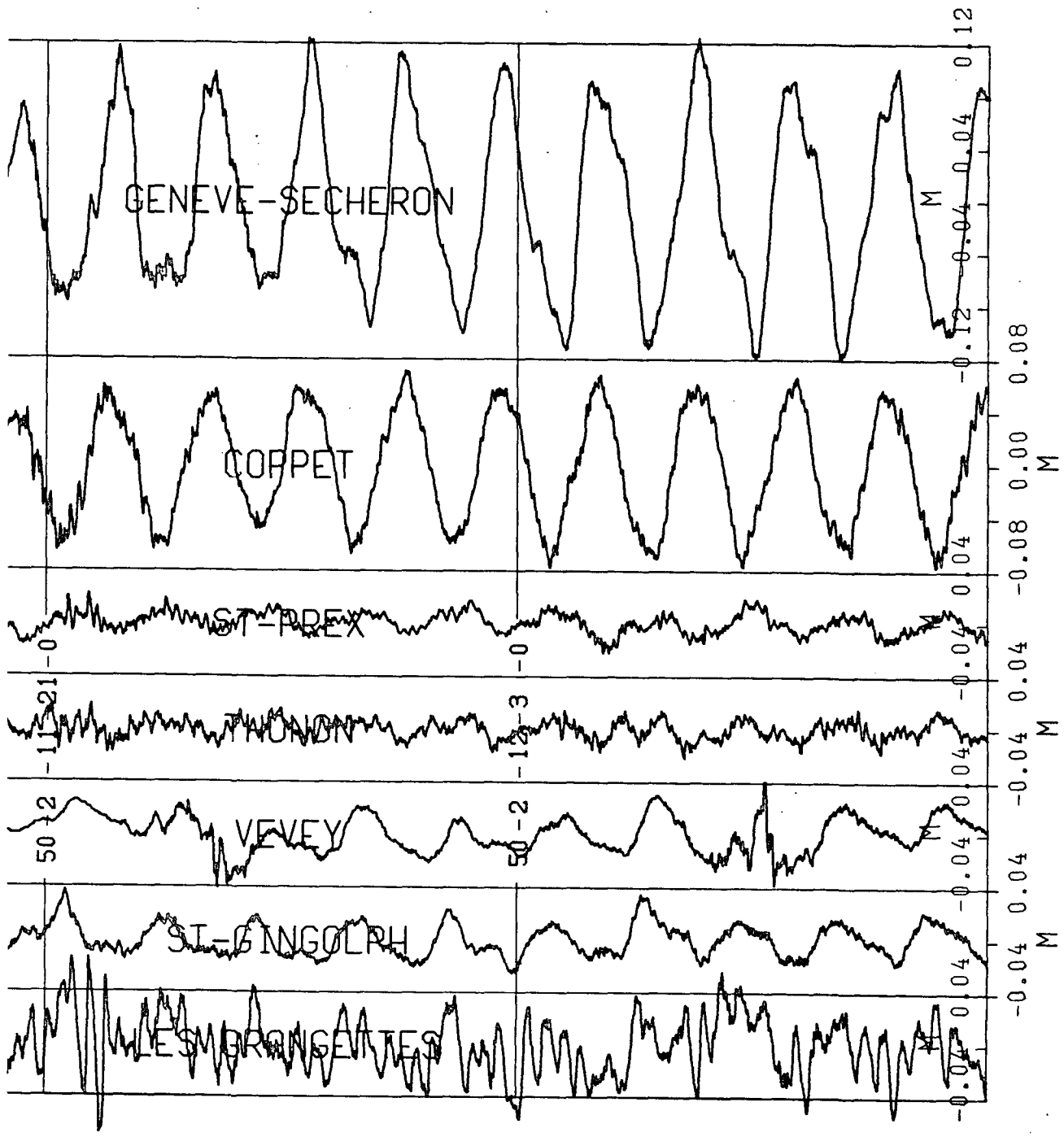


Figure 73:

Trace of data digitized from Figure 32 with removed trends, ready for spectral analysis





frequency that can be produced is exactly that of the Nyquist frequency, the problem of aliasing does not exist in the spectral analysis of outputs from mathematical models as long as the time step, Δt , of the spectral analysis is smaller, or, at the limit, equal to the time step of the mathematical simulation. In the case of the observations shown in Figure 32, the period of 1 minute corresponding to the Nyquist frequency corresponds to 0,5 mm in its original size (1 hour = 3 cm). Visual inspection of Figure 32 (in its original size) showed that nowhere are there fluctuations with a period less than 0,5 mm. Consequently, neither in the analysis of the simulated data, nor in the analysis of the observations will aliasing occur if a time step of $\Delta t = 30$ seconds is used in the spectral analysis.

5.6.3.1 Preparation of data for spectral analysis

In order to perform a numerical spectral analysis, a series of discrete numbers representing the phenomenon to be analysed is required. In the case of the simulation results, this requirement is automatically fulfilled if the model output is specified to be digital. The observations shown in Figure 32 however had to be digitized first. The traces shown in Figure 32 were thus digitized with the aid of a coordinatograph of the Service fédéral des eaux, Berne, whereby each point of change of curvature was digitized resulting in about 1300 points per trace. The digitized data were then drawn by the plotter of the computer of the EPFL as shown in Figure 72. Comparing Figures 32 and 72 one may observe the excellent agreement between the two figures. While drawing the traces shown in Figure 72, least square trend lines were also computed and drawn. Following Mortimer and Fee (1976) trends and means were then removed from each data set as a next step. Finally, values every 30 seconds (corresponding to 0,25 mm on the trace in its original size) were computed by linear interpolation between all points of change of curvature resulting in the traces shown in Figure 73. It should be noted that Figures 32, 72 and 73 have all been re-

produced on the same scale.

5.6.3.2 Spectral analysis

In order to perform spectral analysis a program SPECTR was developed by the author using a subroutine FFT (Fast Fourier Transform) given by Kunt and Coulon (1974). While the FFT algorithm is very fast when compared with conventional Fourier analysis, one disadvantage is however that the total number of points used for analysis must be equal to a power of 2.

Using a time step of $\Delta t = 30$ sec in the present analysis, frequencies will be meaningful only between 0 and 1 cycle/minute. Spectra were thus computed for this range, i.e., 0 - 1440 cycles/day. From these spectra it was found that frequencies higher than about 150 cycles/day contain negligible energy. This can be seen in Figure 74, where two such spectra are shown as an example. Consequently, all further spectra were restricted to the range of 0 - 150 cycles/day. Spectra were computed for all stations that are shown on both, Figures 32 and 70, i.e., Geneva, Coppet, St-Prex, Vevey, St-Gingolph and Thonon. From Figure 30 it can be seen that this selection covers the entire border of the Léman. Also computed were spectra for the observations of Les Grangettes. It has been stated that the quality of a spectrum depends on the number of points that are available for analysis. For comparison it is thus desirable to use spectra that have been calculated from the same number of points. Considering the number of points available for analysis, it should be noted that the digitized 18 hour observations shown in Figure 73 consist of 2160 points each. On the other hand, the 2 day simulations shown in Figure 70 consist of 5760 points each. Furthermore, the first hour of the simulations is not a free oscillation since it is during this time that the wind blows and creates the subsequent oscillations. Spectra were thus calculated for the observations of the first 2048 (i.e., 2^{11}) points resulting in the time between 11 February 1950, 15 hours and 12 February 1950, 8 hours 3 minutes. For the simulations, two

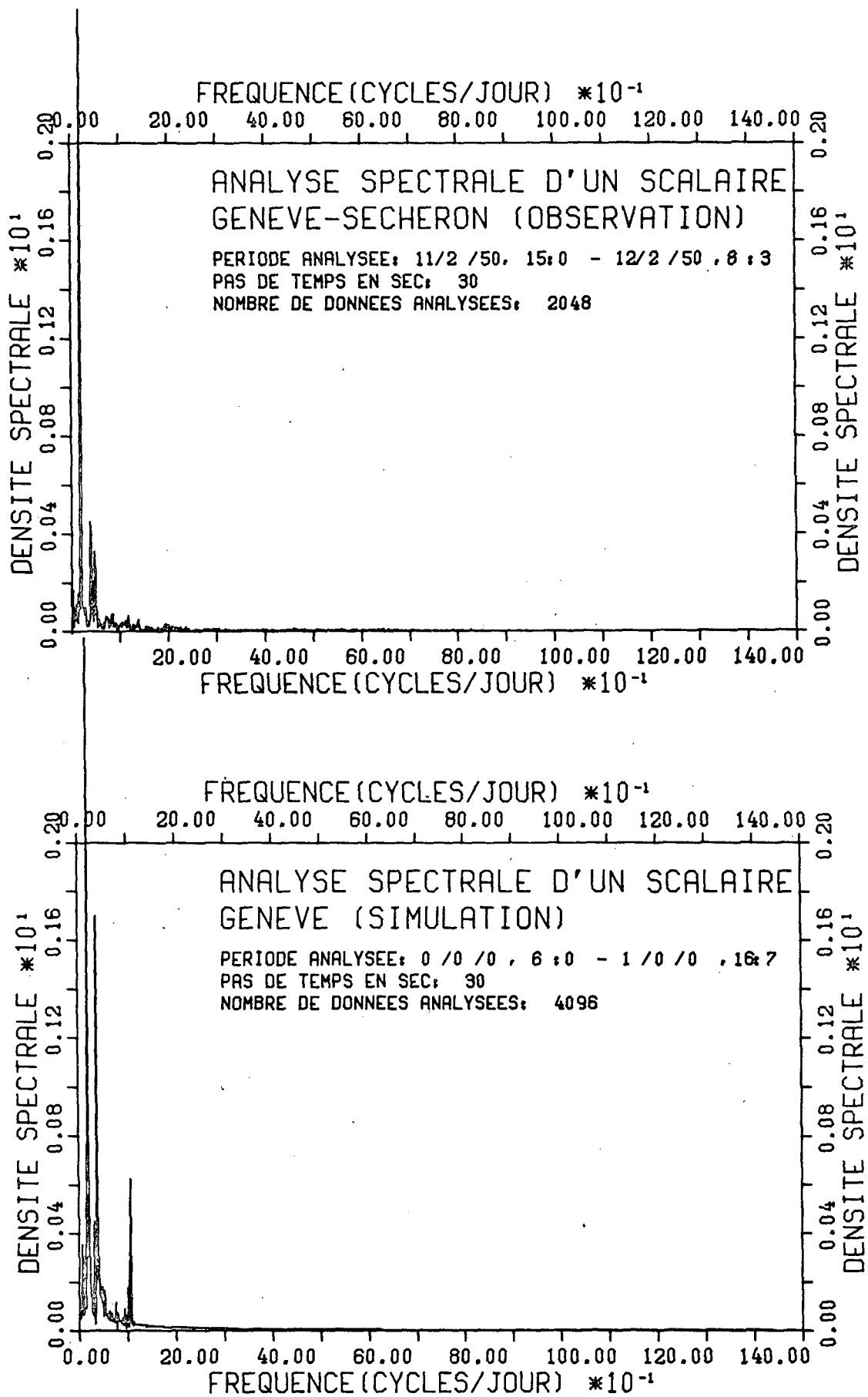


Figure 74: Spectra for the observations and simulations at Geneva for the range of 0 - 1440 cycles/day

2048 point spectra were computed each time: the first, for the time between 6 hours and 23 hours 3 minutes and the second, for the time between 1 day 0 hours and 1 day 17 hours 3 minutes. In this way the first of the two 2048 point spectra started only 5 hours after cessation of the wind, thus guaranteeing analysis of free oscillations. As will be seen, the two 2048 point spectra of the simulations were by no means identical. Finally, 4096 (i.e., 2^{12}) point spectra for the time period between 0 days 6 hours and 1 day 16 hours 7 minutes were computed to obtain more of the information contained in the simulations shown in Figure 70. These spectra are shown in Figure 75 whereby each column shows the spectra of one station. The topmost spectrum is always that of the observations, followed by the two 2048 point spectra of the simulations and, at the bottom, by the 4096 point spectra of the simulations. The scales used in the spectra were always the same. The arrangement of the spectra in columns for each station is for easy comparison of the frequency peaks.

It has been mentioned in § 5.6.2 that the observed seiches shown in Figure 32 and the simulated seiches shown in Figure 70 have similar amplitudes leading to the assumption that the observed seiches were probably created by a wind of the same order of magnitude, i.e., 75 km/h, as the one used for the simulations of the seiches. Comparing the 2048 point spectra of the observations with the 2048 point spectra of the simulations shown in Figure 75, one finds that here too, the amplitudes are, in general, within the same order of magnitude, thus confirming the earlier statement. In practically all spectra, the highest peak is found at a frequency of about 19,6 cycles/day (i.e., a period of 73,5 minutes). In the following discussion, frequencies are always in cycles/day with the period in minutes indicated in parentheses.

Considering first in more detail the spectra of Geneva, one finds that the observations contain three principal frequencies: 19,6 (73,5), 39,2 (36,7) and 48,0 (30,0). The first two fre-

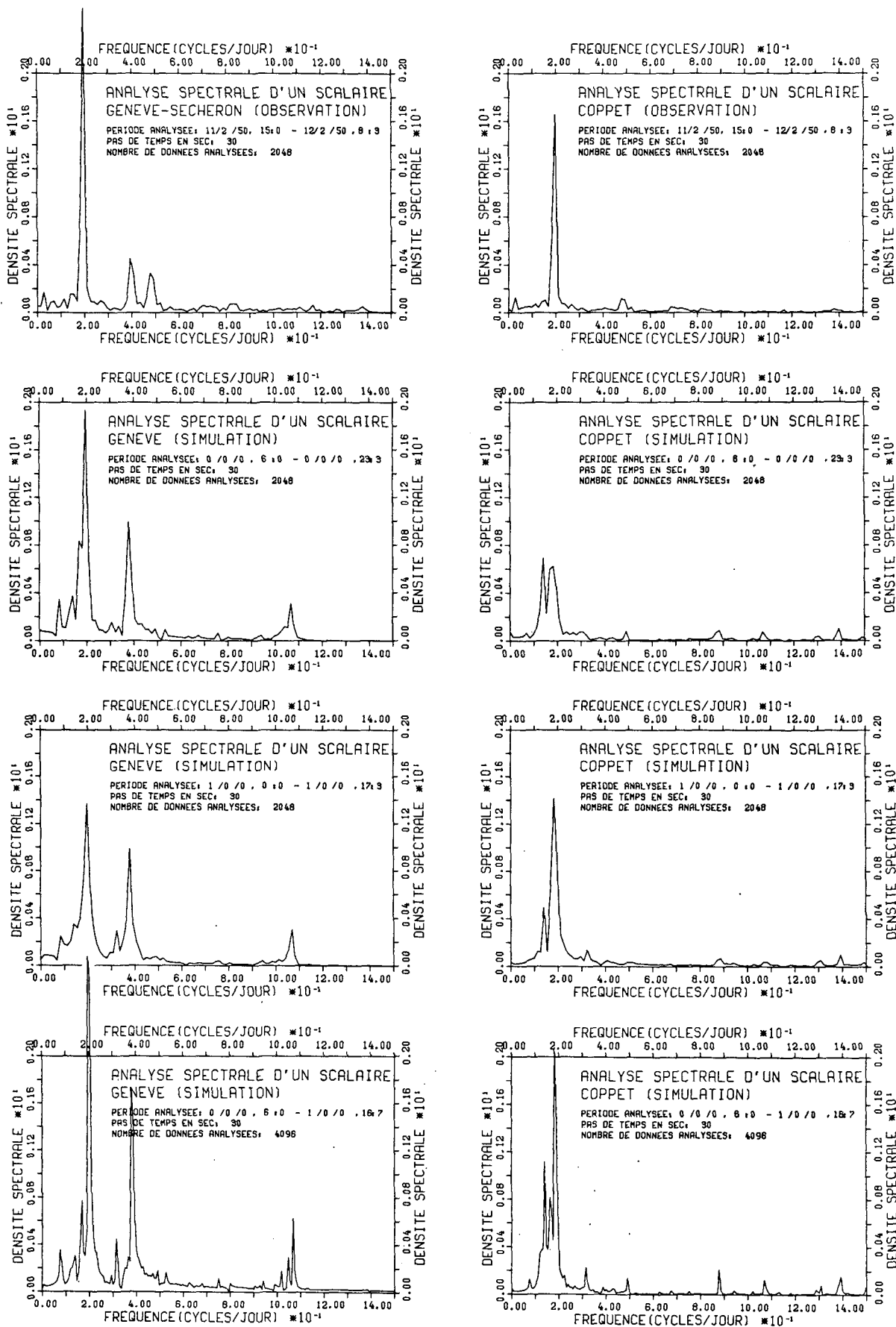


Figure 75: Spectra of observations and simulations for the stations Geneva, Coppet, St-Prex, Vevey, St-Gingolph and Thonon

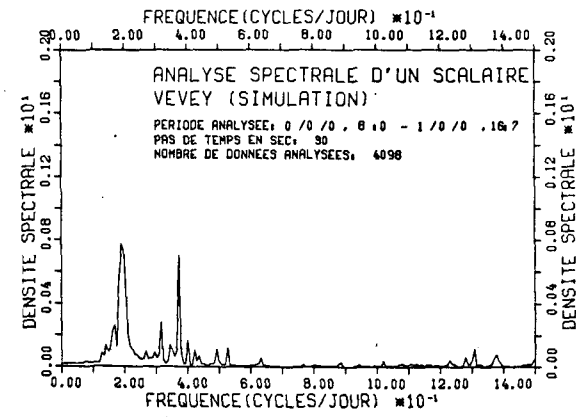
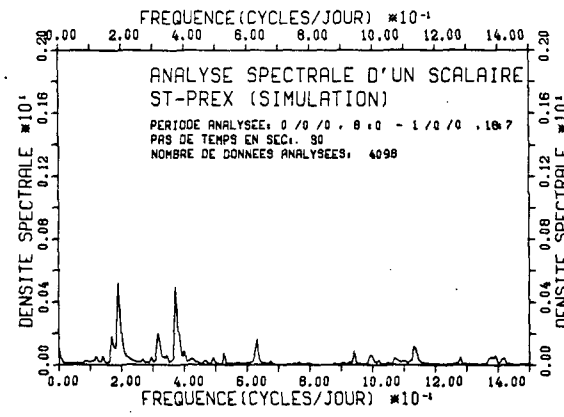
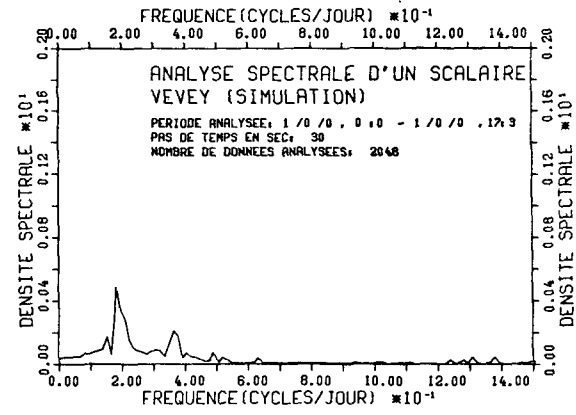
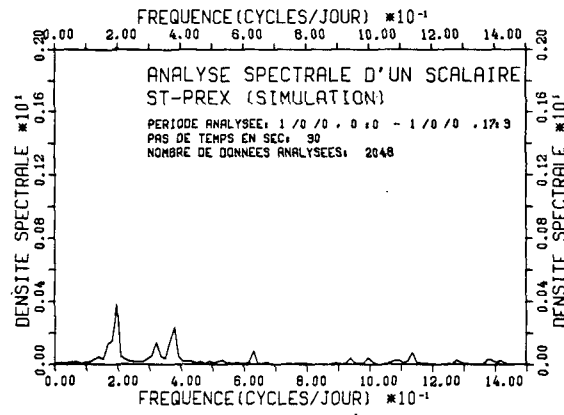
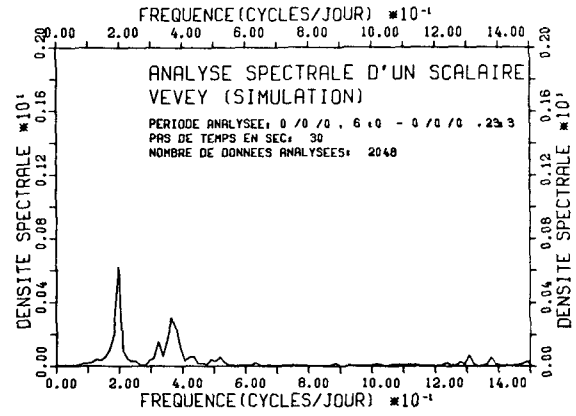
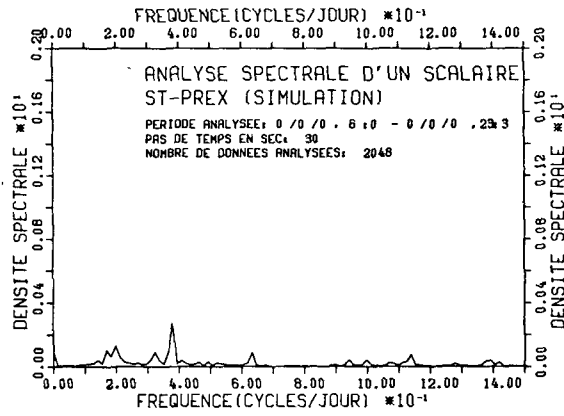
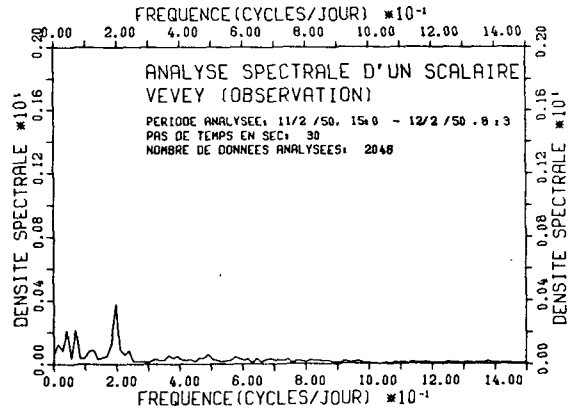
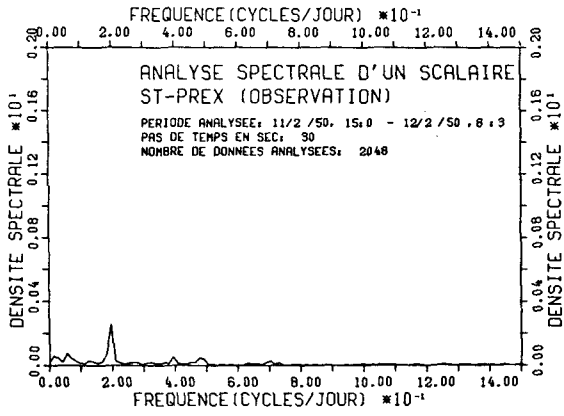


Figure 75: continued

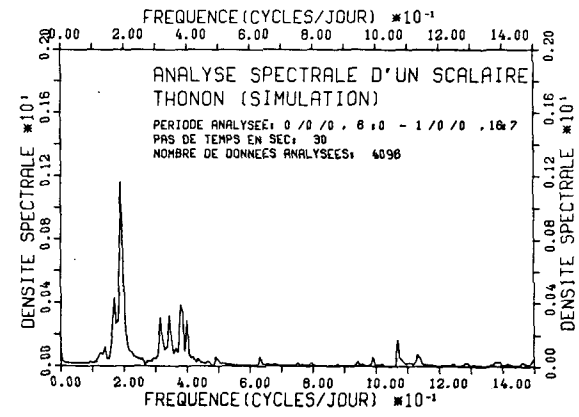
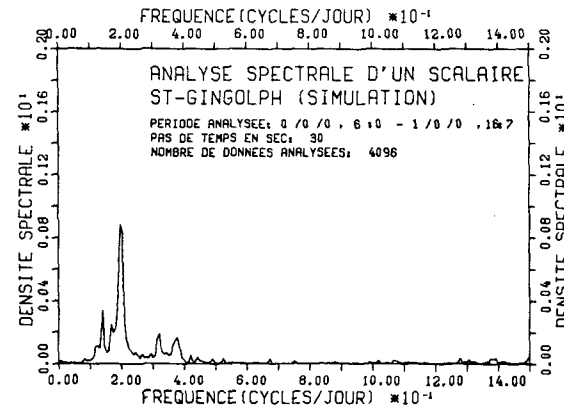
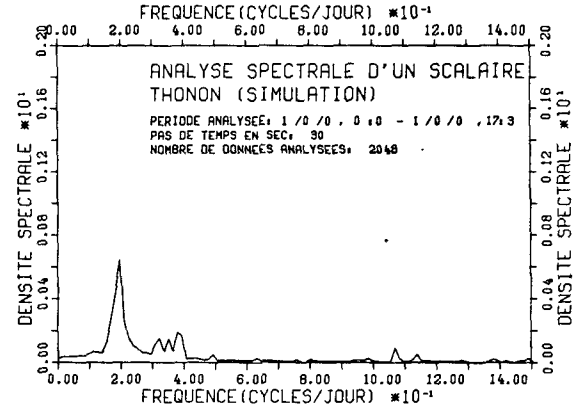
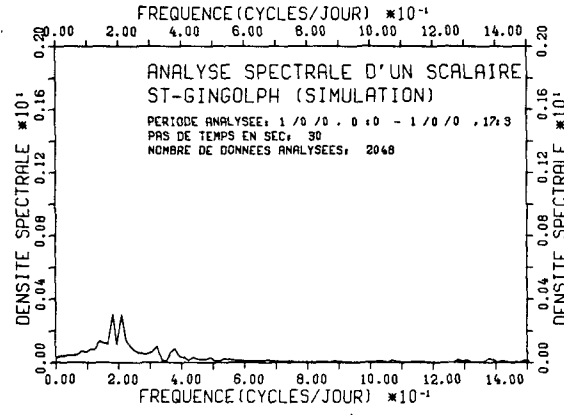
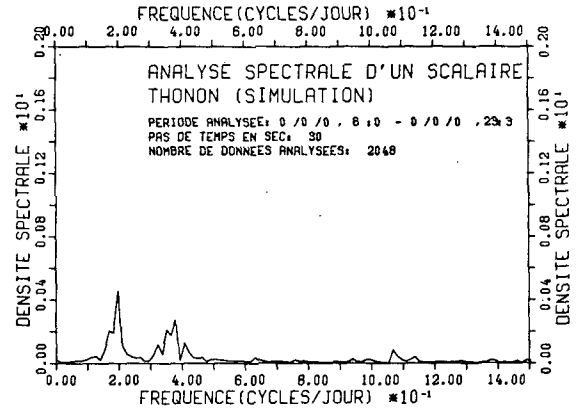
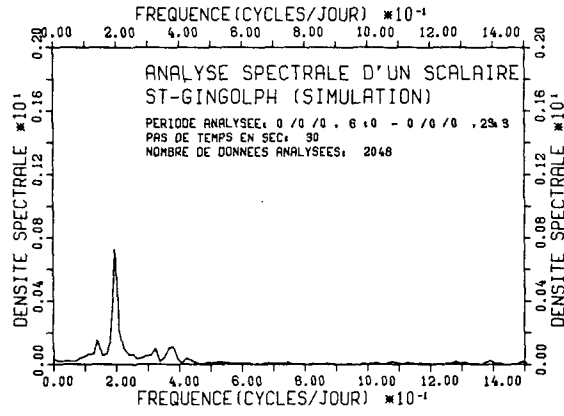
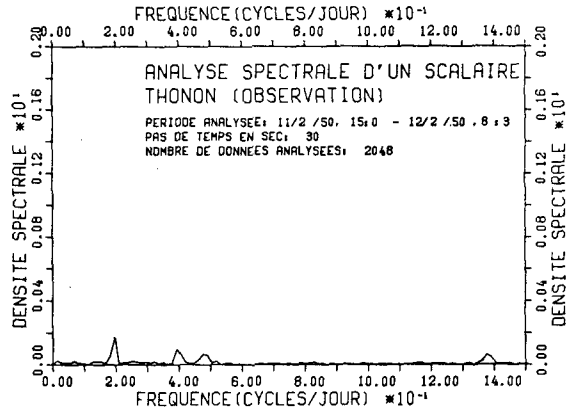
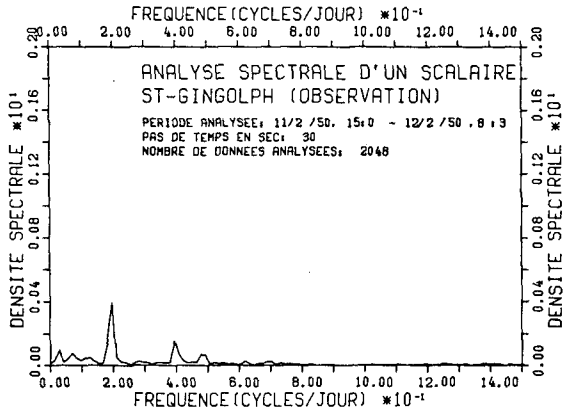


Figure 75: continued

quencies also appear very well in the spectra of the simulations. The third observed frequency however seems to be less well simulated. In the spectra of the simulations for Geneva one finds, on the other hand, another prominent spectral peak near 106,7 (13,5) which does not exist on the spectrum of the Geneva observations.

The spectrum of the observations at Coppet shows two of the Geneva-observation frequencies, i.e., 19,6 (73,5) and 48,0 (30,0). The 39,2 (36,7) frequency of the Geneva observations no longer occurs at Coppet. In the simulation spectra for Coppet the above two frequencies 19,6 (73,5) and 48,0 (30,0) can also be distinguished even though other frequencies appear as well.

In the spectra of St-Prex and Vevey, the 19,6 (73,5) frequency appears again in all spectra, i.e., for the observations and for the simulations. The 39,2 (36,7) frequency peak, although distinguishable in the spectra for the observations, is much more prominent in the spectra for the simulations. Again, a series of higher frequencies appear in the simulation spectra that do not clearly correspond to peaks in the observation spectra.

In the spectra of the St-Gingolph and Thonon observations, the same frequencies as at Geneva can be distinguished: 19,6 (73,5), 39,2 (36,7) and 48,0 (30,0). At the Thonon observation spectra a frequency peak near 138,5 (10,4) can also be noted. All these peaks can be found in the spectra for the simulations, although again, the simulation spectra display a series of further spectral peaks not visible in the observation spectra.

In § 4.3 it has been stated that the observations of Les Grangettes seem to display characteristics which are very different when compared with all other observations. The Service fédéral des eaux (1954) attributes this to some interaction with the mouth of the Rhone. In Figure 76, a spectrum of the observations at Les Grangettes is shown. There it can be seen that even

though the principal frequencies of 19,6 (73,5), 39,2 (36,7) and 48,0 (30,0) are well defined, a large number of other important peaks can be distinguished, confirming the unusual behaviour of this station. Earlier simulations showed that the behaviour at Les Grangettes is very similar to that of St-Gingolph which is to be expected since, in the present model no river mouth of the Rhone is included. In view of this observation, no special spectral analysis for the simulations at Les Grangettes has been performed.

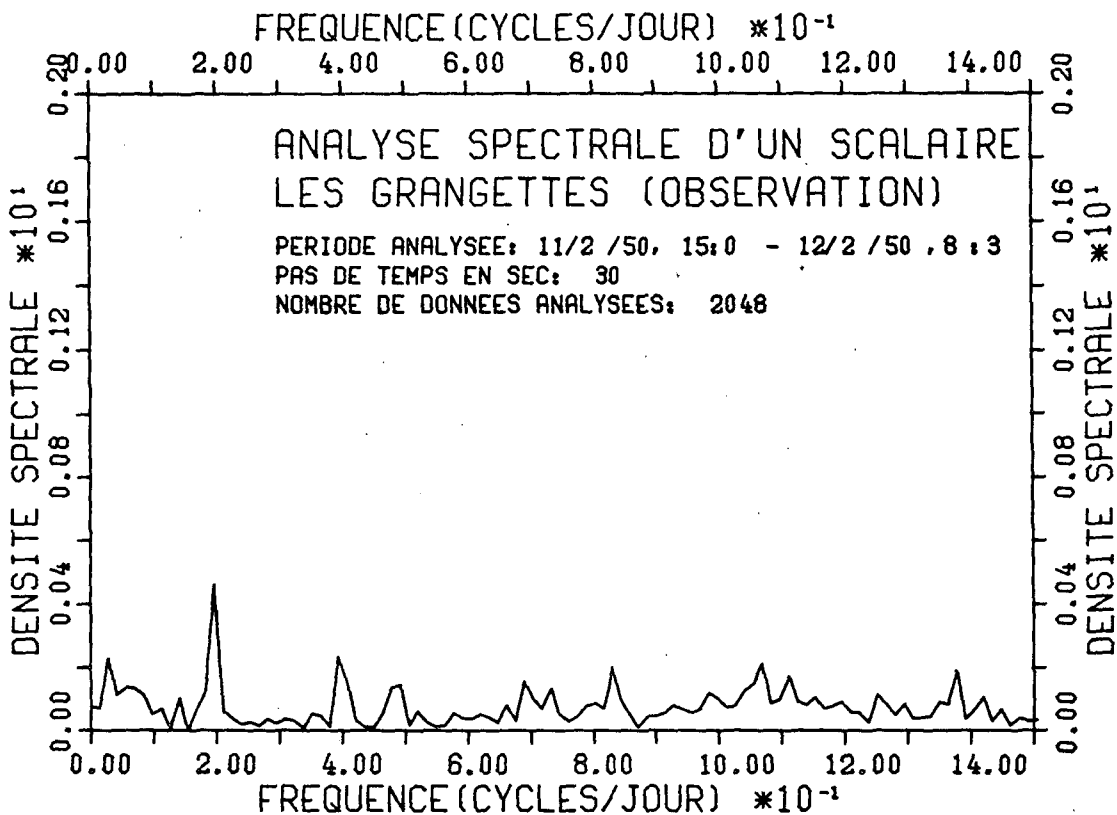


Figure 76: Spectrum for observations at Les Grangettes

Concluding, it can be stated that the present model simulates satisfactorily the first three order fluctuations in the Léman whereby the frequency of 19,6 cycles/day of the first order oscillations corresponds well with earlier theoretical work and observations yielding periods of about 73,5-74,5 minutes.

The second and third order oscillations identified in the spectra of the observations also agree well in frequency with those of the simulations even though their agreement with earlier work might be less good. Higher order fluctuations visible in the simulation spectra do not readily correspond to observed frequencies and are probably due to the choice of time step in the simulations in conjunction with the mesh-characteristics of the irregular finite-difference grid used for the geometric representation of the Léman.

6. Summary and conclusions

A three-dimensional mathematical model for simulation of unsteady currents and water level fluctuations in a homogeneous lake has been developed. Applying linearized, hydrodynamic equations, simulation can be performed for vertically-integrated velocity fields or in a lake that has been subdivided into horizontal layers. The numerical solution is achieved using the Thacker irregular-grid finite-difference scheme, thus combining the advantages of a smooth geometrical representation associated with finite element methods with the fast numerical execution associated with classical finite difference schemes. Also developed were a series of programs and routines providing graphical output in the form of analog traces of water level elevations and currents, in the form of three-dimensional snapshot-like images of the entire lake water surface and the entire velocity vector field and in the form of animated, computer-drawn films showing the changes of the entire moving water surface and of its associated velocity vector field.

The operation of the above programs and procedures has been demonstrated first using a completely irregular grid of 46 points representing a hypothetical test lake. Execution of the model in a one- and a three-layer formulation demonstrated that the simulation results for both formulations are very similar. From these runs it was also found that the system is unstable unless

a smoothing procedure resulting in a strong damping of all motions is introduced. Another result from these runs was that the response of a lake to wind shear stress is quasi-immediate, a fact that could be confirmed by data collected in the Léman by LHYDREP (Graf et al; 1979).

After a literature review on earlier work on water level fluctuations in the Léman, a coarse, irregular grid consisting of only 52 points was established. Using this grid, it was found that water level elevations of the Léman observed during $2\frac{1}{2}$ days could be well simulated with a wind shear stress coefficient of $c_w = 0,003$. Similarly, simulated period, position of node, and ratio of elevations at the extremities of the basin for unimodal seiches, agreed well with earlier observations and with other theoretical work. Those simulations also disclosed that the intersection of the equilibrium water surface and the water surface produced during times of wind set-up, i.e., the wind forced phase, does not coincide with the node of the subsequent free oscillation, i.e., the unimodal longitudinal seiche. Previously published observations confirm this simulation result.

However, because of the strong damping required to stabilize the system, simulation with the coarse irregular grid was not able to reproduce satisfactorily the long persistence (small damping) of the observed seiches. Since it is known from the literature that conventional finite difference schemes do not exhibit this problem, various grid configurations were investigated; and it was found that instabilities are largely associated with the irregularities of a completely irregular grid. Using regular grids with quadratic- and regular-hexagonal mesh, stability was achieved with only slight smoothing and instabilities occurred only if smoothing was totally eliminated. Using grids with flat and irregular bottoms, it was also discovered that discrete seiches exist only if the bottom geometry of a lake is irregular.

Finally, a "smoothed-irregular" grid consisting of 152 points was constructed to fit the Léman basin such that each interior grid point, i.e., each point not situated on the lake boundary, was centrally located with respect to all its surrounding points. This grid behaved identically to the above regular grids. Since excessive smoothing is no longer necessary with this grid, it was possible to simulate seiches of long duration for stations situated around the Léman basin. The simulations satisfactorily reproduced the periods, amplitudes, and much of the detailed structure observed in real Léman seiches (see in particular Figures 70 and 75).

In conclusion, it can be stated that the irregular finite difference model satisfactorily permits simulation of water surface elevations. Because of the "transparent" mathematical structure of this model further features may be easily introduced, for example: non-linear terms; spatially variable wind stress; eddy viscosity varying with velocity; and density stratification. Such additions to the model however should only be made if really justified, since they also require more time for execution.

Appendix*

Derivation of equation 28

In this appendix equation 28 will be derived under the assumption that all velocities have been integrated over the entire depth of the lake, that the eddy viscosity is zero and that the velocities associated with the Coriolis parameter are, in the finite difference approximation, replaced by the means of the past and the future time levels. Equations 8, 9 and 12 become thus:

* This appendix based on a derivation by W.C. Thacker (personal communication, 1979) has been prepared by the author with the support of Y. Depeursinge and Y. Jaccard of the Department of Mathematics of the EPFL.

$$\begin{aligned}
 \frac{\partial U}{\partial t} + gD \frac{\partial H}{\partial x} - fV &= 0 \\
 \frac{\partial V}{\partial t} + gD \frac{\partial H}{\partial y} + fU &= 0 \\
 \frac{\partial H}{\partial t} + \frac{\partial U}{\partial x} + \frac{\partial V}{\partial y} &= 0
 \end{aligned}
 \tag{A1}$$

In finite differences and using a "leap-frog" scheme, equations A1 become, with the above assumptions

$$\begin{aligned}
 \frac{1}{\Delta t} (U^{n+\frac{1}{2}} - U^{n-\frac{1}{2}}) + gD \left(\frac{\partial H}{\partial x} \right)^n - \frac{f}{2} (V^{n+\frac{1}{2}} + V^{n-\frac{1}{2}}) &= 0 \\
 \frac{1}{\Delta t} (V^{n+\frac{1}{2}} - V^{n-\frac{1}{2}}) + gD \left(\frac{\partial H}{\partial y} \right)^n + \frac{f}{2} (U^{n+\frac{1}{2}} + U^{n-\frac{1}{2}}) &= 0 \\
 \frac{1}{\Delta t} (H^{n+1} - H^n) + \left(\frac{\partial U}{\partial x} + \frac{\partial V}{\partial y} \right)^{n+\frac{1}{2}} &= 0
 \end{aligned}
 \tag{A2}$$

In a lake of infinite size and constant depth, which is represented by a uniform mesh, it can be assumed that in the solution of equations A2 the variables U , V and H vary in space and in time, like

$$\exp[i(\vec{k}\vec{x} - \omega t)] \tag{A3}$$

with the amplitudes R_U , R_V and R_H . In expression A3, \vec{k} is a wave vector with the components k_x and k_y in the x and y directions respectively and ω is the frequency of a wave.

Evaluating the individual terms of equations A2 with the aid of expression A3 one finds:

$$\begin{aligned}
 U^{n+\frac{1}{2}} &= R_U e^{i[\vec{k}\vec{x} - \omega(t+\Delta t/2)]} = R_U e^{i(\vec{k}\vec{x} - \omega t)} e^{-i\omega\Delta t/2} \\
 U^{n-\frac{1}{2}} &= R_U e^{i[\vec{k}\vec{x} - \omega(t-\Delta t/2)]} = R_U e^{i(\vec{k}\vec{x} - \omega t)} e^{+i\omega\Delta t/2}
 \end{aligned}$$

and

$$\frac{1}{\Delta t}(U^{n+\frac{1}{2}} - U^{n-\frac{1}{2}}) = \frac{R_U}{\Delta t} e^{i(\vec{k}\vec{x} - \omega t)} (e^{-i\omega\Delta t/2} - e^{+i\omega\Delta t/2}),$$

or with $\sin z = \frac{e^{zi} - e^{-zi}}{2i}$

$$\frac{1}{\Delta t}(U^{n+\frac{1}{2}} - U^{n-\frac{1}{2}}) = \frac{R_U}{\Delta t} e^{i(\vec{k}\vec{x} - \omega t)} [-2i \sin \frac{\omega\Delta t}{2}] \quad (\text{A4})$$

Similarly

$$\frac{1}{\Delta t}(V^{n+\frac{1}{2}} - V^{n-\frac{1}{2}}) = \frac{R_V}{\Delta t} e^{i(\vec{k}\vec{x} - \omega t)} [-2i \sin \frac{\omega\Delta t}{2}] \quad (\text{A5})$$

The terms associated with the Coriolis parameter can be evaluated as follows:

$$\frac{f}{2}(U^{n+\frac{1}{2}} + U^{n-\frac{1}{2}}) = \frac{fR_U}{2} e^{i(\vec{k}\vec{x} - \omega t)} (e^{-i\omega\Delta t/2} + e^{+i\omega\Delta t/2}),$$

or with $\cos z = \frac{e^{zi} + e^{-zi}}{2}$

$$\frac{f}{2}(U^{n+\frac{1}{2}} + U^{n-\frac{1}{2}}) = fR_U e^{i(\vec{k}\vec{x} - \omega t)} [\cos \frac{\omega\Delta t}{2}] \quad (\text{A6})$$

Similarly

$$\frac{f}{2}(V^{n+\frac{1}{2}} + V^{n-\frac{1}{2}}) = fR_V e^{i(\vec{k}\vec{x} - \omega t)} [\cos \frac{\omega\Delta t}{2}] \quad (\text{A7})$$

The analysis of $\frac{1}{\Delta t}(H^{n+1} - H^n)$ may be done as follows:

$$\begin{aligned} \frac{1}{\Delta t}(H^{n+1} - H^n) &= \frac{R_H}{\Delta t} [e^{i[\vec{k}\vec{x} - \omega(t + \Delta t)]} - e^{i(\vec{k}\vec{x} - \omega t)}] \\ &= \frac{R_H}{\Delta t} e^{i(\vec{k}\vec{x} - \omega t)} [e^{-i\omega\Delta t} - 1] \\ &= \frac{R_H}{\Delta t} e^{i(\vec{k}\vec{x} - \omega t)} e^{-i\omega\Delta t/2} [e^{-i\omega\Delta t/2} - e^{+i\omega\Delta t/2}] \\ &= \frac{R_H}{\Delta t} e^{i[\vec{k}\vec{x} - \omega(t + \Delta t/2)]} (e^{-i\omega\Delta t/2} - e^{+i\omega\Delta t/2}) \end{aligned}$$

Thus

$$\frac{1}{\Delta t}(H^{n+1} - H^n) = \frac{R_H}{\Delta t} e^{i[\vec{kx} - \omega(t+\Delta t/2)]} [-2i \sin \frac{\omega \Delta t}{2}] \quad (A8)$$

In order to evaluate the derivatives of equations A2 with respect to the x and y directions, the grid to be used must be known. If one assumes a rectangular grid with a mesh width of Δx and Δy respectively, these terms can be evaluated, whereby $(\partial H / \partial x)^n$ will be approximated by $(H^{x+\Delta x} - H^{x-\Delta x})^n / 2\Delta x$ and noting that $\vec{kx} = k_x x + k_y y$, as follows:

$$\begin{aligned} \left(\frac{H^{x+\Delta x} - H^{x-\Delta x}}{2\Delta x} \right)^n &= \frac{R_H (e^{i[k_x(x+\Delta x) + k_y y - \omega t]} - e^{i[k_x(x-\Delta x) + k_y y - \omega t]})}{2\Delta x} \\ &= \frac{R_H}{2\Delta x} e^{i[k_x x + k_y y - \omega t]} [e^{ik_x \Delta x} - e^{-ik_x \Delta x}] \\ &= \frac{R_H}{\Delta x} e^{i[\vec{kx} - \omega t]} [i \sin(k_x \Delta x)] \end{aligned}$$

or

$$\left(\frac{\partial H}{\partial x} \right)^n = i\alpha R_H e^{i[\vec{kx} - \omega t]} \quad (A9)$$

where

$$\alpha = \frac{1}{\Delta x} \sin(k_x \Delta x) \quad (A10)$$

Similarly

$$\left(\frac{\partial H}{\partial y} \right)^n = i\beta R_H e^{i[\vec{kx} - \omega t]} \quad (A11)$$

where

$$\beta = \frac{1}{\Delta y} \sin(k_y \Delta y) \quad (A12)$$

The velocity gradients become respectively

$$\left(\frac{\partial U}{\partial x}\right)^{n+\frac{1}{2}} = i\alpha R_U e^{i[\vec{k}\vec{x} - \omega(t + \Delta t/2)]} \quad (A13)$$

$$\left(\frac{\partial V}{\partial y}\right)^{n+\frac{1}{2}} = i\beta R_V e^{i[\vec{k}\vec{x} - \omega(t + \Delta t/2)]} \quad (A14)$$

Assigning

$$\phi(n) = e^{i[\vec{k}\vec{x} - \omega t]}$$

and

$$\phi(n + \frac{1}{2}) = e^{i[\vec{k}\vec{x} - \omega(t + \Delta t/2)]}$$

equations A2 become with equations A4-A14

$$\left. \begin{aligned} \phi(n) \left[-R_U \left(\frac{2i}{\Delta t} \sin \frac{\omega \Delta t}{2} \right) + R_H (gD\alpha) - R_V \left(f \cos \frac{\omega \Delta t}{2} \right) \right] &= 0 \\ \phi(n) \left[-R_V \left(\frac{2i}{\Delta t} \sin \frac{\omega \Delta t}{2} \right) + R_H (gD\beta) + R_U \left(f \cos \frac{\omega \Delta t}{2} \right) \right] &= 0 \\ \phi(n + \frac{1}{2}) \left[-R_H \left(\frac{2i}{\Delta t} \sin \frac{\omega \Delta t}{2} \right) + R_U (i\alpha) + R_V (i\beta) \right] &= 0 \end{aligned} \right\} (A15)$$

The system of equations A15 has a solution if and only if the determinant of the matrix of its coefficients vanishes:

$$\begin{vmatrix} -\frac{2i}{\Delta t} \sin \frac{\omega \Delta t}{2} & -f \cos \frac{\omega \Delta t}{2} & gD\alpha \\ f \cos \frac{\omega \Delta t}{2} & -\frac{2i}{\Delta t} \sin \frac{\omega \Delta t}{2} & gD\beta \\ i\alpha & i\beta & -\frac{2i}{\Delta t} \sin \frac{\omega \Delta t}{2} \end{vmatrix} = 0$$

Evaluating the above determinant gives

$$-\left(\frac{2}{\Delta t} \sin \frac{\omega \Delta t}{2}\right)^2 + gD(\alpha^2 + \beta^2) + f^2 \cos^2 \frac{\omega \Delta t}{2} = 0$$

and with $\sin^2 z + \cos^2 z = 1$

$$\cos^2 z = 1 - \sin^2 z$$

$$\left(\frac{2}{\Delta t} \sin \frac{\omega \Delta t}{2}\right)^2 - gD(\alpha^2 + \beta^2) - f^2(1 - \sin^2 \frac{\omega \Delta t}{2}) = 0$$

In an unsteady solution $\omega \neq 0$ and thus

$$\sin^2 \frac{\omega \Delta t}{2} = \frac{gD(\alpha^2 + \beta^2) + f^2}{\frac{4}{\Delta t^2} + f^2} \quad (\text{A16})$$

A stable solution of equations A2 corresponds to a solution of equation A16 that is real. This is the case if the square of the sine-function, on the left hand side of equation A16 varies between zero and unity:

$$0 \leq \frac{gD(\alpha^2 + \beta^2) + f^2}{\frac{4}{\Delta t^2} + f^2} \leq 1$$

or

$$gD(\alpha^2 + \beta^2) + f^2 \leq \frac{4}{\Delta t^2} + f^2 \quad (\text{A17})$$

It should be noted that in equation A17 the Coriolis term vanishes, thus resulting in

$$gD(\alpha^2 + \beta^2) \leq \frac{4}{\Delta t^2} \quad (\text{A18})$$

Assuming a quadratic grid with $\Delta = \Delta x = \Delta y$ one obtains from equations A10 and A12

$$\alpha^2 + \beta^2 = \frac{1}{\Delta^2} [\sin^2(k_x \Delta) + \sin^2(k_y \Delta)] \quad (\text{A19})$$

To determine the upper limit at which equation A18 is still satisfied, the maximum value of equation A19 must be found. Since the maximum value of the sine-function is unity,

$$(\alpha^2 + \beta^2)_{\max} = \frac{2}{\Delta^2}$$

With this equation A18 becomes

$$gD \frac{2}{\Delta^2} \leq \frac{4}{\Delta t^2}$$

or

$$\Delta t \leq \frac{\sqrt{2}}{\sqrt{gD}} \Delta \quad (\text{A20})$$

It should be noted that equation A20 is valid for a quadratic grid of mesh width Δ and that it has been derived for the system of equations A2 with the assumptions stated at the beginning of this paragraph.

If a scheme such as

$$\frac{1}{2\Delta t}(U^{n+1} - U^{n-1}) + gD \left(\frac{\partial H}{\partial x}\right)^n - \frac{f}{2}(V^{n+1} + V^{n-1}) = 0$$

$$\frac{1}{2\Delta t}(V^{n+1} - V^{n-1}) + gD \left(\frac{\partial H}{\partial y}\right)^n + \frac{f}{2}(U^{n+1} + U^{n-1}) = 0$$

$$\frac{1}{2\Delta t}(H^{n+1} - H^{n-1}) + \left(\frac{\partial U}{\partial x} + \frac{\partial V}{\partial y}\right)^n = 0$$

would have been used the result would have been

$$\Delta t \leq \frac{1}{\sqrt{2} \sqrt{gD}} \Delta$$

a result which is clearly more limiting than that of equation A20.

From the considerations so far it can be seen that up to equation A18 the geometry of the regular grid has been of no further consequence. Thus for any other regular grid the analysis will, with the exception of equations A10 and A12, be the same. The factors α and β , being associated with the form and the resolution of the finite-difference grid, occur only in spatial derivatives. As has been stated in § 2.4.2, these derivatives are, in the present irregular-grid finite-difference model, given by

$$\frac{\partial f}{\partial x} = \frac{\sum_{i=1}^N f_i (y_{i+1} - y_{i-1})}{\sum_{i=1}^N x_i (y_{i+1} - y_{i-1})} \quad (44)$$

$$\frac{\partial f}{\partial y} = \frac{\sum_{i=1}^N f_i (x_{i+1} - x_{i-1})}{\sum_{i=1}^N x_i (y_{i+1} - y_{i-1})} \quad (45)$$

where f is either U , V or H .

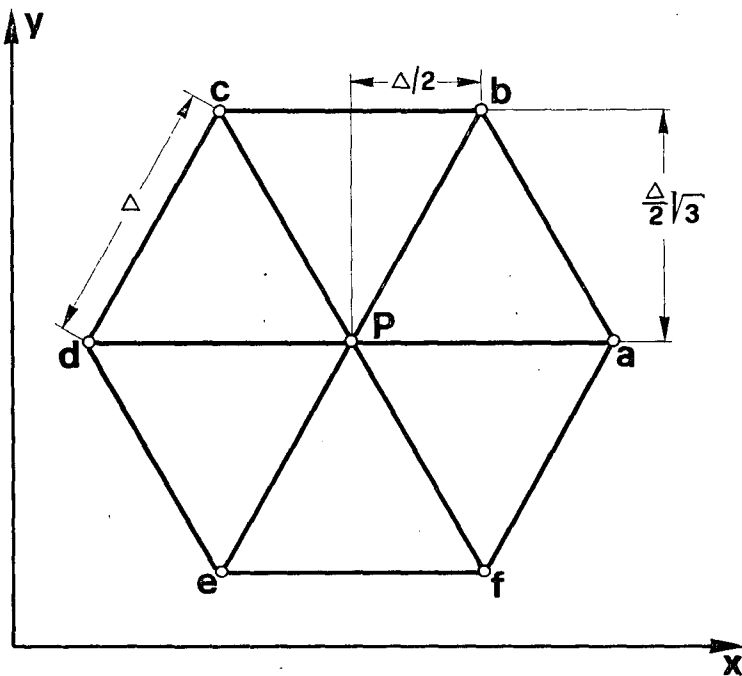


Figure A1:
Point P surrounded
by points a-f in
a regular triangu-
lar grid of
spacing Δ

For a point P , surrounded by a regular triangular grid as shown in Figure A1, equations 44 and 45 become respectively.

$$\frac{\partial f}{\partial x} = \frac{1}{6} \left[4 \frac{f_a - f_d}{x_a - x_d} + \frac{f_b - f_c}{x_b - x_c} + \frac{f_f - f_e}{x_f - x_e} \right] \quad (A21)$$

$$\frac{\partial f}{\partial y} = \frac{1}{2} \left[\frac{f_b - f_f}{y_b - y_f} + \frac{f_c - f_e}{y_c - y_e} \right] \quad (A22)$$

Neglecting for simplicity, in expression A3 the term ωt , the functions $f_a - f_f$ of equations A21 and A22 are given by:

$$\begin{aligned}
 f_a &= f e^{i[k_x(x + \Delta) + k_y y]} \\
 f_b &= f e^{i[k_x(x + \frac{\Delta}{2}) + k_y(y + \frac{\sqrt{3}}{2}\Delta)]} \\
 f_c &= f e^{i[k_x(x - \frac{\Delta}{2}) + k_y(y + \frac{\sqrt{3}}{2}\Delta)]} \\
 f_d &= f e^{i[k_x(x - \Delta) + k_y y]} \\
 f_e &= f e^{i[k_x(x - \frac{\Delta}{2}) + k_y(y - \frac{\sqrt{3}}{2}\Delta)]} \\
 f_f &= f e^{i[k_x(x + \frac{\Delta}{2}) + k_y(y - \frac{\sqrt{3}}{2}\Delta)]}
 \end{aligned}
 \tag{A23}$$

With equations A23 equation A21 becomes therefore

$$\begin{aligned}
 \frac{\partial f}{\partial x} &= \frac{f}{6} e^{i(k_x x + k_y y)} \left[\frac{4}{2\Delta} (e^{ik_x \Delta} - e^{-ik_x \Delta}) \right. \\
 &\quad \left. + \frac{1}{\Delta} e^{ik_y \frac{\sqrt{3}}{2} \Delta} (e^{ik_x \frac{\Delta}{2}} - e^{-ik_x \frac{\Delta}{2}}) + \frac{1}{\Delta} e^{-ik_y \frac{\sqrt{3}}{2} \Delta} (e^{ik_x \frac{\Delta}{2}} - e^{-ik_x \frac{\Delta}{2}}) \right]
 \end{aligned}$$

and

$$\frac{\partial f}{\partial x} = \frac{f}{6\Delta} e^{i(\vec{k} \cdot \vec{x})} \left[4i \sin(k_x \Delta) + 4i \sin(k_x \frac{\Delta}{2}) \cos(k_y \frac{\sqrt{3}}{2} \Delta) \right]$$

In analogy to equation A10, α_Δ becomes

$$\alpha_\Delta = \frac{2}{3\Delta} \left[\sin(k_x \Delta) + \sin(k_x \frac{\Delta}{2}) \cos(k_y \frac{\sqrt{3}}{2} \Delta) \right]$$

or with $\sin z = 2 \sin \frac{z}{2} \cos \frac{z}{2}$

$$\alpha_\Delta = \frac{2}{3\Delta} \left[2 \sin \frac{k_x \Delta}{2} \cos \frac{k_x \Delta}{2} + \sin \frac{k_x \Delta}{2} \cos \frac{k_y \sqrt{3}}{2} \Delta \right]$$

$$\alpha_\Delta = \frac{2}{3\Delta} \sin \frac{k_x \Delta}{2} \left(2 \cos \frac{k_x \Delta}{2} + \cos \frac{k_y \sqrt{3}}{2} \Delta \right)$$

(A24)

Equation A22 becomes similarly

$$\frac{\partial f}{\partial y} = \frac{f}{2\sqrt{3}\Delta} e^{i(k_x x + k_y y)} \left[e^{ik_x \frac{\Delta}{2}} \left(e^{ik_y \frac{\sqrt{3}\Delta}{2}} - e^{-ik_y \frac{\sqrt{3}\Delta}{2}} \right) + e^{-ik_x \frac{\Delta}{2}} \left(e^{ik_y \frac{\sqrt{3}\Delta}{2}} - e^{-ik_y \frac{\sqrt{3}\Delta}{2}} \right) \right]$$

$$\frac{\partial f}{\partial y} = \frac{f}{2\sqrt{3}\Delta} e^{i(k_x \vec{x} + k_y \vec{y})} \left[4i \cos \frac{k_x \Delta}{2} \sin \frac{k_y \sqrt{3}\Delta}{2} \right]$$

and again

$$\beta_{\Delta} = \frac{2}{\sqrt{3}\Delta} \left(\cos \frac{k_x \Delta}{2} \sin \frac{k_y \sqrt{3}\Delta}{2} \right) \quad (\text{A25})$$

Substituting equations A24 and A25 into equation A18 one obtains

$$gD \frac{1}{\Delta^2} \gamma \leq \frac{4}{\Delta t^2} \quad (\text{A26})$$

where

$$\gamma = \left[\frac{2}{3} \sin \frac{k_x \Delta}{2} \left(2 \cos \frac{k_x \Delta}{2} + \cos \frac{k_y \sqrt{3}\Delta}{2} \right) \right]^2 + \left[\frac{2}{\sqrt{3}} \left(\cos \frac{k_x \Delta}{2} \sin \frac{k_y \sqrt{3}\Delta}{2} \right) \right]^2$$

The maximum value of γ can be determined numerically

$$\gamma_{\max} = 1,376981137$$

with γ_{\max} equation A26 yields

$$\Delta t \leq \frac{1,704378316 \Delta}{\sqrt{gD}} \quad (\text{28})$$

In an analysis for finite difference equations where the Coriolis term is associated with the future time level only (equations 29-30), the f term no longer cancels as in equation A17 and the final result gives a time step at least as large

as that given by equation 28.

Concluding, it may be stated that there are two "varieties" of instabilities in the present model. The first variety of instability is created by the irregularity of a grid, the second is due to exceeding a maximum time step as given by equation 28 for a regular grid. Reasonably strong damping of the system however allows to stabilize the first type instability even though the grid is "irregular". This damping has little physical meaning and is of such an intensity that simulation of natural seiches as observed in the Léman becomes impossible. In § 5.5 it has been shown that this strong instability disappears to a very large degree when a "regular" grid is used. In § 5.6 it was seen that an "irregular" grid behaves similarly to a regular grid if all interior points of the grid are selected such that they are located in the center of the points surrounding them. Only for such a "smoothed-irregular" grid may the condition imposed by equation 28 be assumed to be a valid criterion for the choice of an upper limit of the time step, Δt , as a function of a particular grid. Thus, the time step used in § 5.6.2 of the present dissertation was already about one third of the one imposed as a maximum by equation 28. The criterion for this choice of time step was the intention to produce a smooth running animated film. In an irregular grid the time step must generally be selected to be much smaller than the one indicated by equation 28. In that case the time step must be the smaller the less smoothing is being done.

System of units

In the present dissertation, all equations are dimensionally homogeneous. Thus, any consistent system of units may be applied. The system used herein is the SI system, where the force is expressed in Newtons. Thus, according to Newton's second law,

$$N = \text{kg m/s}^2$$

N and kg m/s^2 can be used interchangeably.

In the following list of the major variables used in this work, the dimensions of some variables are indicated in terms of both sides of the above equation to permit an easy control over the dimensions in the equations of this dissertation.

List of symbols

dimensions

A_p :	surface area associated with point P	$[\text{m}^2]$
B :	length or width of lake	$[\text{m}]$
c_b :	bottom shear stress coefficient	$[-]$
c_w :	wind (top) shear stress coefficient	$[-]$
D :	depth of water	$[\text{m}]$
f :	Coriolis parameter or general function	$[1/\text{s}]$ $[]$
g :	acceleration of gravity	$[\text{m/s}^2]$
H :	water surface elevation	$[\text{m}]$
i :	subscript of surrounding point	$[-]$
j :	subscript of layer	$[-]$
\vec{k} :	wave vector as defined for equation A3	$[\text{m}]$
L :	thickness of layer	$[\text{m}]$
M :	number of layers	$[-]$
N :	number of points P_i , surrounding a point, P	$[-]$
n :	point in time in a series of discrete points in time or point in space	$[-]$
P :	point number	$[-]$
p :	pressure	$[\text{kg/m s}^2][\text{N/m}^2]$
R :	wave amplitudes as defined for equation A3	$[\text{m}, \text{m/s}]$
S :	length between successive lake cross-sections	$[\text{m}]$
T :	period of a seiche	$[\text{s}]$
t :	time	$[\text{s}]$

dimensions

U :	wind velocity in x direction	[m/s]
u :	volume transport per unit width in x direction	[m ² /s]
\bar{u} :	mean velocity in x direction	[m/s]
\tilde{u} :	water velocity in x direction	[m/s]
u_t :	component of vector \vec{v}_t in x direction	[m/s]
V :	wind velocity in y direction	[m/s]
\vec{V} :	wind velocity vector in general direction	[m/s]
V_p :	lake volume associated with a point P	[m ³]
v :	volume transport per unit width in y direction	[m ² /s]
\bar{v} :	mean velocity in y direction	[m/s]
\tilde{v} :	water velocity in y direction	[m/s]
v_t :	component of vector \vec{v}_t in y direction	[m/s]
\vec{v} :	water velocity vector in general direction	[m/s]
\vec{v}_t :	vector \vec{v} projected onto boundary tangent	[m/s]
\tilde{w} :	water velocity in the z direction	[m/s]
x :	distance from origin towards east	[m]
y :	distance from origin towards north	[m]
z :	distance from origin upwards	[m]
α :	weighting factor for α -mean	[-]
α_t :	angle of boundary tangent	[°]
β :	angle of wind or current direction	[°]
ϵ :	horizontal eddy viscosity	[kg/ms][Ns/m ²]
η :	vertical eddy viscosity	[kg/ms][Ns/m ²]
ρ :	density of water	[kg/m ³][Ns ² /m ⁴]
ρ_a :	density of air	[kg/m ³][Ns ² /m ⁴]
τ_x :	shear stress in the x direction	[N/m ²]
τ_y :	shear stress in the y direction	[N/m ²]
$\vec{\tau}$:	shear stress vector in general direction	[N/m ²]
$\star\tau$:	shear stress per unit mass of water	[m ² /s ²]
ω :	wave frequency as defined for equation A3	[1/s]

Literature

- Bauer, S.W., Graf, W.H. and Tischer, E. (1977), Les courants dans le Léman en saison froide. Une simulation mathématique, Bull. Techn. Suisse Romande, Vol. 103, No 19.
- Bauer, S.W. (1979), Three-dimensional simulation of time-dependent elevations and currents in a homogeneous lake of arbitrary shape using an irregular-grid finite difference model. In: Hydrodynamics of Lakes, ed. W.H. Graf and C.H. Mortimer, Elsevier Scientific Publishing Company, Amsterdam.
- Bauer, S.W. and Graf, W.H. (1979), Wind induced water circulation of Lake Geneva. In: Marine Forecasting, ed. J.C.J. Nihoul, Elsevier Scientific Publ. Comp., Amsterdam.
- Bauer, S.W. and Perrinjaquet, C. (1979), Data bank and visualization for sequential data with special reference to Lake Geneva. In: Hydrodynamics of Lakes, ed. W.H. Graf and C.H. Mortimer, Elsevier Scientific Publishing Company, Amsterdam.
- Bloomfield, P. (1976), Fourier Analysis of Time Series: An Introduction, John Wiley & Sons, New York.
- Boris, J.P., Hain, K.L. and Fritts, M.J. (1975), Free surface hydrodynamics using a Lagrangian triangular mesh, Proc., First Intern. Conf. Numerical Ship Hydrodynamics, David W. Taylor Naval Ship Research and Development Center.
- Boys, du P. (1891a), Sur le mouvement de balancement rythmé de l'eau des lacs (seiches), Cptes. R. Acad. Sc. Paris, Vol. 62, No 1202 (not seen: ref. Forel, 1895).
- Boys, du P. (1891b), Essai théorique sur les seiches, avec appendice par F.A. Forel, Arch. Genève, Vol. 25, No 628 (not seen: ref. Forel, 1895).
- Chrystal, J. (1904), Some results in the mathematical theory of seiches, Proc. Roy. Soc. Edin., Vol. 25.
- Chrystal, J. (1905), On the hydrodynamical theory of seiches, Trans. Roy. Soc. Edin., Vol. 41, Part 3, No 25.
- Crowley, W.P. (1971), FLAG: A Free-Lagrange Method for numerically simulating hydrodynamic flows in two dimensions, Proc., Second Intern. Conf. Numerical Methods in Fluid Dynamics, University of California, Berkeley, Springer-Verlag, Berlin.

- Defant, A. (1918), Neue Methode zur Ermittlung der Eigenschwingungen (Seiches) von abgeschlossenen Wassermassen (Seen, Buchten, usw.), Ann. Hydrogr. Berlin, Vol. 46 (not seen: ref. Mortimer, 1979).
- Defant, A. (1961), Physical Oceanography, Pergamon, London.
- Donelan, M.A. (1977), Are aquatic micrometeorologists delivering the goods or is the over-water drag coefficient far from constant? In: Symposium on Modelling Transport Mechanisms in Oceans and Lakes, Proc., Manuscript Rep. Series, No 43, Canada Centre of Inlandwaters, Burlington, Ontario.
- Doodson, A.T., Carey, R.M. and Baldwin, R. (1920), Theoretical determination of the longitudinal seiches of Lake Geneva, Trans. Roy. Soc. Edin., Vol. 52, Part 3, No 25.
- Elliott, A.J. (1976), A numerical model of the internal circulation in a branching tidal estuary, Chesapeake Bay Institute, The Johns Hopkins University, Ref. 76-7, Special Rep. 54.
- Fatio de Duillier, J.-C. (1730), Remarques sur l'histoire naturelle du lac de Genève. In: Spon, Histoire de Genève, Vol. 2, p. 463, Genève (not seen: ref. Forel, 1895).
- Forel, F.A. (1873), Etude sur les seiches du Lac Léman*, Bull. Soc. Vaud, Sc. Nat., Vol. 12.
- Forel, F.A. (1876a), La formule des seiches, C.R. Acad. Sci., Paris, Vol. 83.
- Forel, F.A. (1876b), Le limnimètre enregistreur de Morges, Arch. Genève, Vol. 61.
- Forel, F.A. (1897), Le problème de l'Europe, Compt. rend. Acad. Sci., Vol. 2.
- Forel, F.A. (1893), Die Schwankungen des Bodensees, translated into German by Eberhard Graf Zeppelin, Schr. Ver. Gesch. Bodensees, Vol. 22.
- Forel, F.A. (1895), Le Léman, Monographie Limnologique, Tome second, ed. F. Rouge, Librairie de l'Université, Lausanne.

* Due to a colloquial statement in Forel (1895) this paper is in the entire literature falsely referred to as "Première étude sur les seiches".

- Graf, W.H., Perrinjaquet, C., Bauer, S.W., Prost, J.P. and Girod H. (1979), Measuring on Lake Geneva (Le Léman). In: Hydrodynamics of Lakes, ed. W.H. Graf and C.H. Mortimer, Elsevier Scientific Publishing Company, Amsterdam.
- Graf, W.H. and Prost, J.-P. (1979), The aerodynamic drag; experiments on Lake Geneva. In: Hydrodynamics of Lakes, ed. W.H. Graf and C.H. Mortimer, Elsevier Scientific Publishing Company, Amsterdam.
- Hamblin, P.F. and Hollan, E. (1978), On the gravitational seiches of Lake Constance and their generation, Schweiz. Zeitschrift für Hydrologie, Vol. 40, No 1.
- Hansen, W. (1956), Theorie und Errechnung des Wasserstandes und der Strömungen in Randmeeren nebst Anwendung, Tellus, Vol. 8, No 3.
- Hutchinson, G.E. (1975), A Treatise on Limnology, Vol. 1, Part 1, John Wiley & Sons, Inc., New York.
- Kunt, M. and Coulon, de F. (1974), Principe et applications de la transformation de Fourier rapide, Bull. Techn. Suisse Romande, Vol. 100, No 8.
- Liggett, J.A. (1970), Cell method for computing lake circulation, Proc., Am. Soc. Civ. Eng., Vol. 96, No HY3.
- Lindijer, G.H.J. (1976), Three-dimensional circulation models for shallow lakes and seas, general formulation and stationary models, Report on Literature Study, Delft Hydraulics Laboratory, Report R 900 I, Delft.
- Merian, J.R. (1828), Ueber die Bewegung tropfbarer Flüssigkeiten in Gefässen, Basle (not seen: ref. Forel 1876a)
- Mortimer, C.H. (1953), The resonant response of stratified lakes to wind, Revue suisse d'hydrologie, Vol. 15, fasc. 1.
- Mortimer, C.H. (1963), Frontiers in physical limnology with particular reference to long waves in rotating basins, Proc., 6th Conf. Great Lakes Res., Pub. No 10, Great Lakes Res. Div., The University of Michigan.
- Mortimer, C.H. (1974), Lake hydrodynamics, Mitt. Intern. Verein. Limnol. Vol. 20, Stuttgart.
- Mortimer, C.H. (1979), Strategies for coupling of data collection and analysis with dynamic modelling of lake motions. In: Hydrodynamics of Lakes, ed. W.H. Graf and C.H. Mortimer, Elsevier Scientific Publishing Company, Amsterdam.

- Mortimer, C.H. and Fee, E.J. (1976), Free surface oscillations and tides of Lakes Michigan and Superior, Phil. Trans. Roy. Soc. London, Series A, Vol. 281.
- Neumann G. and Pierson, W.J. (1966), Principles of Physical Oceanography, Prentice-Hall Inc., Englewood Cliffs, N.J.
- Prost, J.-P., Bauer, S.W., Graf, W.H. and Girod, H. (1977), Campagne de mesure des courants dans le Léman, Bull. Techn. Suisse Romande, Vol. 103, No 19.
- Ramming, H.G. (1973), Reproduktion physikalischer Prozesse in Küstengebieten, Die Küste, Heft 22.
- Ramming, H.G. (1976), A nested North Sea model with fine resolution in shallow coastal rivers, Mém. Soc. Roy. Sc. de Liège, 6e série, tome X, 9-26.
- Ramming, H.G. (1978a), Numerical investigations of the influence of coastal structures upon the dynamic off-shore process by application of a nested tidal model. In Hydrodynamics of Estuaries and Fjords, ed. J.C.J. Nihoul, Elsevier Scientific Publishing Company, Amsterdam.
- Ramming, H.G. (1978b), The influence of river normalization on the distribution of tidal currents in the River Elbe. Recent results of a numerical model, Proc., International Harbor Congress, Vol. 2, Antwerp.
- Service fédéral des eaux (1954), Les dénivellations du Lac Léman, Département fédéral des postes et des chemins de fer, Berne.
- Simons, T.J. (1973), Development of three-dimensional numerical models of the Great Lakes, Canada Centre for Inland Waters, Scientific Series No 12, Burlington, Ontario.
- Sündermann, J. (1966), Ein Vergleich zwischen der analytischen und der numerischen Berechnung winderzeugter Strömungen und Wasserstände in einem Modellmeer mit Anwendungen auf die Nordsee, Universität Hamburg, Mitteilungen Inst. Meereskunde, No IV.
- Sündermann, J. (1979), Numerical modelling of circulation in lakes. In: Hydrodynamics of Lakes, ed. W.H. Graf and C.H. Mortimer, Elsevier Scientific Publ. Comp., Amsterdam.
- Thacker, W.C. (1977a), Irregular grid finite difference techniques: simulations of oscillations in shallow circular basins, J. Physical Oceanography, Vol. 7, No 2.
- Thacker, W.C. (1977b), Reply to a discussion of Thacker (1977a), J. Physical Oceanography, Vol. 7, No 6.

- Thacker, W.C. (1978a), Comparison of finite-element and finite-difference schemes, Part 1: one-dimensional wave motion, J. Physical Oceanography, Vol. 8, No 4.
- Thacker, W.C. (1978b), Comparison of finite-element and finite-difference schemes, Part 2: two-dimensional wave motion, J. Physical Oceanography, Vol. 8, No 4.
- Thacker, W.C. (1979), Irregular-grid finite-difference techniques for storm surge calculations for curving coastlines. In: Marine Forecasting, ed. J.C.J. Nihoul, Elsevier Scientific Publishing Company, Amsterdam.
- Wu, J. (1969), Wind stress and surface roughness at air-sea interface, J. Geoph. Res., Vol. 74, No. 2.
- Wylie, C.R. Jr. (1960), Advanced Engineering Mathematics, McGraw-Hill, New York.

C U R R I C U L U M V I T A E

Sebastian Wolfgang Bauer was born on December 3, 1941 in Vienna, Austria, to Dipl. Ing. Wolfgang and Gertrud Bauer.

- 1948 - 1952: Elementary school education in Vienna
- 1952 - 1960: Secondary education at the Real-Gymnasium in Waidhofen an der Ybbs, Lower Austria
- 1960 - 1967: Studies of Rural Civil and Water Resources Engineering at the Institute of Agricultural Technology in Vienna, Austria
- 1967 - 1968: Surveying engineer and assistant site manager with an austrian construction company
- 1968 - 1970: Byllesby Fellow in Hydraulics and Hydrology in the Department of Civil Engineering of Lehigh University in Bethlehem, Pennsylvania, U.S.A.
- 1970 - 1975: Research Officer in the Hydrological Research Unit of the University of the Witwatersrand in Johannesburg, South Africa
- 1975 - : Assistant I in the Hydraulics Laboratory of the Swiss Federal Institute of Technology in Lausanne

Diplomas

- July 1960: Matura
- July 1967: Diplom Ingenieur
- Oct. 1970: Master of Science

Publications and Research Reports

1. FREE OVERFALL AS FLOW MEASURING DEVICE; with Walter H. Graf, J. Irrig. and Drainage Div., Amer. Soc. of Civ. Engrs., Vol. 97, No IR1, Mar. 1971.

CLOSURE to discussions, with Walter H. Graf, Vol. 98, No. IR3, Sep. 1972.
2. DESIGN FLOOD DETERMINATION IN SOUTH AFRICA (metrication of HRU report No. 4/69) in collaboration with D.C. Midgley, W.V. Pitman, R.C. Johanson and I.P.G. Hutchison, Hydrological Research Unit, Dep. of Civil Engineering, University of the Witwatersrand, Report No. 1/72, Johannesburg, Dec. 1972.

3. POLYNOMIAL SURFACE FITTING AND DEPTH-AREA ANALYSIS PROGRAM (LEAST SQUARES METHOD), Hydrological Research Unit, Dep. of Civil Engineering, University of the Witwatersrand, Report No. M2/1973, Johannesburg, 1973.
4. INFILTRATION AND ANTECEDANT PRECIPITATION, a discussion, J. Hydraul. Div., Amer. Soc. of Civ. Engrs., Vol. 100, No HY5, May 1974.
5. A MODIFIED HORTON EQUATION FOR INFILTRATION DURING INTERMITTENT RAINFALL, Hydrological Sciences-Bulletin, XIX, Vol. 2, No. 6, 1974.
6. A SIMPLE PROCEDURE FOR SYNTHESIZING DIRECT RUNOFF HYDROGRAPHS, with D.C. Midgley, Hydrological Research Unit, Dep. of Civil Engineering, University of the Witwatersrand, Report No. 1/74, Johannesburg, Mar. 1974.
7. RAINFALL- AND RUNOFF-DATA RETRIEVAL BY DIGITAL COMPUTER, Hydrological Research Unit, Dep. of Civil Engineering, University of the Witwatersrand, Report No. 2/75, Johannesburg, Feb. 1975.
8. MULTIPLE MUSKINGUM FLOOD ROUTING INCLUDING FLOW LOSSES AND RESERVOIR STORAGES, Hydrological Research Unit, Dep. of Civil Engineering, University of the Witwatersrand, Report No 3/75, Johannesburg, May 1975.
9. DESIGN FLOOD SYNTHESIS BY EXCESS RAIN ROUTING, with D.C. Midgley, S. Afr. Instn. civ. Engrs., Trans., Vol. 17, No 8, Aug. 1975.
10. A MATHEMATICAL SWAMP MODEL, Hydrological Research Unit, Dep. of Civil Engineering, University of the Witwatersrand, Report No. 5/75, Johannesburg, Sep. 1975.
11. LES COURANTS DANS LE LEMAN EN SAISON FROIDE, UNE SIMULATION MATHEMATIQUE, with W.H. Graf and E. Tischer, Bull. Technique de la Suisse Romande, No 19, Sep. 1977.
12. CAMPAGNE DE MESURE DES COURANTS DANS LE LEMAN, with J.P. Prost, W.H. Graf and H. Girod, Bull. Technique de la Suisse Romande, No 19, Sep. 1977.
13. SURELEVATION DU BARRAGE DE LALLA TAKERKOUST, Volume 1: EVACUATEUR DE CRUES ET AMENAGEMENTS AVALS, and Volume 2: VIDANGE DE FOND, Essais sur modèle, with J.P. Prost and J. Bruschin, Département de génie civil, Ecole Polytechnique Fédérale de Lausanne, Report No LHYDREP H-304, Lausanne, Dec. 1977.
14. EIN MATHEMATISCHES WASSER-ZIRKULATIONSMODELL FUR SUMPFLANDSCHAFTEN, Wasserwirtschaft, Vol. 68, No 5, May 1978.

15. WIND INDUCED WATER CIRCULATION OF LAKE GENEVA, with W.H. Graf. In: Marine Forecasting, ed. J.C.J. Nihoul, Elsevier Scientific Publ. Comp., Amsterdam, 1979.
16. THREE-DIMENSIONAL SIMULATION OF TIME-DEPENDENT ELEVATIONS AND CURRENTS IN A HOMOGENEOUS LAKE OF ARBITRARY SHAPE USING AN IRREGULAR-GRID FINITE DIFFERENCE MODEL. In: Hydrodynamics of Lakes, ed. W.H. Graf and C.H. Mortimer, Elsevier Scientific Publ. Comp., Amsterdam, 1979.
17. DATA BANK AND -VISUALIZATION FOR SEQUENTIAL DATA WITH SPECIAL REFERENCE TO LAKE GENEVA. In: Hydrodynamics of Lakes, ed. W.H. Graf and C.H. Mortimer, Elsevier Scientific Publ. Comp., Amsterdam, 1979.
18. MEASURING ON LAKE GENEVA (LE LEMAN), with W.H. Graf, C. Perrinjaquet, J.P. Prost and H. Girod. In: Hydrodynamics of Lakes, ed. W.H. Graf and C.H. Mortimer, Scientific Publ. Comp., Amsterdam, 1979.

